Internal Report
DESY F1-89-01
January 1989

JET PROPERTIES IN e^+e^- ANNIHILATION AT THE CENTER OF MASS ENERGIES BETWEEN 14 AND 44 GeV

by

Krzysztof Genser

Internal Report
DESY F1-89-01
January 1989

Jet Properties in e^+e^- Annihilation at the Center of Mass Energies between 14 and 44 GeV

Krzysztof Genser

A thesis submitted in partial fulfillment of the requirements
for the degree of Doctor of Philosophy (Physics)
at the University of Warsaw

December 1988

Abstract

Jet properties in the e^+e^- annihilation at a center-of-mass energy of 44 GeV were studied with the data collected in the TASSO detector at PETRA. In addition the earlier data at a center-of-mass energy of 14 and 22 GeV, as well as the new data at a center-of-mass energy of 35 GeV, were analysed with the same evaluation procedures for all the energies. Corrected distributions are presented of global shape variables such as sphericity, aplanarity, thrust and Parisi C and D variables, as well as the inclusive charged particle distributions of e.g. particle momenta, scaled momenta, momenta perpendicular and parallel to the event axis, and particle rapidities over the range of center-of-mass energy from 14 to 44 GeV. The center-of-mass energy evolution of the average sphericity, thrust, aplanarity and particle momenta is shown. The total hadronic cross section for the center-of-mass energy interval $39 \div 47$ GeV is given.

Contents

Introduction 10

1. Multiparticle Production Models 12
- 1.1 Introduction 12
- 1.2 Lund Monte Carlo programme JETSET 6.3 13

2. Description of Jet Properties 14
- 2.1 Introduction 14
- 2.2 Observables 14

3. The Experiment 16
- 3.1 Experimental Data 16
- 3.2 The PETRA Storage Ring 18
- 3.3 The TASSO Detector 20
  - 3.3.1 The Vertex Detector (VXD) 20
  - 3.3.2 The Central Proportional Chamber (CPC) 22
  - 3.3.3 The Cylindrical Drift Chamber (DC) 23
  - 3.3.4 The Inner Time-of-Flight Counters (ITOF) 24
  - 3.3.5 The Magnet Coil 24
  - 3.3.6 The Forward Detector 26
- 3.4 Data Acquisition and Data Reduction 27
  - 3.4.1 Introduction 27
  - 3.4.2 Hadronic Data 28
  - 3.4.3 Luminosity 30

4. Monte Carlo Event Generators 32
- 4.1 Hadronic Event Generators 32
- 4.2 Background Event Generators 34
- 4.3 Radiative Corrections 36

5. Monte Carlo Detector Simulation 37
- 5.1 Introduction 37
- 5.2 MONSTER 37
- 5.3 Detector Studies at 44 GeV 38
  - 5.3.1 Noise inside the DC and CPC 38
  - 5.3.2 Efficiency of the CPC and DC 42
  - 5.3.3 Resolution of the DC 42
  - 5.3.4 Cross-talk in the DC 42
  - 5.3.5 TASSO Detector Response and the improved MONSTER Monte Carlo 62
- 5.4 Comparison of the Data and the Monte Carlo Results 64

6. Total Cross Section 70

7. Particle Momentum Spectra 73
- 7.1 Introduction 73
  - 7.1.1 Corrections 73
  - 7.1.2 The Statistical and Systematic Errors 74
- 7.2 Particle Momentum Spectra 74
  - 7.2.1 Momentum Distribution 74
  - 7.2.2 Scaled Momentum Distribution 79
- 7.3 Distribution of global Event Parameters 83
  - 7.3.1 Sphericity Distribution 83
  - 7.3.2 Aplanarity Distribution 83
  - 7.3.3 Thrust Distribution 87
  - 7.3.4 Parisi C and D Variables Distribution 87
  - 7.3.5 Angular Distribution of the Event Axis 96
- 7.4 Single Particle Distributions with Respect to the Event Axis 98
  - 7.4.1 Longitudinal and transverse Momentum Distributions 98
  - 7.4.2 Scaled longitudinal and transverse Momentum Distributions 110

7.4.3 Particle and Momentum Flow around the Thrust Axis 110

7.4.4 Rapidity Distribution 123

7.5 Single Particle Distributions with Respect to the oriented Event Axis 125

7.5.1 Orientation of the Event Axis 126

7.5.2 Rapidity Distribution 130

7.5.3 Scaled Momentum Distribution 130

8. Comparison of the Data with the Monte Carlo Calculations and with Data from other Experiments 150

8.1 Data at 44 GeV versus Lund LLA+O(α_s) and Lund O(α_s^2) Monte Carlo programs 150

8.1.1 Introduction 160

8.1.2 Event Parameters and Inclusive Spectra 161

8.1.3 Energy Dependence of the Observables 161

8.2 Comparison of the TASSO and MARK II Results 163

Summary 164

Literature 172

Members of the TASSO Collaboration 177

List of Tables

Table 3.1 Event data samples. 16

Table 3.2 Material in the TASSO vertex detector. 24

Table 3.3 Principal dimensions of the CPC. 25

Table 4.1 Lund Monte Carlo parameters used at W=14, 22, 35 and 44 GeV. 35

Table 4.2 Background contamination. 36

Table 5.1 DC residuals in two prong events at $\overline{W}$=44 GeV. 51

Table 5.2 Cross-talk probabilities for the 0° DC layers at $\overline{W}$=44 GeV. 54

Table 5.3 χ^2 per degree of freedom for some uncorrected distributions at $\overline{W}$=14, 22, 35 and 44 GeV. 69

Table 6.1 Contributions to the systematic error of R at $\overline{W}$=44 GeV. 71

Table 6.2 Comparison of R measurements. 72

Table 7.1 Cuts and conditions used for systematic errors estimation. 75

Table 7.2 Average values of track and event parameters. 75

Table 7.3 Normalized momentum distributions $1/\sigma_{tot}\, d\sigma/dp$ (GeV/c)$^{-1}$. 77

Table 7.4 Normalized scaled momentum distributions $1/\sigma_{tot}\, d\sigma/dx_p$, where $x_p = 2p/W$. 79

Table 7.5 Normalized scaled momentum distributions $1/\sigma_{tot}\, d\sigma/dx_p$, where $x_p = 2p/W$ in the binning used in fits. 82

Table 7.6 Fit results to the s-dependence of the scaled cross section $1/\sigma_{tot}\, d\sigma/dx_p = c_1(1 + c_2 \ln(s/s_o))$, where s_o = 1 GeV^2. 82

Table 7.7 Normalized $\ln(1/x_p)$ distributions $1/\sigma_{tot}\, d\sigma/d\ln(1/x_p)$, where $x_p = 2p/W$. 85

Table 7.8 Normalized sphericity distributions $1/N\, dN/dS$. 87

Table 7.9 Normalized aplanarity distributions $1/N\, dN/dA$. 90

Table 7.10 Normalized thrust distributions $1/N\, dN/dT$. 90

Table 7.11 Normalized Parisi C distributions $1/N\, dN/dC$. 94

Table 7.12 Normalized Parisi D distributions $1/N\, dN/dD$. 94

Table 7.13 Angular distributions of the sphericity axis $1/N\, dN/d\cos\Theta_S$. 96

Table 7.14 Angular distributions of the thrust axis $1/N\, dN/d\cos\Theta_T$. 98

Table 7.15 Angular distributions of the Parisi Tensor axis $1/N\, dN/d\cos\Theta_P$. 101

Table 7.16 Fit result to the angular dependence of the event axis $1/N\, dN/d\cos\theta_{S,T,P} \sim (1 + a_{S,T,P}\cos^2\theta)$. 102

Table 7.17 Normalized longitudinal momentum distributions $1/\sigma_{tot}\, d\sigma/dp_{\parallel}$ (Gev/c)$^{-1}$. 104

Table 7.18 Normalized transverse momentum distributions $1/\sigma_{tot}\, d\sigma/dp_{\perp}$ (GeV/c)$^{-1}$. 106

Table 7.19 Normalized distributions of the transverse momentum squared $1/\sigma_{tot}\, d\sigma/dp_\perp^2$ (GeV/c)$^{-2}$. 108

Table 7.20 Normalized distributions of the average transverse momentum squared $1/N\, dN/d < p_\perp^2 >$ (GeV/c)$^{-2}$. 113

Table 7.21 Normalized distributions of the average transverse momentum squared *in* the event plane $1/N\, dN/d < p_{\perp in}^2 >$ (GeV/c)$^{-2}$. 113

Table 7.22 Normalized distributions of the average transverse momentum squared *out* of the event plane $1/N\, dN/d < p_{\perp out}^2 >$ (GeV/c)$^{-2}$. 116

Table 7.23 Normalized distributions of the scaled longitudinal momentum $1/\sigma_{tot}\, d\sigma/dx_\parallel$, where $x_\parallel = 2p_\parallel/W$. 116

Table 7.24 Normalized distributions of the scaled longitudinal momentum $1/\sigma_{tot}\, d\sigma/dx_\parallel$, where $x_\parallel = 2p_\parallel/W$ in the binning used in fits. 118

Table 7.25 Fit results to the s-dependence of the scaled cross section $1/\sigma_{tot}\, d\sigma/dx_\parallel = c_1(1 + c_2 \ln(s/s_o))$, where $s_o = 1$ GeV^2. 118

Table 7.26 Normalized distributions of the scaled transverse momentum $1/\sigma_{tot}\, d\sigma/dx_\perp$, where $x_\perp = 2p_\perp/W$. 121

Table 7.27 Normalized distributions of the angle α between the charged particle direction and the thrust axis $1/\sigma_{tot}\, d\sigma/d\alpha$. 123

Table 7.28 Charged momentum flow around the thrust axis. 125

Table 7.29 Normalized rapidity distributions with respect to the thrust axis $1/\sigma_{tot}\, d\sigma/dy$ (folded around $y = 0$). 127

Table 7.30 Normalized rapidity distributions with respect to the Parisi tensor axis $1/\sigma_{tot}\, d\sigma/dy$ (folded around $y = 0$). 129

Table 7.31 Normalized rapidity distributions with respect to the oriented Parisi tensor axis $1/\sigma_{tot}\, d\sigma/dy$ (part 1). 138

Table 7.32 Normalized rapidity distributions with respect to the oriented Parisi tensor axis $1/\sigma_{tot}\, d\sigma/dy$ (part 2). 139

Table 7.33 Maxima of the $1/\sigma_{tot}\, d\sigma/d\ln(1/x_p)$ spectra and the corresponding Λ values for all particles and for narrow and wide jet separately (for $\Theta = 180^\circ$ and $\Theta = 40^\circ$). 140

Table 7.34 Normalized $\ln(1/x_p)$ distributions $1/\sigma_{tot}\, d\sigma/d\ln(1/x_p)$, where $x_p = 2p/W$, for charged particles in the narrow jet. 142

Table 7.35 Normalized $\ln(1/x_p)$ distributions $1/\sigma_{tot}\, d\sigma/d\ln(1/x_p)$, where $x_p = 2p/W$, for charged particles in the wide jet. 144

Table 7.36 Normalized $\ln(1/x_p)$ distributions $1/\sigma_{tot}\, d\sigma/d\ln(1/x_p)$, where $x_p = 2p/W$, for charged particles in the narrow jet emitted in a 40° cone around the event axis. 146

Table 7.37 Normalized $\ln(1/x_p)$ distributions $1/\sigma_{tot}\, d\sigma/d\ln(1/x_p)$, where $x_p = 2p/W$, for charged particles in the wide jet emitted in a 40° cone around the event axis. 148

Table 7.38 Maxima of the $1/\sigma_{tot}\, d\sigma/d\ln(1/x_p)$ spectra for $\Lambda = .38$ and $\Theta = 180^\circ$ and $\Theta = 40^\circ$. 149

List of Figures

Figure 3.1 The 44 GeV data. 17

Figure 3.2 Layout of PETRA in DESY. 18

Figure 3.3 Monthly integrated luminosity collected by TASSO. 19

Figure 3.4 History of PETRA e^+e^- center-of-mass energy. 20

Figure 3.5 TASSO detector looking from southeast. 21

Figure 3.6 Southeast side of the TASSO detector looking from southwest. 21

Figure 3.7 Northwest side of the TASSO detector looking from above. 22

Figure 3.8 TASSO vertex detector inside the DC and CPC. 23

Figure 3.9 TASSO cylindrical drift chamber. Cut along the beam axis. 25

Figure 3.10 TASSO cylindrical drift chamber. Drift cell geometry. 26

Figure 3.11 TASSO forward detector and luminosity monitor. 26

Figure 3.12 Scheme of the TASSO luminosity monitor. 27

Figure 3.13 TASSO coordinate system. 28

Figure 5.1 Two random trigger events. 39

Figure 5.2 Angular distribution of hits in the random trigger event sample. 40

Figure 5.3 An simulated Bhabha event with an overlaid random trigger event. 41

Figure 5.4 Efficiency of 1-st–4-th 0° layers of the DC. 43

Figure 5.5 Efficiency of 5-th–8-th 0° layers of the DC. 44

Figure 5.6 Efficiency of 9-th 0° and 1-st–3-rd stereo layers of the DC. 45

Figure 5.7 Efficiency of 4-th–6-th stereo layers of the DC. 46

Figure 5.8 Efficiency of 1-st–4-th layers of the CPC. 47

Figure 5.9 Efficiency of the CPC and DC. 48

Figure 5.10 Residuals $(\mathrm{d_H} - \mathrm{d_T})$ in the DC. 49

Figure 5.11 Residuals $(\mathrm{d_{WH}} - \mathrm{d_{WT}})$ in the DC. 50

Figure 5.12 Picture explaining the terminology in the cross-talk investigation. 51

Figure 5.13 Results of the cross-talk investigations in the 5-th 0° layer of the DC. 53

Figure 5.14 Number of hits associated with the tracks in the two prong event sample at $\overline{W}$=44 GeV. 55

Figure 5.15 Number of unassociated hits in the two prong event sample at $\overline{W}$=44 GeV in the DC. 56

Figure 5.16 Number of unassociated hits in the two prong event sample at $\overline{W}$=44 GeV in the CPC. 57

Figure 5.17 Number of hits associated with the tracks in the hadronic event sample at $\overline{W}$=44 GeV. 58

Figure 5.18 Number of unassociated hits in the hadronic event sample at $\overline{W}$=44 GeV in the DC. 59

Figure 5.19 Number of unassociated hits in the hadronic event sample at $\overline{W}$=44 GeV in the CPC. 60

Figure 5.20 Number of hits associated with the tracks in the old hadronic event sample at $\overline{W}$=35 GeV in the CPC and in the DC. 61

Figure 5.21 Number of unassociated hits in the old hadronic event sample at $\overline{W}$=35 GeV in the DC. 62
Figure 5.22 Number of unassociated hits in the old hadronic event sample at $\overline{W}$=35 GeV in the CPC. 63
Figure 5.23 Uncorrected charged multiplicity distribution at $\overline{W}$=44 GeV 65
Figure 5.24 Uncorrected $\cos\theta_{track}$ distribution at $\overline{W}$=44 GeV. 66
Figure 5.25 Uncorrected p_{xy} distribution at $\overline{W}$=44 GeV. 67
Figure 5.26 Uncorrected $\sum p/W$ distribution at $\overline{W}$=44 GeV. 68
Figure 7.1 Normalized momentum distributions $1/\sigma_{tot}\, d\sigma/dp$ $(\mathrm{GeV}/c)^{-1}$ at $\overline{W}$=14, 22, 35 and 44 GeV. 76
Figure 7.2 Average values of the total ($< p >$), transverse ($< p_T >$), and longitudinal ($< p_\parallel >$) momentum as a function of W. 78
Figure 7.3 Normalized scaled momentum distributions $1/\sigma_{tot}\, d\sigma/dx_p$, where $x_p = 2p/W$ at $\overline{W}$=14, 22, 35 and 44 GeV. 80
Figure 7.4 Normalized scaled momentum distributions $1/\sigma_{tot}\, d\sigma/dx_p$, where $x_p = 2p/W$ at $\overline{W}$=14, 22, 35 and 44 GeV. 81
Figure 7.5 Normalized $\ln(1/x_p)$ distributions $1/\sigma_{tot}\, d\sigma/d\ln(1/x_p)$, where $x_p = 2p/W$ at $\overline{W}$=14, 22, 35 and 44 GeV. 84
Figure 7.6 Normalized sphericity distributions $1/N\, dN/dS$ at $\overline{W}$=14, 22, 35 and 44 GeV. 86
Figure 7.7 Normalized aplanarity distributions $1/N\, dN/dA$ at $\overline{W}$=14, 22, 35 and 44 GeV. 88
Figure 7.8 Average sphericity ($< S >$) and aplanarity ($< A >$) as a function of W. 89
Figure 7.9 Normalized thrust distributions $1/N\, dN/dT$ at $\overline{W}$=14, 22, 35 and 44 GeV. 91
Figure 7.10 Average value of 1−thrust ($< 1 - T >$) as a function of W. 92
Figure 7.11 Normalized Parisi C distributions $1/N\, dN/dC$ at $\overline{W}$=14, 22, 35 and 44 GeV. 93
Figure 7.12 Normalized Parisi D distributions $1/N\, dN/dD$ at $\overline{W}$=14, 22, 35 and 44 GeV. 95
Figure 7.13 Angular distributions of the sphericity axis $1/N\, dN/d\cos\Theta_S$ at $\overline{W}$=14, 22, 35 and 44 GeV. 97
Figure 7.14 Angular distributions of the thrust axis $1/N\, dN/d\cos\Theta_T$ at $\overline{W}$=14, 22, 35 and 44 GeV. 99
Figure 7.15 Angular distributions of the Parisi Tensor axis $1/N\, dN/d\cos\Theta_P$ at $\overline{W}$=14, 22, 35 and 44 GeV. 100
Figure 7.16 Normalized longitudinal momentum distributions $1/\sigma_{tot}\, d\sigma/dp_\parallel$ $(\mathrm{Gev}/c)^{-1}$ at $\overline{W}$=14, 22, 35 and 44 GeV. 103
Figure 7.17 Normalized transverse momentum distributions $1/\sigma_{tot}\, d\sigma/dp_\perp$ $(\mathrm{GeV}/c)^{-1}$ at $\overline{W}$=14, 22, 35 and 44 GeV. 105
Figure 7.18 Normalized distributions of the transverse momentum squared $1/\sigma_{tot}\, d\sigma/dp_\perp^2$ $(\mathrm{GeV}/c)^{-2}$ at $\overline{W}$=14, 22, 35 and 44 GeV. 107
Figure 7.19 Average value of the transverse momentum squared ($< p_\perp^2 >$) as a function of W. 109

Figure 7.20 Average values of the average transverse momentum squared *in* ($\ll p^2_{\perp in} \gg$) and *out* ($\ll p^2_{\perp out} \gg$) of the event plane as a function of W. 111
Figure 7.21 Normalized distributions of the average transverse momentum squared $1/N\, dN/d < p_\perp^2 >$ $(\mathrm{GeV}/c)^{-2}$ at $\overline{W}$=14, 22, 35 and 44 GeV. 112
Figure 7.22 Normalized distributions of the average transverse momentum squared *in* the event plane $1/N\, dN/d < p^2_{\perp in} >$ $(\mathrm{GeV}/c)^{-2}$ at $\overline{W}$=14, 22, 35 and 44 GeV. 114
Figure 7.23 Normalized distributions of the average transverse momentum squared *out* of the event plane $1/\sigma_{tot}\, d\sigma/d < p^2_{\perp out} >$ $(\mathrm{GeV}/c)^{-2}$ at $\overline{W}$=14, 22, 35 and 44 GeV. 115
Figure 7.24 Normalized distributions of the scaled longitudinal momentum $1/\sigma_{tot}\, d\sigma/dx_\parallel$, where $x_\parallel = 2p_\parallel/W$ at $\overline{W}$=14, 22, 35 and 44 GeV. 117
Figure 7.25 Normalized distributions of the scaled longitudinal momentum $1/\sigma_{tot}\, d\sigma/dx_\parallel$, where $x_\parallel = 2p_\parallel/W$ at $\overline{W}$=14, 22, 35 and 44 GeV. 119
Figure 7.26 Normalized distributions of the scaled transverse momentum $1/\sigma_{tot}\, d\sigma/dx_\perp$, where $x_\perp = 2p_\perp/W$ at $\overline{W}$=14, 22, 35 and 44 GeV. 120
Figure 7.27 Normalized distributions of the angle α between the charged particle direction and the thrust axis $1/\sigma_{tot}\, d\sigma/d\alpha$ at $\overline{W}$=14, 22, 35 and 44 GeV. 122
Figure 7.28 Charged momentum flow around the thrust axis at $\overline{W}$=14, 22, 35 and 44 GeV. 124
Figure 7.29 Normalized rapidity distributions with respect to the thrust axis $1/\sigma_{tot}\, d\sigma/dy$ (folded around $y = 0$) at $\overline{W}$=14, 22, 35 and 44 GeV. 126
Figure 7.30 Normalized rapidity distributions with respect to the Parisi tensor axis $1/\sigma_{tot}\, d\sigma/dy$ (folded around $y = 0$) at $\overline{W}$=14, 22, 35 and 44 GeV. 128
Figure 7.31 Monte Carlo rapidity distributions with respect to the oriented thrust axis. 131
Figure 7.32 Monte Carlo rapidity distributions with respect to the oriented sphericity axis. 132
Figure 7.33 Monte Carlo rapidity distributions with respect to the oriented Parisi tensor axis. 133
Figure 7.34 Particle mass effects on the Monte Carlo rapidity distribution. 134
Figure 7.35 Uncorrected rapidity distributions with respect to the oriented Parisi tensor axis at $\overline{W}$=44 GeV. TASSO data and Lund Monte Carlo results. 135
Figure 7.36 Monte Carlo studies on rapidity distribution with respect to the oriented Parisi tensor axis. 136
Figure 7.37 Normalized rapidity distributions with respect to the oriented Parisi tensor axis $1/\sigma_{tot}\, d\sigma/dy$ at $\overline{W}$=14, 22, 35 and 44 GeV. 137
Figure 7.38 Normalized $\ln(1/x_p)$ distributions $1/\sigma_{tot}\, d\sigma/d\ln(1/x_p)$, where $x_p = 2p/W$, for charged particles in the narrow jet at $\overline{W}$=14, 22, 35 and 44 GeV. 141
Figure 7.39 Normalized $\ln(1/x_p)$ distributions $1/\sigma_{tot}\, d\sigma/d\ln(1/x_p)$, where $x_p = 2p/W$, for charged particles in the wide jet at $\overline{W}$=14, 22, 35 and 44 GeV. 143

Figure 7.40 Normalized $\ln(1/x_p)$ distributions $1/\sigma_{tot}\, d\sigma/d\ln(1/x_p)$, where $x_p = 2p/W$, for charged particles in the narrow jet emitted in a 40° cone around the event axis at $\overline{W}$=14, 22, 35 and 44 GeV. 145
Figure 7.41 Normalized $\ln(1/x_p)$ distributions $1/\sigma_{tot}\, d\sigma/d\ln(1/x_p)$, where $x_p = 2p/W$, for charged particles in the wide jet emitted in a 40° cone around the event axis at $\overline{W}$=14, 22, 35 and 44 GeV. 147
Figure 8.1 Normalized sphericity distributions $1/N\, dN/dS$ at $\overline{W}$=44 GeV 152
Figure 8.2 Normalized aplanarity distributions $1/N\, dN/dA$ at $\overline{W}$=44 GeV. 153
Figure 8.3 Normalized distributions of the average transverse momentum squared *in* the event plane $1/N\, dN/d < p^2_{\perp in} >$ (GeV/c)$^{-2}$ at $\overline{W}$=44 GeV. 154
Figure 8.4 Normalized distributions of the average transverse momentum squared *out* the event plane $1/N\, dN/d < p^2_{\perp out} >$ (GeV/c)$^{-2}$ at $\overline{W}$=44 GeV. 155
Figure 8.5 Normalized scaled momentum distributions $1/\sigma_{tot}\, d\sigma/dx_p$, where $x_p = 2p/W$ at $\overline{W}$=44 GeV. 156
Figure 8.6 Normalized $\ln(1/x_p)$ distributions $1/\sigma_{tot}\, d\sigma/d\ln(1/x_p)$, where $x_p = 2p/W$ at $\overline{W}$=44 GeV. 157
Figure 8.7 Normalized thrust distributions $1/N\, dN/dT$ at $\overline{W}$=44 GeV. 158
Figure 8.8 Normalized $\ln(1/x_p)$ distributions $1/\sigma_{tot}\, d\sigma/d\ln(1/x_p)$, where $x_p = 2p/W$, for charged particles in the narrow jet at $\overline{W}$=44 GeV. 159
Figure 8.9 Normalized $\ln(1/x_p)$ distributions $1/\sigma_{tot}\, d\sigma/d\ln(1/x_p)$, where $x_p = 2p/W$, for charged particles in the wide jet at $\overline{W}$=44 GeV. 160
Figure 8.10 Normalized $\ln(1/x_p)$ distributions $1/\sigma_{tot}\, d\sigma/d\ln(1/x_p)$, where $x_p = 2p/W$, for charged particles in the narrow jet emitted in a 40°cone around the event axis at $\overline{W}$=44 GeV. 161
Figure 8.11 Normalized $\ln(1/x_p)$ distributions $1/\sigma_{tot}\, d\sigma/d\ln(1/x_p)$, where $x_p = 2p/W$, for charged particles in the wide jet emitted in a 40°cone around the event axis at $\overline{W}$=44 GeV. 162
Figure 8.12 Normalized scaled momentum distributions $1/\sigma_{tot}\, d\sigma/dx_p$, where $x_p = 2p/W$. TASSO and MARK II data. 164
Figure 8.13 Normalized sphericity distributions $1/N\, dN/dS$. TASSO and MARK II data. 165
Figure 8.14 Normalized aplanarity distributions $1/N\, dN/dA$. TASSO and MARK II data. 166
Figure 8.15 Normalized thrust distributions $1/N\, dN/dT$. TASSO and MARK II data. 167
Figure 8.16 Normalized transverse momentum distributions $1/\sigma_{tot}\, d\sigma/dp_\perp$ (GeV/c)$^{-1}$. TASSO and MARK II data. 168
Figure 8.17 Normalized distributions of the transverse momentum squared $1/\sigma_{tot}\, d\sigma/dp^2_\perp$ (GeV/c)$^{-2}$. TASSO and MARK II data. 169
Figure 8.18 Normalized rapidity distributions with respect to the thrust axis $1/\sigma_{tot}\, d\sigma/dy$ (folded around $y = 0$). TASSO and MARK II data. 170

Introduction

Study of jets in the e^+e^- collisions has already a long history and began in 1975, when the two-jet structure was discovered on the statistical basis by the SLAC-LBL Collaboration at SPEAR [SCH75, HAN75] through the analysis of the sphericity distributions [BJO70]. The angular distribution of the sphericity axis was in agreement with the assumption that the quarks possess spin 1/2.

In 1978 the DORIS experiments [BER78, DAR78, BIE78] observed new phenomena at the Υ resonance which, according to the PLUTO analysis [BER81p] with the triplicity method, were interpreted as the Υ three gluon decay. Further analysis indicated, that the gluon possess spin 1 [KOL79].

The jets were first "seen" directly as collimated streams of particles by the PLUTO Collaboration at PETRA [PLU79] in 1978. In 1979 the TASSO Collaboration at PETRA found a new process, which led to three-jet events [TAS79b] interpreted as hard gluon bremsstrahlung. Study of the Ellis-Karliner angle [ELL79] led again to the conclusion, that the data favour a gluon of spin 1 [TAS80b].

Since that time many different aspects of the jet production in the e^+e^- annihilation have been studied (for reviews see e.g. [ALI88, DOR87, WU84, KRA84, SOE81], which made it possible to test the theory of quark and gluon interactions (quantum chromodynamic — QCD, see e.g. [MUT87] and references therein).

Perturbative calculations in QCD are possible only for processes with large four momentum transfer ($Q^2 \gg \Lambda^2$), where Λ is a QCD scale parameter of about $0.1 \div 1$ GeV. As the particles registered in the experiment result from processes with Q^2 comparable with Λ^2, one is forced to use phenomenological models (the so called fragmentation models), which describe the conversion of primary partons (quark and gluons) into hadrons.

Study of the fragmentation at different center-of-mass energies gives an important insight into the mechanism of hadron production and allows a comprehensive test of models. The TASSO Collaboration has data over a large center-of-mass energy range, namely from 14 to 44 GeV.

The primary goal of this analysis was to obtain information about jet properties in the e^+e^- annihilation at a center-of-mass energy of 44 GeV. Since the earlier analysis [TAS84j], methods have been improved, so the data taken at lower energies were reanalyzed with the same techniques as used for the 44 GeV data to avoid systematic biases. Moreover, the new TASSO data at a center-of-mass energy of 35 GeV, collected during the year 1986, were analysed too.

The outline of this work is as follows: In the first chapter the Lund Monte Carlo programme JETSET 6.3 is briefly described. Chapter two explains the techniques used to study the jet properties. In the third chapter the experimental data and the TASSO experiment together with its data acquisition and data reduction systems are described. Chapter four and five give details of the Monte Carlo event generators and the Monte Carlo detector simulation programme used in the analysis. In chapter six and seven the obtained results are presented and a critical comparison with the older TASSO results is made. Chapter eight compares the results with other experiments and with the predictions of Monte Carlo models.

CHAPTER 1

Multiparticle Production Models

1.1 Introduction

There have been many models of multiparticle production developed over the last twenty years or so, but the most widespread use found those, which were available in a form of a Monte Carlo programme. The models to be mentioned are [SJO88] those of: Artru-Mennessier [ART74] (historically probably the first one), Field-Feynman [FIE78], Hoyer *et al.* [HOY79], Ali *et al.* [ALI80b], the Lund group [AND79], Weber [WEB84], and Gottschalk-Moris [GOT87].

Each of the models consist in principle of two parts, one dealing with the QCD calculations and the second one taking care about the subsequent parton fragmentation.

Concerning the QCD calculations, the models can be divided into two general groups, namely those in which partons are produced according to the perturbative description in terms of first [ELL76] or second [ALI80a, GAE80, ELL81, VER81, FAB82, KUN81, GOT82, ALI84, GUT84, GOT85, KRA86, GUT87] order in α_s of QCD matrix elements and those in which partons are produced according to a leading logarithm approximation (LLA) [DOK80, REY81, ALT82] to the full QCD structure.

With respect to the fragmentation three main schemes were developed, namely: independent fragmentation (IF) [FIE78], string fragmentation (SF) [AND79] and cluster fragmentation (CF) [FOX80, FIE83, GOT84].

In the two recent studies [MII88, TAS88b] two multiparticle production models were found to be the best in describing features of hadronic events in the e^+e^- annihilation. Both of them are available in the Monte Carlo programme JETSET 6.3 by the Lund group [SJO86, SJO87].

1.2 Lund Monte Carlo programme JETSET 6.3

The Lund Monte Carlo programme provides two main options on the parton level: the matrix element option (denoted further as Lund O(α_s^2)) and the parton shower option (denoted further as Lund LLA+O(α_s)). In both cases the partons fragment according to the Lund string prescription.

In case of Lund O(α_s^2) the initial partons are generated according to the matrix elements calculations of [GUT84] up to the second order in α_s. There are two main parameters for this option: the QCD scale parameter $\Lambda_{\overline{MS}}$ and the minimum scaled invariant mass-squared $y_{min} = m^2_{min}/W^2$ of any two partons in three- or four-jet events (where W is the center-of-mass energy of the e^+e^- system).

In the Lund LLA+O(α_s) option, the initial partons are generated according to the Lund showering algorithm [BEN87a,b]. The shower evolves according to the Altarelli-Parisi equations [ALT77], applied to the basic $q \to qg$, $g \to gg$, $g \to q\bar{q}$ branchings. In the very first branching corrections are introduced to match on the first order matrix elements [ELL76] for the $q\bar{q}g$ production. In subsequent branchings constrains are imposed on the evolution variables to obtain the angular ordering (the so called "coherent" shower) [MUE81, ERM81, BAS83]. There are two main parameters for the Lund shower: the LLA QCD scale parameter Λ_{LLA} and the invariant mass cutoff m^p_{min} below which partons are not assumed to radiate.

After the parton configuration is finally determined, a colour triplet string is stretched between the final quarks, the gluons being the kinks on the string [AND83a,b, SJO84, AND85]. The longitudinal quark fragmentation is governed by the symmetric Lund fragmentation function [AND83b]:

$$f(z) = \frac{1}{z}(1-z)^a e^{-\frac{bm_\perp^2}{z}} \;; \quad m_\perp^2 = p_\perp^2 + m^2,$$

where m is the outgoing hadron mass, $p_\perp$ is its transverse momentum, z is the fraction of remaining $E + p_\parallel$ (energy and longitudinal momentum) taken by the hadron and a, b are free parameters. The $p_\perp$ quarks spectrum is generated according to the Gassian spectrum $e^{-p_\perp^2/2\sigma_q^2}$, where σ_q is a next free parameter.

In the analysis described in the following chapters the Lund LLA+O(α_s) and Lund O(α_s^2) models were used to study the jet properties in the e^+e^- annihilation in terms of shape variables and inclusive distributions of momenta of final charged particles.

CHAPTER 2

Description of Jet Properties

2.1 Introduction

In this analysis the jet nature of hadronic events was studied mostly in terms of shape variables associated with the sphericity tensor [BJO70], first order momentum tensor [PAR78, ELI81, BRO87] and thrust [BRA64, FAR77]. These observables were used to determine the event axis. Single particle distributions were then obtained with respect to it. Only the information about the charged particles was used.

2.2 Observables

Observables not associated with any axis are the track momentum p* (and its average over the whole event sample $< p >$), the scaled momentum $x_p = 2p/W$ (where W is the center-of-mass energy) and $\ln(1/x_p)$. The use of $\ln(1/x_p)$ was suggested e.g. in [DOK88] as an observable to study the soft gluon emission.

The sphericity tensor may be defined as

$$T^{(2)}_{\alpha\beta} = \sum_{j=1}^{N} p_{j\alpha} p_{j\beta}$$

where $\alpha, \beta = x, y, z$; $j = 1, \ldots, N$ particles. If one divides it by $\sum p_j^2$, one obtains the normalized tensor with eigenvalues:

$$Q_k = \frac{\sum(\vec{p}_j \cdot \hat{n}_k)^2}{\sum p_j^2}$$

which correspond to the eigenvectors $\hat{n}_k$. The eigenvalues satisfy the relations:

$$Q_1 + Q_2 + Q_3 = 1 \quad \text{and} \quad 0 \le Q_1 \le Q_2 \le Q_3$$

---

* Throughout this thesis p denotes $|\vec{p}|$.

and are correspondingly measures of flatness, width and length of the event. The sphericity S is defined by:

$$S = \frac{3}{2}(Q_1 + Q_2) \quad \text{and the aplanarity } A \text{ by} \quad A = \frac{3}{2}Q_1.$$

The vectors $\vec{n}_2$ and $\vec{n}_3$ define the so called event plane and the vector $\vec{n}_3$ defines the event (here: sphericity) axis. S approaches 0 for back-to-back two-jet events. Ideal spherical events have $S = 1$. The sphericity axis was used as the event axis, with respect to which transverse and parallel components of the momenta were defined. The quantities studied were S, A, $p_\perp$, $< p_\perp >$, $x_\perp = 2p_\perp/W$, $p_\parallel$, $< p_\parallel >$, $x_\parallel = 2p_\parallel/W$, $p_\perp^2$, $< p_\perp^2 >$, the average of the transverse momentum components *in* and *out of* the event plane: $< p^2_{\perp out} >$, $\ll p^2_{\perp out} \gg$, $< p^2_{\perp in} >$, $\ll p^2_{\perp in} \gg$, where the averages for $< p^2_{\perp out} >$, and $< p^2_{\perp in} >$ are taken over particles of an event and $\ll p^2_{\perp out} \gg$, $\ll p^2_{\perp in} \gg$ denote the averages of $< p^2_{\perp out} >$ and $< p^2_{\perp in} >$ over the whole event sample. Almost all the above mentioned quantities are sensitive to parton transverse momenta and therefore to the gluon emission.

The tensor defined as:

$$T^{(1)}_{\alpha\beta} = \frac{\sum_{j=1}^{N} \frac{p_{j\alpha} p_{j\beta}}{|p_j|}}{\sum_{j=1}^{N} |p_j|}$$

where $\alpha, \beta = x, y, z$; $j = 1, \ldots, N$ particles, was also used to study the event shape. It has eigenvalues

$$L_k = \frac{\sum \frac{(\vec{p}_j \cdot \vec{n}_k)^2}{|p_j|}}{\sum p_j},$$

which correspond to the eigenvectors $\vec{n}_k$. The eigenvalues satisfy the relations:

$$L_1 + L_2 + L_3 = 1, \quad \text{and} \quad 0 \leq L_1 \leq L_2 \leq L_3$$

and its meaning is similar as for those of sphericity. Parisi [PAR78] has defined variables C and D related to the L_k by

$$D = 27 L_1 L_2 L_3 \quad \text{and} \quad C = 3(L_1 L_2 + L_2 L_3 + L_3 L_1).$$

D and C span the range from 0 to 1. For a two-jet event both C and D vanish, while for a planar event $C = 3L_3(1 - L_3)$ and D vanishes. D is only nonzero for non-planar events. It is obvious that C and D are sensitive to the gluon emission, but in contrast to S and A they are linear in the momenta and are calculable in QCD on the parton level. (From now on the tensor $T^{(1)}_{\alpha\beta}$ will be called Parisi tensor.)

Another measure employed to describe the event jet structure is thrust, which is defined as:

$$T = \text{Max} \frac{\sum_{j=1}^{N} |p_{\parallel j}|}{\sum_{j=1}^{N} |p_j|}$$

where $p_\parallel$ is the longitudinal particle momentum relative to the jet axis, which, is chosen such as to maximize $\sum |p_{\parallel j}|$. T ranges from $\frac{1}{2}$ to 1. Extreme two-jet events have $T = 1$.

Once the event axis is defined the rapidity y [FEY69] of a particle may be calculated. It is defined by

$$y = \frac{1}{2} \ln \frac{E + p_\parallel}{E - p_\parallel}$$

where E and $p_\parallel$ are particle energy and parallel component of momentum calculated with respect to the event axis.

CHAPTER 3

The Experiment

3.1 Experimental Data

The high energy data analysed in this thesis were collected with the TASSO detector at the PETRA storage ring at DESY between March 1983 and December 1985. The center-of-mass energy ranged from 39.32 to 46.78 GeV with the average of 43.7 GeV. Fig. 3.1 shows the distribution of event number as a function of center-of-mass energy. The total integrated luminosity was 34.95 pb^{-1}, resulting in 6299 hadronic events (this high energy data will be thereafter called "44 GeV data"). A summary of 44 GeV data as well as the other data analysed in this work is given in Table 3.1.

Table 3.1

The data samples used in this analysis. The center-of-mass energy range, average center-of-mass energy, integrated luminosity, collected number of events.

Data set name	Range of C.M. Energy (GeV)	Average C.M. Energy (GeV)	$\int Ldt$) (pb^{-1})	N° of events
14 GeV	14.02 ÷ 14.04	14.03	1.63	2704
22 GeV	21.99 ÷ 22.00	21.98	2.79	1889
35 GeV	34.91 ÷ 35.10	35.00	110.	31175
44 GeV	39.32 ÷ 46.78	43.70	35.0	6299

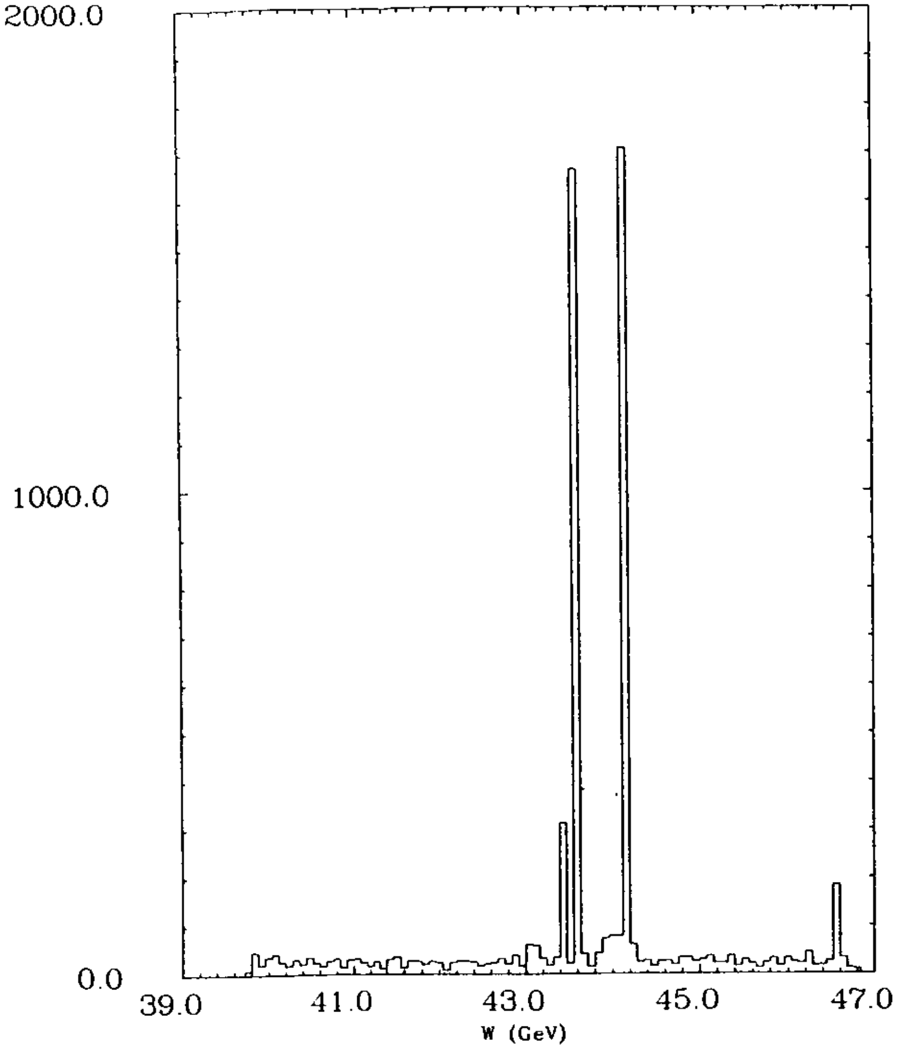

Fig. 3.1. The 44 GeV data. Number of events taken at various values of center-of-mass energy.

3.2 The PETRA Storage Ring

As mentioned before, the data analysed in this work have been taken with the TASSO detector located at the PETRA storage ring in the DESY laboratory in Hamburg, West Germany.

DESY (Deutsches Elektronen-Synchrotron) was established in 1959 and its name was derived from the first accelerator, a 7 GeV electron synchrotron.

PETRA (Positron Elektron Tandem Ring Anlage) was an electron positron (e^+e^-) storage ring. Its was put into operation in September 1978 and was operated over 8 years till November 1986 [PET1-5]. During that period it was the highest energy e^+e^- machine in the world. Its center-of-mass energy ranged from about 12 GeV up to over 46 GeV. The layout of PETRA is shown in Fig. 3.2.

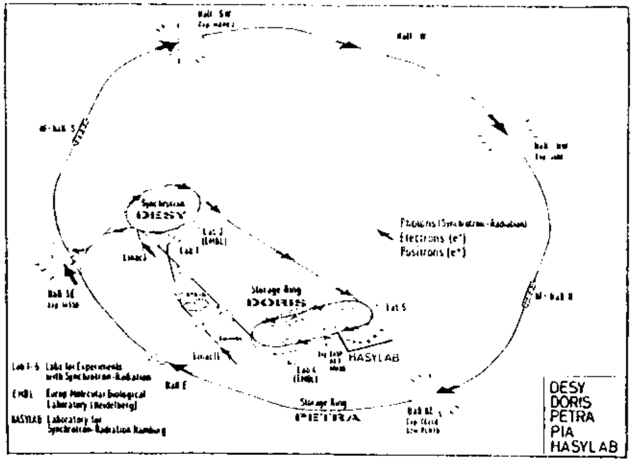

Fig. 3.2. Layout of the PETRA storage ring and its accompanying facilities in the DESY Laboratory.

The whole injecting and accelerating process was as follows: The electrons were produced and accelerated to the energy of 55 MeV in a linear accelerator (LINAC I). Afterwards they were injected into DESY, the original electron synchrotron, accelerated up to 7 GeV and injected into PETRA. To obtain positrons, electrons were produced and accelerated to 250 MeV in another large linear accelerator (LINAC II). The positrons were produced by showering these electrons in a tungsten target. So obtained positrons were subsequently accelerated by LINAC II to 450 MeV and then injected into PIA (Positron Intensity Accumulator, a small storage ring). They were stored there to obtain required beam intensity by the phase space compression. After a sufficient number of positrons was accumulated, they were injected into DESY, accelerated to 7 GeV and then injected into PETRA. Once two electron bunches and two positrons bunches had gained enough particles, PETRA accelerated them to the required beam energy.

PETRA had a circumference of 2.3 km. Its eight curved sections were equipped with sextupole magnets, quadrupole magnets and bending magnets. Four long straight sections were used for rf (radio-frequency) accelerating cavities and four short sections for experiments: CELLO and PLUTO in Hall NE, JADE in Hall NW, MARK-J in Hall SW and TASSO in Hall SE.

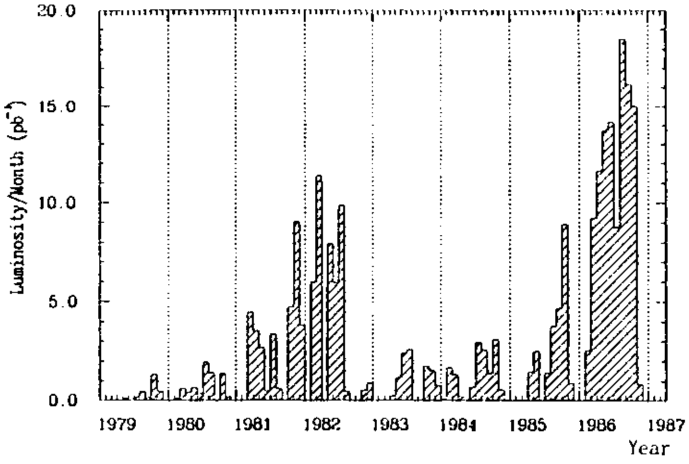

Fig. 3.3. Monthly integrated luminosity collected by TASSO.

One of the parameters characterizing a storage ring is the luminosity L. The luminosity at an interaction point can be expressed as

$$L = \frac{f n^+ n^-}{4\pi\sigma_x\sigma_y}$$

where: $n^\pm$ is the number of $e^\pm$ per bunch, f is the frequency at which the bunches collide in the interaction region and σ_x, σ_y are the r.m.s. values of the beam width in the horizontal and vertical direction in that region.

The luminosity multiplied by a cross section gives the expected number of reactions per second for the specific process. The monthly integrated luminosity collected by the TASSO detector together with the PETRA center-of-mass energies are shown in Fig. 3.3 and 3.4 [SU87].

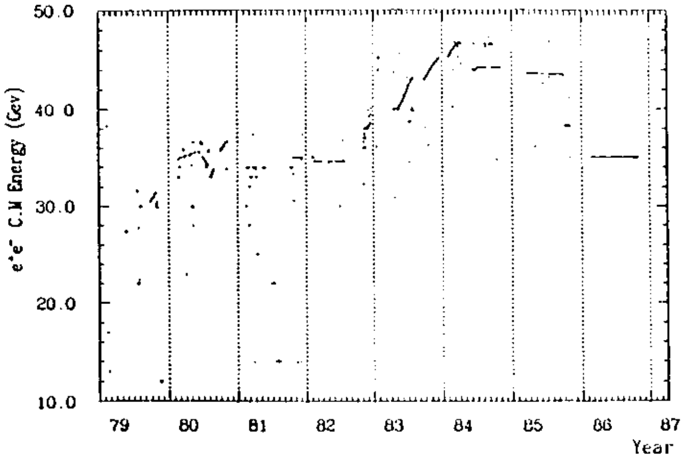

Fig. 3.4. History of PETRA e^+e^- center-of-mass energy.

3.3 The TASSO Detector

The complete TASSO (Two Arm Solenoid Spectrometer) detector is shown in Fig. 3.5-3.7 in the arrangement after the installation of the vertex detector. There were three main parts: the central detector contained inside the solenoid, the external detector and the forward detector. The central detector consisted of the vertex detector, the central proportional chamber, the drift chamber and the inner time-of-flight counters. The external detector was formed by the liquid argon barrel calorimeter, [TAS82a, WIC84] the liquid argon end-cap calorimeter and the hadron arms (from which the name TASSO has been derived). The hadron arms consisted of the planar tube chamber (PTC) [SIE83], the Cherenkov counters [TAS81], the shower counters [TAS80], the time-of-flight counters [BEL81], and the muon chambers [OGG81].

Below follows a description of those parts of the detector which were important for the analysis presented in this thesis. The components will be described going outwards, starting from the innermost one.

3.3.1 The Vertex Detector (VXD)

The vertex detector [CAM83, BIN85] which was added to the TASSO detector in 1982 and whose external dimensions were constrained by already existing components is shown in Fig. 3.8. The detector was 57 cm long, its most innermost part was a thin beam pipe, which at the same time was a part of the PETRA vacuum system. Next followed a small chamber, which was planned to be used to absorb photons produced in the beam pipe. Then, there was a Kapton sheet followed by an aluminium foil, which was an equipotential

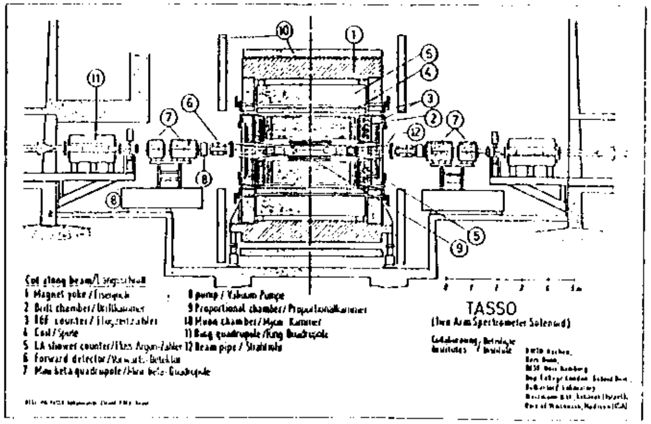

Fig. 3.5. The TASSO detector looking from southeast. Vertical cut along the beam axis.

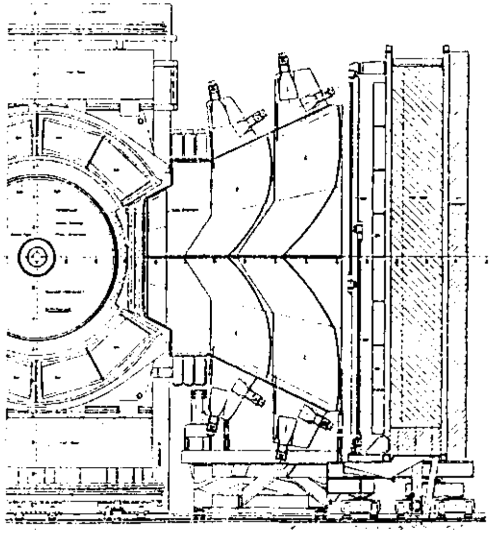

Fig. 3.6. Southeast side of the TASSO detector looking from southwest. Vertical cut through the central point, perpendicular to the beam axis.

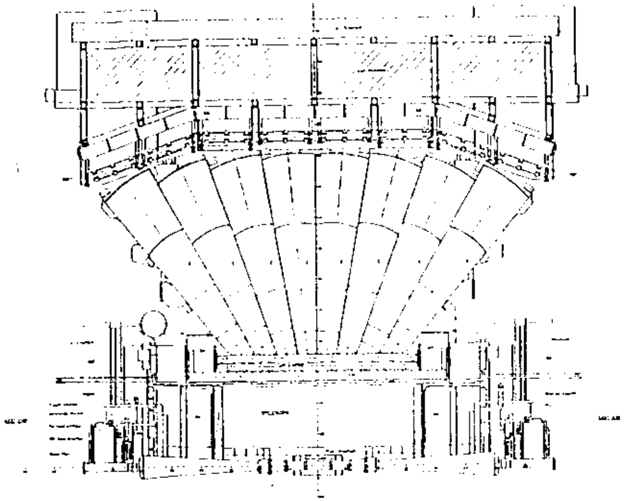

Fig. 3.7. Northwest side of the TASSO detector looking from above. Horizontal cut along the beam axis.

surface. The sensitive part of the VXD was formed by eight layers of anode wires, which were divided into two groups. The exact pattern of anode wires, cathode wires and guard wires is shown in Fig. 3.8c. The VXD worked in a drift chamber mode. The high voltage was applied to the anode wires, the cathode wires were held at ground and the guard wires were held at a small positive potential. There were 72 sense wires in each layer of the inner group and 108 sense wires in each layer of the outer group of anode wires. Next to the last wire layer there was another copper equipotential layer followed by another Kapton sheet. Finally, the detector was enclosed in a pressure vessel consisting of an aluminium cylinder with fiberglass end-flanges.

The detector was operated with an argon/CO_2 95:5 mixture under a pressure of 3 bar. Argon was bubbled through ethanol and the CO_2 through water. The exact description of the material in the VXD can be found in Table 3.2 [CAM83].

3.3.2 The Central Proportional Chamber (CPC)

The sketch of the central proportional chamber [YOU80a, CAM83, DOW80, JAR80] can be seen in Fig. 3.8a,b. The chamber was 149 cm long, with an inner radius of 16 cm and an outer radius of 30.5 cm. It consisted of 4 concentric proportional chambers. Each chamber had 480 equally spaced wires running parallel to the beam axis and 120 inner and 120 outer cathode strips, which formed helices about the beam axis with a rake angle of 36.5°, the inner and outer layers having opposite sense of rotation. The corresponding wire of each chamber was positioned at the same azimuthal angle. The chamber walls were

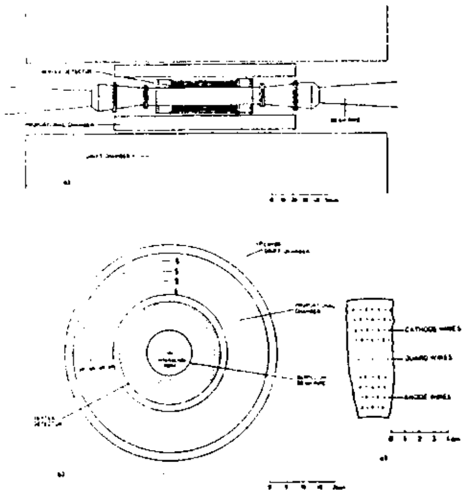

Fig. 3.8. The TASSO vertex detector inside the DC and CPC. a — cut along the beam axis, b — cut perpendicular to the beam axis, c —fragment of the wire pattern.

made out of expanded Styrofoam. These walls formed a backing for the cathode strips, which were formed on 1.9 mm Kapton sheets by a photographic process. The walls were held in position by aluminium end-rings. The basic dimensions of the CPC are contained in Table 3.3 [YOU80a]. The chamber was operated in the proportional mode, using a 75.0:25.0:0.25 argon/isobutane/freon mixture, out of which 25% of argon was additionally bubbled through methylal.

3.3.3 The Cylindrical Drift Chamber (DC)

The cylindrical drift chamber [BOE80, BOE81] is shown on the Fig. 3.9 and 3.10 The chamber was 352 cm long with an inner radius of 32 cm and an outer radius of 128 cm. The inner tube was made of a 5 mm thick fiberglass-epoxy. The outer shell consisted of 6 mm thick aluminium. The DC had 15 layers of drift cells, each cell with the identical geometry shown in Fig. 3.10. Nine layers had wires parallel to the beam axis (the so called "0°" layers). The wires of the remaining six layers were strung at a small angle with respect to the beam axis (the so called "stereo" layers). There were a total of 2340 drift cells in the chamber. The cell pattern had a 12-fold symmetry — it was repeated every 30°. Four of the 0° layers were rotated by half a cell size, so that the sense wires did not line up at the boundaries of the 30° sectors. Five separating cylinders divided the chamber into 6 compartments. The chamber was operated with a 50:50 argon/ethane mixture. The data about the chamber layers can be found in [BOE80].

Table 3.2

Material in the TASSO vertex detector.

Inner Radius (cm)	Material	Thickness (cm)	Radiation length %	Extreme position in z (cm)	Part
6.6665	Cu	0.0015	0.10	19.75	Coating of beam Pipe
6.668	Be	0.17	0.51	19.75	beam Pipe
6.848	70% Ar/ 30% CO_2	0.644	0.0006	19.75	"Xenon" chamber
7.496	Kapton	0.0125	0.04	28.28	Equipotential
7.507	Al	0.005	0.06	28.28	Equipotential
~ 11.46	70% Ar/ 30% CO_2 at 1.2 atm.	7.89	0.07	29.37	Gas
15.40	Cu	0.0030	0.2	29.37	Equipotential
15.403	Kapton	0.0125	0.04	29.37	Equipotential
15.95	Al	0.15	1.69	40.6	Pressure vessel

3.3.4 The Inner Time-of-Flight Counters (ITOF)

The inner time-of-flight scintillation counters [TAS79, MAR82] were placed between the outer wall of the drift chamber and the magnetic coil at a radius of 132 cm. There were 48 counters of the dimensions of 390 x 17 x 2 cm^3 and an attenuation length of 2 m. Each counter was viewed from both ends by a photomultiplier.

3.3.5 The Magnet Coil

The magnet coil [TAS79, FIS80] was 440 cm long with an inner radius of 135 cm. It was providing a field of about 0.5 T, when it was being operated at a full current of 5200 A. The field was constant over the whole volume of the inner detector to within about 6%. The largest variations occurred at small radii at the coil edges.

Table 3.3

Principal dimensions of the CPC.

Plane		Radius (cm)	No. of Channels	Orientation	Strip Width	Separation (mm)
1	Inner Cathode	18.02	120	-36.5°	6.30	1.26
	Anode	18.72	480	0.0°	-	2.5
	Outer Cathode	19.42	120	+36.5°	6.79	1.36
2	Inner Cathode	21.07	120	-36.5°	7.37	1.47
	Anode	21.77	480	0.0°	-	2.8
	Outer Cathode	22.97	120	+36.5°	7.86	1.57
3	Inner Cathode	24.13	120	-36.5°	8.44	1.70
	Anode	24.83	480	0.0°	-	3.3
	Outer Cathode	25.53	120	+36.5°	8.93	1.79
4	Inner Cathode	27.18	120	-36.5°	9.51	1.90
	Anode	27.88	480	0.0°	-	3.7
	Outer Cathode	28.58	120	+36.5°	10.00	2.00

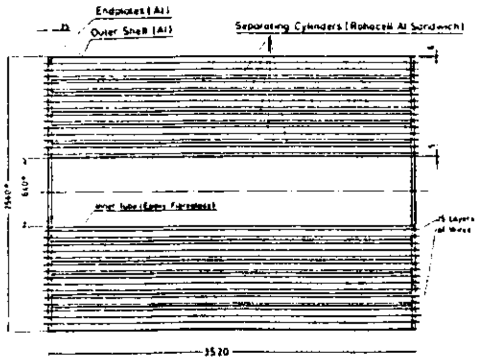

Fig. 3.9. The TASSO cylindrical drift chamber. Cut along the beam axis.

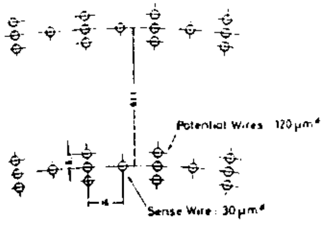

Fig. 3.10. The TASSO cylindrical drift chamber. Drift cell geometry.

3.3.6 The Forward Detector

The forward detector (among others used to measure the luminosity) in its version after May 1982 is shown on the Fig. 3.11-3.12 [JOC84] and Fig. 3.7. One part of it was placed on the east and another one on the west side of the central detector. Each module had a hodoscope of scintillation counters H (see Fig. 3.11), three layers of planar proportional tube chambers P and lead-scintillator sandwich shower counters S. The modules covered the angular range of $0 \leq \Phi \leq 2\pi$ and 28 mrad $\leq \Theta, \pi - \Theta \leq$ 118 mrad and were segmented into eight submodules ($\Delta\Phi = \pi/4$). In addition, there were two sets of small plastic scintillation counters A and C to measure small angle scattering around 50 mrad. The counters were arranged in eight identical arms. Each arm consisted of one acceptance defining counter A ($40 \times 70 \times 5$ mm^3) and a somewhat larger counter C ($60 \times 90 \times 5$ mm^3). The positioning of both types of counters was done with high precision. The distance of the A and C counters from the beam axis was (after July 1983) a=140 mm and b=120 mm (see Fig. 3.11).

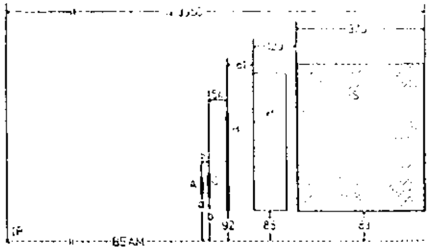

Fig. 3.11. The TASSO forward detector and luminosity monitor in the version after May 1982. Cut along the vector d (see Fig. 3.12).

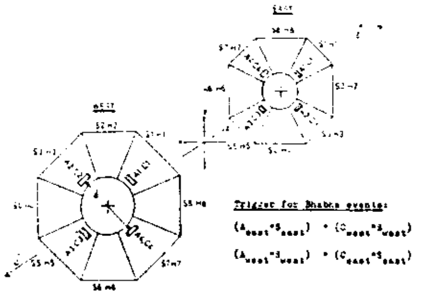

Fig. 3.12. Scheme of the TASSO luminosity monitor in the version after May 1982.

3.4 Data Acquisition and Data Reduction

3.4.1 Introduction

Each component of the detector was equipped with specific electronics, which enabled the readout of the collected information. The total complete readout of the detector required some tens of milliseconds. The average amount of information per event was of the order of 5 kbytes.

PETRA was operated in the four bunch mode with a bunch collision every 3.8 μs in one interaction region. If for each collision one interesting event had occurred, there would have been about 10^{10} events expected per day out of which about 10^6 could have been read out.

One sees, that it is impossible to store such an amount of data and that the readout time was about four orders of magnitude longer than the time between bunch collisions. Moreover, from the average daily luminosity of about 60 nb^{-1} and from the hadronic cross section at 44 GeV center-of-mass energy of about .18 nb one can estimate that about 10 hadronic events should be expected per day. This is also another reason why one had to decide as soon as possible if the last collision had been an interesting one and either read out the detector and reset it, or only reset it and wait for the next bunch collision. The decisions to read out the event or not were taken by the so called triggering system. Since the processes studied with the TASSO detector were quite different in nature, each of them had to have its own trigger(s).

After an event was read out it had to be stored and processed later on by event reconstruction and data reduction programs.

In the following part of this chapter only triggers and programs relevant for the hadronic processes and for the luminosity measurement will be described (in their configuration after 1984). But before it will be done, some details of the TASSO coordinate system will be explained. It is depicted in Fig. 3.13, where $x - y$ $(R - \phi)$ plane is shown.

The origin of the system was placed in the geometrical center of the detector. The x axis pointed towards the center of PETRA ring, the y axis pointed upwards and the z axis pointed towards the positrons flight direction and was chosen such, that the system was right- handed. A track in the $R - \phi$ plane was described by three parameters: r_0 — the radius of the curvature of the track, d_0 —the distance of the closest approach to the origin, and ϕ_0 — the angle of the track to the x axis at its closest approach to the origin. Additionally z_0 —the track z coordinate at its closest approach to the origin and Θ — the track polar angle completed the track description in the full space.

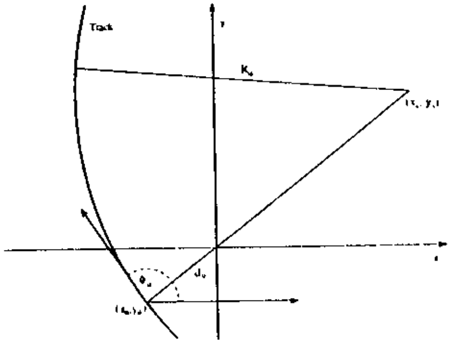

Fig. 3.13. The TASSO coordinate system.

3.4.2 Hadronic Data

The data flow was organized as follows: the data taking computer (VAX 11/750) after getting a signal from the beam pickup system, waited for a signal from the triggering system. When there was a valid trigger, a signal was sent to the front-end processor (MOTOROLA 68000), which performed the read out of the detector and formatting the data. The data were subsequently read out by the data taking computer.

For the hadronic data two trigger processors were of the main interest. These were the drift chamber processor PREPRO [SHI80] and the central proportional chamber CPC processor [YOU80a,JAR80].

The CPC processor was formed by two parts, the first one being the anode CPC-48-Bit processor, which was looking for tracks in the $R - \phi$ plane and the cathode processor, which was providing the z information. The CPC-48-Bit processor demanded hits in the corresponding $R - \phi$ sectors in at least 3 out of 4 layers of the CPC. The hit patterns had to agree with the assumption that the track momentum perpendicular to the beam was higher than 250 MeV.

The DC processor PREPRO was not only analysing the information from the drift chamber, but it also combined it with the information coming from the CPC and ITOF counters. The PREPRO was looking for tracks in the DC by using signals from six 0° layers. A hit pattern was regarded as a valid track in the DC, when it agreed with a hit mask, which had been hard wired into the PREPRO. There were 15 such masks for every out of 72 wires in the first DC layer. They corresponded to the different track momenta within -250 MeV $\div$ $+250$ MeV p_{xy} range (for most of the 44 GeV center-of-mass energy running the transversal momentum threshold was 320 MeV). There had to be at least 5 out of possible 6 hits on the track path in the DC. Additionally there had to be the corresponding CPC bit set and the corresponding ITOF counter had to respond to regard the hit pattern as a valid PREPRO track. If one DC track could be associated with two ITOF counters it was regarded as two tracks. If two DC tracks were associated with the same ITOF counter they were counted as one track only.

Two PREPRO triggers were most important for the hadronic data: the so called majority trigger and the coplanar trigger. The majority trigger demanded 5 (or less at lower energies, but never less then 2) PREPRO tracks. The coplanar trigger demanded two tracks which were colinear in $R-\phi$ plane within 12° (the so called "coplanar fine" trigger) or 25° (the so called "coplanar coarse" trigger). For most of the 44 GeV center-of-mass energy running the coplanar coarse trigger was switched off.

When a valid trigger was set and the event was read out, it was sent to the IBM main frame computer via a special link, to be stored on a magnetic tape and analysed further afterwards. On some events a preliminary reconstruction by the 370E emulators was done before sending to save the IBM CPU time. The preliminary event reconstruction was performed by a special programme called FOREST [CAS81].

In the first step of the event analysis on the IBM main frame computer, an event was reconstructed by the programme FOREST (if there was not enough time to do it on the 370E emulators) and if this programme found at least 3 tracks in the $R-\phi$ plane, all of them with $|d_0| \leq 2.5$ cm, and if at least 2 tracks could have been found in $R-\phi-z$ space with $|d_0| \leq 2.5$ cm and $|z_0| \leq 15$ cm the event was passed on to be reconstructed by a programme called MILL [CAS81], which is a more elaborated version of programme FOREST. MILL takes into account also the $R-\phi$ information coming from the CPC and has higher single track reconstruction efficiency, which amounts 97% for all tracks with $p_{xy} > .1$ GeV/c. FOREST reconstructs tracks with $p_{xy} < .225$ GeV/c with an efficiency of 40%, tracks in the range .25 GeV/c $< p_{xy} \leq .75$ GeV/c with an efficiency of 88% and the remaining tracks with an efficiency of 95 $\div$ 98%. The r.m.s. of the relative momentum resolution of the DC+MILL was $\sigma_p/p = .016\sqrt{1+p^2}$, where p is the track momentum in GeV/c. The angular resolution was typically $\sigma_\phi = 4$ mrad in the azimuth and $\sigma_\Theta = 6$ mrad in the polar angle [TAS84j].

After full MILL reconstruction, charged tracks were accepted if they satisfied the following requirements:

1.) three dimensional reconstruction;

2.) $|d_0| < 5$ cm;

3.) $p_{xy} > .1$ GeV/c;

4.) $|\cos\Theta| \leq .87$;

5.) $|z_0 - z_v| < 20$ cm, where z_v is the z coordinate of the event vertex calculated with the tracks passing the above requirements.

A hadronic event was required to fulfill the following conditions (one should keep in mind, that only charged particles were taken into account):

1.) at least 5 (4) good tracks for a center-of-mass energy $W > 27$ GeV ($W \leq 27$ GeV);

2.) the effective mass of the 3 particle system in events with 1 and 3 ($W \leq 15$ GeV) or 3 and 3 ($W \geq 15$ GeV) particles in each hemisphere (defined by the sphericity tensor) less than the τ mass;

3.) for $W \leq 15$ GeV, at least one track in each hemisphere (defined with the beam axis) and $|\sum Q| \leq 3$, where Q is the particle electric charge;

4.) $|z_v| < 6$ cm;

5.) the momentum sum of accepted particle $\sum p$ had to satisfy $\sum p > .265 \cdot W$.

Events passing all the above cuts were scanned independently by two members of the TASSO collaboration to reject events with artefact tracks, showering high multiplicity Bhabha events or beam-beam pipe interactions events.

In this analysis in addition to the mentioned above cuts in the determination of the event axis related quantities such as e.g. $p_\perp$ to suppress events with the hard photon radiation in the initial state, it was required that $|\cos\Theta_n| > 0.20$, where Θ_n is the angle between the normal to the event plane and the beam direction. To ensure a large acceptance for the particles in the jets, all quantities which depended on the event axis were determined by using events with $|\cos\Theta_{S,T,P}| \leq 0.7$, where $\Theta_{S,T,P}$ is the angle between the sphericity or thrust, or Parisi tensor axis and the beam direction. To avoid fluctuations in the event shape variable distributions all particle momenta which were reconstructed to be larger than $1.5 \cdot p_{beam}$ were rescaled (conserving the direction) to be equal to $1.5 \cdot p_{beam}$.

3.4.3 Luminosity

The luminosity determination was based on the measurement of the Bhabha event rate at a small polar angle, where the Bhabha cross section is large. It was performed using the forward detector [HIL80, JOC84]. The luminosity trigger required at least one out of eight possible coincidences of a H and a S counter pairs and the corresponding H and S pair opposite to the interaction point (Fig. 3.11 and 3.12).

The luminosity was computed, based on the QED Monte Carlo calculations of the Bhabha cross section up to the order of α^3 [BER73,74] for the specific detector configuration taking into account the A counter event rate. Because of the high event rate the statistical error for the luminosity measurement was negligible. The list below shows the single contributions to the systematic error:

1.) accidental coincidences ±2.0%;

2.) showering in the material of the beam pipe and collimators ±2.0%;

3.) missing higher order QED cross-section corrections and Monte Carlo statistics ±1.3%;

4.) geometrical alignment ±1.0%;

5.) showering in the material of the A and C counters ±.5%;

6.) beam position and inclination uncertainties ±.5%;

7.) backward scattering from the S counters ±.2%;

8.) magnetic field inhomogeneities ±.15%.

The total systematic error estimated by adding the different contributions quadratically amounted to be about 3.5-4.5%.

The luminosity was also derived from the wide angle Bhabha scattering registered by the tracking detectors (CPC and DC) [TAS88a]. The coplanar PREPRO trigger was demanded. The following cuts were used to select a wide angle Bhabha event:

1.) two oppositely charged tracks;
2.) acolinearity angle ξ between the two tracks $\xi < 10^\circ$;
3.) $|\cos\Theta| \leq .8$ for each track;
4.) $p > .2 \cdot p_{beam}$ for each track and $\sum p > .7 \cdot p_{beam}$;
5.) the vertex of both tracks had to match the nominal interaction point within .6 cm perpendicular to the beam and 7.5 cm along the beam;
6.) the time-of-flight for each track to be within $-3.0 > t^{meas} - t^{predicted} > 2.0$ ns.

The overall systematic uncertainty for the luminosity determined with this method was 3.0-3.5%. The final luminosity was calculated as an average of results of the two methods. Since both of them agree, a systematic error of 3% was assumed [TAS88a].

CHAPTER 4

Monte Carlo Event Generators

4.1 Hadronic Event Generators

To correct the data (see subsect. 7.1.1) the Lund LLA+O(α_s) Monte Carlo programme (see section 1.2) was used to produce sets of Monte Carlo events at all center-of-mass energies studied. To estimate systematic errors resulting from the Monte Carlo event generator, second set of Monte Carlo events was produced with Lund O(α_s^2) Monte Carlo.

Since it is important that the event generator reproduces the data it is used to correct for, some parameters of the Monte Carlo were adjusted to get an agreement between the data and the Monte Carlo. A tuning method similar to that of a previous TASSO publication [TAS84a] was applied. Because at the beginning of the tuning there were no corrected data at 44 GeV, a sort of iterative procedure was applied to obtain a satisfactory set of Monte Carlo events at this energy. Since at the time when the work was started Lund O(α_s^2) was already a well established code and the Lund LLA+O(α_s) was an rather fresh option, it was originally decided to use the Lund O(α_s^2) Monte Carlo.

One should stress, that the Monte Carlo was used first of all as a tool to obtain the corrected data and not to determine coupling constants or other parameters.

The Tuning Procedure: The tuned parameters were: The QCD scale parameter $\Lambda_{\overline{MS}}$, σ_q the r.m.s. of the Gaussian $p_\perp$ quark spectrum and the parameters a and b of the symmetric Lund fragmentation function. This function was used for the light quarks only. For b and c quarks the Peterson fragmentation function [PET83]

$$f(z) \sim \frac{1}{z(1 - \frac{1}{z} - \frac{\epsilon_q}{1-z})}$$

was used, where z is the fraction of remaining $E + p_\parallel$ (energy plus longitudinal momentum) taken by a hadron. Two sets of ϵ_c and ϵ_b were tried while performing the fits described below, namely $\epsilon_c = .07, \epsilon_b = .01$ and $\epsilon_c = .05, \epsilon_b = .005$. Both sets had values close to the measured by TASSO values [TAS84a, TAS84b], but the former was giving better description of the data and was used in the further analysis. In fits with the symmetric Lund fragmentation function used for b and c quarks the χ^2 of the fit was of about 20% higher than with the Peterson fragmentation function.

Since, as mentioned before, there were no corrected data at 44 GeV, the tuning of the Lund O(α_s^2) Monte Carlo was started with the old TASSO 34.6 GeV corrected data used for the strong coupling constant studies [TAS84a].

The same distributions as in that study were considered (for definitions see Chapter 2), namely $1/N\, dN/dQ_2$, $1/N\, dN/dQ_1$, $1/N\, dN/dL_2$, $1/N\, dN/dL_1$, $1/\sigma_{tot}\, d\sigma/dp^{(S)}_{\perp in}$, $1/\sigma_{tot}\, d\sigma/dp^{(S)}_{\perp out}$, $1/\sigma_{tot}\, d\sigma/dp^{(P)}_{\perp in}$, $1/\sigma_{tot}\, d\sigma/dp^{(P)}_{\perp out}$, $1/\sigma_{tot}\, d\sigma/d\, x_p$, where S or P denotes $p_\perp$ calculated with respect to the sphericity tensor axis or Parisi tensor axis.

First, a lattice of 4 × 4 × 4 points in the $\Lambda_{\overline{MS}}$, a and σ_q space was produced. (For this preliminary fit parameter b was left at the default value of .70) For every lattice point 4000 Monte Carlo events at a center-of-mass energy of 34.6 GeV were generated (in a way to be consistent with the "corrected data", see subsect. 7.1.1) and the above mentioned distributions were calculated. The content of every bin of every distribution was parameterized by a second order polynomial in $\Lambda_{\overline{MS}}$, a and σ_q, whose parameters were chosen to give a good description of the Monte Carlo data. The values for $\Lambda_{\overline{MS}}$, a and σ_q were obtained by a simultaneous fit of these parameterizations to all the above listed distributions, with the minimization programme MINUIT [JAM75]. The linear momentum dependence in Parisi tensor and the quadratic momentum dependence in the sphericity tensor should guarantee an overall good agreement between the data and the Monte Carlo. The following values of parameters were obtained:

$$\Lambda_{\overline{MS}} = .57 \text{ GeV}, \quad a = .81, \quad \sigma_q = .412 \text{ GeV/c}.$$

Next, Lund $O(\alpha_s^2)$ Monte Carlo with these parameters was run at 44 GeV to produce about 5500 events, which were followed through the MONSTER detector simulation described in the next chapter. This Monte Carlo event sample was then used to obtain the preliminary corrected data at 44 GeV.

In the next step, a 4 × 4 × 4 lattice of Monte Carlo points in the $\Lambda_{\overline{MS}}$, a and σ_q space was produced, this time at a center-of-mass energy of 44 GeV. Again the same distributions were used for the tuning and the best parameter values were obtained. This time these were

$$\Lambda_{\overline{MS}} = .70 \text{ GeV}, \quad a = .96, \quad \sigma_q = .400 \text{ GeV/c}.$$

As one can see, the $\Lambda_{\overline{MS}}$ value went up significantly. Next, these parameters were used to produce a large number of events (about 30000 before the selection cuts), again using MONSTER detector simulation.

At this stage also background events described in the next section were added to the sample of events after the detector simulation and the second version of the corrected data at a center-of-mass energy of 44 GeV was obtained. To obtain next version of the corrected data the following was done: A four dimensional 4 × 4 × 4 × 4 grid of Lund $O(\alpha_s^2)$ Monte Carlo points in the $\Lambda_{\overline{MS}}$, a, b and σ_q space was produced at a center-of-mass energy of 44 GeV. Again the tuning was performed, this time using the second version of the corrected data (with the background correction included). The following values at parameters were obtained:

$$\Lambda_{\overline{MS}} = .74 \text{ GeV}, \quad a = 1.10, \quad b = .84, \quad \sigma_q = .420 \text{ GeV/c}.$$

The Lund $O(\alpha_s^2)$ Monte Carlo with these parameter value was run again to produce final (with this Monte Carlo generator) sample of abut 30000 hadronic events before selection cuts. These events, together with formerly produced background events, were applied to produce the third version of the corrected data at 44 GeV.

To be able to estimate the systematic errors coming from the Monte Carlo generator employed, the Lund LLA+$O(\alpha_s)$ Monte Carlo was tuned, using this third version of the corrected data. The following values of the parameters were obtained:

$$\Lambda_{LLA} = .44 \text{ GeV}, \quad a = .87, \quad b = 1.05, \quad \sigma_q = .371 \text{ GeV/c}.$$

The same number of hadronic events as with Lund $O(\alpha_s^2)$ Monte Carlo was produced with this Lund LLA+$O(\alpha_s)$ Monte Carlo (in all cases using the Peterson fragmentation function for b and c quarks with $\epsilon_c = .07, \epsilon_b = .01$.

After a comparison of the data as measured with the TASSO detector with the fully simulated Monte Carlo events was done, it was realized, that indeed the Lund LLA+$O(\alpha_s)$ was describing the data better than the Lund $O(\alpha_s^2)$ (see Table 5.3). After stating this the Lund LLA+$O(\alpha_s)$ Monte Carlo was run at 14, 22 and 35 GeV center-of-mass energies always using the same parameter as for 44 GeV, namely:

$$\Lambda_{LLA} = .44 \text{ GeV}, \quad a = .87, \quad b = 1.05, \quad \sigma_q = .371 \text{ GeV/c}.$$

The agreement between data and Monte Carlo was always good (see Table 5.3).

It was also checked, that the Lund $O(\alpha_s^2)$ programme with the parameters as from the fit at a center-of-mass energy of 35 GeV:

$$\Lambda_{\overline{MS}} = .57 \text{ GeV}, \quad a = .81, \quad \sigma_q = .412 \text{ GeV/c}$$

was properly describing the data at 35, 22 and 14 GeV. The old [HOY79] Monte Carlo was always giving much worse results as compared to both Lund $O(\alpha_s^2)$ and Lund LLA+$O(\alpha_s)$ Monte Carlo. At each center-of-mass energy background events were added to the hadronic events.

The following table (Table 4.1) shows final parameter values of Lund $O(\alpha_s^2)$ and Lund LLA+$O(\alpha_s)$ programs used at each center-of-mass energy. The number of events produced are also shown.

4.2 Background Event Generators

Possible background to the hadronic processes was already estimated in [TAS82b, DAU86]. The only significant contribution to the background was identified to originate form the $e^+e^- \to e^+e^-\gamma\gamma \to e^+e^-$hadrons (thereafter denoted as $\gamma\gamma$) and $e^+e^- \to \tau^+\tau^-$ (thereafter denoted as $\tau^+\tau^-$) processes.

To obtain the proper number of $\gamma\gamma$ and $\tau^+\tau^-$ events passing hadronic cuts, Monte Carlo event generators [BER84, YOU80b] were used.

One of the important parameters characterizing the $\gamma\gamma$ process is the invariant mass of the produced two photon system $W_{\gamma\gamma}$. It is clear, that events with small $W_{\gamma\gamma}$ have small chance to pass the 5-th hadronic cut mentioned in subsect. 3.4.2 ($\sum p > .265 \cdot W$). It is also obvious, that events with small $W_{\gamma\gamma}$ will have rather small multiplicity. Because of these reasons the minimal invariant mass of the two photon system $W_{\gamma\gamma min}$ in the $\gamma\gamma$ Monte Carlo generator was chosen such that $W_{\gamma\gamma min} \leq 0.5 \cdot .265 \cdot W/0.6$ (0.6 to account for missing neutrals [TAS84j].) It was checked, that the number of events with $W_{\gamma\gamma} < W_{\gamma\gamma min}$ passing the selection criteria was negligible.

Table 4.1

Number of events produced and parameter values of Lund $O(\alpha_s^2)$ and Lund LLA+$O(\alpha_s)$ programs used while correcting the data at $\overline{W}$=14, 22, 35 and 44 GeV.

	14 GeV	22 GeV	35 GeV	44 GeV
	Lund LLA+$O(\alpha_s)$			
$\Lambda_{LLA}[GeV]$	.44	.44	.44	.44
a	.87	.87	.87	.87
b	1.05	1.05	1.05	1.05
σ_q [GeV/c]	.371	.371	.371	.371
	Lund $O(\alpha_s^2)$			
$\Lambda_{\overline{MS}}$ [GeV]	.57	.57	.57	.74
a	.96	.96	.96	1.10
b	0.70	0.70	0.70	0.84
σ_q [GeV/c]	.400	.400	.400	.420
N° of MC events	12740	8450	75120	30560
N° of data events	2704	1869	31175	6299

In the $\tau^+\tau^-$ Monte Carlo generator the τ decay modes were set according to the [PDG86] and the exclusive branching ratios were rescaled to match on the topological branching ratios.

At each energy a number of background events was produced, which corresponded to the number of hadronic events produced and to the cross section ratios. The following percentage of $\gamma\gamma$ and $\tau^+\tau^-$ events was found to contaminate the hadronic sample after selection cuts (Table 4.2). The numbers are in agreement with those presented in [TAS82], but slightly disagree with those in [DAU86]. Part of the difference may originate from the fact, that the detector simulation was different in both analyses.

The $\gamma\gamma$ and $\tau^+\tau^-$ events populate specific kinematic regions. These are mostly low multiplicity ($\tau^+\tau^-$ and $\gamma\gamma$) and low $\sum p_{charged}$ ($\gamma\gamma$) events.

The tighter hadronic cuts described in Chapter 6 and subsect. 7.1.2 made to estimate systematic errors should preferentially remove $\gamma\gamma$ and $\tau^+\tau^-$ events, so one can hope, that the uncertainty originating from these processes should be estimated properly.

Table 4.2

The background contamination in hadronic event sample from $\tau^+\tau^-$ and $\gamma\gamma$ processes.

proces	14 GeV	22 GeV	35 GeV	44 GeV
$\gamma\gamma$	0.59% ± 0.08%	1.51% ± 0.15%	1.46% ± 0.05%	1.34% ± 0.08%
$\tau^+\tau^-$	1.23% ± 0.12%	1.15% ± 0.14%	0.85% ± 0.04%	0.94% ± 0.07%
$\sum$	1.83% ± 0.14%	2.66% ± 0.21%	2.31% ± 0.07%	2.28% ± 0.10%

4.3 Radiative Corrections

In all the Monte Carlo generators used, when they were run with radiative effects switched on, the programme based on the work of Berends and Kleiss [BER81] was applied.

CHAPTER 5

Monte Carlo Detector Simulation

5.1 Introduction

The main difficulty with the correction of the data at a center-of-mass energy of 44 GeV was the fact, that this was the limit of the beam energy achievable by PETRA. The running conditions were unfavorable. The synchrotron radiation and beam-beam pipe event rate was high, which led to high background. The tracking chambers had a high current and there were many noise hits. All that led to some doubts if the existing Monte Carlo detector simulation prepared for the "clean" standard conditions was still giving good results at 44 GeV.

In order to answer this question the noise, efficiency, spatial resolution and cross-talk of the central tracking chambers were investigated and the obtained results were used to improve the existing Monte Carlo detector simulation. The so called random trigger events (explained further in this chapter) were overlaid with the generated Monte Carlo events to reproduce the detector response at the 44 GeV running properly (as suggested in [MAE85]). The exact procedure and results of the mentioned investigations are sketched below, preceded by a short description of the appropriate routines of the used Monte Carlo programme.

5.2 MONSTER

The TASSO detector simulation programme MONSTER [MONST] worked as follows: It took an event as produced by an event generator, e.g. by Lund O(α_s^2), then it placed the event vertex in the right position of the TASSO detector frame, taking into account the beam position and its smearing. Afterwards, it tracked the particles step wise through all the components of the detector, in small steps in the inner part (inside the magnet coil) and in big steps in the outer part (outside the coil). MONSTER allowed for multiple scattering, energy loss, photon conversions, nuclear interactions and decay of the particles. After all the particles or their decay products were tracked through all the detector components, the programme simulated the detector response considering resolutions, efficiencies, cross-talks and noises. Although the programme was fairly sophisticated, it did not simulate the synchrotron radiation and beam-beam pipe events. It did not allow for delta electrons, light emission, and photoelectrons either. (Results of an investigation of some of the above effects in the VXD can be found in [SU86]). The noise was simulated only by generating uncorrelated hits with a random pattern and frequency.

5.3 Detector Studies at 44 GeV

In order to find the efficiencies, resolutions and the noise for the 44 GeV running, the TASSO detector response was investigated. Since in the study presented in this thesis the decision was taken to work with charged particles and to use results of the MILL track reconstruction programme, only the central drift chamber and the central proportional chamber were investigated.

5.3.1 Noise inside the DC and CPC

The examination of the tracking devices begun from the noise study. It was done by analysing of about 13000 random trigger events. Since the random trigger event is a rather specific notion, it will be explained briefly now. This is an event taken at a beam crossing, which was chosen by a random number generator. As pointed out in subsect. 3.4.1 the number of bunch collisions in one interaction region in PETRA was of the order of 10^{10} per day. The corresponding total number of all the Bhabha, $\gamma\gamma$, hadronic, $\mu^+\mu^-$ and $\tau^+\tau^-$ events was of the order of 10^2. From comparison of these two numbers one sees, that a random trigger event should be predominantly an "empty" event. It was believed, that such events would carry an information about the synchrotron radiation, beam-beam pipe interactions and the noise in the chambers and in the electronics, i.e. all the processes which were difficult to simulate numerically.

The investigation has shown, that the detector response was very different from event to event. There were "quiet" events with about 44 hit wires in the DC and 35 hit wires in the CPC on the average and "noisy" events (defined here by the overflow in an hit storage bank for the CPC) with an average of 87 and 337 hits in the DC and CPC correspondingly.

Fig. 5.1 shows two complicated random trigger events (coming from the "noisy" event sample). One can see many series of consecutive hits, hits coming from tracks usually originating far from the expected interaction point and of course one can observe very strong correlations among the hits and correlations between the hits in the CPC and the DC.

The angular distribution of the hits in the random trigger events for the first and last layer of the DC and in the first and second layer of the CPC are shown in Fig. 5.2. The distributions for the third and the fourth layer of the CPC (not shown) are influenced mostly by the hardware cut on the length of the hit storage bank for the CPC: The total stored number of the anode wire hits together with the cathode hits could be no more than 400. The cut was throwing away good anode hits when the running conditions were "noisy" (see e.g. Fig. 5.1).

In Fig. 5.2 one can easily observe the synchrotron radiation pattern both in the DC and in the CPC. "Hot" and "dead" wires can be seen also.

All these results showed, that it was difficult to simulate all these features numerically and probably the best idea was to overlay the random trigger events with Monte Carlo events, in order to reproduce all the characteristics properly. Therefore, a special routine was written to take care of this overlaying. The routine was also simulating the hardware cut on the length on the hit storage bank for the CPC and the single hit electronics feature in the DC. An example of a random trigger event overlaid with a simple Monte Carlo Bhabha event is shown in Fig. 5.3.

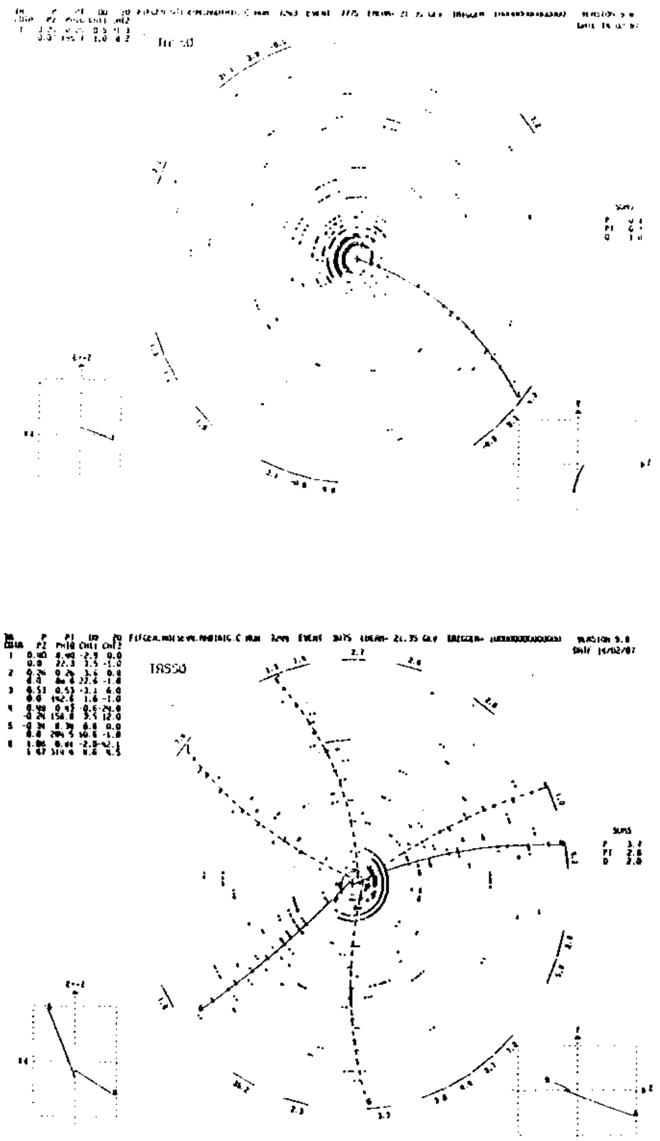

Fig. 5.1. Two random trigger events. W=42.7 GeV ("noisy" event sample, see text).

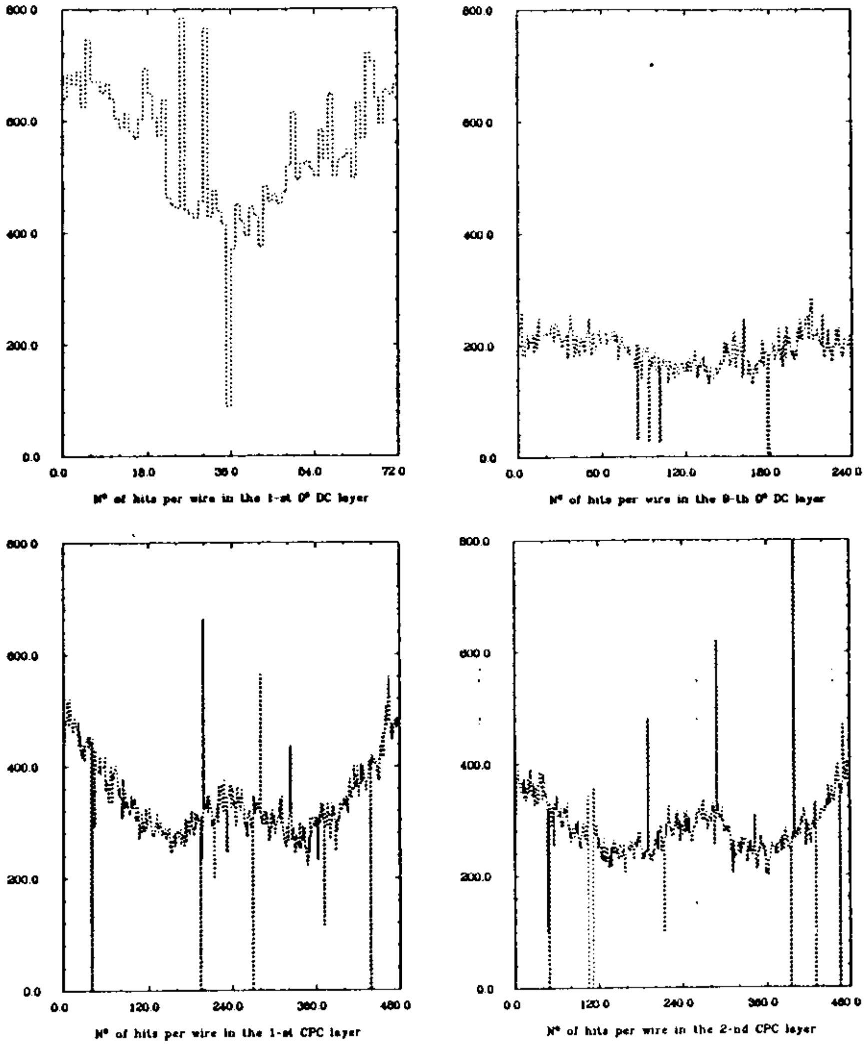

Fig. 5.2. The angular distribution of the hits in the random trigger event sample in the 1-st and 9-th 0° layer of the DC and in the 1-st and 2-nd layer of the CPC at $\overline{W}$=44 GeV. On the abscissa the wire number is shown, on each figure the range corresponds to 2π.

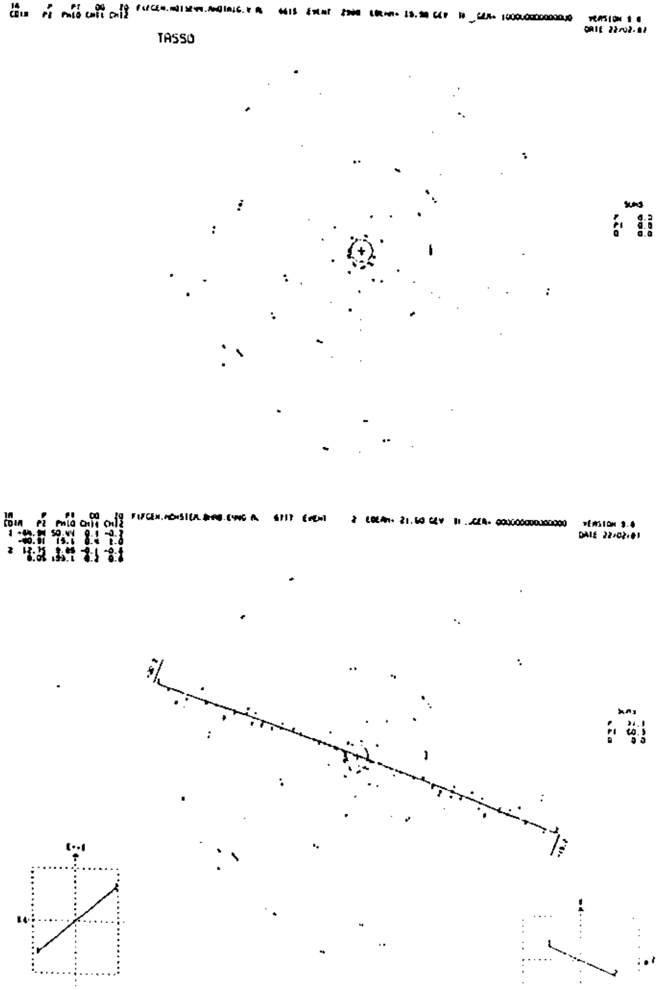

Fig. 5.3. An simulated Bhabha event with an overlaid random trigger event.

5.3.2 Efficiency of the CPC and DC

After implementation of the overlaying of the random trigger events with the Monte Carlo events, the efficiency of the DC and the CPC in the hadronic events was studied. MILL tracks with $|d_0| < 5$ cm, 44.4 GeV $> p_{xy} > .1$ GeV, $|\cos\Theta| \leq .75$, $|z_0| < 5$ cm were used. A special efficiency routine was written to simulate the efficiency of both tracking devices. The Fig. 5.4-5.9 show efficiencies of the DC and the CPC, together with the results of the Monte Carlo simulation, obtained using the new noise and efficiency routines. One can see, that there were some significant inefficiencies in the 9-th 0° and 2-nd and 4-th stereo DC layers and in the 4-th CPC layer. The decreasing efficiency of the CPC with the increasing layer radius was caused mainly by the CPC storage bank cutoff and is also strongly influenced by the noise intensity in the considered data sample. One sees, that the distributions are satisfactorily reproduced by the Monte Carlo routines.

5.3.3 Resolution of the DC

The next item in the detector study was the resolution investigation. But before it was done, the beam position and its spread for the considered running period were incorporated into MONSTER, using the results described in [LOE87].

The resolution of the DC was studied using MILL tracks from two prong events (these were mostly Bhabha events). The tracks had to fulfil the following conditions: $|d_0| < 2$ cm, $|\Delta d_0| < 2$ cm, 44.4 GeV $> p_{xy} > 5.0$ GeV, $|\cos\Theta| \leq .75$, $|z_0| < 5$ cm, $|\Delta z_0| < 5$ cm, be back to back within 20° and have hits in all the 15 layers of the DC.

As a measure of the resolution two kinds of residuals were employed: 1. the distance between the hit position and the track, which the hit is associated with ($d_H - d_T$); 2. the difference between the distances between the wire and the hit and the wire and the track ($d_{WH} - d_{WT}$). The first one (1) is very well suited to study the drift chamber layer alignment and the second one (2) to study the drift time-distance relation. Table 5.1 shows residuals in the considered data sample from the 44 GeV running, compared with results obtained with a Monte Carlo sample with the Gaussian smearing of the "true" hit position of 300 μm. Fig. 5.10-5.11 show the residuals for some selected DC layers. One can see that there were some problems with the drift time-distance relations in the 6-th and 7-th 0° layers and in the 5-th and 6-th stereo layers, which for the 6-th and 7-th 0° layer is visible as a shift of about 300 μm on Fig. 5.11. Except for the problems with the drift time relation the Monte Carlo reproduces the results quite well.

5.3.4 Cross-talk in the DC

The last item in the detector investigations was the cross-talk study in the 0° layers of the DC. Also this study was performed using the two prong events mentioned above with additional requirements, that the events were "quiet". This time it meant no more than 10 hits per DC layer, no more than 20 hits per CPC layer, no more than 4 clusters with 2 or more hits in the 3 consecutive wires, no more than 1 cluster of 5 consecutive hits, no cluster with 7 or more hits in 12 consecutive wires in a single DC layer. These criteria should leave the events with the real cross-talk hits and remove the noisy events.

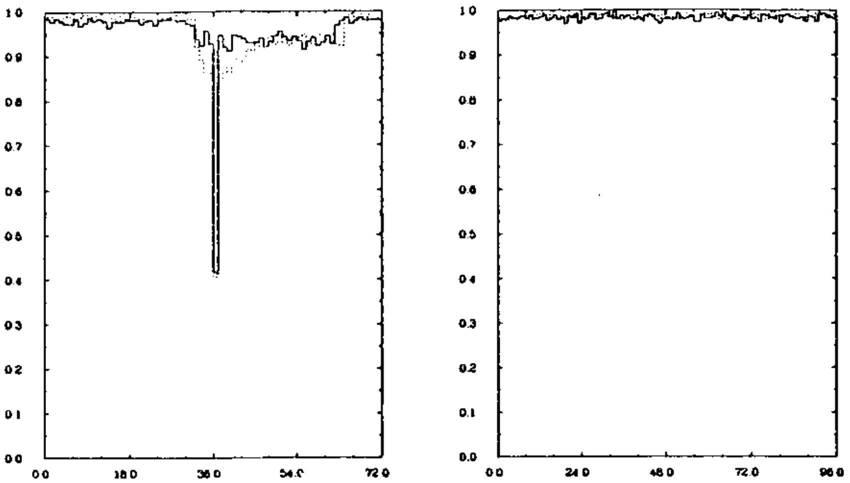

Efficiency of the 1-st 0° DC layer

Efficiency of the 2-nd 0° DC layer

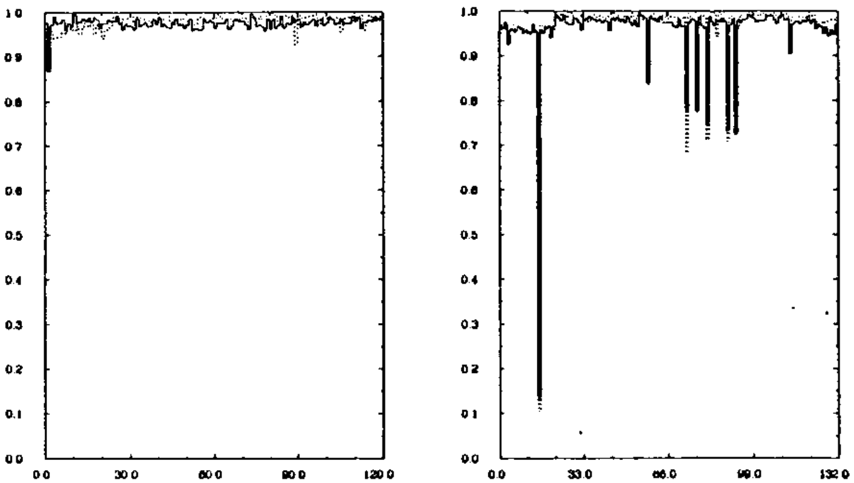

Efficiency of the 3-rd 0° DC layer

Efficiency of the 4-th 0° DC layer

Fig. 5.4. The efficiency of 1-st–4-th 0° layers of the DC at $\overline{W}=44$ GeV. On the abscissa the wire number is shown, on each figure the range corresponds to 2π. Dotted line describes the data, full line describes the Monte Carlo simulation.

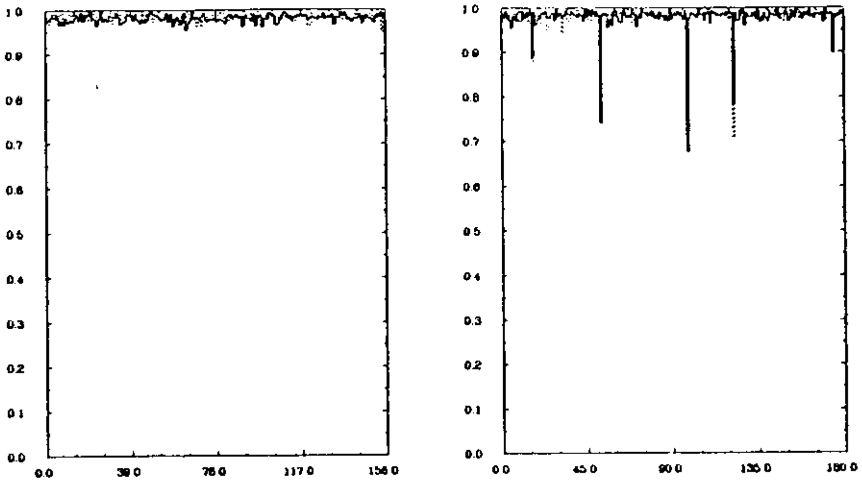

Efficiency of the 5-th 0° DC layer

Efficiency of the 6-th 0° DC layer

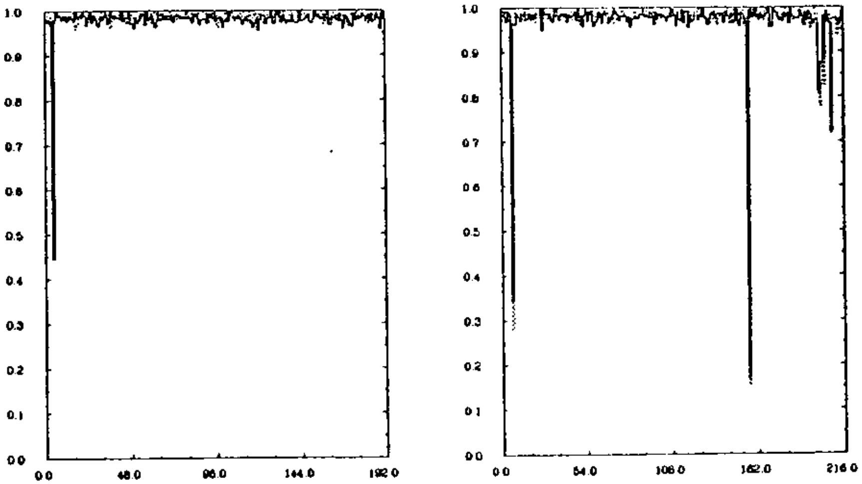

Efficiency of the 7-th 0° DC layer

Efficiency of the 8-th 0° DC layer

Fig. 5.5. The efficiency of 5-th–8-th 0° layers of the DC at $\overline{W}=44$ GeV. On the abscissa the wire number is shown, on each figure the range corresponds to 2π. Dotted line describes the data, full line describes the Monte Carlo simulation.

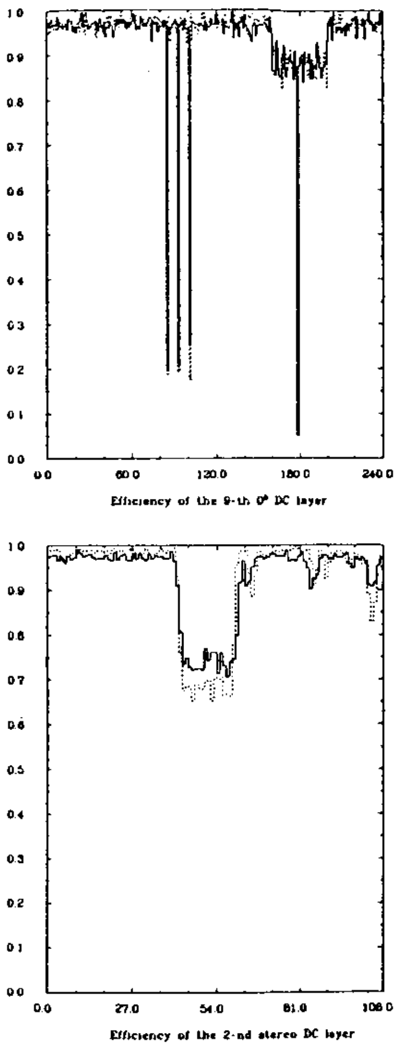
Efficiency of the 9-th 0° DC layer

Efficiency of the 1-st stereo DC layer

Efficiency of the 2-nd stereo DC layer

Efficiency of the 3-rd stereo DC layer

Fig. 5.6. The efficiency of 9-th 0° and 1-st–3-rd stereo layers of the DC at $\overline{W}$=44 GeV. On the abscissa the wire number is shown, on each figure the range corresponds to 2π. Dotted line describes the data, full line describes the Monte Carlo simulation.

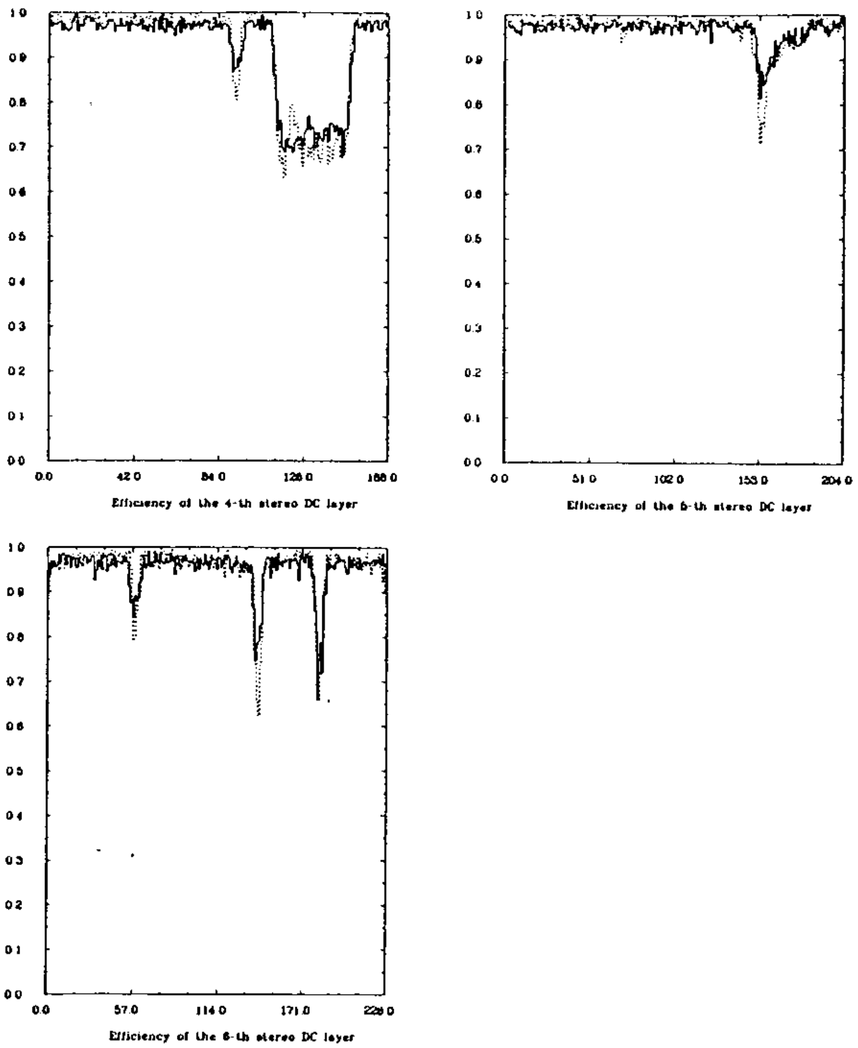
Efficiency of the 4-th stereo DC layer

Efficiency of the 5-th stereo DC layer

Efficiency of the 6-th stereo DC layer

Fig. 5.7. The efficiency of 4-th–6-th stereo layers of the DC at $\overline{W}$=44 GeV. On the abscissa the wire number is shown, on each figure the range corresponds to 2π. Dotted line describes the data, full line describes the Monte Carlo simulation.

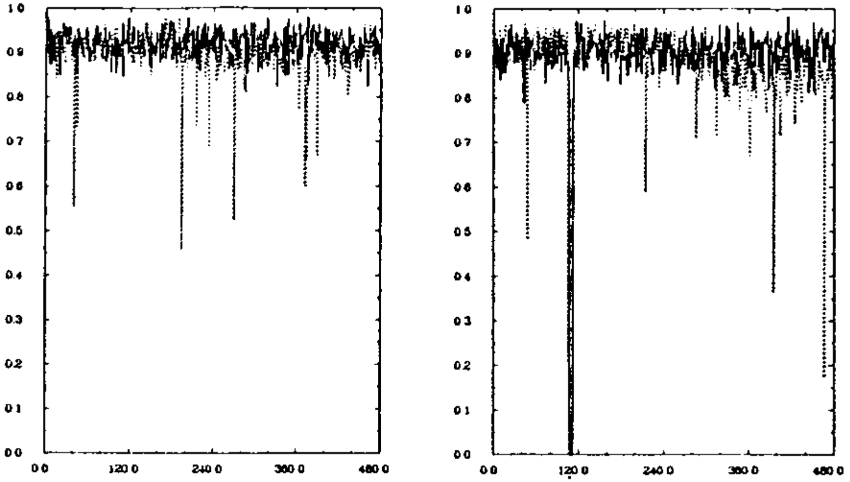

Efficiency of the 1-st CPC layer

Efficiency of the 2-nd CPC layer

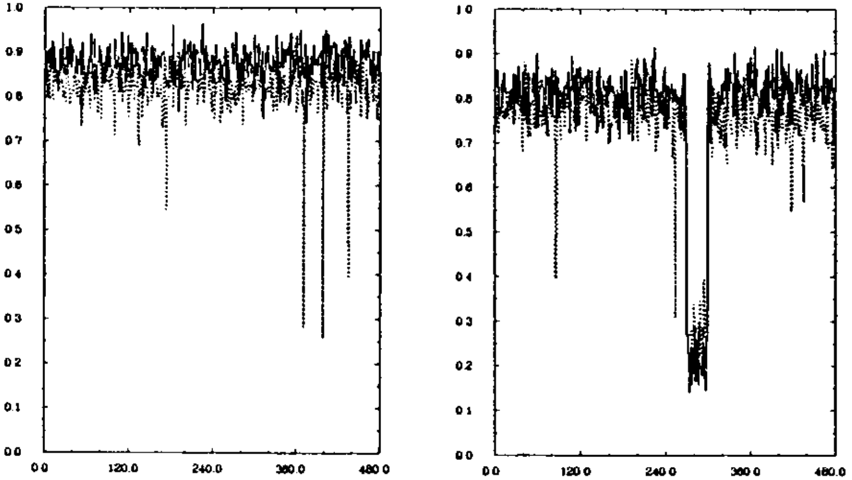

Efficiency of the 3-rd CPC layer

Efficiency of the 4-th CPC layer

Fig. 5.8. The efficiency of 1-st–4-th layers of the CPC at $\overline{W}$=44 GeV. On the abscissa the wire number is shown, on each figure the range corresponds to 2π. Dotted line describes the data, full line describes the Monte Carlo simulation.

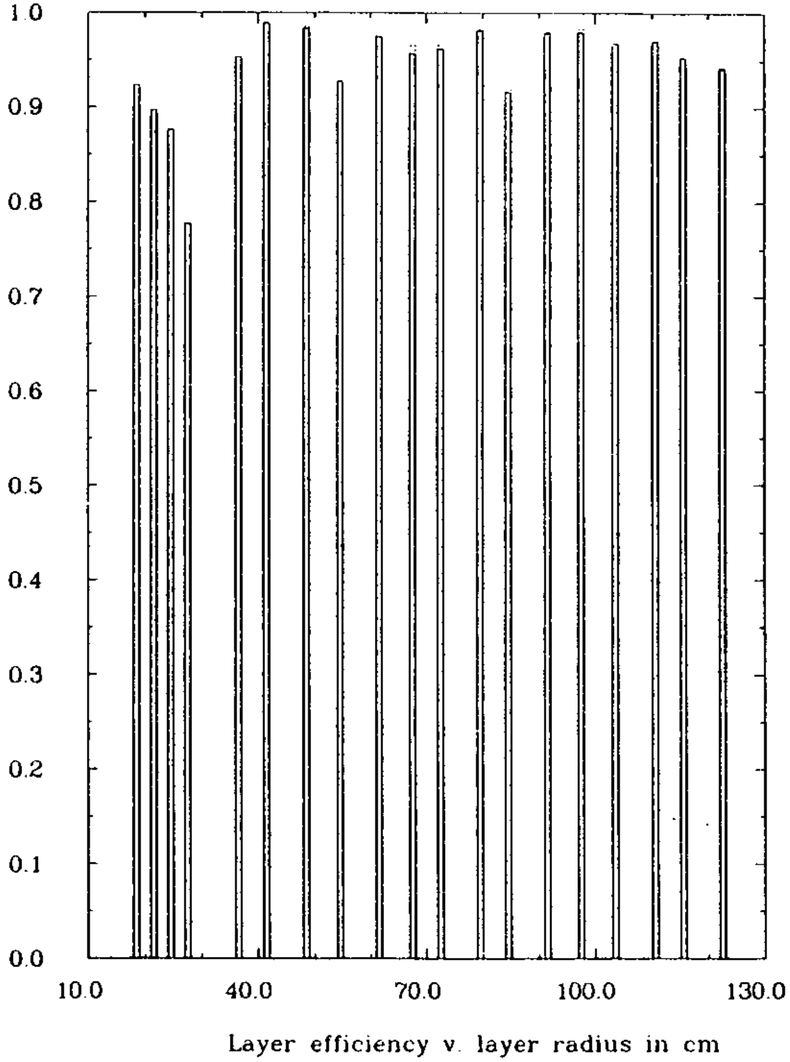

Fig. 5.9. The efficiency of the CPC and DC at $\overline{W}$=44 GeV. On the abscissa the layer radius is shown. Dotted line describes the data, full line describes the Monte Carlo simulation.

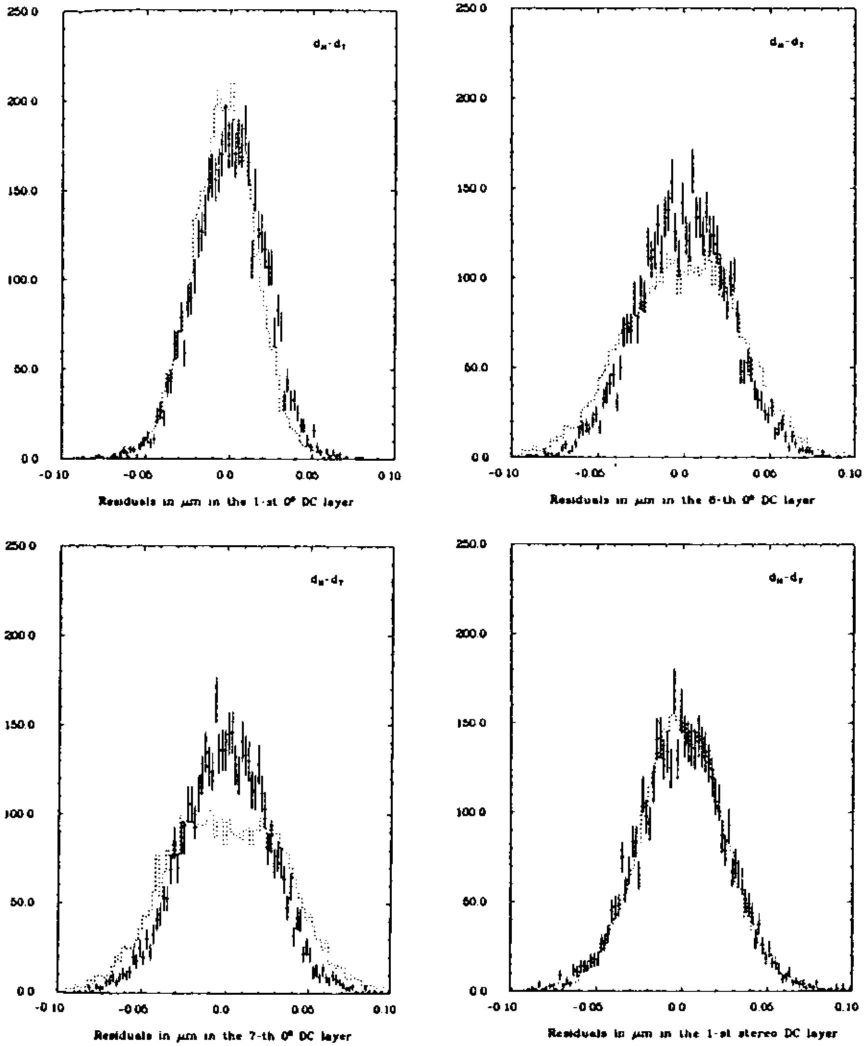

Fig. 5.10. Distributions of the ($d_H - d_T$) residuals (in μm) in the 1-st, 6-th and 7-th 0° and the 2-nd stereo layers of the DC.

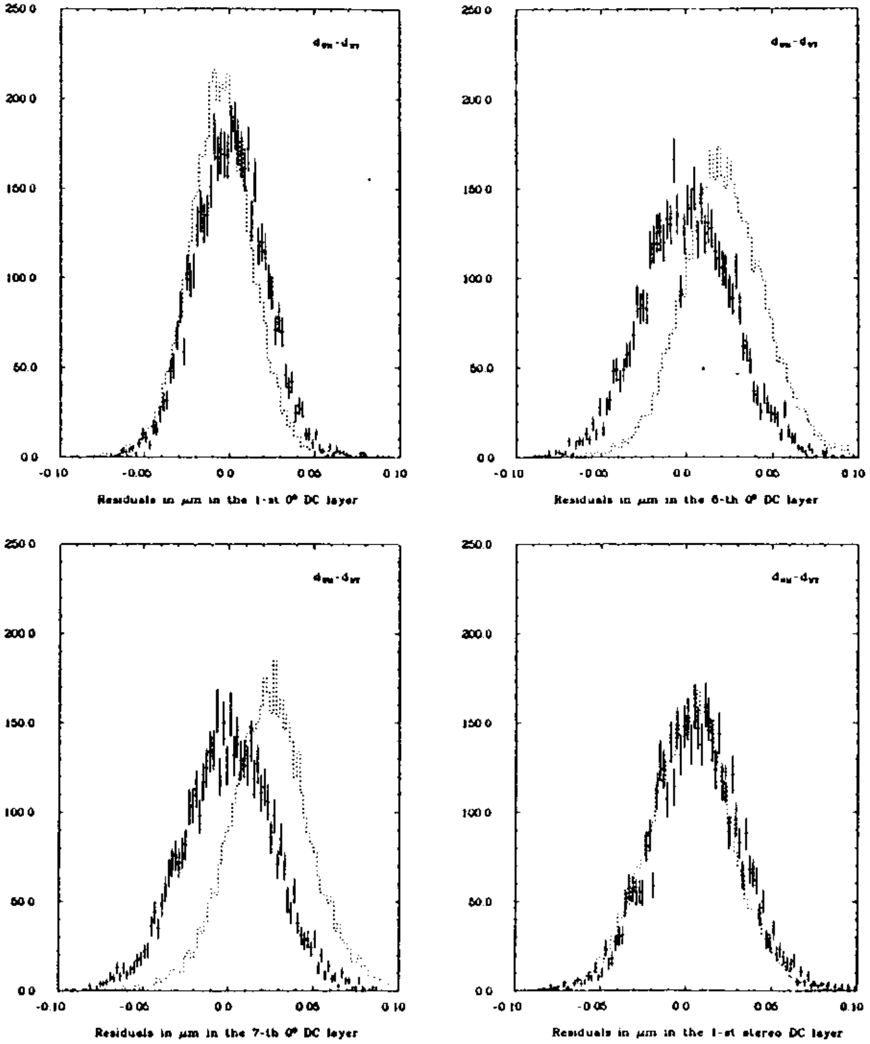

Fig. 5.11. Distributions of the ($d_{WH} - d_{WT}$) residuals (in μm) in the 1-st, 6-th and 7-th 0° and 2-nd stereo layers of the DC.

Table 5.1

DC residuals (r.m.s. in μm) in two prong events, MILL tracks, 15 hits per track, (1–9 are the 0° layers and 10–15 are the stereo layers).

	DATA		MC	
DC layer	$d_H - d_T$	$d_{WH} - d_{WT}$	$d_H - d_T$	$d_{WH} - d_{WT}$
1	210	207	212	212
2	245	245	266	266
3	254	252	271	271
4	280	278	269	269
5	266	257	261	261
6	335	256	267	267
7	356	256	270	270
8	250	252	257	257
9	191	191	172	172
10	265	264	267	260
11	291	291	311	306
12	301	298	306	302
13	316	305	307	304
14	373	330	302	301
15	310	270	247	246

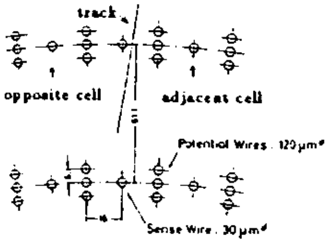

Fig. 5.12. Picture explaining the terminology used in the cross-talk investigation.

The cross-talk was studied by looking for additional hits in the neighborhood of hits associated with a track which crossed a layer. The terminology used in this subsection is explained in Fig. 5.12.

The following plots (Fig. 5.13) show (for the 5-th layer as an example) the probability of finding a hit in the cell adjacent to the cell crossed by a track (when there was a hit in the cell crossed by the track) versus the distance wire–track. The distance hit–wire for the adjacent hit versus the distance hit–wire for the hit associated with the track is also shown. The results indicate, that the cross-talk, if any, was very small (≈ 2%), there were no significant correlations between the track position and the cross-talk probability and between the track position and the cross-talk hit position.

Table 5.2 shows the exclusive (in the sense, that one case can enter into one column only) probabilities of finding a hit in the adjacent cell, in the opposite cell and in both cells (see Fig. 5.12). The numbers are small, the probability was about 2% and was falling with the layer radius, which indicates noise and/or synchrotron radiation as the origin of those hits. There was a small difference between the probabilities for the adjacent and the opposite cell (≈ .3%) indicating that there was some cross-talk, which is also indicated by the probability of having both neighbour cell hit, which is about .2% too big as compared to the pure noise hits. The comparison of the above numbers with the probability of finding a hit in a cell in the specific layer in a corresponding sample of random trigger events indicates that the cross-talk itself was ≈ .5% in the adjacent cell, ≈ 25% in the opposite cell and ≈ .13% in both cells. In the Monte Carlo sample, which was analysed to obtain the results presented in the Table 5.2 the cross-talk was assumed to be .3%, .0% and .0% correspondingly.

5.3.5 TASSO Detector Response and the improved MONSTER Monte Carlo

After all these investigations had been finished and all the results had been implemented into MONSTER, comparisons were made to check the quality of the detector simulation.

Beside comparisons shown before (for efficiencies, residuals and cross-talk), comparisons of the number of hits per track in the data and in the Monte Carlo event samples were made. The results for the two prong events are shown on the Fig. 5.14-5.16. The agreement between the data and the Monte Carlo is very good. The same plots were made for the hadronic events (Fig. 5.17-5.19). Here the agreement is worst, but it is equally good or perhaps even better than for the old detector simulation for the quiet 35 GeV running (Fig. 5.20-5.22). The disagreement comes probably from the lack of simulation of δ-electrons, light emission and wrong drift time-distance relation for some of the DC layers.

This ends the description of some aspects of the detector simulation used for the 44 GeV running. At 35 GeV the same routines were used, at 14 and 22 GeV the old Monte Carlo [MONST] was used.

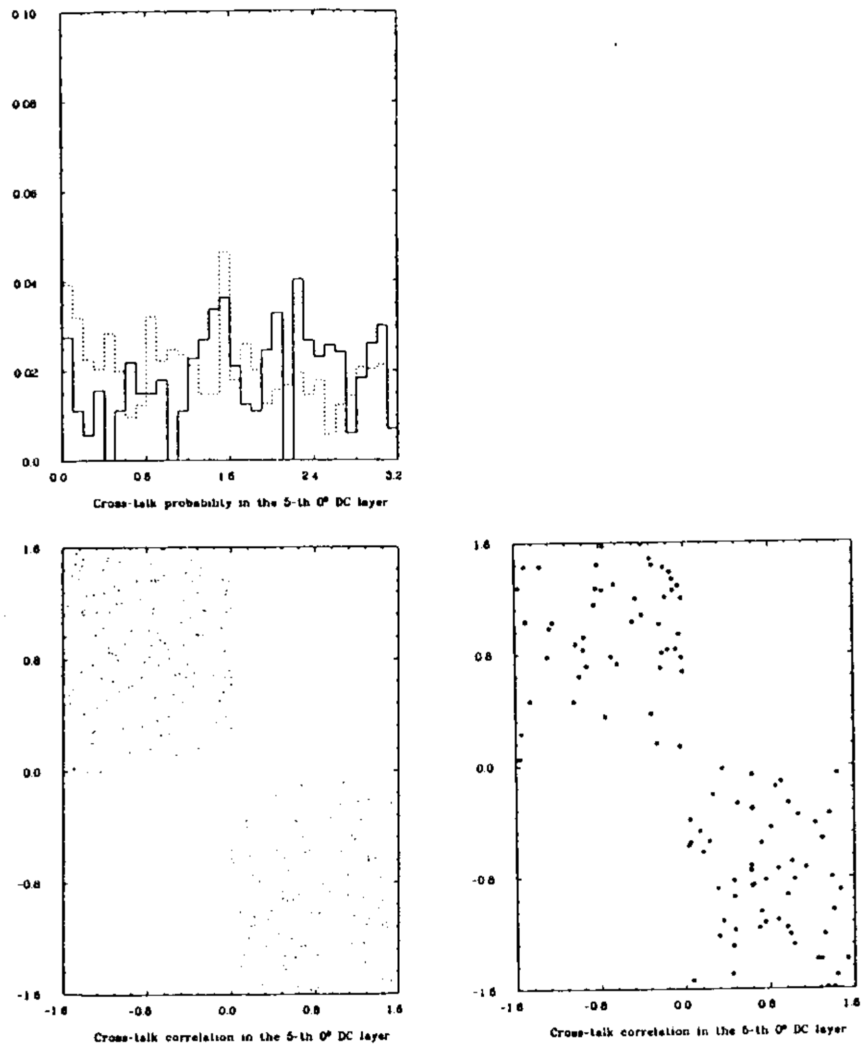

Fig. 5.13. Results of the cross-talk investigations in the 5-th 0° layer of the DC. Top: Average cross-talk probability in the drift cells as a function of the track position. The abscissa range corresponds to the full cell width of 32 mm. The wire position is marked with 1.6. The dotted line describes the data, the full line is based on the Monte Carlo simulation. Bottom: Correlation between the position of the hit associated with the track and the position of the hit found in the adjacent cell. Zero corresponds to the position of the field wires (see Fig. 3.10) between the cells. Small dots describe the data, the big dots describe the Monte Carlo simulation.

Table 5.2

Cross-talk probabilities for the 0° DC layers at $\overline{W}$=44 GeV.

	probability in %		
	DATA		
DC layer	adjacent cell	opposite cell	both cells
1	3.81	3.48	0.46
2	2.86	2.55	0.22
3	2.36	2.04	0.15
4	2.20	1.92	0.13
5	1.95	1.79	0.09
6	1.82	1.66	0.08
7	1.91	1.62	0.18
8	1.86	1.63	0.11
9	1.60	1.66	0.23
	MC		
DC layer	adjacent cell	opposite cell	both cells
1	3.30	2.89	0.23
2	2.67	2.30	0.07
3	2.11	1.69	0.12
4	2.07	1.48	0.05
5	1.78	1.52	0.09
6	1.71	1.28	0.05
7	1.64	1.34	0.03
8	1.71	1.53	0.00
9	1.05	1.19	0.02
Input:	0.30	0.00	0.00

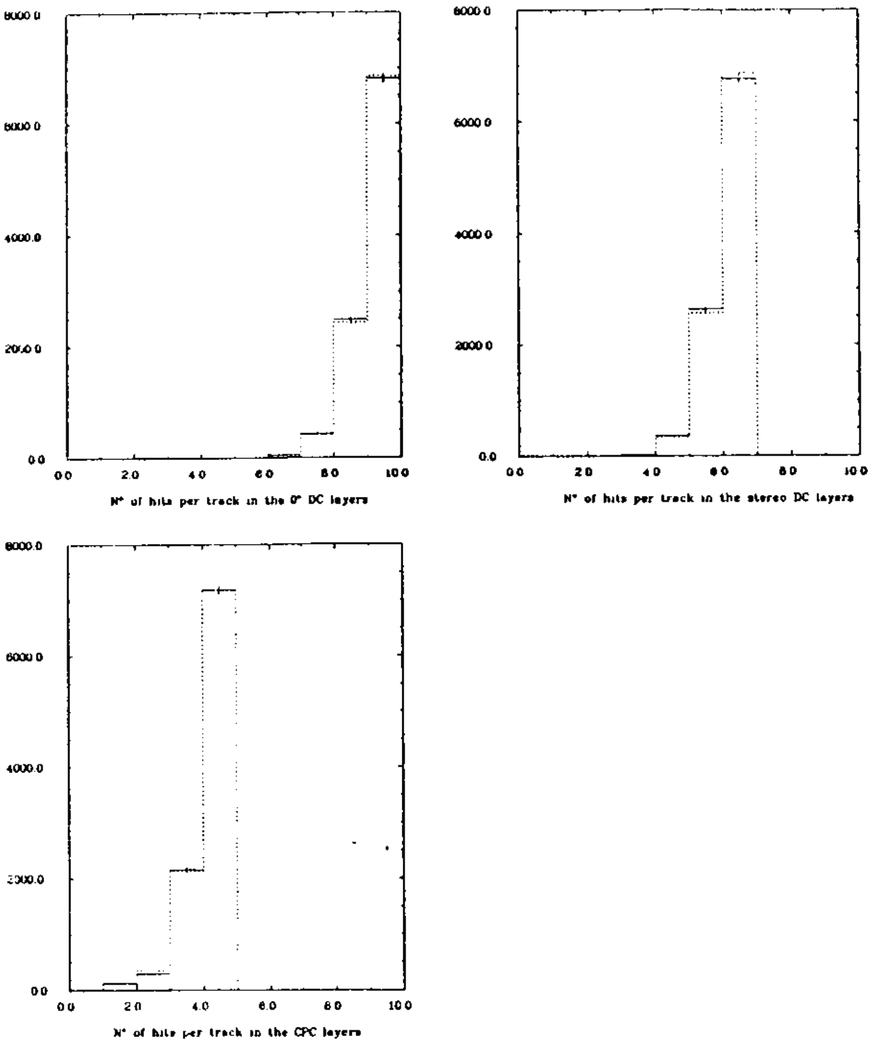

Fig. 5.14. Number of hits associated with the tracks in the two prong event sample at $\overline{W}$=44 GeV in the 0° and stereo layers of the DC and in the CPC. The dotted line describes the data, the crosses describe the Monte Carlo simulation.

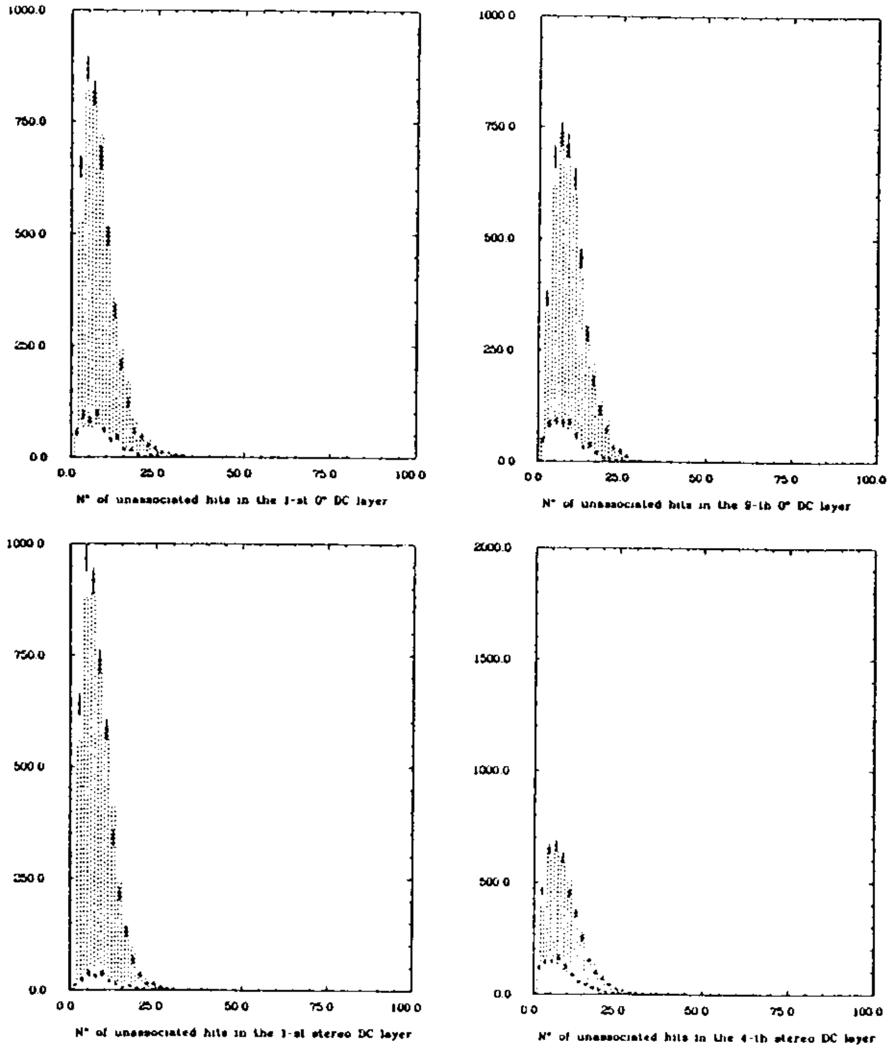

Fig. 5.15. Number of unassociated hits in the two prong event sample at $\overline{W}$=44 GeV in the 1-st and 9-th 0° and 1-st and 4-th stereo layers of the DC. The dotted line describes the data, the crosses describe the Monte Carlo simulation.

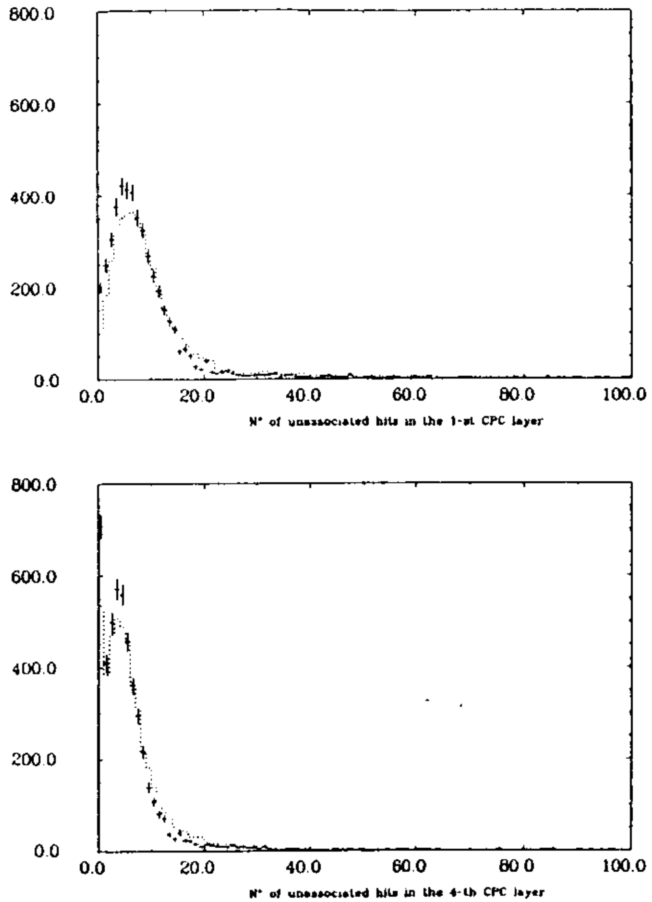

Fig. 5.16. Number of unassociated hits in the two prong event sample at $\overline{W}=44$ GeV in the 1-st and 4-th layer of the CPC. The dotted line describes the data, the crosses describe the Monte Carlo simulation.

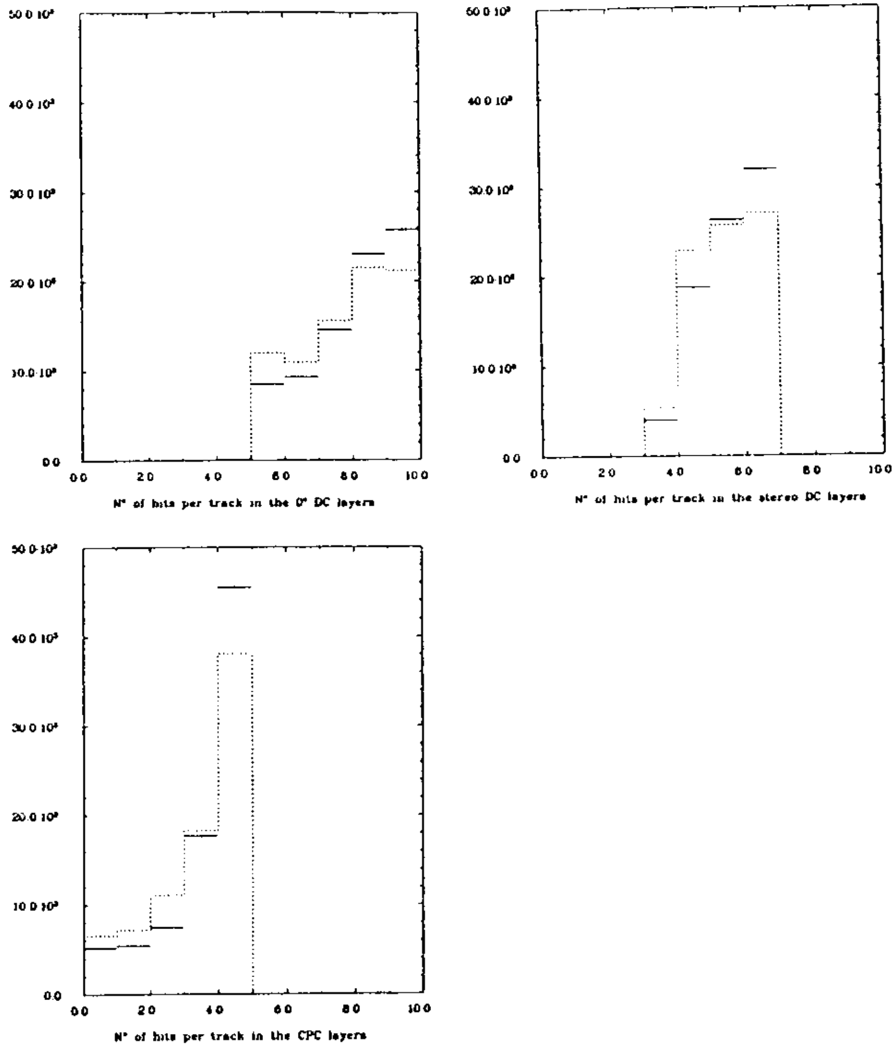

Fig. 5.17. Number of hits associated with the tracks in the hadronic event sample at $\overline{W}=44$ GeV in the 0° and stereo layers of the DC and in the CPC. The dotted line describes the data, the crosses describe the Monte Carlo simulation.

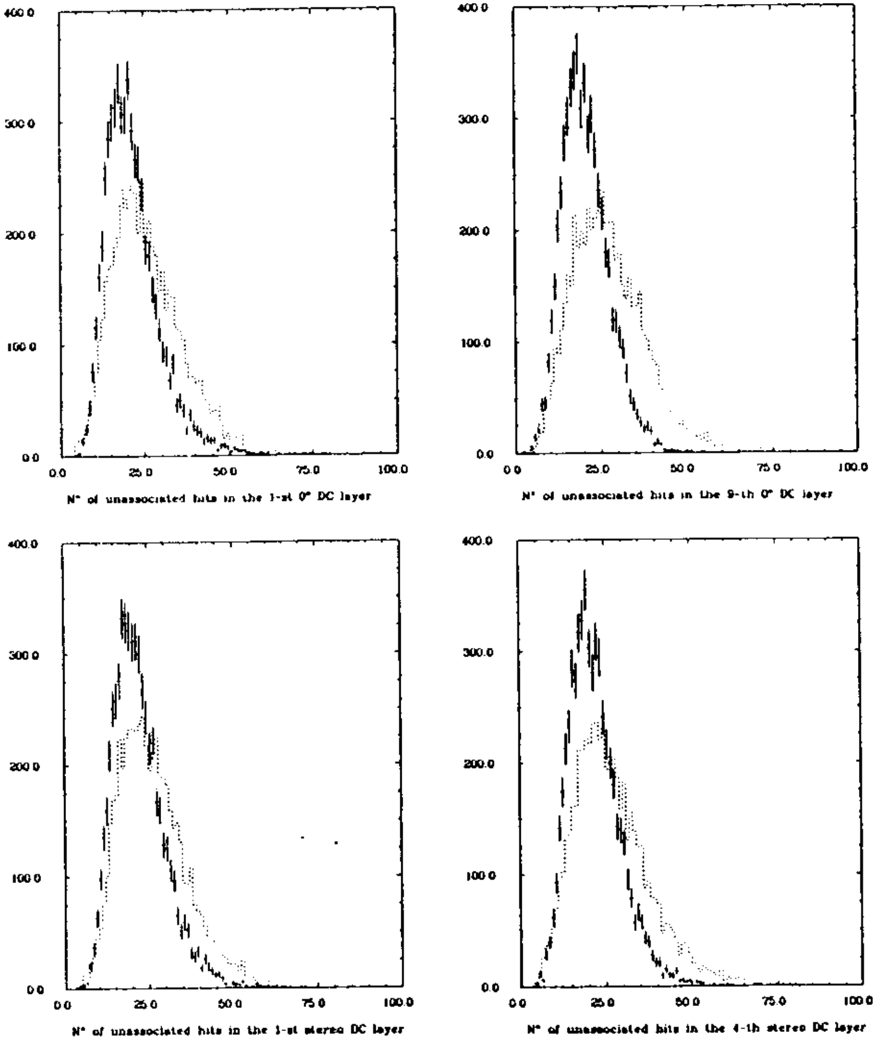

Fig. 5.18. Number of unassociated hits in the hadronic event sample at $\overline{W}$=44 GeV in the 1-st and 9-th 0° and 1-st and 4-th stereo layers of the DC. The dotted line describes the data, the crosses describe the Monte Carlo simulation.

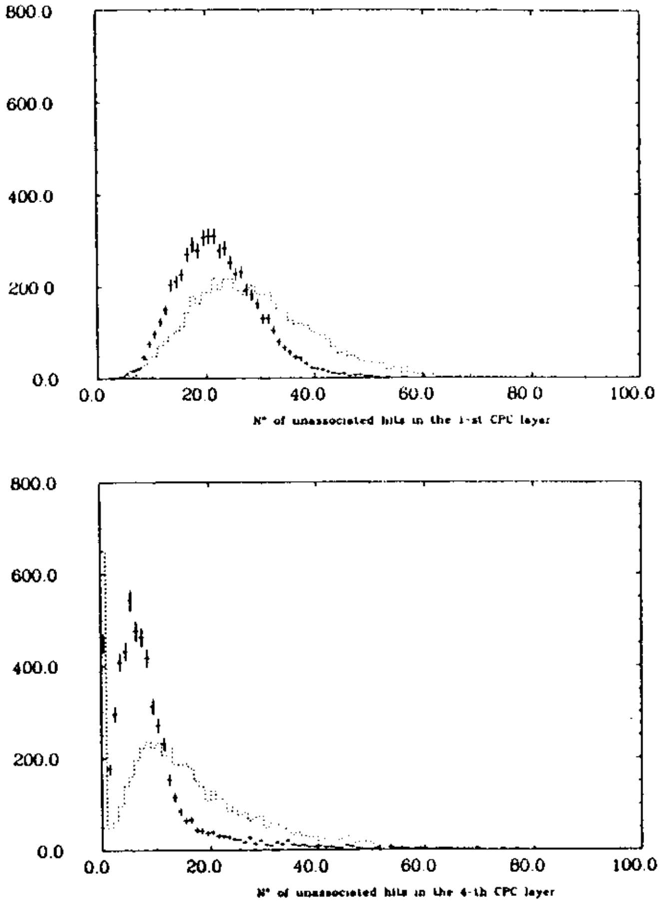

Fig. 5.19. Number of unassociated hits in the hadronic event sample at $\overline{W}$=44 GeV in the 1-st and 4-th layer of the CPC. The dotted line describes the data, the crosses describe the Monte Carlo simulation.

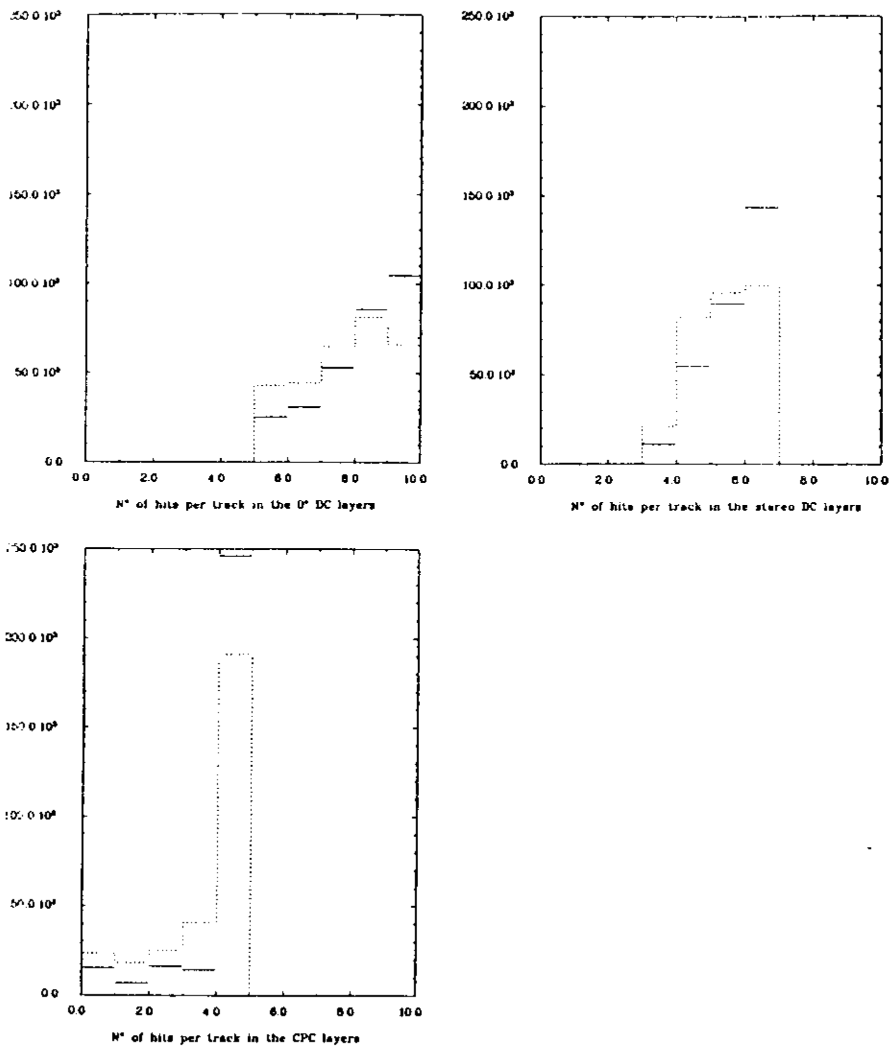

Fig. 5.20. Number of hits associated with the tracks in the old hadronic event sample at $\overline{W}$=35 GeV in the 0° and stereo layers of the DC and in the CPC. The dotted line describes the data, the crosses describe the Monte Carlo simulation.

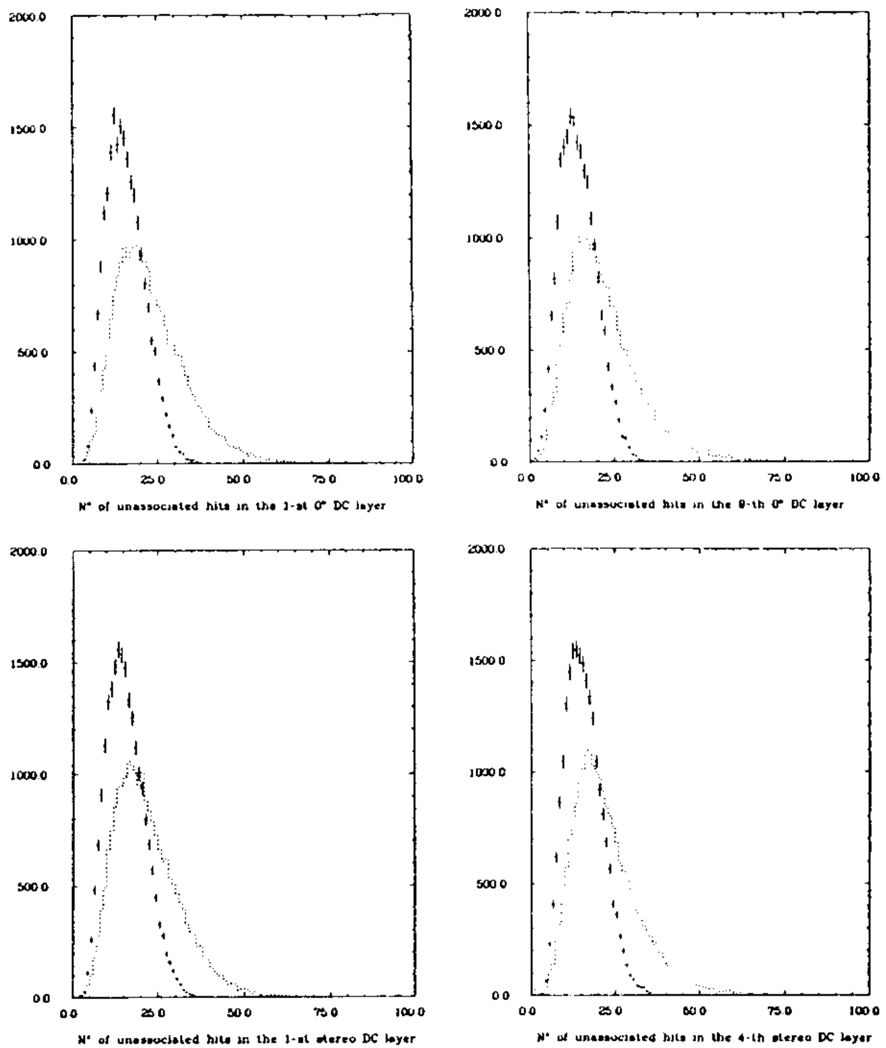

Fig. 5.21. Number of unassociated hits in the old hadronic event sample at $\overline{W}$=35 GeV in the 1-st and 9-th 0° and 1-st and 4-th stereo layers of the DC. The dotted line describes the data, the crosses describe the Monte Carlo simulation.

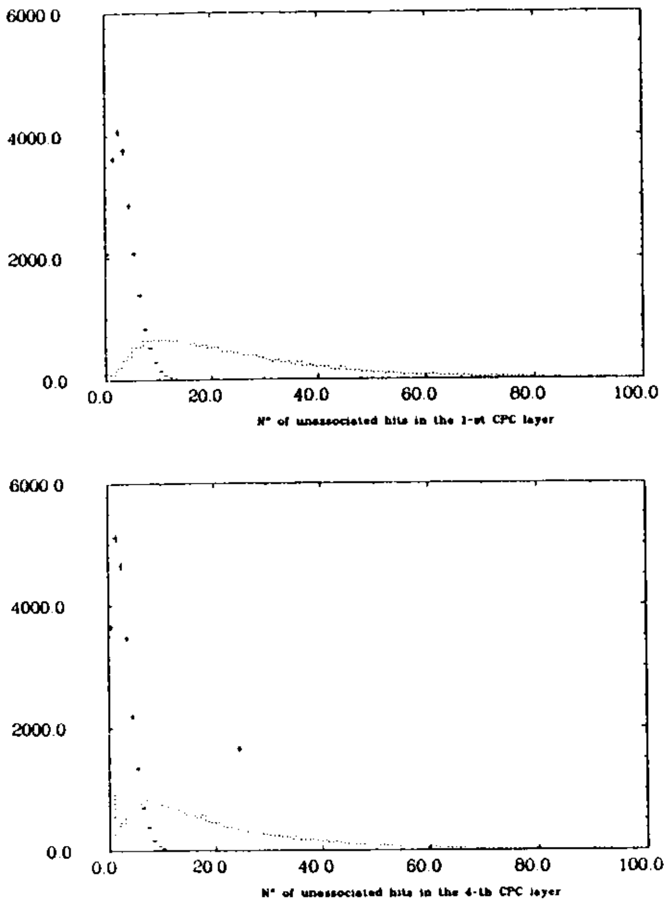

Fig. 5.22. Number of unassociated hits in the old hadronic event sample at $\overline{W}=35$ GeV in the 1-st and 4-th layer of the CPC. The dotted line describes the data, the crosses describe the Monte Carlo simulation.

5.4 Comparison of the Data and the Monte Carlo Results

As it has already been shown, a quite good agreement between TASSO detector response and MONSTER detector simulation at 44 GeV was achieved.

Fig. 5.23-5.26 and Table 5.3 show a comparison of some ("uncorrected") distributions, as measured with the TASSO detector, with the fully simulated (including radiative corrections, detector response, event reconstruction and selection cuts) Monte Carlo events. Fig. 5.23-5.26 show distributions of some of the variables used to make selection cuts (see subsect. 3.4.2) for the 44 GeV data sample, namely charged multiplicity n_{ch}, $\cos\theta_{track}$, particle momentum perpendicular to the beam p_{xy} and $\sum p/W$. One sees, that despite some small discrepancies for $n_{ch}=5$, $\cos\theta_{track}\approx .78$, $p_{xy}=.2$ the overall agreement between the data and the Monte Carlo is good. Table 5.3 shows $\chi^2/d.o.f.$ for most of the uncorrected distributions presented in the corrected version in Chapter 7. Since, at each energy the number of events in the Monte Carlo sample was 3 times (except 35 GeV where only 1.7 times) bigger than the number of the data events the χ^2 are dominated by the statistical errors on the data.

While making comparisons of χ^2 for two different energies one should remember, that the number of events in the data is different at different center-of-mass energies and that χ^2 increases with the event number. The number of events was the same for each generator. The background events were included.

The overall agreement between the data and the Lund LLA+O(α_s) Monte Carlo at 44 GeV is good. As mentioned already in Chapter 4 (see Table 4.1) the Lund LLA+O(α_s) Monte Carlo was run with the same parameters at all energies and the agreement between the data and the Monte Carlo was always good. The agreement for the Lund O(α_s^2) Monte Carlo is still satisfactory, although two sets of parameters had to be used (see Table 4.1). The old [HOY79] Monte Carlo has significant problems in describing the data at all energies.

The distributions most difficult to reproduce were those dealing with transverse momenta, x_p and aplanarity.

The 44 GeV data are described best by the Monte Carlo showing importance of the careful tuning, which was done at this energy.

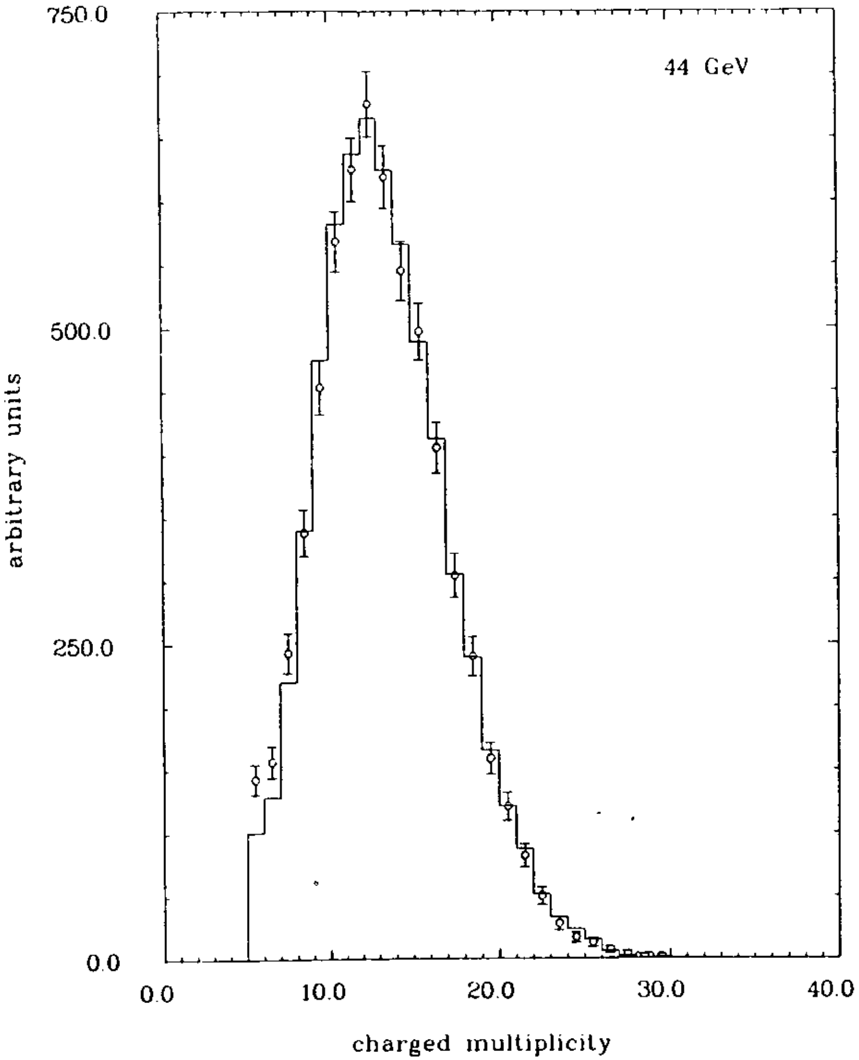

Fig. 5.23. Uncorrected charged multiplicity distribution at $\overline{W}=44$ GeV. The points describe the data, the full line shows the Monte Carlo prediction.

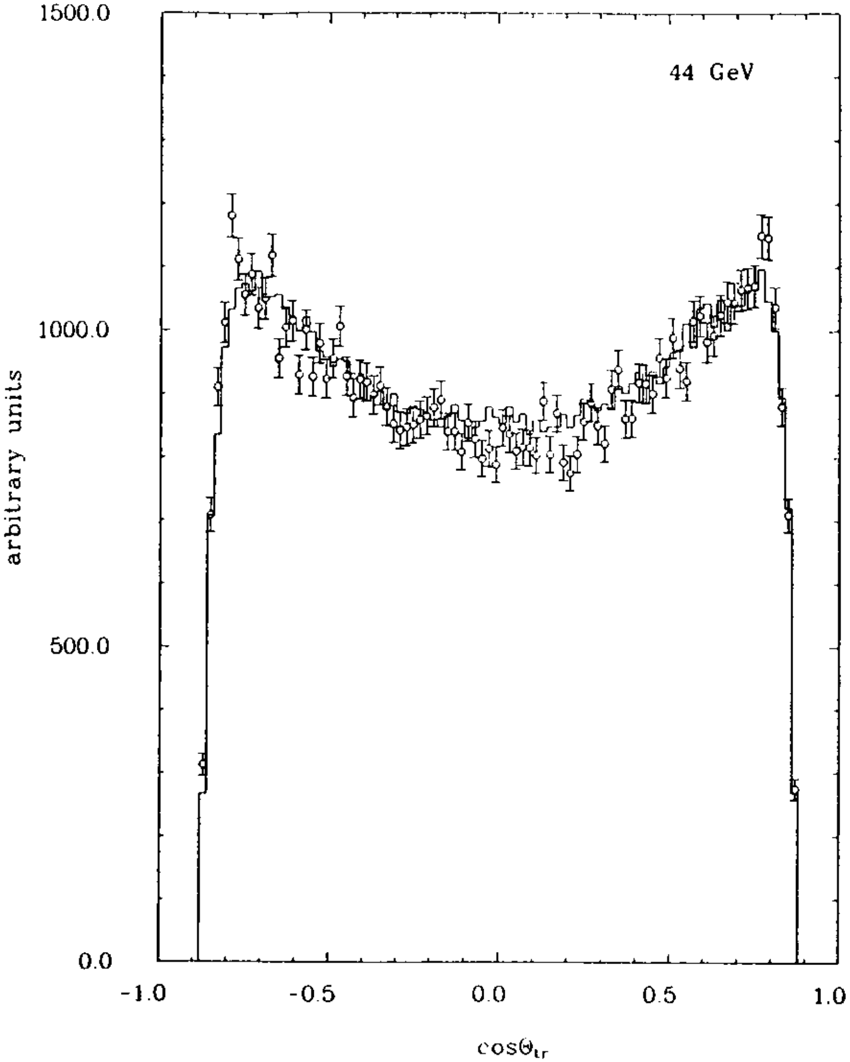

Fig. 5.24. Uncorrected $\cos\theta_{track}$ distribution at $\overline{W}=44$ GeV. The points describe the data, the full line shows the Monte Carlo prediction.

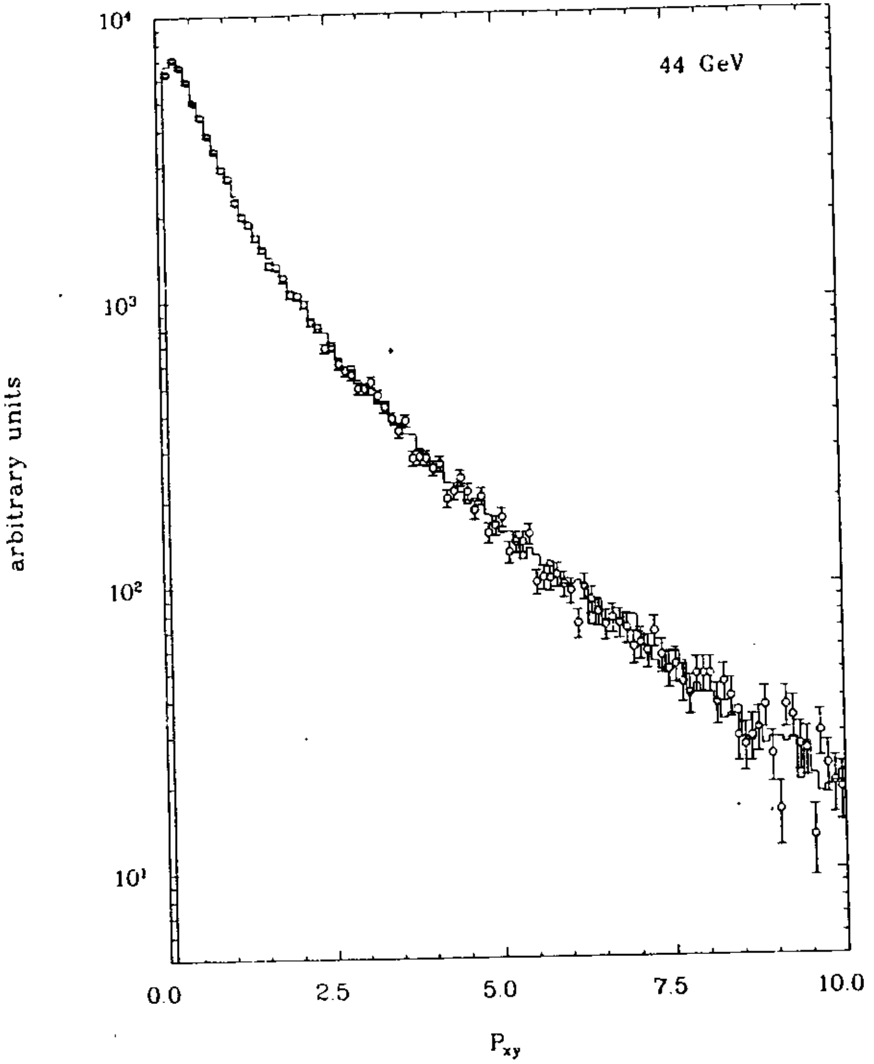

Fig. 5.25. Uncorrected p_{xy} distribution at $\overline{W}$=44 GeV. The points describe the data, the full line shows the Monte Carlo prediction.

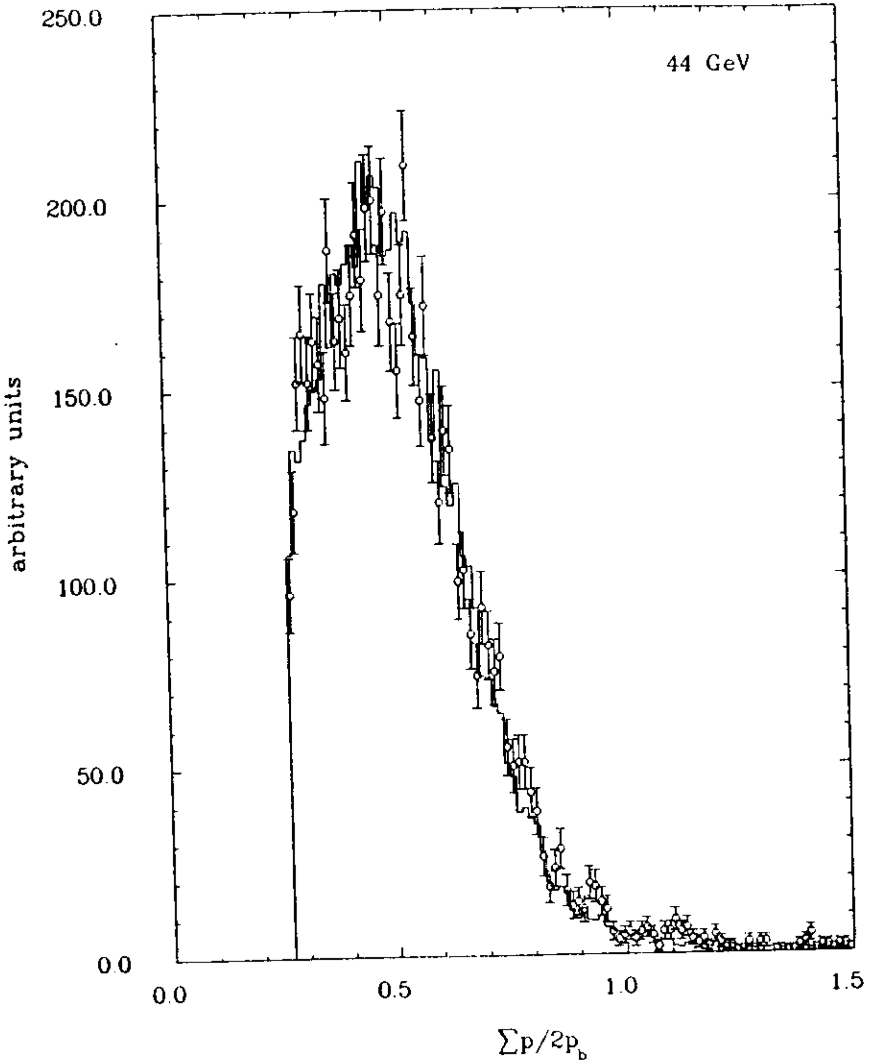

Fig. 5.26. Uncorrected $\sum p/W$ distribution at $\overline{W}$=44 GeV. The points describe the data, the full line shows the Monte Carlo prediction.

Table 5.3

χ^2 per degree of freedom for some uncorrected distributions at $\overline{W}$=14, 22, 35 and 44 GeV as a measure of the agreement between the data and the Monte Carlo simulation. HO, LM and LL denote Hoyer [HOY79], Lund $O(\alpha_s^2)$ and Lund LLA+$O(\alpha_s)$ Monte Carlo.

$\frac{\chi^2}{n.d.f.}$	14 GeV			22 GeV			35 GeV			44 GeV	
variable	HO	LM	LL	HO	LM	LL	HO	LM	LL	LM	LL
n_{ch}	3.4	2.1	0.75	2.9	1.6	0.37	17.	5.2	2.4	1.4	0.99
x_p	8.7	2.2	2.3	4.6	1.2	1.2	46.	5.8	5.5	2.2	1.5
S	4.9	1.8	1.3	3.8	0.95	0.57	20.	1.0	1.4	1.9	0.68
A	6.8	1.3	1.4	6.1	0.64	0.99	57.	8.0	1.3	3.7	1.1
T	4.3	3.0	1.4	3.8	0.89	0.33	26.	2.4	1.7	3.2	2.3
C	4.1	2.9	2.3	4.6	1.5	0.88	27.	3.5	3.7	1.8	1.7
D	4.8	3.3	1.2	5.6	0.88	1.0	35.	6.4	2.7	3.2	0.80
$\langle p_\parallel \rangle$	4.9	1.9	1.1	3.4	1.8	0.87	28.	6.9	3.8	2.5	1.0
$\langle p_\perp \rangle$	8.5	4.7	3.3	4.5	2.4	1.9	52.	11.	10.	2.5	2.1
$\langle p^2_{\perp in} \rangle$	3.4	1.1	0.65	2.1	0.95	0.84	34.	0.60	1.1	0.45	0.96
$\langle p^2_{\perp out} \rangle$	2.3	0.69	0.57	3.4	0.41	0.98	62.	9.4	4.3	3.9	1.9
y	3.7	1.9	1.3	5.1	2.2	0.73	39.	9.3	2.6	3.8	1.4

CHAPTER 6

Total Cross Section

The total cross section for the annihilation into hadrons according to the reaction $e^+e^- \rightarrow$ hadrons was determined by evaluating the acceptance ϵ for Monte Carlo events with the radiative corrections (see section 4.3) applied. The final result was obtained by the equation:

$$\sigma_{tot} = \frac{N_{meas}}{L\epsilon(1+\delta)}$$

where L is the collected luminosity and δ is the correction for the increase of the cross section due to the radiative effects. The hadronic cross section is often expressed by its ratio R to the theoretical cross section σ_o for the process $e^+e^- \rightarrow \mu^+\mu^-$ calculated in the lowest order of the QED without weak interactions. Therefore

$$R = \frac{\sigma_{tot}}{\sigma_o},$$

where $\sigma_o = \frac{4\pi}{3}\frac{\alpha^2}{s}$, s is the square of the center-of-mass energy in units of GeV and α is the fine structure constant. For the 44 GeV the result is

$$R = 4.113 \pm .052\ (\text{stat.}) \pm .085\ (\text{syst.}).$$

The additional systematic error of 3.0% coming from luminosity measurement and 2.5% [TAS82b, TAS84c] coming from missing terms in the radiative correction calculations should be added. The single contributions to the systematic error coming from the changes in the various cuts and conditions are summarized in the Table 6.1. The final result including all the errors reads:

$$R = 4.11 \pm .19$$

It is in a nice agreement with the results of other PETRA experiments: CELLO 3.97 ± .12, $\overline{W}$ = 43.50 GeV [CEL87]; JADE 4.13 ± .21, $\overline{W}$ = 43.25 GeV [JAD81, JAD83, JAD85]; MARK J 4.13 ± .24, $\overline{W}$ = 43.82 GeV [MJ81, MJ86]*.

The R value for 14, 22, 35, and 44 GeV are presented in Table 6.2

---

* The data from the other experiments were obtained by calculating an average for the data between 39 and 47 GeV.

Table 6.1

Contributions to the systematic error of R at $\overline{W}$=44 GeV.

Cut or Condition	Default	Contribution
$d_0 \le 3$ cm	≤ 5 cm	.45%
$p_{xy} \ge .2$ GeV	$\ge .1$ GeV	.21%
$\lvert\cos\Theta_{track}\rvert \le .8$	$\le .87$	.63%
$\lvert z_{track} - z_{vert}\rvert \le 15$ cm	≤ 20 cm	.51%
$n_{ch} \ge 7$	≥ 5	1.16%
$\frac{\Sigma p}{W} \ge .3$	$\ge .265$	.11%
track trigger on in the MC and track triggers only in the DATA	all MC events and all triggers	1.16%
Lund $O(\alpha_s^2)$ MC used to calculate the acceptance	Lund LLA+$O(\alpha_s)$	.07%

Table 6.2

Comparison of R measurements.

$\overline{W}$	R	Experiment
14.03	4.12 ± .06 ± .11 ± .16* 4.12 ± .21	this evaluation
21.98	3.86 ± .09 ± .08 ± .15 3.86 ± .19	
34.62	4.15 ± .02 ± .08 ± .16 4.15 ± .18	
44.70	4.11 ± .05 ± .08 ± .16 4.11 ± .19	
14.03	4.14 ± .35	old TASSO
21.98	3.96 ± .24	[TAS82b]
34.58	4.08 ± .21	[TAS84j]
44.20	4.22 ± .26	[TAS84c]
14.04	4.01 ± .16	CELLO
22.00	3.86 ± .16	
35.50		
43.50	3.97 ± .12	
14.04	3.94 ± .14	JADE
22.00	4.11 ± .13	
34.63	4.01 ± .12	
43.25	4.13 ± .21	
14.03	3.71 ± .20	MARK J
21.99	3.55 ± .19	
34.64	3.83 ± .20	
43.82	4.13 ± .24	

* The first error is statistical, the second is systematic coming from selection cuts and Monte Carlo, the third is systematic coming from luminosity measurement and missing terms in the radiative corrections calculations.

CHAPTER 7

Particle Momentum Spectra

7.1 Introduction

The distributions as measured with any real detector are not the "true" distributions, which could be measured with an ideal detector, which would detect particles without interacting with them, had 100% acceptance and would detect particles in the moment just after production and only those coming from the process under study (here: $e^+e^- \to$ hadrons). The measured distributions are also not the "true" ones because the colliding positron and electron may radiate a photon and change the initial center-of-mass energy. Nevertheless one can try to make appropriate corrections to get the distributions close to the "true" ones.

7.1.1 Corrections

The distributions presented in this chapter were obtained by correcting the measured distributions for the initial state radiation (see section 4.3), the background contamination from $\tau^+\tau^-$ and $\gamma\gamma$ processes (see section 4.2), particle decays, the detector effects (see Chapter 5) and the selection procedure (see subsect. 3.4.2).

The exact correcting procedure was as follows: Firstly, a set of N_{gen} events was generated using a Monte Carlo programme (see section 4.1) at a fixed center-of-mass energy with no QED radiative corrections, yielding the distributions $n_{gen}(x)$ of charged particles for different intervals of the observable x. All the primary produced particles or those produced in the decay of particles with the average lifetimes smaller than $3 \cdot 10^{-10}$ s were considered. Secondly, both hadronic and background events were generated including QED radiative effects and were followed through the TASSO detector simulation programme, generating hits in the tracking chambers. Energy loss, multiple scattering, photon conversions, nuclear interactions in the material of the detector and particle decays as well as the detector efficiencies, resolutions, noises and cross-talks were taken into account. The events were then passed through the same track reconstruction and acceptance programs as used for the real data, yielding N_{det} accepted events, corresponding to the distributions $n_{det}(x)$. For every bin "i" of every distribution $n(x)$, a correction factor $C^i(x)$ was calculated as:

$$C^i(x) = \frac{n^i_{gen}(x)}{N_{gen}} \Big/ \frac{n^i_{det}(x)}{N_{det}}.$$

The corrected distributions $n^i_{corr}(x)$ were then derived from the measured distributions $n^i_{meas}(x)$ with a total of N_{meas} events, using the formula:

$$n^i_{corr}(x) = C^i(x)\frac{n^i_{meas}(x)}{N_{meas}}.$$

7.1.2 The Statistical and Systematic Errors

The statistical errors include the statistical errors on the data and the statistical errors on the correction factors. In the Monte Carlo sample with the radiative corrections and full detector simulation there were 3 times (except for 35 GeV were only 1.7 times) more events (after selection cuts) than in the corresponding data sample. Because, in the Monte Carlo sample without radiative corrections and without detector effects there were $10 \div 15$ times (except 35 GeV were only 2.3 times) more events than in the data sample, the statistical errors are dominated by those of the data.

At all center-of-mass energies two types of the systematic errors were considered, namely those coming from the differences between the data and the Monte Carlo and those coming from the type of Monte Carlo used. The former were estimated by changing the selection cuts (including the track triggering), whereas the latter by taking the difference between the corrected distribution obtained with the Lund LLA+O(α_s) and Lund O(α_s^2) Monte Carlo.

Table 7.1 itemizes the considered systematic error sources influencing the distributions of the studied quantities. For each bin of each distribution and for the average values the errors shown further in this chapter are the statistical and systematic errors combined in quadrature.

7.2 Particle Momentum Spectra

7.2.1 Momentum Distribution

The normalized differential cross section $1/\sigma_{tot}\, d\sigma/dp$ for the inclusive charged particle production is presented in Fig. 7.1 and in Table 7.3. The cross section decreases steeply with momentum. The distributions become broader with the center-of-mass energy. The number of low momentum ($p \approx .25$ GeV) particles is almost constant with energy. The energy dependence of the average momentum $< p >$ is shown in Fig. 7.2 and in Table 7.2. The average momentum rises approximately linearly with energy.

There are some discrepancies between the present result and the old TASSO result at energies below 39 GeV [TAS84j]. They are quite significant in the first two bins of Table 7.3. They are understood as the effect of an averaging procedure applied to the corrections in the past: The correcting function varies rapidly in this region and the correction coefficients differ significantly from 1. The function was previously assumed to be too smooth [MAE87p].

Table 7.1

Cuts and conditions used for systematic errors estimation.

Cut or Condition	Default
$d_0 \leq 3$ cm	$d_0 \leq 5$ cm
$p_{xy} \geq .2$ GeV	$p_{xy} \geq .1$ GeV
$\|\cos\theta_{track}\| \leq .80$	$\|\cos\theta_{track}\| \leq .87$
$\|z_{tr} - z_{vert}\| \leq 15$ cm	$\|z_{tr} - z_{vert}\| \leq 20$ cm
$n_{ch} \geq 7(6)$	$n_{ch} \geq 5(4)$
$\|\cos\theta_{T,S,P}\| \leq .65$	$\|\cos\theta_{T,S,P}\| \leq .70$
$\frac{\Sigma_p}{W} \geq .3$	$\frac{\Sigma_p}{W} \geq .265$
track triggers on in the MC track triggers only in the DATA	all MC events and all triggers
Lund $O(\alpha_s^2)$ MC used for correcting	Lund LLA+$O(\alpha_s)$

Table 7.2

Average values of track and event parameters. The errors are statistical and systematic combined in quadrature.

	14 GeV	22 GeV	35 GeV	44 GeV
$< S >$	0.2252 ± 0.0075	0.1528 ± 0.0075	0.1155 ± 0.0047	0.1053 ± 0.0035
$< A >$	0.0613 ± 0.0057	0.0386 ± 0.0029	0.0261 ± 0.0019	0.0213 ± 0.0015
$< T >$	0.8499 ± 0.0085	0.8876 ± 0.0073	0.9079 ± 0.0045	0.9157 ± 0.0049
$< C >$	0.5355 ± 0.0099	0.4324 ± 0.0083	0.3600 ± 0.0029	0.3325 ± 0.0069
$< D >$	0.246 ± 0.010	0.1586 ± 0.0065	0.1127 ± 0.0044	0.0947 ± 0.0023
$< p >$	0.913 ± 0.016	1.211 ± 0.022	1.590 ± 0.013	1.833 ± 0.020
$< p_\parallel >$	0.771 ± 0.015	1.064 ± 0.023	1.436 ± 0.017	1.661 ± 0.021
$< p_\perp >$	0.3466 ± 0.0056	0.3889 ± 0.0064	0.4342 ± 0.0038	0.4695 ± 0.0049
$< p_\perp^2 >$	0.1773 ± 0.0050	0.243 ± 0.012	0.3339 ± 0.0066	0.4175 ± 0.0095
$\ll p_\perp^2 \gg$	0.1866 ± 0.0060	0.256 ± 0.020	0.3425 ± 0.0075	0.418 ± 0.022
$\ll p_{\perp in}^2 \gg$	0.1389 ± 0.0050	0.193 ± 0.017	0.2685 ± 0.0075	0.334 ± 0.023
$\ll p_{\perp out}^2 \gg$	0.0476 ± 0.0038	0.0628 ± 0.0040	0.0734 ± 0.0037	0.0834 ± 0.0037

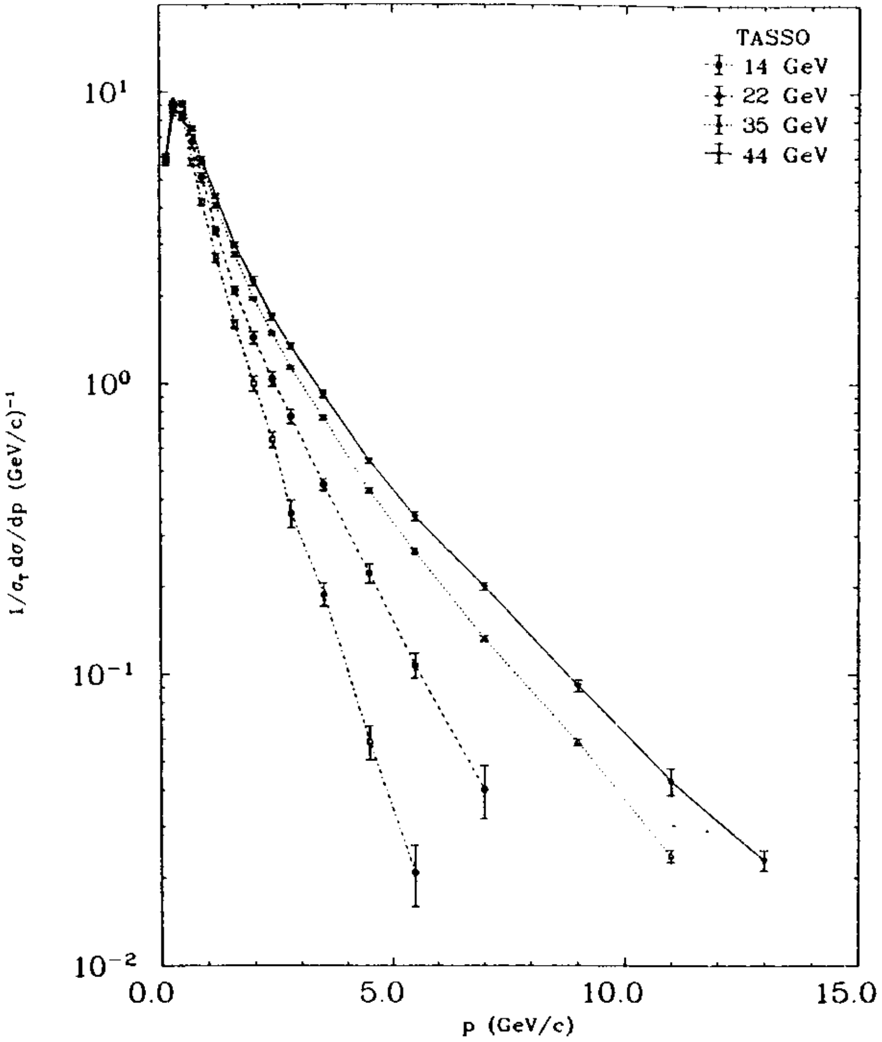

Fig. 7.1. Normalized momentum distributions $1/\sigma_{tot}\, d\sigma/dp$ $(GeV/c)^{-1}$ at W=14, 22, 35 and 44 GeV. The lines only connect the points. The errors are statistical and systematic combined in quadrature.

Table 7.3

Normalized momentum distributions $1/\sigma_{tot}\, d\sigma/dp$ $(\mathrm{GeV}/c)^{-1}$. The errors are statistical and systematic combined in quadrature.

p (GeV/c)	14 GeV	22 GeV	35 GeV	44 GeV
0.1 - 0.2	5.78 ± 0.19	5.85 ± 0.26	6.07 ± 0.11	5.95 ± 0.20
0.2 - 0.3	8.25 ± 0.51	8.16 ± 0.39	8.73 ± 0.27	8.74 ± 0.18
0.3 - 0.4	9.18 ± 0.30	9.49 ± 0.34	9.88 ± 0.23	9.56 ± 0.26
0.4 - 0.5	8.99 ± 0.31	8.77 ± 0.28	9.66 ± 0.21	9.55 ± 0.27
0.5 - 0.6	7.46 ± 0.26	7.91 ± 0.44	8.74 ± 0.17	8.62 ± 0.24
0.6 - 0.7	6.17 ± 0.30	7.23 ± 0.45	7.92 ± 0.15	7.98 ± 0.18
0.7 - 0.8	5.35 ± 0.19	6.30 ± 0.36	6.94 ± 0.10	7.10 ± 0.19
0.8 - 1.0	4.20 ± 0.12	5.10 ± 0.20	5.735 ± 0.098	5.93 ± 0.13
1.0 - 1.2	3.01 ± 0.17	3.88 ± 0.20	4.514 ± 0.086	4.831 ± 0.098
1.2 - 1.4	2.395 ± 0.090	2.84 ± 0.20	3.647 ± 0.064	3.98 ± 0.12
1.4 - 1.6	1.864 ± 0.077	2.301 ± 0.099	2.993 ± 0.057	3.267 ± 0.090
1.6 - 1.8	1.328 ± 0.077	1.88 ± 0.11	2.545 ± 0.058	2.747 ± 0.071
1.8 - 2.0	1.097 ± 0.081	1.477 ± 0.097	2.131 ± 0.032	2.39 ± 0.13
2.0 - 2.2	0.904 ± 0.069	1.41 ± 0.10	1.787 ± 0.029	2.112 ± 0.071
2.2 - 2.4	0.758 ± 0.062	1.174 ± 0.086	1.585 ± 0.027	1.804 ± 0.060
2.4 - 2.6	0.528 ± 0.059	0.903 ± 0.084	1.399 ± 0.027	1.598 ± 0.059
2.6 - 2.8	0.398 ± 0.051	0.828 ± 0.068	1.213 ± 0.032	1.401 ± 0.061
2.8 - 3.0	0.318 ± 0.042	0.713 ± 0.060	1.056 ± 0.023	1.291 ± 0.053
3.0 - 3.5	0.230 ± 0.019	0.534 ± 0.041	0.874 ± 0.016	1.033 ± 0.033
3.5 - 4.0	0.147 ± 0.023	0.364 ± 0.030	0.652 ± 0.015	0.805 ± 0.033
4.0 - 6.0	0.0397 ± 0.0055	0.165 ± 0.010	0.3468 ± 0.0058	0.4459 ± 0.0092
6.0 - 8.0	0.00285 ± 0.00086	0.0402 ± 0.0083	0.1325 ± 0.0030	0.2000 ± 0.0061
8.0 - 10.0		0.0118 ± 0.0029	0.0585 ± 0.0016	0.0914 ± 0.0044
10.0 - 12.0		0.00050 ± 0.00028	0.0238 ± 0.0012	0.0430 ± 0.0044
12.0 - 14.0			0.0097 ± 0.0012	0.0230 ± 0.0018
14.0 - 18.0			0.00156 ± 0.00055	0.00767 ± 0.00066
18.0 - 22.0				0.00111 ± 0.00021
$< p >$	0.913 ± 0.016	1.211 ± 0.022	1.590 ± 0.013	1.833 ± 0.020

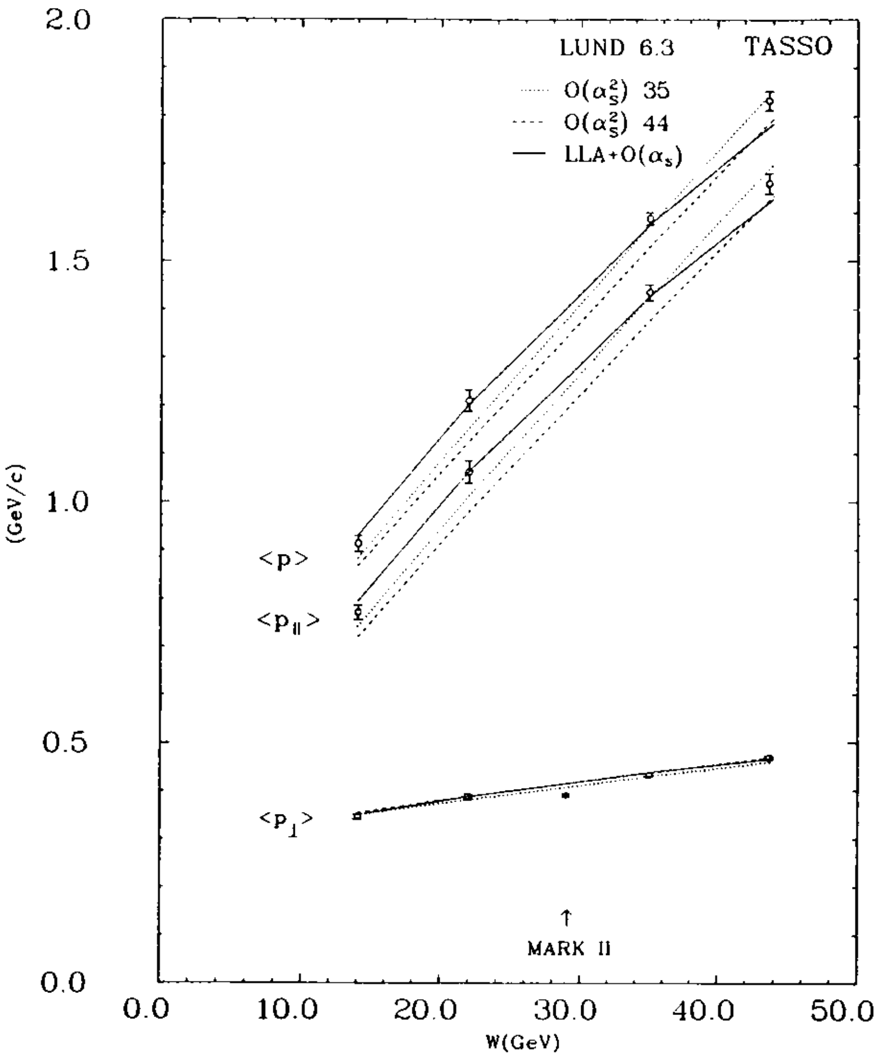

Fig. 7.2. Average values of the total ($< p >$), transverse ($< p_T >$) and longitudinal ($< p_\parallel >$) momentum as a function of W. The curves show predictions of the Lund $O(\alpha_s^2)$ Monte Carlo tuned at 35 and 44 GeV and predictions of the Lund LLA$+O(\alpha_s)$ Monte Carlo tuned at 44 GeV.

Table 7.4

Normalized scaled momentum distributions $1/\sigma_{tot}\, d\sigma/dx_p$, where $x_p = 2p/W$.

x_p	14 GeV	22 GeV	35 GeV	44 GeV
0.02 - 0.03	47.2 ± 1.7	94.0 ± 3.9	169.3 ± 2.4	191.8 ± 3.9
0.03 - 0.04	56.5 ± 3.6	102.2 ± 3.3	143.7 ± 2.7	152.7 ± 3.0
0.04 - 0.05	66.3 ± 2.1	90.7 ± 3.9	115.5 ± 1.6	118.5 ± 2.9
0.05 - 0.06	62.9 ± 2.7	85.9 ± 3.6	93.3 ± 1.5	95.0 ± 2.7
0.06 - 0.08	58.0 ± 2.3	65.7 ± 2.0	69.2 ± 1.2	70.5 ± 1.3
0.08 - 0.10	44.9 ± 1.7	50.3 ± 2.1	49.7 ± 1.1	49.0 ± 1.7
0.10 - 0.12	36.1 ± 1.3	35.4 ± 1.5	36.33 ± 0.43	37.17 ± 0.89
0.12 - 0.14	29.4 ± 1.0	27.0 ± 1.3	28.08 ± 0.37	28.67 ± 0.64
0.14 - 0.16	22.05 ± 0.96	21.8 ± 1.3	22.43 ± 0.35	22.66 ± 0.61
0.16 - 0.18	18.9 ± 1.7	17.1 ± 1.2	18.02 ± 0.31	17.79 ± 0.76
0.18 - 0.20	16.01 ± 0.95	15.16 ± 0.95	14.38 ± 0.28	13.45 ± 0.47
0.20 - 0.25	11.58 ± 0.42	10.78 ± 0.47	10.24 ± 0.16	10.06 ± 0.32
0.25 - 0.30	7.44 ± 0.48	7.05 ± 0.38	6.43 ± 0.11	6.18 ± 0.23
0.30 - 0.35	5.28 ± 0.30	4.65 ± 0.38	4.23 ± 0.10	4.08 ± 0.18
0.35 - 0.40	3.15 ± 0.35	3.13 ± 0.32	2.719 ± 0.067	2.66 ± 0.14
0.40 - 0.50	1.75 ± 0.11	1.76 ± 0.15	1.587 ± 0.037	1.517 ± 0.072
0.50 - 0.60	0.95 ± 0.13	0.82 ± 0.13	0.782 ± 0.028	0.631 ± 0.052
0.60 - 0.70	0.342 ± 0.056	0.41 ± 0.11	0.341 ± 0.023	0.331 ± 0.031
0.70 - 0.80	0.181 ± 0.041	0.193 ± 0.050	0.162 ± 0.018	0.129 ± 0.017
0.80 - 1.00	0.058 ± 0.017	0.056 ± 0.025	0.030 ± 0.012	0.0309 ± 0.0059
$< x_p >$	0.1302 ± 0.0023	0.1102 ± 0.0020	0.0908 ± 0.0008	0.0839 ± 0.0009

7.2.2 Scaled Momentum Distribution

Fig. 7.3 and Table 7.4 present the normalized cross section $1/\sigma_{tot}\, d\sigma/dx_p$, where x_p is the fractional particle momentum, $x_p = 2p/W$. There is an increase of the cross section with W for $x_p \lesssim .1$ GeV and a steep fall for $x_p > .2$ for all the energies. It is better visible in Fig. 7.4 and Table 7.5, which show $1/\sigma_{tot}\, d\sigma/dx_p$ for fixed x_p intervals plotted versus $s = W^2$. One sees, that except for the first interval the $1/\sigma_{tot}\, d\sigma/dx_p$ scales with s and is constant within $10 \div 20\%$. The amount of the scale breaking was quantified by fitting the data to the following form suggested by QCD [BAI79, ALT79] *:

$$1/\sigma_{tot} d\sigma/dx_p = c_1 (1 + c_2 \ln(s/s_o))$$

---

* Because the function of that form is quite inconvenient for the fitting programs the linear function of the form $b_1 + b_2 \ln(s/s_o)$ was fitted too, and it was made sure that the results of both fits agree.

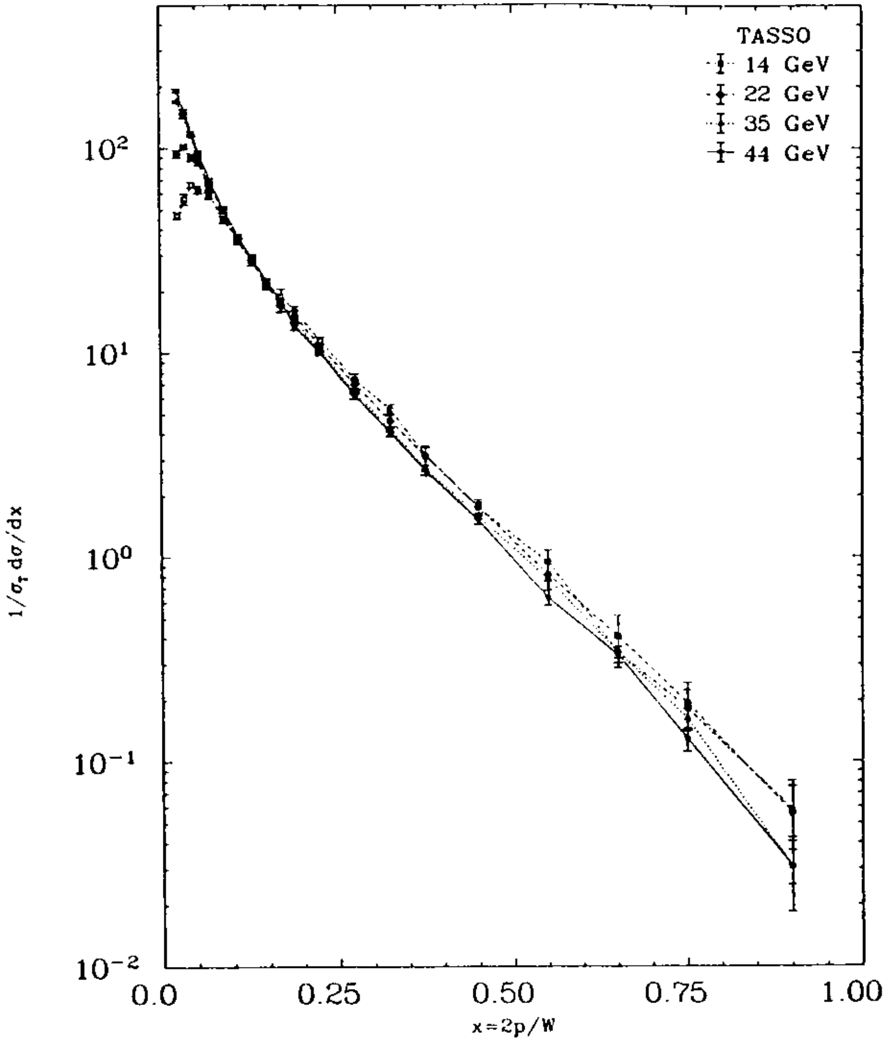

Fig. 7.3. Normalized scaled momentum distributions $1/\sigma_{tot}\, d\sigma/dx_p$, where $x_p = 2p/W$ at $\overline{W}$=14, 22, 35 and 44 GeV.

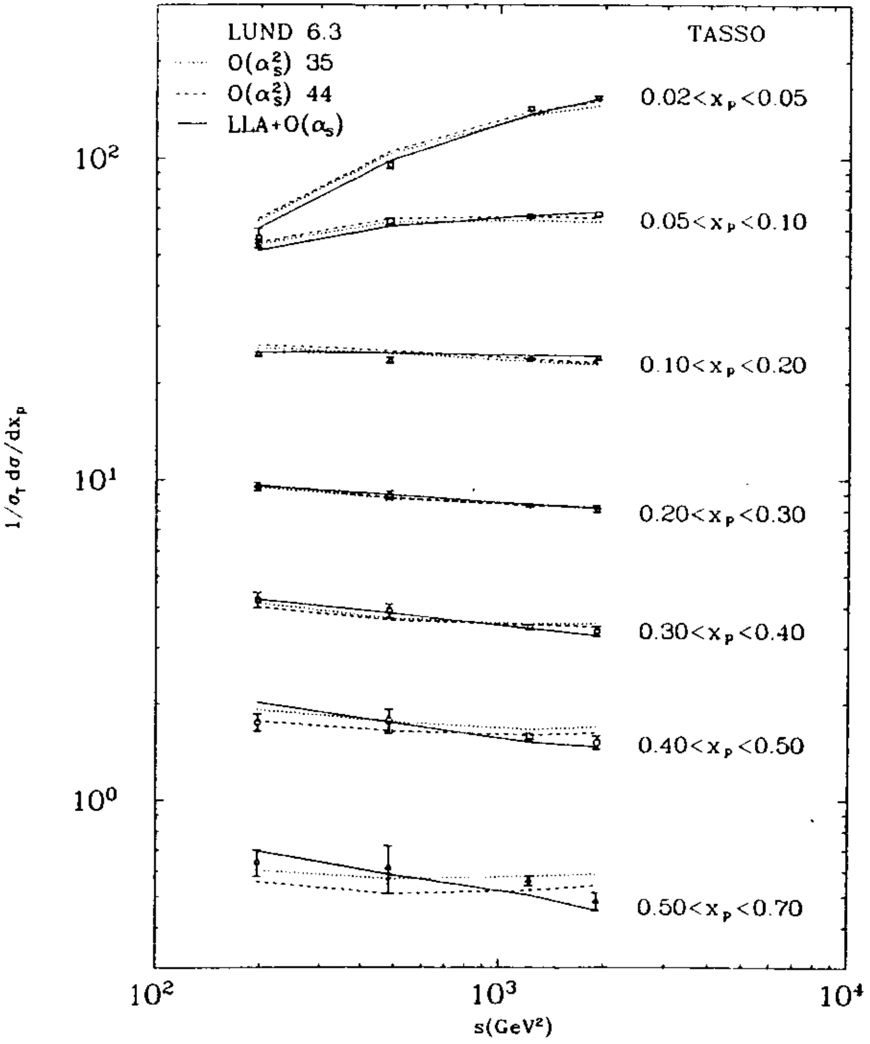

Fig. 7.4. Normalized scaled momentum distributions $1/\sigma_{tot}\, d\sigma/dx_p$, where $x_p = 2p/W$ at $\overline{W}$=14, 22, 35 and 44 GeV.

Table 7.5

Normalized scaled momentum distributions $1/\sigma_{tot}\, d\sigma/dx_p$, where $x_p = 2p/W$ in the binning used in fits.

x_p	14 GeV	22 GeV	35 GeV	44 GeV
0.02 – 0.05	56.4 ± 3.9	95.4 ± 2.6	142.9 ± 2.0	154.4 ± 2.4
0.05 – 0.10	54.1 ± 1.7	63.6 ± 1.6	66.23 ± 0.92	67.2 ± 1.2
0.10 – 0.20	24.51 ± 0.46	23.48 ± 0.49	23.85 ± 0.18	23.95 ± 0.38
0.20 – 0.30	9.51 ± 0.28	8.92 ± 0.29	8.335 ± 0.098	8.12 ± 0.20
0.30 – 0.40	4.21 ± 0.22	3.89 ± 0.19	3.476 ± 0.069	3.37 ± 0.12
0.40 – 0.50	1.75 ± 0.11	1.76 ± 0.15	1.557 ± 0.037	1.517 ± 0.072
0.50 – 0.70	0.640 ± 0.061	0.61 ± 0.10	0.562 ± 0.019	0.484 ± 0.031

Table 7.6

Fit results to the s-dependence of the scaled cross section $1/\sigma_{tot}\, d\sigma/dx_p = c_1(1 + c_2 \ln(s/s_0))$, where $s_0 = 1$ GeV^2.

x_p	c_1	c_2	$c_1 \cdot c_2$
0.02 – 0.05	−179. ± 12.	−0.2498 ± 0.0070	44.6 ± 1.7
0.05 – 0.10	28.0 ± 6.8	0.191 ± 0.068	5.33 ± 0.82
0.10 – 0.20	25.2 ± 1.6	−0.0072 ± 0.0087	−0.18 ± 0.23
0.20 – 0.30	12.75 ± 0.95	−0.0486 ± 0.0071	−0.62 ± 0.14
0.30 – 0.40	6.22 ± 0.70	−0.0615 ± 0.0090	−0.383 ± 0.099
0.40 – 0.50	2.34 ± 0.37	−0.045 ± 0.015	−0.107 ± 0.053
0.50 – 0.70	1.03 ± 0.21	−0.066 ± 0.015	−0.068 ± 0.029

The result of the fit is given in Table 7.6. Both the data presented in Table 7.4 as well as the fit result in Table 7.6 show some disagreement as compared to the old TASSO [TAS84j] published results. In case of Table 7.4 most of it is coming, probably, again from the too smooth correcting function applied in the past. It was checked, that both at 14 and 22 GeV the results obtained using [HOY79] (the Monte Carlo used to correct the data in [TAS84j]) and Lund O(α_s^2) Monte Carlo agree within the errors. As far as Table 7.6 is concerned, except the first two bins the c_1 and c_2 coefficients are usually different as compared to the published values (smaller in the absolute value than the old published ones) by more than 2÷3 standard deviations. Since all the coefficients are different in that way, it is statistically significant. The difference comes probably from the errors mentioned in discussing results from Table 7.4. As fas as the first two bins in Table 7.6 are concerned the published values are probably a result of a crude error (choosing wrong minimum) in fitting the function of the form $c_1\,(1 + c_2 \cdot \ln(s/s_o))$ instead of $a + b \cdot \ln(s/s_o)$.

Another way of looking at the scaled momentum distribution (usually employed in multigluon emission studies, see e.g. [DOK88] and references therein) is to plot $x_p d\sigma/dx_p$ versus $\ln(1/x_p)$ instead of plotting $d\sigma/dx_p$ against x_p, which allows to have a closer look at the low x_p values. From Fig. 7.5 (Table 7.7) one can clearly see, that the growth of the multiplicity with energy is due to the increase of slow (as compared to the beam momentum) particle production. The multigluon emission aspect will be discussed at the end of this chapter.

7.3 Distribution of global Event Parameters

7.3.1 Sphericity Distribution

Fig. 7.6 (Table 7.8) shows the sphericity (see Chapter 2) distributions. As one can see every single distribution has a maximum in the region of well collimated events and the contribution of the events with low sphericity increases as energy goes up. Only a very slow decrease of the cross section above S=.1 is visible, especially for $W \gtrsim 22$ GeV. The energy dependence of the average sphericity is presented in Fig. 7.8. As can be seen, the average sphericity decreases with energy, indicating that the events become more and more collimated on the average with increasing center-of-mass energy. The 14, 22 and 35 GeV results differ drastically from the [TAS84j] result. The difference comes mainly from the fact, that the sphericity distributions are very sensitive to the Monte Carlo used to correct the data. The use of independent jet O(α_s) Monte Carlo [HOY79], which does not reproduce the data, produces significantly different sphericity distribution as compared to results obtained with Lund LLA+O(α_s) Monte Carlo. The sphericity distributions corrected with the [HOY79] Monte Carlo have its maximum shifted towards the low values (two-jet events region). Since Lund LLA+O(α_s) Monte Carlo reproduces the data quite well, one can hope, that new distributions are close to the "true" ones.

7.3.2 Aplanarity Distribution

The aplanarity (see Chapter 2) distributions are presented in Fig. 7.7 and in Table 7.9. The energy dependence of the average value of the aplanarity is shown in Fig. 7.8. As one can see the events get less aplanar as energy increases. Also the aplanarity distributions are very different as compared to the old published ones [TAS84j] and they are also very sensitive to the Monte Carlo used to correct them.

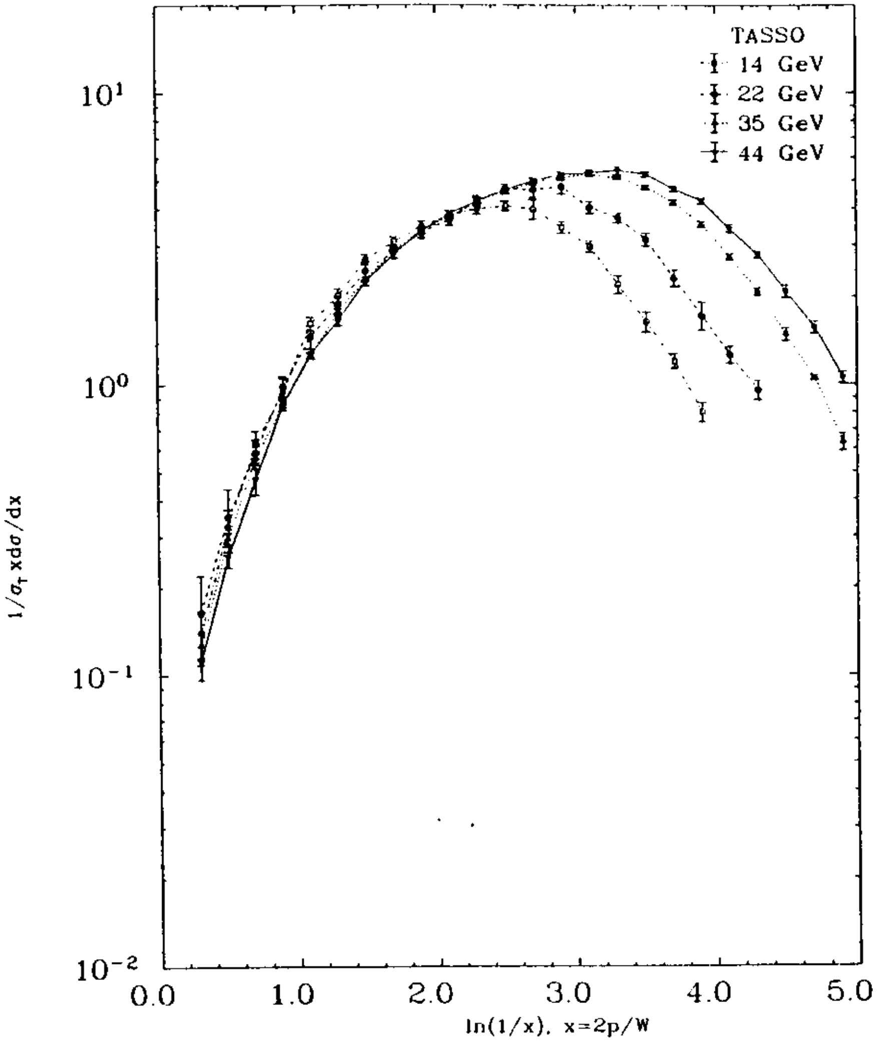

Fig. 7.5. Normalized $\ln(1/x_p)$ distributions $1/\sigma_{tot}\, d\sigma/d\ln(1/x_p)$, where $x_p = 2p/W$ at $\overline{W}$=14, 22, 35 and 44 GeV.

Table 7.7

Normalized $\ln(1/x_p)$ distributions $1/\sigma_{tot}\, d\sigma/d\ln(1/x_p)$, where $x_p = 2p/W$.

$\ln(1/x_p)$	14 GeV	22 GeV	35 GeV	44 GeV
0.0 – 0.2	0.052 ± 0.026	0.033 ± 0.016	0.0222 ± 0.0088	0.0195 ± 0.0043
0.2 – 0.4	0.140 ± 0.025	0.164 ± 0.056	0.127 ± 0.013	0.111 ± 0.015
0.4 – 0.6	0.325 ± 0.047	0.351 ± 0.086	0.297 ± 0.013	0.257 ± 0.022
0.6 – 0.8	0.624 ± 0.068	0.581 ± 0.067	0.559 ± 0.020	0.474 ± 0.057
0.8 – 1.0	0.95 ± 0.10	0.986 ± 0.084	0.860 ± 0.026	0.865 ± 0.046
1.0 – 1.2	1.620 ± 0.085	1.46 ± 0.13	1.256 ± 0.028	1.277 ± 0.053
1.2 – 1.4	2.02 ± 0.11	1.88 ± 0.13	1.780 ± 0.033	1.663 ± 0.070
1.4 – 1.6	2.68 ± 0.11	2.45 ± 0.16	2.294 ± 0.042	2.259 ± 0.078
1.6 – 1.8	3.09 ± 0.12	2.86 ± 0.14	2.888 ± 0.040	2.798 ± 0.094
1.8 – 2.0	3.49 ± 0.15	3.31 ± 0.15	3.369 ± 0.047	3.367 ± 0.098
2.0 – 2.2	3.81 ± 0.13	3.67 ± 0.16	3.741 ± 0.042	3.855 ± 0.098
2.2 – 2.4	3.99 ± 0.16	4.26 ± 0.19	4.264 ± 0.078	4.26 ± 0.13
2.4 – 2.6	4.08 ± 0.15	4.68 ± 0.19	4.587 ± 0.076	4.66 ± 0.18
2.6 – 2.8	3.98 ± 0.30	4.63 ± 0.27	4.878 ± 0.067	4.99 ± 0.11
2.8 – 3.0	3.44 ± 0.16	4.74 ± 0.26	5.106 ± 0.083	5.23 ± 0.12
3.0 – 3.2	2.97 ± 0.14	4.03 ± 0.19	5.244 ± 0.080	5.31 ± 0.13
3.2 – 3.4	2.19 ± 0.15	3.71 ± 0.14	5.100 ± 0.070	5.40 ± 0.16
3.4 – 3.6	1.63 ± 0.13	3.13 ± 0.16	4.737 ± 0.080	5.25 ± 0.12
3.6 – 3.8	1.198 ± 0.070	2.31 ± 0.15	4.206 ± 0.081	4.68 ± 0.10
3.8 – 4.0	0.799 ± 0.061	1.72 ± 0.19	3.532 ± 0.086	4.26 ± 0.10
4.0 – 4.2	0.478 ± 0.095	1.257 ± 0.083	2.734 ± 0.068	3.41 ± 0.10
4.2 – 4.4		0.953 ± 0.073	2.082 ± 0.064	2.784 ± 0.075
4.4 – 4.6		0.56 ± 0.10	1.487 ± 0.075	2.08 ± 0.10
4.6 – 4.8			1.051 ± 0.022	1.566 ± 0.072
4.8 – 5.0			0.632 ± 0.044	1.053 ± 0.049

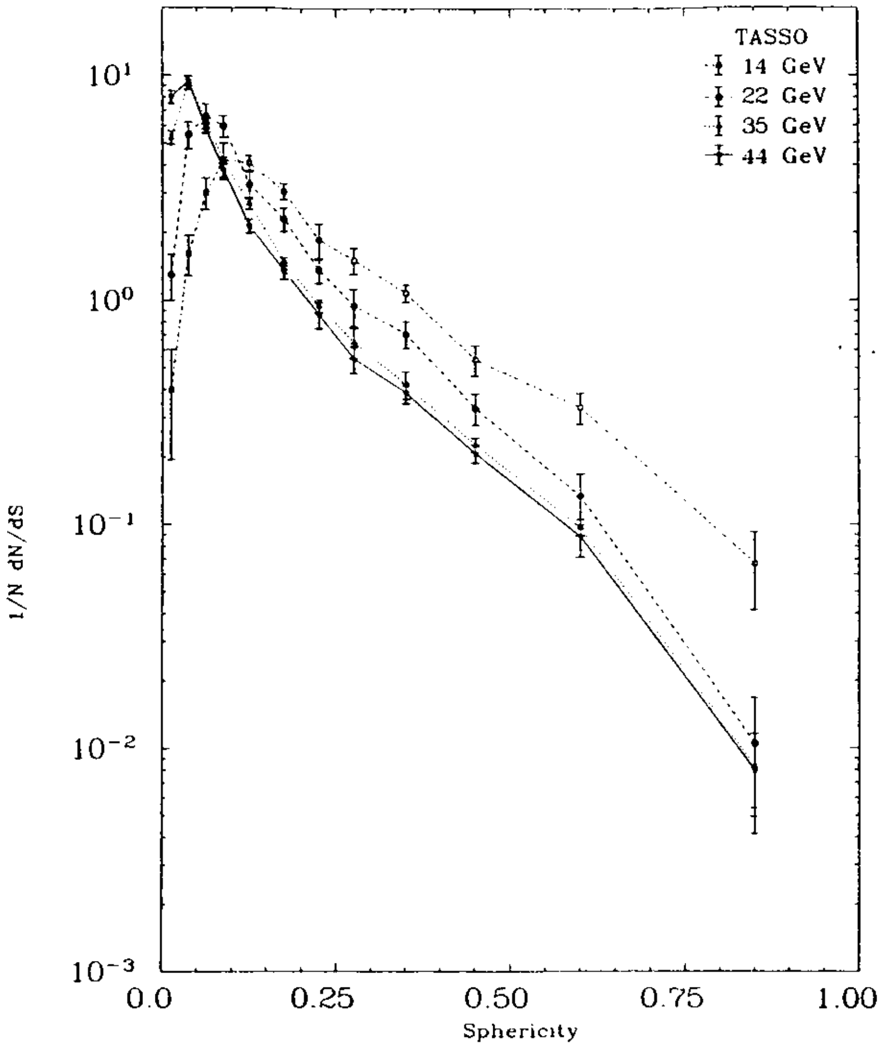

Fig. 7.6. Normalized sphericity distributions $1/N\, dN/dS$ at $\overline{W}$=14, 22, 35 and 44 GeV.

Table 7.8

Normalized sphericity distributions $1/N\, dN/dS$.

S	14 GeV	22 GeV	35 GeV	44 GeV
0.000 - 0.025	0.40 ± 0.20	1.30 ± 0.30	5.30 ± 0.37	8.02 ± 0.54
0.025 - 0.050	1.61 ± 0.33	5.46 ± 0.74	9.31 ± 0.63	9.45 ± 0.43
0.050 - 0.075	3.01 ± 0.49	6.61 ± 0.84	6.32 ± 0.27	5.83 ± 0.31
0.075 - 0.100	4.21 ± 0.78	5.96 ± 0.65	4.19 ± 0.15	3.80 ± 0.26
0.100 - 0.150	4.09 ± 0.31	3.28 ± 0.45	2.70 ± 0.16	2.14 ± 0.15
0.150 - 0.200	3.06 ± 0.25	2.30 ± 0.28	1.485 ± 0.062	1.35 ± 0.11
0.200 - 0.250	1.85 ± 0.33	1.36 ± 0.17	0.938 ± 0.061	0.86 ± 0.11
0.250 - 0.300	1.50 ± 0.20	0.94 ± 0.18	0.646 ± 0.100	0.544 ± 0.073
0.300 - 0.350	1.09 ± 0.15	0.87 ± 0.18	0.485 ± 0.080	0.455 ± 0.055
0.350 - 0.400	1.05 ± 0.18	0.56 ± 0.12	0.359 ± 0.043	0.320 ± 0.049
0.400 - 0.450	0.58 ± 0.14	0.330 ± 0.053	0.254 ± 0.028	0.217 ± 0.044
0.450 - 0.500	0.509 ± 0.083		0.198 ± 0.018	0.193 ± 0.060
0.500 - 0.550	0.34 ± 0.10	0.150 ± 0.037	0.138 ± 0.019	0.150 ± 0.049
0.550 - 0.600	0.34 ± 0.12		0.120 ± 0.019	0.083 ± 0.025
0.600 - 0.650	0.348 ± 0.073	0.115 ± 0.051	0.084 ± 0.013	0.084 ± 0.025
0.650 - 0.700			0.0469 ± 0.0081	0.043 ± 0.016
0.700 - 1.000	0.067 ± 0.025	0.0104 ± 0.0063	0.0082 ± 0.0033	0.0079 ± 0.0025
$< S >$	0.2252 ± 0.0075	0.1528 ± 0.0075	0.1155 ± 0.0047	0.1053 ± 0.0035

7.3.3 Thrust Distribution

Fig. 7.9 depicts the thrust (see Chapter 2) distributions, which are described numerically in Table 7.10. The energy dependence of the average thrust value is presented in Fig. 7.10. Similar conclusion and remarks about the event collimation and about Monte Carlo model dependence as in the case of sphericity and aplanarity can be drawn for thrust.

7.3.4 Parisi C and D Variables Distribution

The distributions of Parisi event shape variables C and D (see Chapter 2) are presented in Fig. 7.11 and 7.12 and in Table 7.11 and 7.12. Also these variables show, that the contribution of two-jet events increases and that events become less and less aplanar as the center-of-mass energy increases. It was found, that also these distributions are sensitive to the Monte Carlo used to correct the data.

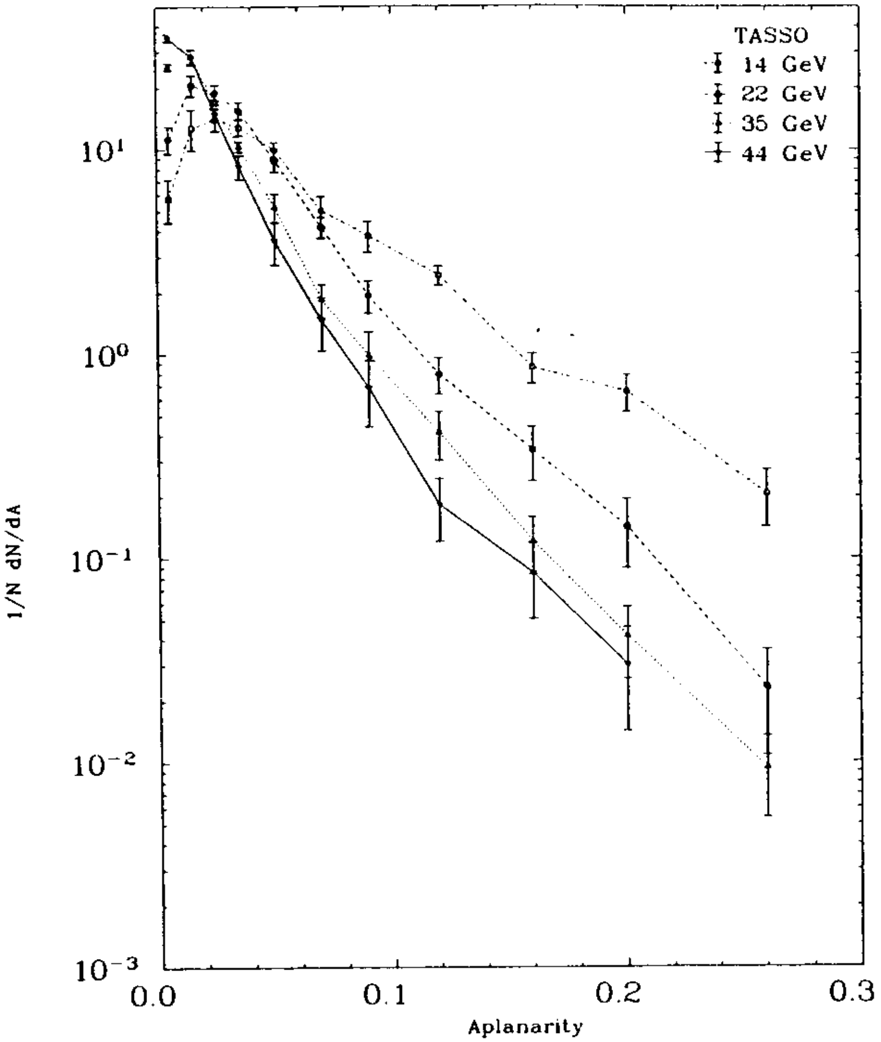

Fig. 7.7. Normalized aplanarity distributions $1/N\, dN/dA$ at $\overline{W}$=14, 22, 35 and 44 GeV.

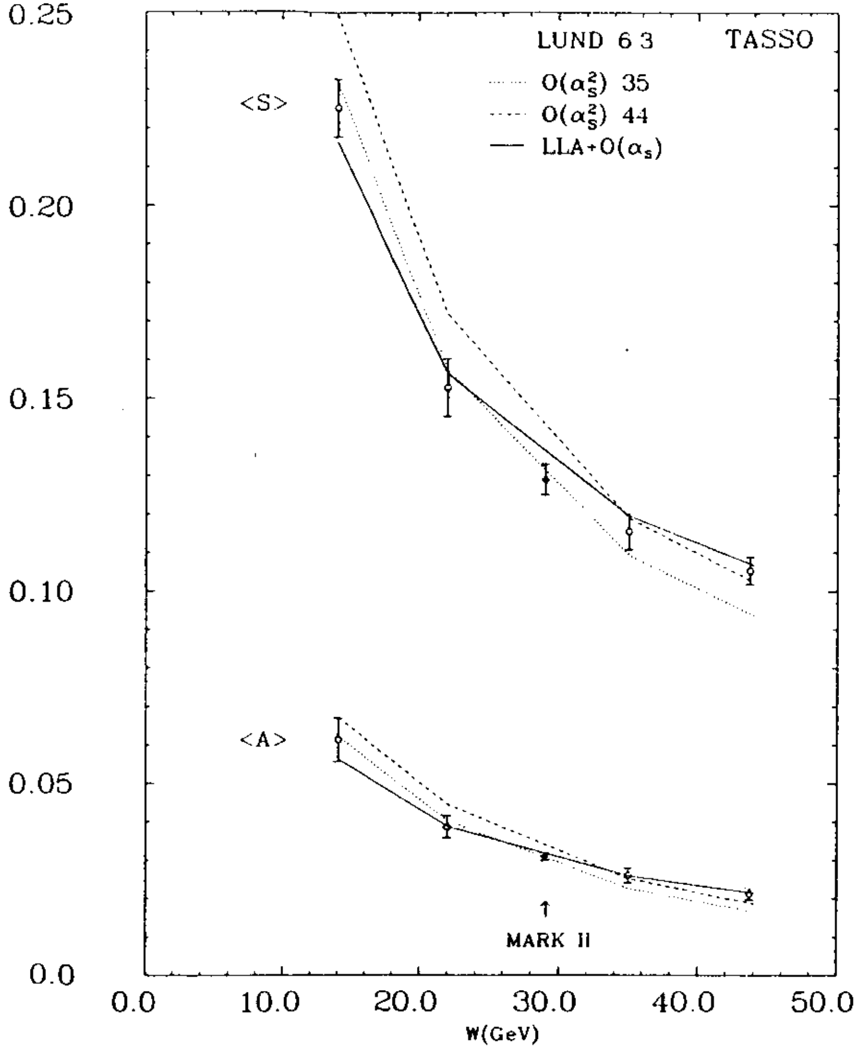

Fig. 7.8. The average sphericity ($< S >$) and aplanarity ($< A >$) as a function of W. The curves show predictions of the Lund O(α_s^2) Monte Carlo tuned at 35 and 44 GeV and predictions of the Lund LLA+O(α_s) Monte Carlo tuned at 44 GeV.

Table 7.9

Normalized aplanarity distributions $1/N\, dN/dA$.

A	14 GeV	22 GeV	35 GeV	44 GeV
0.00 - 0.01	5.8 ± 1.5	11.2 ± 1.9	25.4 ± 1.7	35.3 ± 1.9
0.01 - 0.02	12.8 ± 2.9	20.6 ± 2.4	28.4 ± 2.6	28.4 ± 2.1
0.02 - 0.03	14.0 ± 1.7	18.0 ± 1.7	17.00 ± 0.65	14.9 ± 1.1
0.03 - 0.04	12.8 ± 1.2	15.5 ± 1.5	10.30 ± 0.65	8.3 ± 1.1
0.04 - 0.06	9.97 ± 0.98	8.9 ± 1.2	5.25 ± 0.88	3.59 ± 0.87
0.06 - 0.10	4.43 ± 0.71	3.05 ± 0.38	1.43 ± 0.32	1.08 ± 0.33
0.10 - 0.15	2.16 ± 0.37	0.78 ± 0.16	0.37 ± 0.11	0.180 ± 0.060
0.15 - 0.20	0.68 ± 0.14	0.210 ± 0.065	0.083 ± 0.025	0.046 ± 0.025
0.20 - 0.30	0.32 ± 0.16	0.039 ± 0.023	0.0136 ± 0.0053	0.0157 ± 0.0080
$< A >$	0.0613 ± 0.0057	0.0386 ± 0.0029	0.0261 ± 0.0019	0.0213 ± 0.0015

Table 7.10

Normalized thrust distributions $1/N\, dN/dT$.

T	14 GeV	22 GeV	35 GeV	44 GeV
0.60 - 0.64	0.47 ± 0.23	0.07 ± 0.20	0.037 ± 0.020	0.019 ± 0.014
0.64 - 0.68	0.62 ± 0.24	0.218 ± 0.074	0.164 ± 0.027	0.171 ± 0.048
0.68 - 0.72	1.16 ± 0.31	0.37 ± 0.12	0.328 ± 0.065	0.236 ± 0.042
0.72 - 0.76	1.61 ± 0.23	0.81 ± 0.23	0.583 ± 0.093	0.57 ± 0.11
0.76 - 0.80	1.92 ± 0.36	1.22 ± 0.17	0.869 ± 0.079	0.84 ± 0.11
0.80 - 0.84	3.32 ± 0.45	2.27 ± 0.29	1.44 ± 0.13	1.12 ± 0.13
0.84 - 0.88	4.52 ± 0.73	4.06 ± 0.38	2.65 ± 0.25	2.48 ± 0.16
0.88 - 0.90	6.05 ± 0.55	5.7 ± 1.2	4.04 ± 0.40	3.55 ± 0.30
0.90 - 0.92	6.7 ± 1.2	7.23 ± 0.87	6.04 ± 0.66	4.85 ± 0.49
0.92 - 0.94	5.6 ± 1.6	8.60 ± 0.82	8.6 ± 1.1	6.8 ± 1.1
0.94 - 0.96	3.1 ± 1.1	7.8 ± 1.9	10.65 ± 0.36	11.67 ± 0.66
0.96 - 0.98	0.97 ± 0.31	2.9 ± 1.0	7.5 ± 1.4	10.3 ± 1.9
0.98 - 1.00	0.132 ± 0.066	0.33 ± 0.18	1.14 ± 0.33	1.97 ± 0.63
$< T >$	0.8499 ± 0.0085	0.8876 ± 0.0073	0.9079 ± 0.0045	0.9157 ± 0.0049

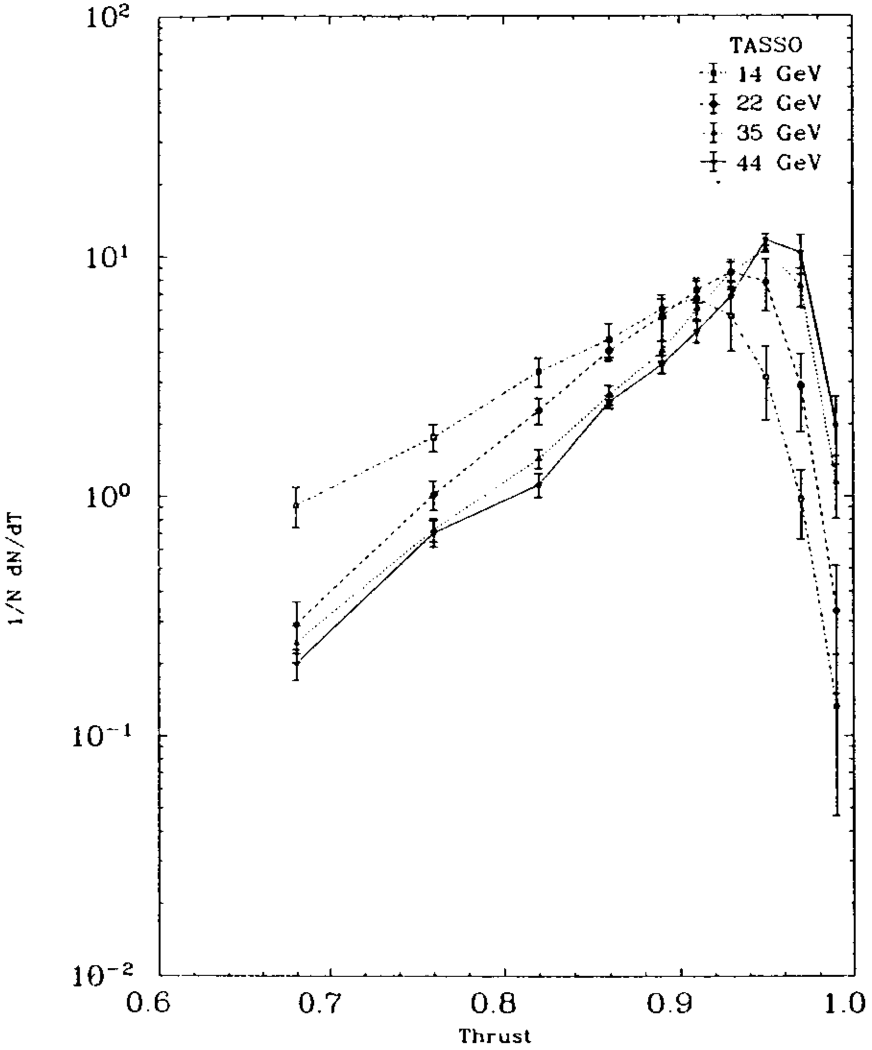

Fig. 7.9. Normalized thrust distributions $1/N\, dN/dT$ at $\overline{W}$=14, 22, 35 and 44 GeV.

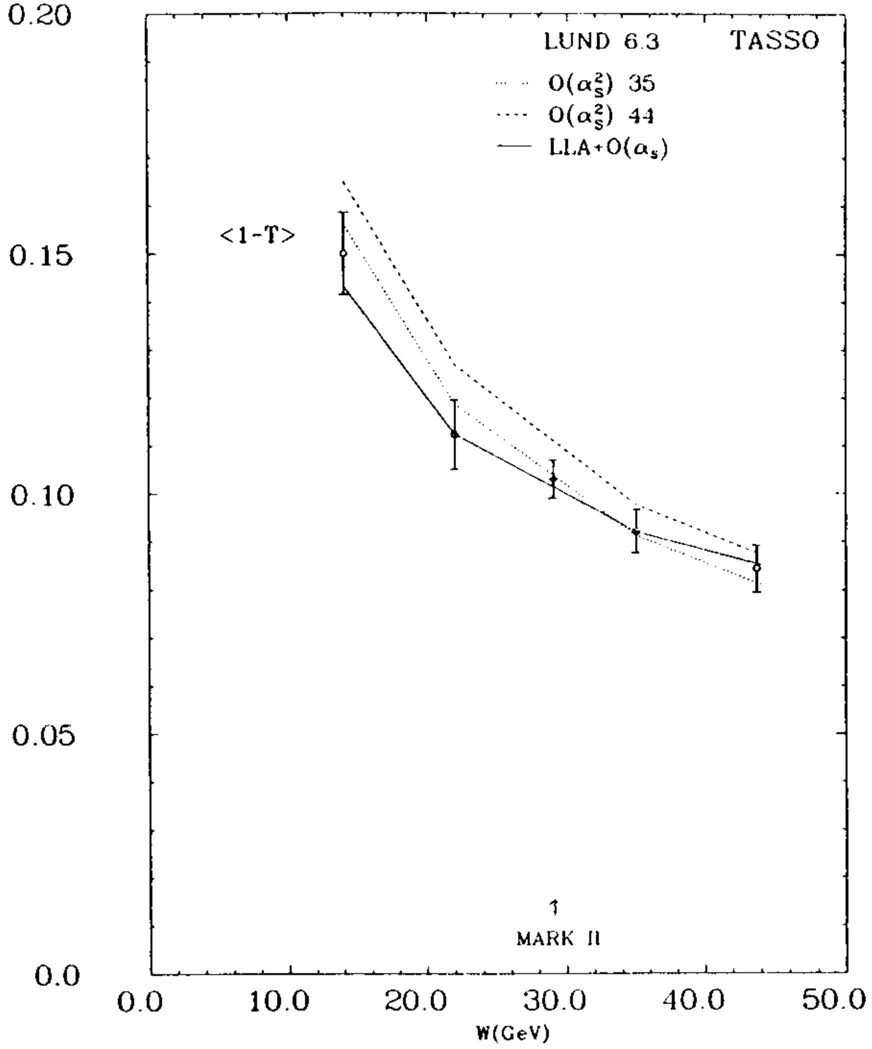

Fig. 7.10. Average value of 1−thrust (< 1 − T >) as a function of W. The curves show predictions of the Lund O(α_s^2) Monte Carlo tuned at 35 and 44 GeV and predictions of Lund LLA+O(α_s) Monte Carlo tuned at 44 GeV.

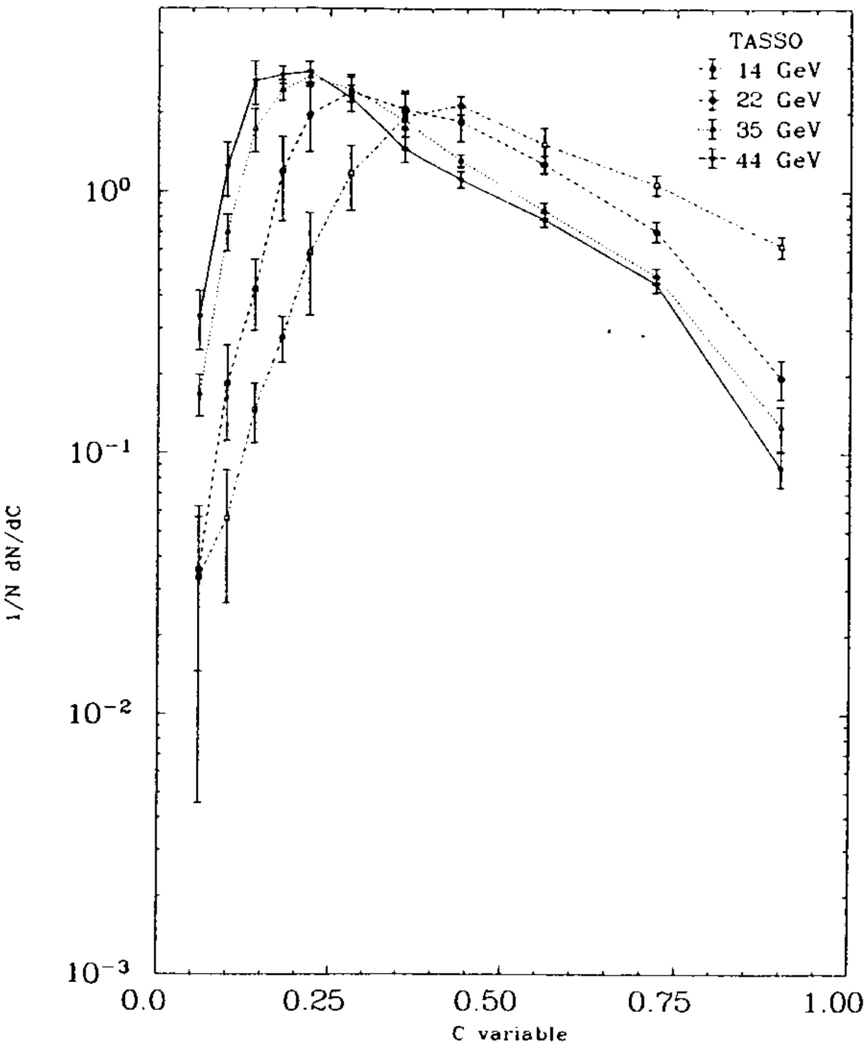

Fig. 7.11. Normalized Parisi C distributions $1/N\, dN/dC$ at $\widetilde{W}$=14, 22, 35 and 44 GeV.

Table 7.11

Normalized Parisi C distributions $1/N\, dN/dC$.

C	14 GeV	22 GeV	35 GeV	44 GeV
0.04 - 0.08	0.033 ± 0.029	0.036 ± 0.021	0.169 ± 0.031	0.332 ± 0.086
0.08 - 0.12	0.056 ± 0.030	0.185 ± 0.073	0.70 ± 0.11	1.25 ± 0.29
0.12 - 0.16	0.147 ± 0.037	0.42 ± 0.13	1.74 ± 0.33	2.64 ± 0.50
0.16 - 0.20	0.277 ± 0.055	1.20 ± 0.42	2.44 ± 0.22	2.79 ± 0.22
0.20 - 0.24	0.58 ± 0.25	1.97 ± 0.55	2.74 ± 0.13	2.85 ± 0.27
0.24 - 0.28	1.11 ± 0.42	2.36 ± 0.49	2.54 ± 0.19	2.67 ± 0.35
0.28 - 0.32	1.23 ± 0.33	2.43 ± 0.45	2.36 ± 0.39	1.90 ± 0.23
0.32 - 0.36	1.75 ± 0.59	2.09 ± 0.31	1.98 ± 0.28	1.49 ± 0.34
0.36 - 0.40	2.13 ± 0.44	2.05 ± 0.63	1.777 ± 0.097	1.43 ± 0.15
0.40 - 0.44	1.83 ± 0.29	1.80 ± 0.47	1.45 ± 0.12	1.16 ± 0.10
0.44 - 0.48	2.49 ± 0.37	1.89 ± 0.43	1.192 ± 0.081	1.08 ± 0.12
0.48 - 0.56	1.41 ± 0.27	1.38 ± 0.17	0.957 ± 0.075	0.960 ± 0.085
0.56 - 0.64	1.62 ± 0.28	1.17 ± 0.21	0.747 ± 0.063	0.621 ± 0.046
0.64 - 0.72	1.20 ± 0.11	0.90 ± 0.15	0.540 ± 0.052	0.456 ± 0.039
0.72 - 0.80	0.95 ± 0.15	0.53 ± 0.13	0.422 ± 0.033	0.442 ± 0.062
0.80 - 1.00	0.622 ± 0.059	0.195 ± 0.033	0.127 ± 0.024	0.088 ± 0.014
$< C >$	0.5355 ± 0.0099	0.4324 ± 0.0083	0.3600 ± 0.0029	0.3325 ± 0.0069

Table 7.12

Normalized Parisi D distributions $1/N\, dN/dD$.

D	14 GeV	22 GeV	35 GeV	44 GeV
0.00 - 0.04	1.77 ± 0.50	3.88 ± 0.88	8.15 ± 0.53	10.39 ± 0.86
0.04 - 0.08	3.11 ± 0.92	5.59 ± 0.70	5.76 ± 0.65	5.25 ± 0.67
0.08 - 0.12	3.66 ± 0.71	4.06 ± 0.55	3.36 ± 0.21	2.86 ± 0.40
0.12 - 0.20	2.54 ± 0.20	2.40 ± 0.25	1.742 ± 0.058	1.56 ± 0.11
0.20 - 0.30	1.66 ± 0.22	1.39 ± 0.16	0.889 ± 0.082	0.757 ± 0.061
0.30 - 0.40	0.89 ± 0.24	0.70 ± 0.12	0.411 ± 0.045	0.332 ± 0.055
0.40 - 0.60	0.629 ± 0.087	0.274 ± 0.052	0.168 ± 0.040	0.106 ± 0.035
0.60 - 1.00	0.197 ± 0.036	0.045 ± 0.011	0.0184 ± 0.0055	0.0134 ± 0.0041
$< D >$	0.246 ± 0.010	0.1586 ± 0.0065	0.1127 ± 0.0044	0.0947 ± 0.0023

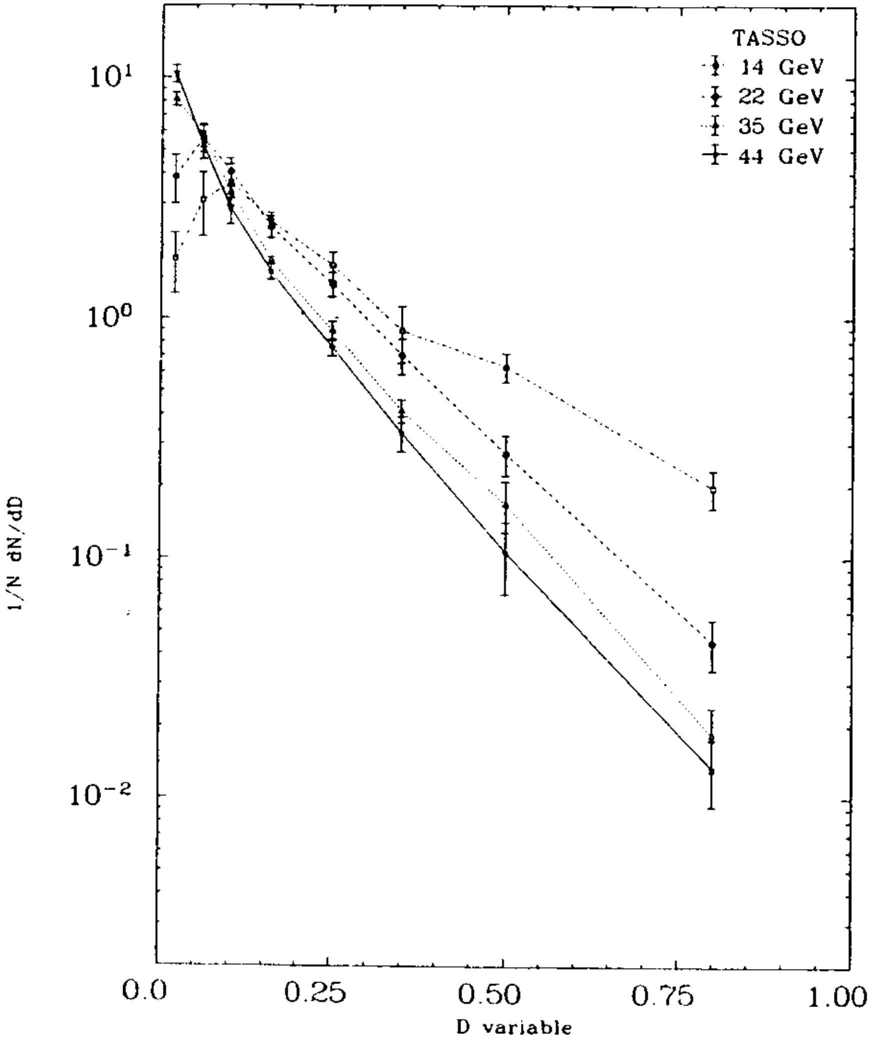

Fig. 7.12. Normalized Parisi D distributions $1/N\, dN/dD$ at $\overline{W}$=14, 22, 35 and 44 GeV.

7.3.5 Angular Distribution of the Event Axis

Fig. 7.13-7.15 and Table 7.13-7.15 present the angular distributions of the sphericity, thrust and Parisi tensor axes with respect to the beam axis for the center-of-mass energy equal to 12, 22, 35 and 44 GeV. All the distributions are well described by a function of the form:

$$\frac{1}{N}\frac{dN}{d\cos\Theta_{S,T,P}} \sim (1+\cos^2\Theta)$$

shown by the curves in Fig. 7.13-7.15. The result of the fits of the form:

$$\frac{1}{N}\frac{dN}{d\cos\Theta_{S,T,P}} \sim (1+a_{S,T,P}\cos^2\Theta)$$

are shown in Table 7.16.

Table 7.13

Angular distributions of the sphericity axis $1/N\, dN/d\cos\Theta_S$.

$\cos\Theta_S$	14 GeV	22 GeV	35 GeV	44 GeV
0.00 – 0.05	0.719 ± 0.081	0.640 ± 0.085	0.693 ± 0.034	0.681 ± 0.069
0.05 – 0.10	0.706 ± 0.091	0.81 ± 0.12	0.750 ± 0.033	0.741 ± 0.055
0.10 – 0.15	0.830 ± 0.093	0.57 ± 0.11	0.736 ± 0.034	0.783 ± 0.063
0.15 – 0.20	0.798 ± 0.092	0.707 ± 0.090	0.725 ± 0.035	0.744 ± 0.054
0.20 – 0.25	0.97 ± 0.15	0.90 ± 0.13	0.714 ± 0.035	0.724 ± 0.081
0.25 – 0.30	0.752 ± 0.088	0.782 ± 0.096	0.816 ± 0.032	0.740 ± 0.088
0.30 – 0.35	0.97 ± 0.11	0.664 ± 0.094	0.801 ± 0.034	0.861 ± 0.067
0.35 – 0.40	0.78 ± 0.11	0.650 ± 0.097	0.860 ± 0.041	0.869 ± 0.059
0.40 – 0.45	0.823 ± 0.087	0.94 ± 0.16	0.837 ± 0.036	0.944 ± 0.063
0.45 – 0.50	0.914 ± 0.098	1.06 ± 0.17	0.922 ± 0.034	0.879 ± 0.060
0.50 – 0.55	1.08 ± 0.11	0.92 ± 0.12	0.969 ± 0.041	0.927 ± 0.059
0.55 – 0.60	0.98 ± 0.10	1.07 ± 0.13	0.963 ± 0.039	0.922 ± 0.083
0.60 – 0.65	1.02 ± 0.12	1.06 ± 0.11	1.093 ± 0.043	0.981 ± 0.063
0.65 – 0.70	1.035 ± 0.095	1.24 ± 0.19	1.040 ± 0.065	1.142 ± 0.088
0.70 – 0.75	1.14 ± 0.12	1.33 ± 0.14	1.226 ± 0.042	1.23 ± 0.11
0.75 – 0.80	1.16 ± 0.15	1.29 ± 0.14	1.238 ± 0.055	1.345 ± 0.091

There is no deviation from the $(1+\cos^2\Theta)$ dependence at a center-of-mass energy of 44 GeV. It indicates, that the $e^+e^- \rightarrow q\bar{q}$ is the dominating process, but one should be aware of other result presented in Table 7.16, which also shows fit results to the Monte Carlo distributions obtained with the Lund LLA+O(α_s), Lund O(α_s^2) and [HOY79] generators. Only 14 GeV data agree with the Monte Carlo within one standard deviation. At 44 GeV two standard deviations and at 22 and 35 GeV three standard deviations are needed to

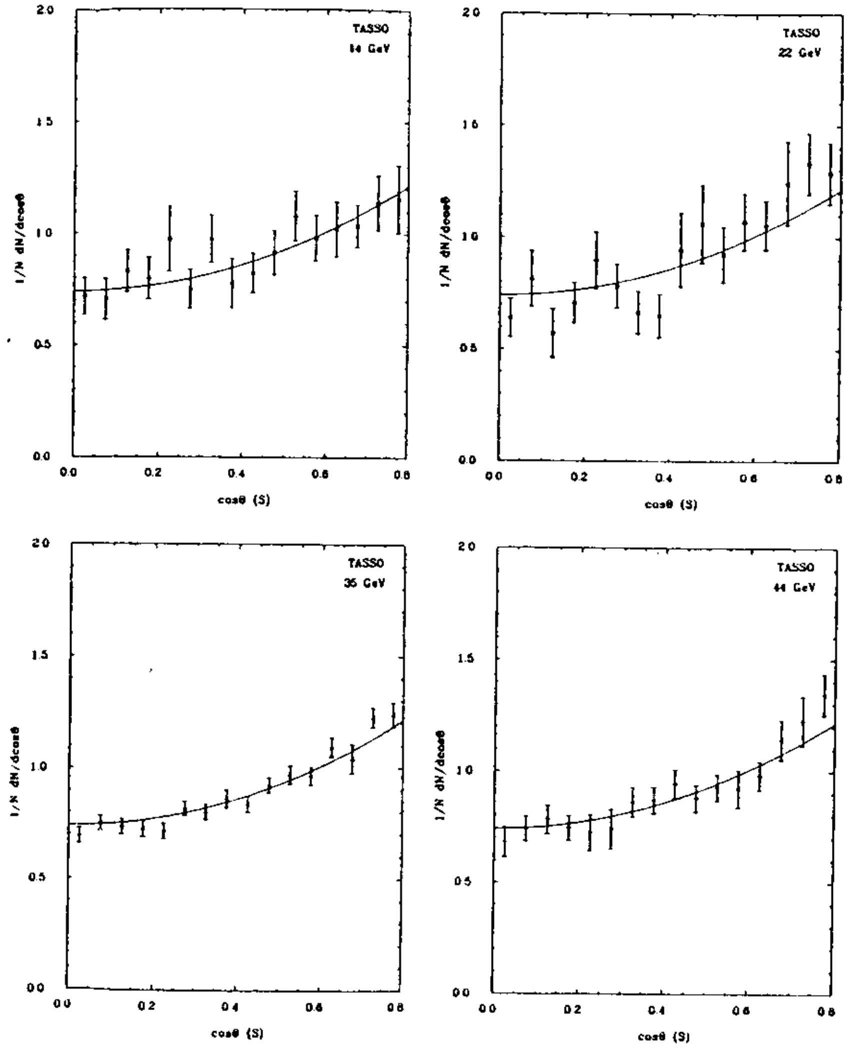

Fig. 7.13. Angular distributions of the sphericity axis $1/N\, dN/d\cos\Theta_S$ at $\overline{W}$=14, 22, 35 and 44 GeV. The curves are proportional to $1+\cos\Theta$.

match the data and the Monte Carlo. Agreement among different Monte Carlos is much better than between the data and the Monte Carlo.

This strange result might come e.g. from two sources: 1. from wrong z-coordinate measurement by means of the stereo wires of the DC, which led to wrong $\cos\Theta$ determination, or 2. from differences between the angular distributions in the Monte Carlo and in the data especially for the $e^+e^- \rightarrow q\bar{q}g$ process. However the whole problem requires probably more extensive studies, which were beyond the scope of this thesis.

Table 7.14

Angular distributions of the thrust axis $1/N\, dN/d\cos\Theta_T$.

$\cos\Theta_T$	14 GeV	22 GeV	35 GeV	44 GeV
0.00 – 0.05	0.71 ± 0.11	0.73 ± 0.13	0.698 ± 0.036	0.715 ± 0.065
0.05 – 0.10	0.787 ± 0.094	0.77 ± 0.12	0.747 ± 0.038	0.742 ± 0.059
0.10 – 0.15	0.866 ± 0.095	0.583 ± 0.097	0.781 ± 0.031	0.793 ± 0.059
0.15 – 0.20	0.791 ± 0.079	0.673 ± 0.090	0.713 ± 0.039	0.728 ± 0.051
0.20 – 0.25	0.702 ± 0.086	0.75 ± 0.11	0.754 ± 0.031	0.744 ± 0.061
0.25 – 0.30	1.01 ± 0.15	0.88 ± 0.12	0.729 ± 0.056	0.882 ± 0.071
0.30 – 0.35	0.94 ± 0.11	0.646 ± 0.081	0.854 ± 0.040	0.755 ± 0.055
0.35 – 0.40	0.771 ± 0.086	0.807 ± 0.097	0.850 ± 0.034	0.897 ± 0.090
0.40 – 0.45	0.86 ± 0.10	1.06 ± 0.14	0.835 ± 0.040	0.892 ± 0.070
0.45 – 0.50	0.884 ± 0.087	0.93 ± 0.12	0.911 ± 0.048	0.875 ± 0.060
0.50 – 0.55	0.92 ± 0.14	1.04 ± 0.13	0.940 ± 0.036	0.954 ± 0.062
0.55 – 0.60	1.03 ± 0.13	0.94 ± 0.12	1.085 ± 0.058	0.892 ± 0.086
0.60 – 0.65	1.02 ± 0.12	1.32 ± 0.15	0.988 ± 0.072	0.972 ± 0.069
0.65 – 0.70	1.08 ± 0.14	1.34 ± 0.28	1.148 ± 0.059	1.143 ± 0.070
0.70 – 0.75	1.07 ± 0.11	1.17 ± 0.13	1.147 ± 0.077	1.29 ± 0.10
0.75 – 0.80	1.24 ± 0.17	1.05 ± 0.14	1.265 ± 0.060	1.28 ± 0.13

7.4 Single Particle Distributions with Respect to the Event Axis

7.4.1 Longitudinal and transverse Momentum Distributions

In this subsection the sphericity axis will be used as the event axis.

Fig. 7.16 (Table 7.17) displays the distributions of the longitudinal momentum. The distributions have a maximum at $p_{\parallel} = 0$. When $p_{\parallel}$ becomes larger than ≈ 2 GeV the distributions become very similar to the p distributions (see Fig. 7.1). The spectra become broader as energy increases, which means, that the contribution of faster particles increases. The number of particles with small $p_{\parallel}$ remains almost constant with energy. The center-of-mass energy dependence of the average $p_{\parallel}$ is shown in Fig. 7.2.

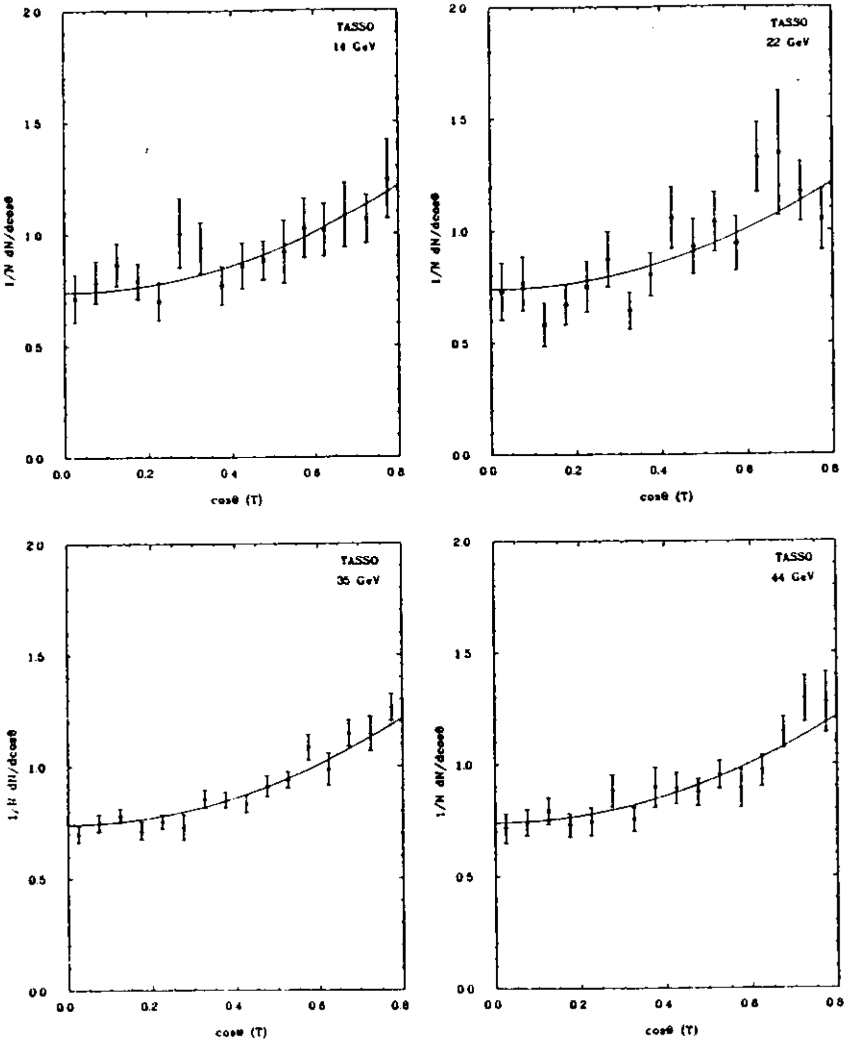

Fig. 7.14. Angular distributions of the thrust axis $1/N\, dN/d\cos\Theta_T$ at $\overline{W}$=14, 22, 35 and 44 GeV. The curves are proportional to $1+\cos\Theta$.

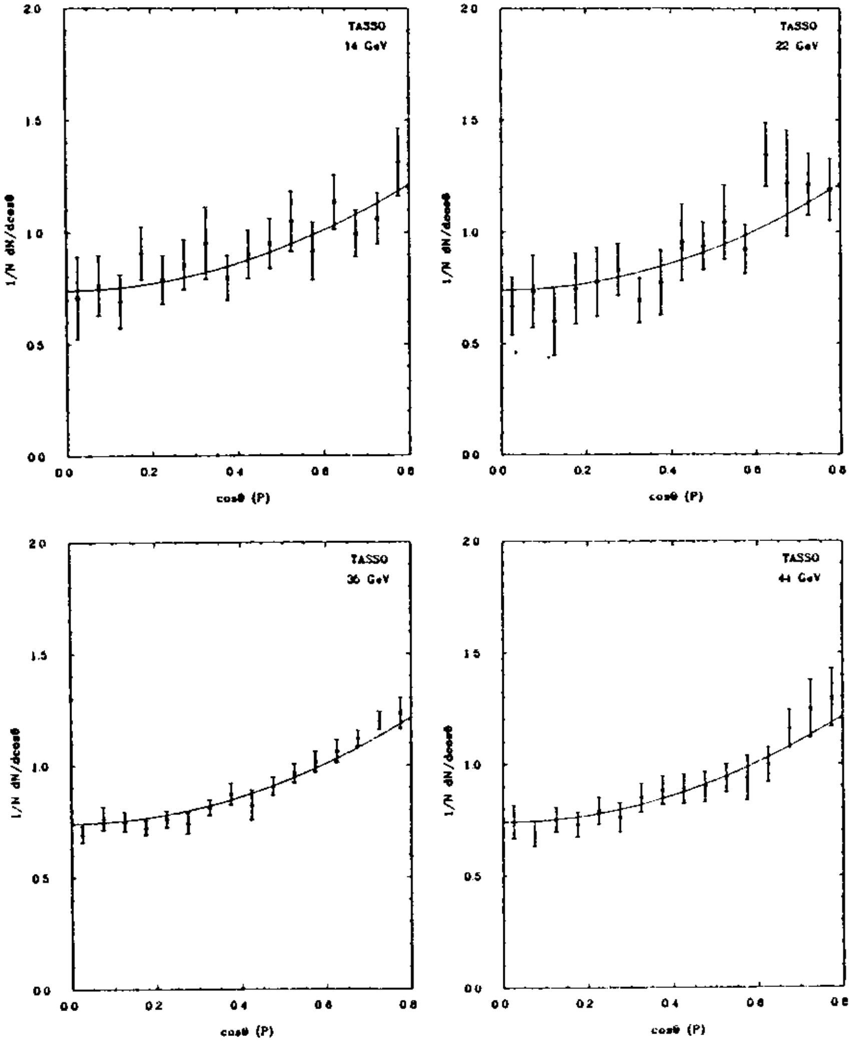

Fig. 7.15. Angular distributions of the Parisi Tensor axis $1/N\, dN/d\cos\Theta_P$ at $\overline{W}$=14, 22, 35 and 44 GeV. The curves are proportional to $1+\cos\Theta$.

Table 7.15

Angular distributions of the Parisi Tensor axis $1/N\, dN/d\cos\Theta_P$.

$\cos\Theta_P$	14 GeV	22 GeV	35 GeV	44 GeV
0.00 – 0.05	0.71 ± 0.18	0.67 ± 0.13	0.692 ± 0.036	0.742 ± 0.075
0.05 – 0.10	0.76 ± 0.13	0.73 ± 0.16	0.764 ± 0.053	0.691 ± 0.058
0.10 – 0.15	0.69 ± 0.12	0.60 ± 0.15	0.748 ± 0.044	0.752 ± 0.056
0.15 – 0.20	0.91 ± 0.12	0.75 ± 0.16	0.722 ± 0.031	0.729 ± 0.055
0.20 – 0.25	0.79 ± 0.11	0.78 ± 0.15	0.760 ± 0.037	0.791 ± 0.061
0.25 – 0.30	0.85 ± 0.11	0.83 ± 0.12	0.742 ± 0.047	0.761 ± 0.065
0.30 – 0.35	0.95 ± 0.16	0.69 ± 0.10	0.811 ± 0.035	0.849 ± 0.064
0.35 – 0.40	0.80 ± 0.10	0.77 ± 0.15	0.872 ± 0.048	0.882 ± 0.064
0.40 – 0.45	0.90 ± 0.11	0.95 ± 0.17	0.823 ± 0.067	0.888 ± 0.067
0.45 – 0.50	0.95 ± 0.11	0.94 ± 0.11	0.907 ± 0.041	0.897 ± 0.069
0.50 – 0.55	1.05 ± 0.13	1.05 ± 0.17	0.965 ± 0.043	0.938 ± 0.063
0.55 – 0.60	0.91 ± 0.13	0.92 ± 0.11	1.017 ± 0.047	0.937 ± 0.098
0.60 – 0.65	1.13 ± 0.12	1.35 ± 0.14	1.063 ± 0.052	0.996 ± 0.077
0.65 – 0.70	0.99 ± 0.11	1.22 ± 0.24	1.119 ± 0.037	1.157 ± 0.086
0.70 – 0.75	1.06 ± 0.11	1.21 ± 0.14	1.200 ± 0.041	1.25 ± 0.13
0.75 – 0.80	1.31 ± 0.15	1.19 ± 0.14	1.234 ± 0.072	1.30 ± 0.13

The presented distributions differ from those shown in [TAS84j]. The distributions had a maximum near $p_{\parallel} = .14$ GeV and were decreasing as $p_{\parallel} \to 0$, in contradiction with the newly obtained result. It was checked, that although the uncorrected distribution behave in that way, (mainly due to the $p_{xy} \geq .1$ GeV cut) the corrected distribution increases as $p_{\parallel} \to 0$ and the correction function increases steeply in this region. If one calculates the correction function with insufficient resolution, (e.g. by smoothing), one obtains the effect of a decrease near $p_{\parallel} = 0$.

Fig. 7.17 and Table 7.18 present the distribution of the transverse momentum. The distributions decrease as $p_{\perp} \to 0$. They become broader as energy increases. Fig. 7.2 shows how the average $p_{\perp}$ depends on energy. The energy dependence of the average p and $p_{\parallel}$ are also shown. Fig. 7.2 is another evidence (apart from the S, A, T, C and D distributions), that the events become more and more collimated with the increase of center-of-mass energy, because the $< p_{\parallel} >$ increases about seven times faster than $< p_{\perp} >$. Fig. 7.18 (Table 7.19) shows the distributions of the transverse momentum squared. For all the $p_{\perp}^2$ intervals the cross section increases with the increase of energy.

Fig. 7.19 gives the energy dependence of the average transverse momentum squared. As it was already visible in Fig. 7.2 the transverse momentum increases with energy.

The momentum distributions shown so far were either inclusive distributions with one entry for one particle or distributions of average momenta over a whole event sample at

Table 7.16

Fit result to the angular dependence of the event axis $1/N\, dN/d\cos\theta_{S,T,P} \sim (1 + a_{S,T,P}\cos^2\theta)$.

DATA	14 GeV	22 GeV	35 GeV	44 GeV
a_S	0.89 ± 0.22	1.74 ± 0.33	1.26 ± 0.10	1.19 ± 0.17
a_T	0.84 ± 0.23	1.41 ± 0.32	1.20 ± 0.11	1.15 ± 0.17
a_P	0.87 ± 0.26	1.50 ± 0.37	1.29 ± 0.10	1.20 ± 0.19
Lund LLA+O(α_s)				
a_S	0.875 ± 0.026	0.965 ± 0.033	0.940 ± 0.034	0.921 ± 0.026
a_T	0.879 ± 0.026	0.954 ± 0.033	0.976 ± 0.035	0.934 ± 0.026
a_P	0.907 ± 0.026	0.966 ± 0.033	0.966 ± 0.034	0.934 ± 0.026
Lund O(α_s^2)				
a_S	0.777 ± 0.052	0.941 ± 0.059	0.932 ± 0.025	0.902 ± 0.025
a_T	0.763 ± 0.052	0.898 ± 0.058	0.929 ± 0.025	0.903 ± 0.025
a_P	0.804 ± 0.053	0.905 ± 0.058	0.930 ± 0.025	0.898 ± 0.025
[HOY79]				
a_S	0.82 ± 0.11	0.92 ± 0.14	0.963 ± 0.042	
a_T	0.86 ± 0.11	0.84 ± 0.14	0.967 ± 0.042	
a_P	0.80 ± 0.11	0.88 ± 0.14	0.955 ± 0.042	

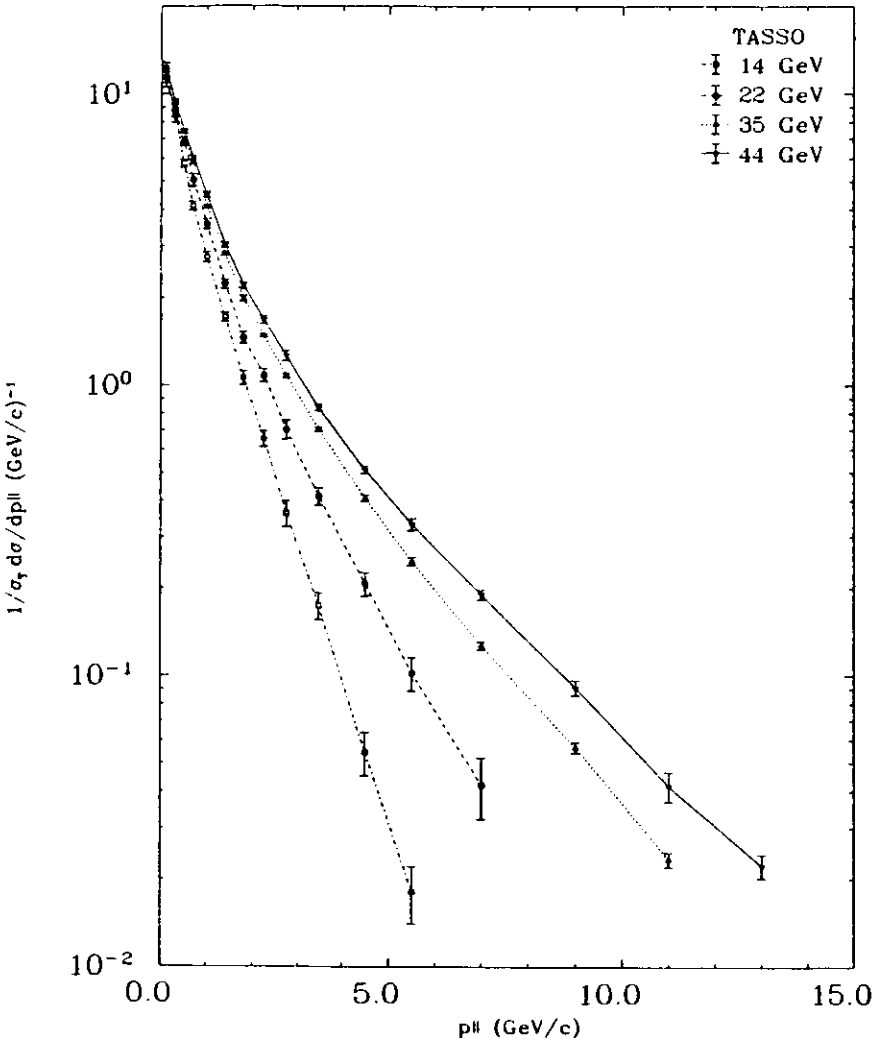

Fig. 7.16. Normalized longitudinal momentum distributions $1/\sigma_{tot}\, d\sigma/dp_\parallel$ (Gev/c)$^{-1}$ at $\overline{W}$=14, 22, 35 and 44 GeV.

Table 7.17

Normalized longitudinal momentum distributions $1/\sigma_{tot}\, d\sigma/dp_\parallel$ (Gev/c)$^{-1}$.

$p_\perp$ (GeV/c)	14 GeV		22 GeV		35 GeV		44 GeV	
0.00 - 0.05	13.51	±0.83	12.6	±1.2	14.06	±0.57	13.80	±0.83
0.05 - 0.10	11.85	±0.85	12.61	±0.74	12.44	±0.63	12.35	±0.56
0.10 - 0.15	11.1	±1.2	10.40	±0.69	11.52	±0.76	11.84	±0.88
0.15 - 0.20	9.37	±0.94	10.1	±1.3	11.02	±0.69	11.23	±0.49
0.20 - 0.25	9.73	±0.60	9.16	±0.57	10.46	±0.36	10.35	±0.31
0.25 - 0.30	8.10	±0.71	8.98	±0.50	9.68	±0.18	9.82	±0.37
0.30 - 0.35	8.42	±0.42	8.84	±0.49	9.08	±0.16	9.03	±0.38
0.35 - 0.40	7.39	±0.59	7.74	±0.64	8.62	±0.19	8.28	±0.23
0.40 - 0.45	6.58	±0.44	7.49	±0.44	8.11	±0.22	8.41	±0.32
0.45 - 0.50	6.18	±0.34	7.03	±0.48	7.69	±0.15	7.54	±0.23
0.50 - 0.60	5.15	±0.23	6.46	±0.31	6.96	±0.11	6.93	±0.18
0.60 - 0.70	4.33	±0.30	5.38	±0.32	6.21	±0.14	6.50	±0.15
0.70 - 0.80	3.95	±0.27	4.75	±0.38	5.48	±0.10	5.63	±0.14
0.80 - 0.90	3.32	±0.17	4.38	±0.30	4.838	±0.091	5.19	±0.16
0.90 - 1.00	2.84	±0.17	3.61	±0.26	4.232	±0.079	4.76	±0.17
1.00 - 1.20	2.45	±0.15	3.16	±0.14	3.683	±0.070	4.07	±0.15
1.20 - 1.40	1.96	±0.11	2.48	±0.12	3.019	±0.048	3.26	±0.10
1.40 - 1.60	1.48	±0.11	1.99	±0.11	2.631	±0.070	2.820	±0.097
1.60 - 1.80	1.175	±0.070	1.55	±0.12	2.165	±0.049	2.397	±0.083
1.80 - 2.00	0.954	±0.076	1.38	±0.11	1.805	±0.050	2.030	±0.064
2.00 - 3.00	0.510	±0.034	0.893	±0.038	1.281	±0.014	1.473	±0.045
3.00 - 4.00	0.174	±0.018	0.413	±0.028	0.702	±0.012	0.835	±0.022
4.00 - 5.00	0.0545	±0.0094	0.207	±0.019	0.406	±0.011	0.509	±0.015
5.00 - 6.00	0.0180	±0.0040	0.102	±0.013	0.2462	±0.0079	0.330	±0.016
6.00 - 8.00	0.0028	±0.0010	0.042	±0.010	0.1269	±0.0040	0.1898	±0.0076
8.00 - 10.00			0.0104	±0.0032	0.0567	±0.0025	0.0909	±0.0054
10.00 - 12.00			0.00046	±0.00032	0.0234	±0.0014	0.0417	±0.0049
12.00 - 14.00					0.0099	±0.0012	0.0222	±0.0021
14.00 - 18.00					0.00143	±0.00049	0.00761	±0.00089
18.00 - 22.00							0.00099	±0.00020
$< p_\parallel >$	0.771	±0.015	1.064	±0.023	1.436	±0.017	1.661	±0.021

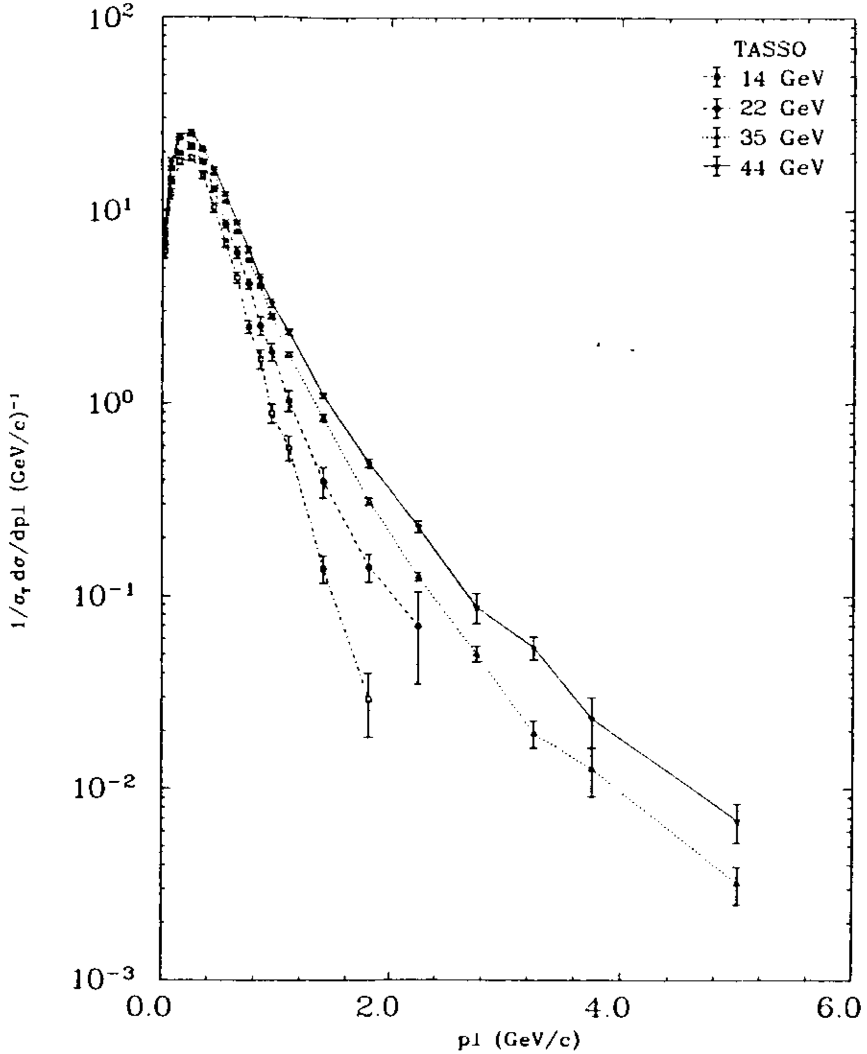

Fig. 7.17. Normalized transverse momentum distributions $1/\sigma_{tot}\, d\sigma/dp_\perp$ (GeV/c)$^{-1}$ at $\overline{W}$=14, 22, 35 and 44 GeV.

Table 7.18

Normalized transverse momentum distributions $1/\sigma_{tot}\, d\sigma/dp_\perp$ (GeV/c)$^{-1}$.

$p_\perp$ (GeV/c)	14 GeV	22 GeV	35 GeV	44 GeV
0.00 - 0.05	6.11 ± 0.49	6.79 ± 0.46	7.70 ± 0.38	8.50 ± 0.49
0.05 - 0.10	12.11 ± 0.73	14.29 ± 0.66	16.43 ± 0.45	17.70 ± 0.92
0.10 - 0.15	17.03 ± 0.96	18.1 ± 1.0	21.96 ± 0.41	23.19 ± 0.62
0.15 - 0.20	18.65 ± 0.81	21.5 ± 1.1	24.96 ± 0.46	25.54 ± 0.64
0.20 - 0.25	18.28 ± 0.00	21.58 ± 0.87	25.43 ± 0.45	26.08 ± 0.67
0.25 - 0.30	19.10 ± 0.65	21.3 ± 1.5	23.95 ± 0.36	24.00 ± 0.56
0.30 - 0.35	16.31 ± 0.83	18.97 ± 0.75	21.88 ± 0.29	22.69 ± 0.60
0.35 - 0.40	14.19 ± 0.90	16.7 ± 1.0	19.13 ± 0.56	19.48 ± 0.58
0.40 - 0.45	11.30 ± 0.85	13.71 ± 0.74	16.50 ± 0.24	17.94 ± 0.59
0.45 - 0.50	9.33 ± 0.48	12.03 ± 0.76	14.35 ± 0.22	15.02 ± 0.45
0.50 - 0.60	6.73 ± 0.33	8.47 ± 0.44	11.04 ± 0.16	12.17 ± 0.28
0.60 - 0.70	4.46 ± 0.29	6.02 ± 0.42	7.73 ± 0.14	8.69 ± 0.22
0.70 - 0.80	2.48 ± 0.19	4.15 ± 0.25	5.49 ± 0.10	6.27 ± 0.23
0.80 - 0.90	1.69 ± 0.19	2.52 ± 0.29	4.008 ± 0.085	4.43 ± 0.25
0.90 - 1.00	0.89 ± 0.10	1.84 ± 0.19	2.810 ± 0.077	3.30 ± 0.16
1.00 - 1.20	0.589 ± 0.088	1.03 ± 0.12	1.786 ± 0.054	2.344 ± 0.077
1.20 - 1.40	0.196 ± 0.040	0.51 ± 0.11	1.049 ± 0.039	1.338 ± 0.057
1.40 - 1.60	0.082 ± 0.041	0.269 ± 0.058	0.622 ± 0.038	0.846 ± 0.044
1.60 - 1.80	0.030 ± 0.018	0.164 ± 0.046	0.379 ± 0.019	0.563 ± 0.036
1.80 - 2.00	0.030 ± 0.022	0.123 ± 0.053	0.239 ± 0.016	0.412 ± 0.034
2.00 - 2.50		0.070 ± 0.035	0.1261 ± 0.0066	0.229 ± 0.016
2.50 - 3.00		0.0086 ± 0.0059	0.0500 ± 0.0048	0.087 ± 0.016
3.00 - 4.00			0.0155 ± 0.0018	0.0385 ± 0.0030
4.00 - 6.00			0.00320 ± 0.00071	0.0068 ± 0.0016
$< p_\perp >$	0.3466 ± 0.0056	0.3889 ± 0.0064	0.4342 ± 0.0038	0.4695 ± 0.0049

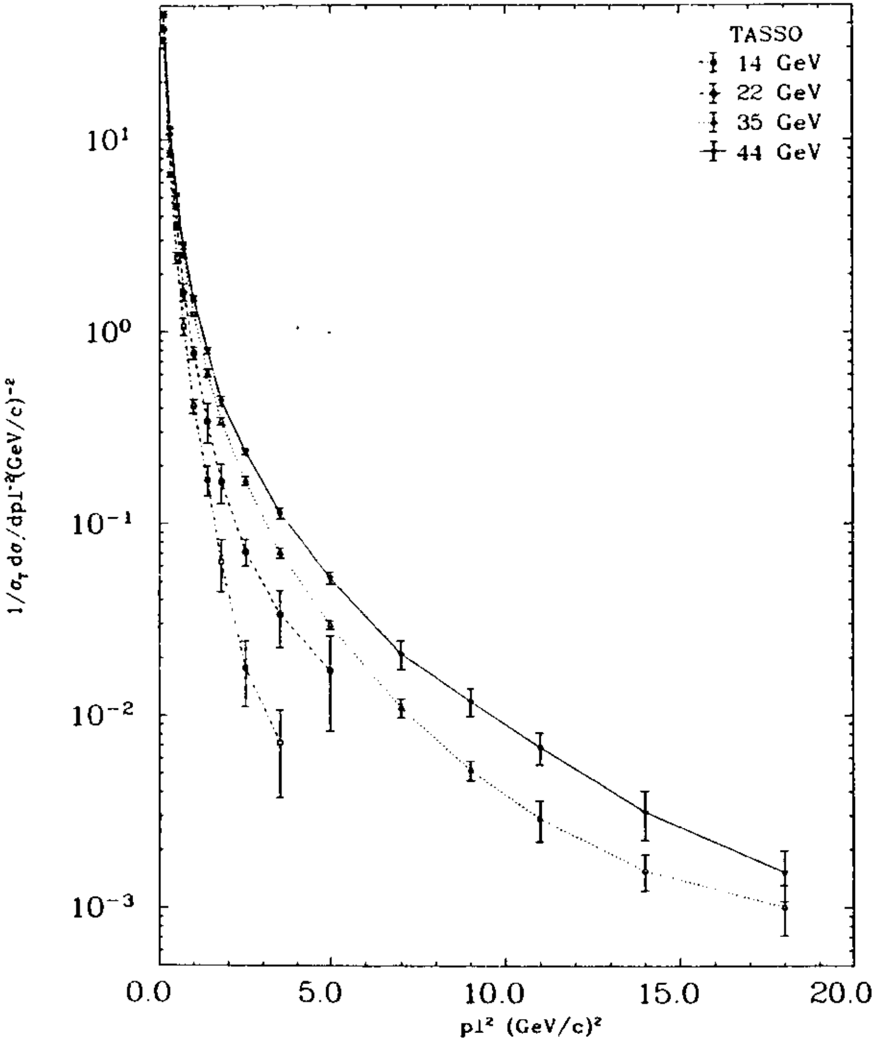

Fig. 7.18. Normalized distributions of the transverse momentum squared $1/\sigma_{tot}\, d\sigma/dp_\perp^2$ $(\mathrm{GeV}/c)^{-2}$ at $\overline{W}$=14, 22, 35 and 44 GeV.

Table 7.19

Normalized distributions of the transverse momentum squared $1/\sigma_{tot}\, d\sigma/dp_\perp^2$ $(\mathrm{GeV}/c)^{-2}$.

$p_\perp^2$ $(\mathrm{GeV}/c)^2$	14 GeV	22 GeV	35 GeV	44 GeV
0.00 – 0.01	91.1 ±5.2	105.4 ±3.6	120.6 ±3.8	130.0 ±6.4
0.01 – 0.02	67.8 ±5.2	72.4 ±5.4	89.5 ±1.9	93.9 ±3.2
0.02 – 0.04	55.3 ±2.1	62.8 ±3.2	72.5 ±1.3	74.9 ±1.0
0.04 – 0.06	41.1 ±2.5	48.3 ±2.3	57.0 ±1.1	58.7 ±1.4
0.06 – 0.08	36.9 ±1.5	40.3 ±2.2	46.65 ±0.84	47.8 ±1.9
0.08 – 0.10	29.2 ±1.6	36.3 ±1.8	38.11 ±0.51	40.9 ±1.4
0.10 – 0.12	24.1 ±1.4	26.8 ±1.6	32.50 ±0.56	33.2 ±1.2
0.12 – 0.14	20.4 ±1.2	23.1 ±1.4	27.6 ±1.0	26.9 ±1.1
0.14 – 0.16	18.0 ±1.6	21.9 ±1.6	24.04 ±0.54	25.63 ±0.89
0.16 – 0.18	13.0 ±1.1	17.6 ±1.6	21.07 ±0.46	22.3 ±1.1
0.18 – 0.20	13.1 ±1.2	15.1 ±1.1	17.89 ±0.47	20.30 ±0.74
0.20 – 0.25	9.82 ±0.54	12.67 ±0.82	15.27 ±0.24	15.92 ±0.46
0.25 – 0.30	7.32 ±0.50	8.43 ±0.70	11.62 ±0.23	12.75 ±0.39
0.30 – 0.35	5.24 ±0.38	7.04 ±0.56	8.92 ±0.19	9.96 ±0.34
0.35 – 0.40	3.00 ±0.37	5.79 ±0.51	7.21 ±0.16	7.91 ±0.36
0.40 – 0.60	2.43 ±0.16	3.58 ±0.17	4.585 ±0.070	5.20 ±0.13
0.60 – 0.80	1.07 ±0.11	1.62 ±0.17	2.512 ±0.060	2.83 ±0.12
0.80 – 1.20	0.411 ±0.035	0.776 ±0.057	1.241 ±0.027	1.505 ±0.054
1.20 – 1.60	0.170 ±0.030	0.343 ±0.080	0.610 ±0.029	0.802 ±0.029
1.60 – 2.00	0.063 ±0.019	0.166 ±0.039	0.343 ±0.016	0.436 ±0.026
2.00 – 3.00	0.0178 ±0.0067	0.071 ±0.011	0.1678 ±0.0087	0.2382 ±0.0097
3.00 – 4.00	0.0072 ±0.0035	0.034 ±0.011	0.0704 ±0.0043	0.1134 ±0.0076
4.00 – 6.00		0.0172 ±0.0088	0.0297 ±0.0015	0.0521 ±0.0037
6.00 – 8.00			0.0110 ±0.0012	0.0210 ±0.0036
8.00 – 10.00			0.00519 ±0.00061	0.0118 ±0.0020
10.00 – 12.00			0.00291 ±0.00070	0.0068 ±0.0013
12.00 – 14.00			0.00188 ±0.00051	0.0031 ±0.0011
14.00 – 16.00			0.00124 ±0.00037	0.0033 ±0.0012
16.00 – 18.00			0.00088 ±0.00030	0.00180 ±0.00067
18.00 – 20.00			0.00126 ±0.00064	0.00125 ±0.00063
20.00 – 30.00			0.000222 ±0.000077	0.00063 ±0.00023
$\langle p_\perp^2 \rangle$	0.1773 ±0.0050	0.243 ±0.012	0.3339 ±0.0066	0.4175 ±0.0095

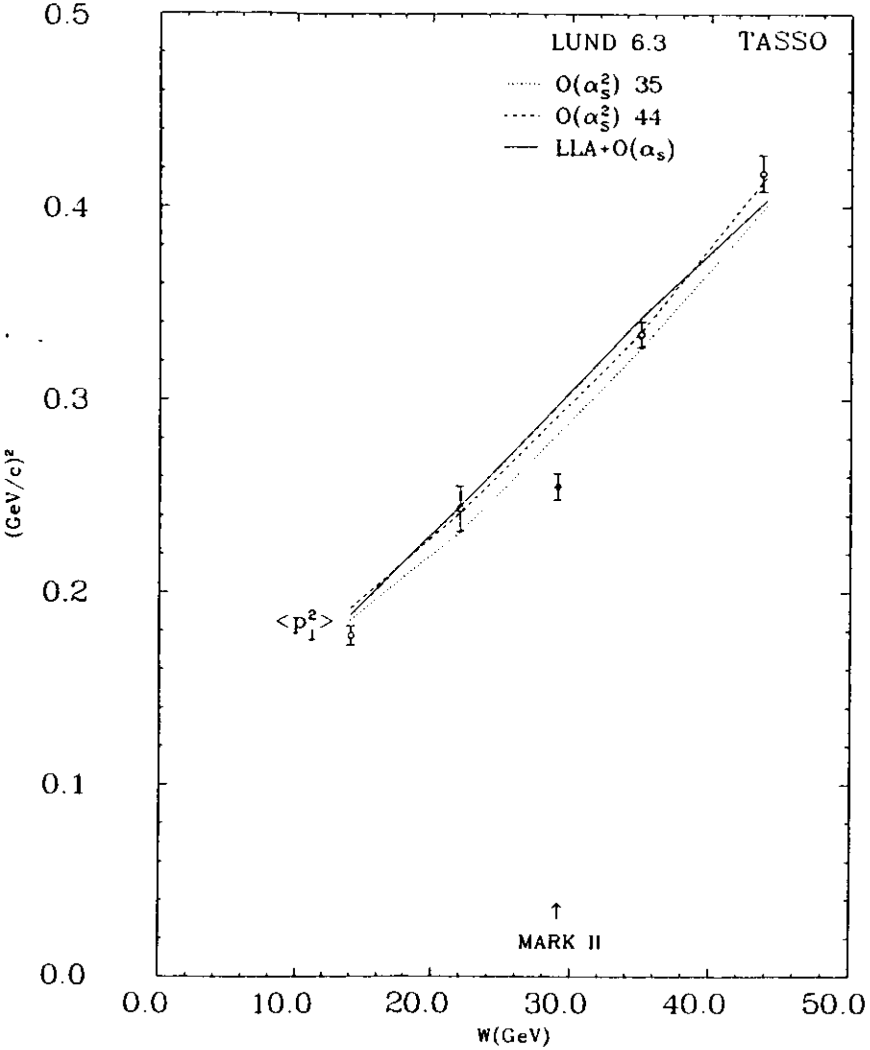

Fig. 7.19. Average value of the transverse momentum squared ($< p_\perp^2 >$) as a function of W. The curves show predictions of the Lund O(α_s^2) Monte Carlo tuned at 35 and 44 GeV and predictions of the Lund LLA+O(α_s) Monte Carlo tuned at 44 GeV.

one center-of-mass energy. The next three figures (Fig. 7.21-7.23) (Table 7.20-7.22) show distributions of the average momenta (over an event) transverse momenta squared and its components *in* and *out* of the event plane with one entry for one event.

The averages (over the whole event sample) $\ll p^2_{\perp in} \gg$ and $\ll p^2_{\perp out} \gg$ are given in Fig. 7.20 (Table 7.2). Both $\ll p^2_{\perp in} \gg$ and $\ll p^2_{\perp out} \gg$ increase with energy, but $\ll p^2_{\perp in} \gg$ increases also about seven times faster than $\ll p^2_{\perp out} \gg$, indicating that the increase of the transverse momentum with energy is mainly due to the production of planar events.

7.4.2 Scaled longitudinal and transverse Momentum Distributions

The scaled longitudinal and transverse momentum distributions with respect to the sphericity axis are displayed in Fig. 7.24-7.26 (Table 7.23-7.26). The scaling of the $1/\sigma_{tot}\, d\sigma/dx_\parallel$ cross section is more "exact" than in the corresponding range of the x_p distribution, especially near $x_\parallel = .03$. It is better visible in Table 7.25 (which corresponds to Table 7.6), where the coefficients c_1 and c_2 of the function of the form $c_1\,(1 + c_2 \cdot \ln(s/s_0))$ fitted to the data points in the given intervals are presented. (For completeness also Table 7.24 and Fig. 7.25 corresponding to Table 7.5 and Fig. 7.4 are given.) As one can see, the absolute value of the $c_1 \cdot c_2$ coefficients is smaller in the $x_\parallel$ case in all but two x intervals.

The normalized scaled transverse momentum cross section does not scale in the whole $14 \div 44$ GeV center-of-mass energy range, but it seems that the scaling for $x_T \gtrsim .04$ is approached somewhere about $W = 35$ GeV, although more data at higher energy ($W >$ 44 GeV) is needed to confirm that.

7.4.3 Particle and Momentum Flow around the Thrust Axis

Fig. 7.27 (Table 7.27) shows the distributions of the angle α between the event axis (here: thrust axis) and the charged particle direction. The distributions have a maximum somewhere between 5° and 20°. It shifts towards lower values as center-of-mass energy increases.

With the increase of center-of-mass energy also the number of particles emitted at small angles with respect to the event axis increases rapidly whereas the number of particles at angles $\alpha \gtrsim 40^\circ$ increases very slowly. The Fig. 7.28 (Table 7.28) shows the charged momentum flow $\frac{d\Phi_f}{d\alpha}$ around the event axis. The particle momenta are normalized to the total momentum sum of the charged particles in an event and $\frac{d\Phi_f}{d\alpha}$ is defined as:

$$\frac{d\Phi_f}{d\alpha} = \frac{1}{\sigma_{tot} \sum p} \int p\, dp\, \frac{d^2\sigma}{dp\, d\alpha}$$

There is also a rapid increase of the momentum flow in the region close to the event axis ($\alpha \lesssim 10^\circ$) with the increase of center-of-mass energy. In the remaining angular region ($\alpha \gtrsim 15^\circ$) the momentum flow not only does not increase but even decreases slowly as center-of-mass energy increases.

The last two plots (Fig. 7.27 and 7.28) are again an evidence that events become more and more collimated with the increase of the center-of-mass energy. They show, that the main contribution to the increase of the multiplicity comes from the particles emitted

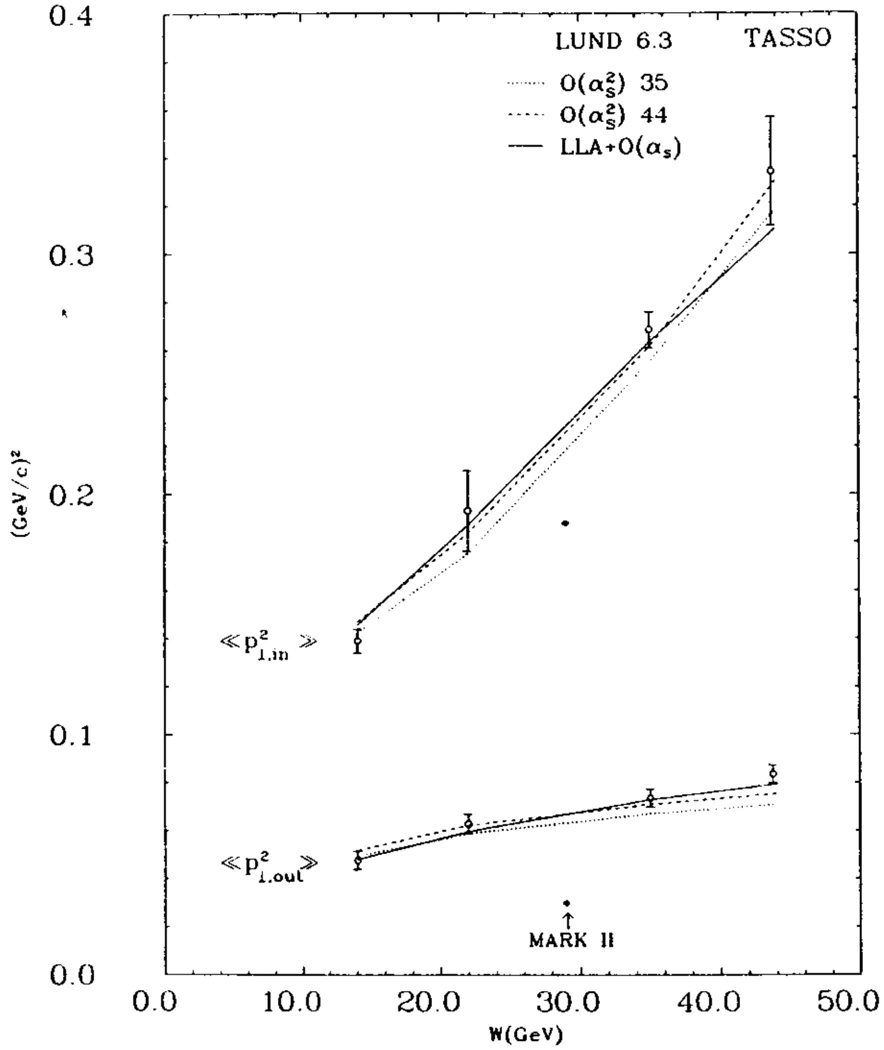

Fig. 7.20. Average values of the average transverse momentum squared *in* ($\ll p^2_{\perp in} \gg$) and *out* ($\ll p^2_{\perp out} \gg$) of the event plane as a function of W. The curves show predictions of the Lund $O(\alpha_s^2)$ Monte Carlo tuned at 35 and 44 GeV and predictions of the Lund LLA+$O(\alpha_s)$ Monte Carlo tuned at 44 GeV.

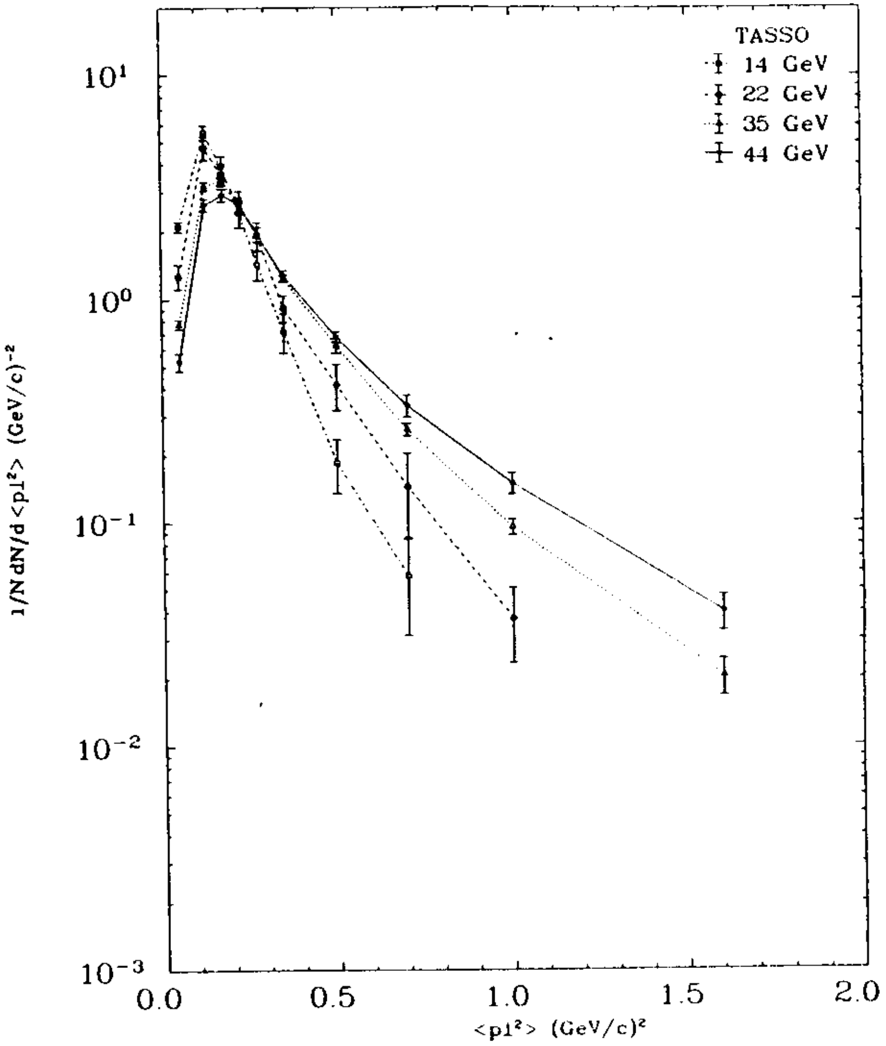

Fig. 7.21. Normalized distributions of the average transverse momentum squared $1/N\,dN/d<p_\perp^2>$ (GeV/c)$^{-2}$ at $\overline{W}$=14, 22, 35 and 44 GeV.

Table 7.20

Normalized distributions of the average transverse momentum squared $1/N\, dN/d < p_\perp^2 >$ $(\mathrm{GeV}/c)^{-2}$

$< p_\perp^2 >$ $(\mathrm{GeV}/c)^2$	14 GeV	22 GeV	35 GeV	44 GeV
0.00 - 0.10	2.11 ± 0.11	1.27 ± 0.16	0.774 ± 0.038	0.527 ± 0.048
0.10 - 0.15	5.55 ± 0.40	4.75 ± 0.57	3.21 ± 0.14	2.64 ± 0.17
0.15 - 0.20	3.91 ± 0.44	3.62 ± 0.41	3.39 ± 0.12	2.93 ± 0.18
0.20 - 0.25	2.43 ± 0.35	2.73 ± 0.31	2.59 ± 0.12	2.64 ± 0.22
0.25 - 0.30	1.43 ± 0.22	1.93 ± 0.27	1.00 ± 0.11	1.95 ± 0.14
0.30 - 0.40	0.72 ± 0.14	0.91 ± 0.13	1.239 ± 0.040	1.276 ± 0.077
0.40 - 0.60	0.186 ± 0.050	0.416 ± 0.097	0.621 ± 0.045	0.680 ± 0.037
0.60 - 0.80	0.058 ± 0.027	0.145 ± 0.059	0.261 ± 0.017	0.335 ± 0.038
0.80 - 1.20		0.037 ± 0.014	0.0956 ± 0.0078	0.150 ± 0.016
1.20 - 2.00		0.0031 ± 0.0023	0.0205 ± 0.0038	0.0399 ± 0.0072
$\ll p_\perp^2 \gg$	0.1866 ± 0.0060	0.256 ± 0.020	0.3425 ± 0.0075	0.418 ± 0.022

Table 7.21

Normalized distributions of the average transverse momentum squared *in* the event plane $1/N\, dN/d < p_{\perp in}^2 >$ $(\mathrm{GeV}/c)^{-2}$.

$< p_{\perp in}^2 >$ $(\mathrm{GeV}/c)^2$	14 GeV	22 GeV	35 GeV	44 GeV
0.00 - 0.05	2.43 ± 0.25	1.43 ± 0.27	1.00 ± 0.11	0.58 ± 0.17
0.05 - 0.10	6.72 ± 0.41	5.63 ± 0.39	4.07 ± 0.13	3.44 ± 0.25
0.10 - 0.15	4.66 ± 0.40	4.59 ± 0.39	4.00 ± 0.14	3.47 ± 0.23
0.15 - 0.20	2.44 ± 0.26	2.62 ± 0.26	2.82 ± 0.11	2.83 ± 0.18
0.20 - 0.30	1.14 ± 0.21	1.42 ± 0.16	1.598 ± 0.052	1.626 ± 0.099
0.30 - 0.40	0.41 ± 0.11	0.59 ± 0.10	0.853 ± 0.049	0.916 ± 0.054
0.40 - 0.50	0.122 ± 0.056	0.37 ± 0.11	0.476 ± 0.030	0.558 ± 0.042
0.50 - 1.00	0.034 ± 0.011	0.087 ± 0.022	0.1730 ± 0.0083	0.240 ± 0.015
1.00 - 2.00		0.0029 ± 0.0020	0.0209 ± 0.0031	0.0392 ± 0.0064
$\ll p_{\perp in}^2 \gg$	0.1389 ± 0.0050	0.193 ± 0.017	0.2685 ± 0.0075	0.334 ± 0.023

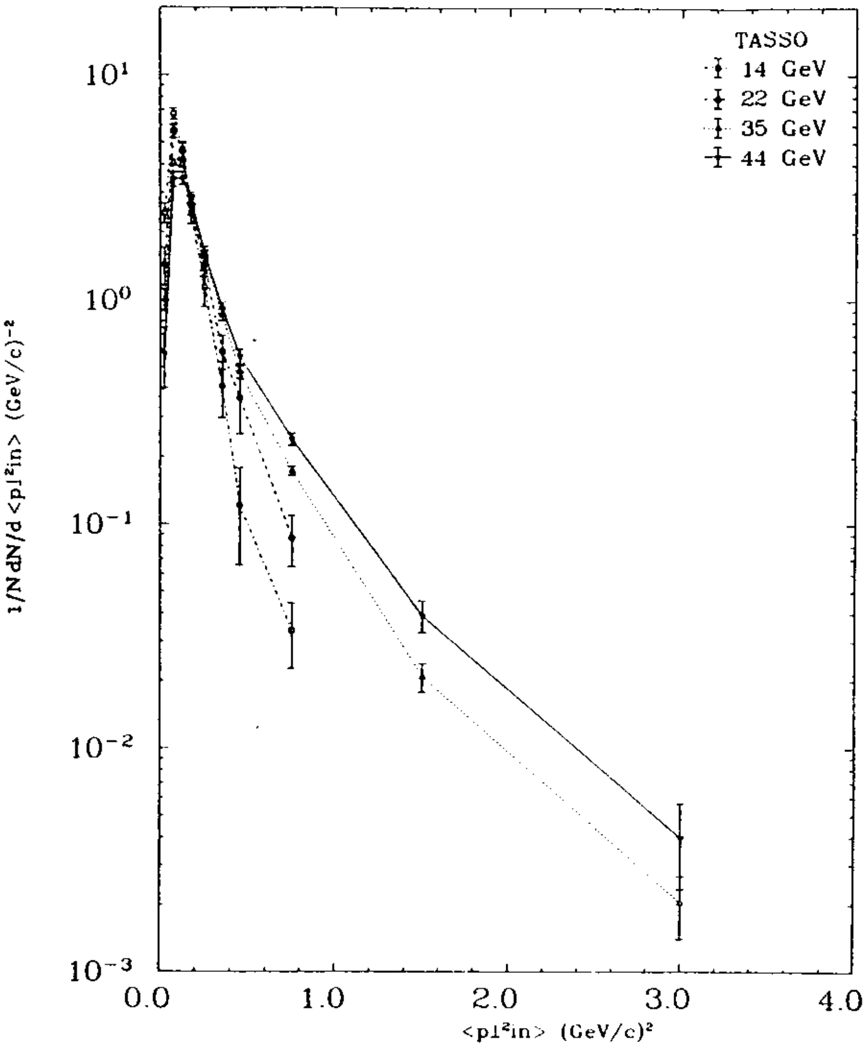

Fig. 7.22. Normalized distributions of the average transverse momentum squared *in* the event plane $1/N\, dN/d < p_{\perp in}^2 >$ $(\mathrm{GeV}/c)^{-2}$ at $\overline{W}$=14, 22, 35 and 44 GeV.

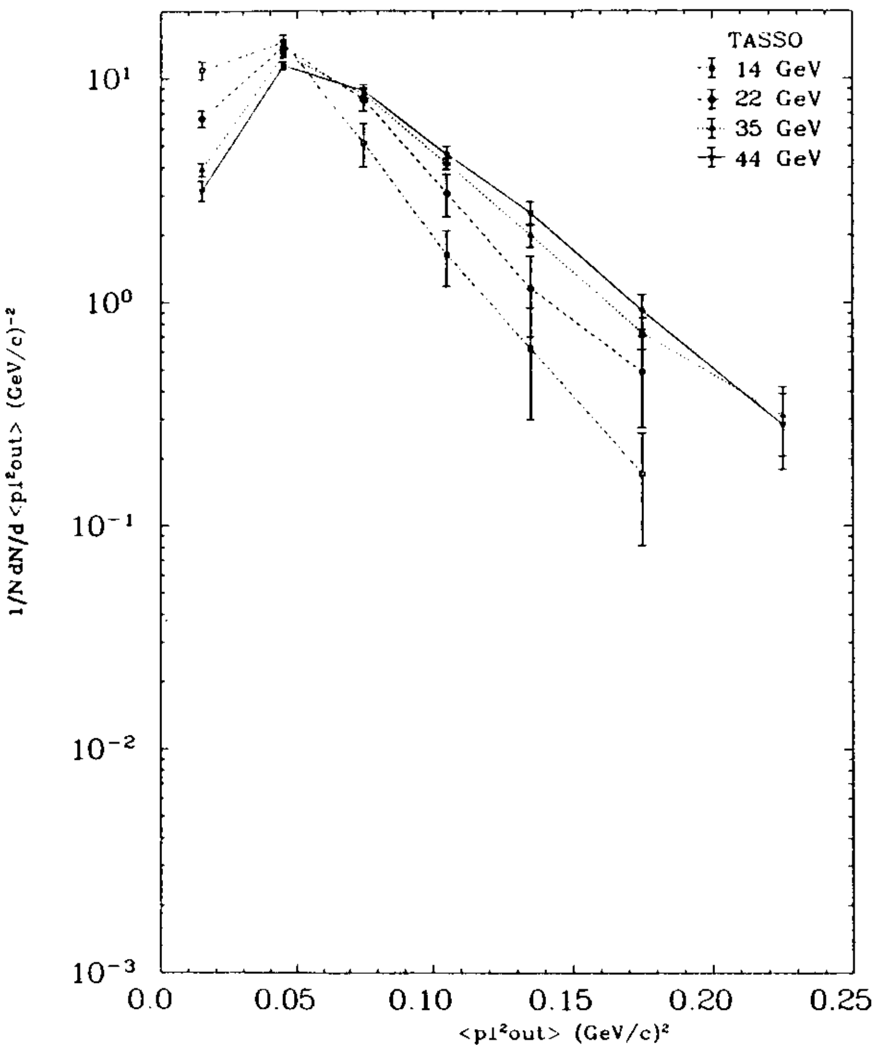

Fig. 7.33. Normalized distributions of the average transverse momentum squared *out* of the event plane $1/N\, dN/d < p^2_{\perp out} >$ $(\mathrm{GeV}/c)^{-2}$ at $\overline{W}$=14, 22, 35 and 44 GeV.

Table 7.22

Normalized distributions of the average transverse momentum squared *out* of the event plane $1/N\, dN/d < p^2_{\perp out} >$ $(\mathrm{GeV}/c)^{-2}$.

$< p^2_{\perp out} >$ $(\mathrm{GeV}/c)^2$	14 GeV	22 GeV	35 GeV	44 GeV
0.00 - 0.03	10.91 ± 0.99	6.63 ± 0.57	3.92 ± 0.27	3.16 ± 0.33
0.03 - 0.06	14.5 ± 1.1	13.89 ± 0.90	12.81 ± 0.45	11.38 ± 0.44
0.06 - 0.09	5.1 ± 1.1	8.04 ± 0.90	8.49 ± 0.58	8.78 ± 0.59
0.09 - 0.12	1.63 ± 0.46	3.06 ± 0.66	4.15 ± 0.24	4.58 ± 0.38
0.12 - 0.15	0.62 ± 0.32	1.15 ± 0.45	2.00 ± 0.24	2.51 ± 0.30
0.15 - 0.20	0.171 ± 0.089	0.36 ± 0.16	0.73 ± 0.12	0.92 ± 0.16
0.20 - 0.25			0.31 ± 0.11	0.28 ± 0.11
0.25 - 0.50			0.049 ± 0.018	0.089 ± 0.038
$\ll p^2_{\perp out} \gg$	0.0476 ± 0.0038	0.0628 ± 0.0040	0.0734 ± 0.0037	0.0834 ± 0.0037

Table 7.23

Normalized distributions of the scaled longitudinal momentum $1/\sigma_{tot}\, d\sigma/dx_{\parallel}$, where $x_{\parallel} = 2p_{\parallel}/W$.

$x_{\parallel}$	14 GeV	22 GeV	35 GeV	44 GeV
0.02 - 0.03	66.3 ± 2.6	99.1 ± 4.5	140.0 ± 2.1	154.8 ± 2.5
0.03 - 0.04	64.0 ± 5.0	86.5 ± 4.3	113.7 ± 1.8	123.9 ± 2.5
0.04 - 0.05	58.5 ± 2.4	76.1 ± 3.6	91.8 ± 1.4	98.3 ± 2.5
0.05 - 0.06	50.2 ± 2.7	64.2 ± 3.4	73.7 ± 1.1	80.9 ± 3.7
0.06 - 0.08	41.7 ± 1.5	51.2 ± 2.1	57.01 ± 0.63	59.8 ± 1.4
0.08 - 0.10	31.0 ± 1.6	38.7 ± 1.5	43.0 ± 1.3	43.6 ± 1.8
0.10 - 0.12	26.4 ± 1.8	31.6 ± 1.4	31.38 ± 0.45	32.99 ± 0.87
0.12 - 0.14	21.5 ± 1.3	22.2 ± 1.1	25.60 ± 0.36	26.7 ± 1.3
0.14 - 0.16	17.81 ± 0.90	20.0 ± 1.2	20.42 ± 0.37	20.17 ± 0.94
0.16 - 0.18	15.6 ± 1.3	14.19 ± 0.91	16.21 ± 0.36	16.35 ± 0.56
0.18 - 0.20	13.0 ± 1.1	13.6 ± 1.1	13.54 ± 0.34	12.80 ± 0.50
0.20 - 0.25	9.36 ± 0.51	9.86 ± 0.66	9.50 ± 0.19	9.37 ± 0.34
0.25 - 0.30	6.58 ± 0.44	6.16 ± 0.52	6.06 ± 0.16	5.80 ± 0.24
0.30 - 0.35	4.61 ± 0.34	4.30 ± 0.48	3.96 ± 0.13	3.83 ± 0.23
0.35 - 0.40	2.77 ± 0.27	3.04 ± 0.37	2.65 ± 0.11	2.67 ± 0.20
0.40 - 0.50	1.64 ± 0.15	1.61 ± 0.18	1.522 ± 0.057	1.50 ± 0.10
0.50 - 0.60	0.94 ± 0.18	0.82 ± 0.17	0.744 ± 0.038	0.639 ± 0.057
0.60 - 0.80	0.231 ± 0.035	0.315 ± 0.073	0.257 ± 0.016	0.222 ± 0.021
0.80 - 1.00	0.057 ± 0.018	0.042 ± 0.020	0.028 ± 0.011	0.0269 ± 0.0052

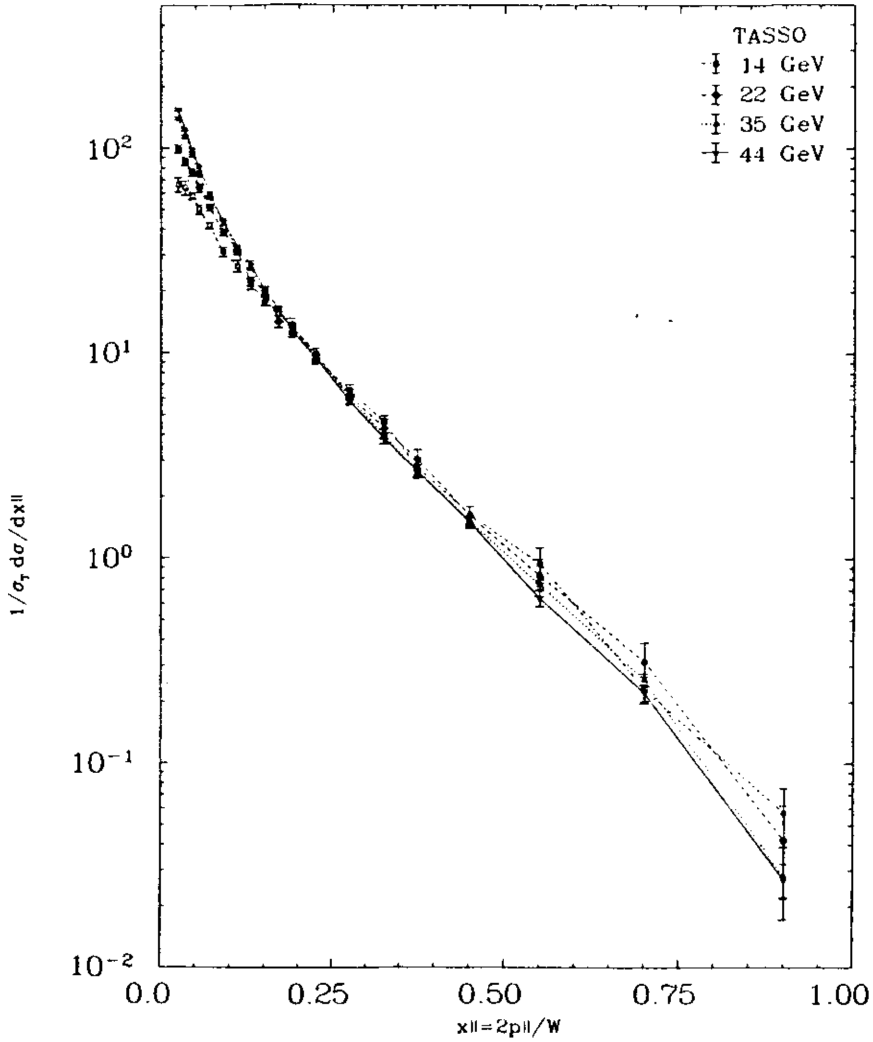

Fig. 7.24. Normalized distributions of the scaled longitudinal momentum $1/\sigma_{tot}\, d\sigma/dx_\parallel$, where $x_\parallel = 2p_\parallel/W$ at $\overline{W}$=14, 22, 35 and 44 GeV.

Table 7.24

Normalized distributions of the scaled longitudinal momentum $1/\sigma_{tot}\, d\sigma/dx_\parallel$, where $x_\parallel = 2p_\parallel/W$ in the binning used in fits.

$x_\parallel$	14 GeV	22 GeV	35 GeV	44 GeV
0.02 – 0.05	62.8 ± 3.5	87.2 ± 2.5	115.2 ± 1.5	125.7 ± 1.7
0.05 – 0.10	39.1 ± 1.4	48.8 ± 1.3	54.76 ± 0.70	57.6 ± 1.4
0.10 – 0.20	18.88 ± 0.43	20.31 ± 0.48	21.42 ± 0.21	21.81 ± 0.43
0.20 – 0.30	7.96 ± 0.32	8.01 ± 0.31	7.78 ± 0.15	7.59 ± 0.22
0.30 – 0.40	3.69 ± 0.26	3.67 ± 0.29	3.304 ± 0.093	3.24 ± 0.14
0.40 – 0.50	1.64 ± 0.15	1.61 ± 0.18	1.522 ± 0.057	1.50 ± 0.10
0.50 – 0.70	0.615 ± 0.076	0.62 ± 0.13	0.546 ± 0.024	0.478 ± 0.031

Table 7.25

Fit results to the s- dependence of the scaled cross section $1/\sigma_{tot}\, d\sigma/dx_\parallel = c_1(1 + c_2 \ln(s/s_o))$, where $s_o = 1$ GeV^2.

$x_\parallel$	c_1	c_2	$c_1 \cdot c_2$
0.02 – 0.05	−85. ± 10.	−0.329 ± 0.023	28.1 ± 1.5
0.05 – 0.10	−2.01 ± 0.24	−3.98 ± 0.60	7.98 ± 0.73
0.10 – 0.20	12.0 ± 1.6	0.110 ± 0.033	1.32 ± 0.23
0.20 – 0.30	9.0 ± 1.1	−0.019 ± 0.015	−0.17 ± 0.15
0.30 – 0.40	4.91 ± 0.86	−0.045 ± 0.017	−0.22 ± 0.12
0.40 – 0.50	1.99 ± 0.52	−0.033 ± 0.029	−0.066 ± 0.074
0.50 – 0.70	1.01 ± 0.25	−0.067 ± 0.018	−0.067 ± 0.035

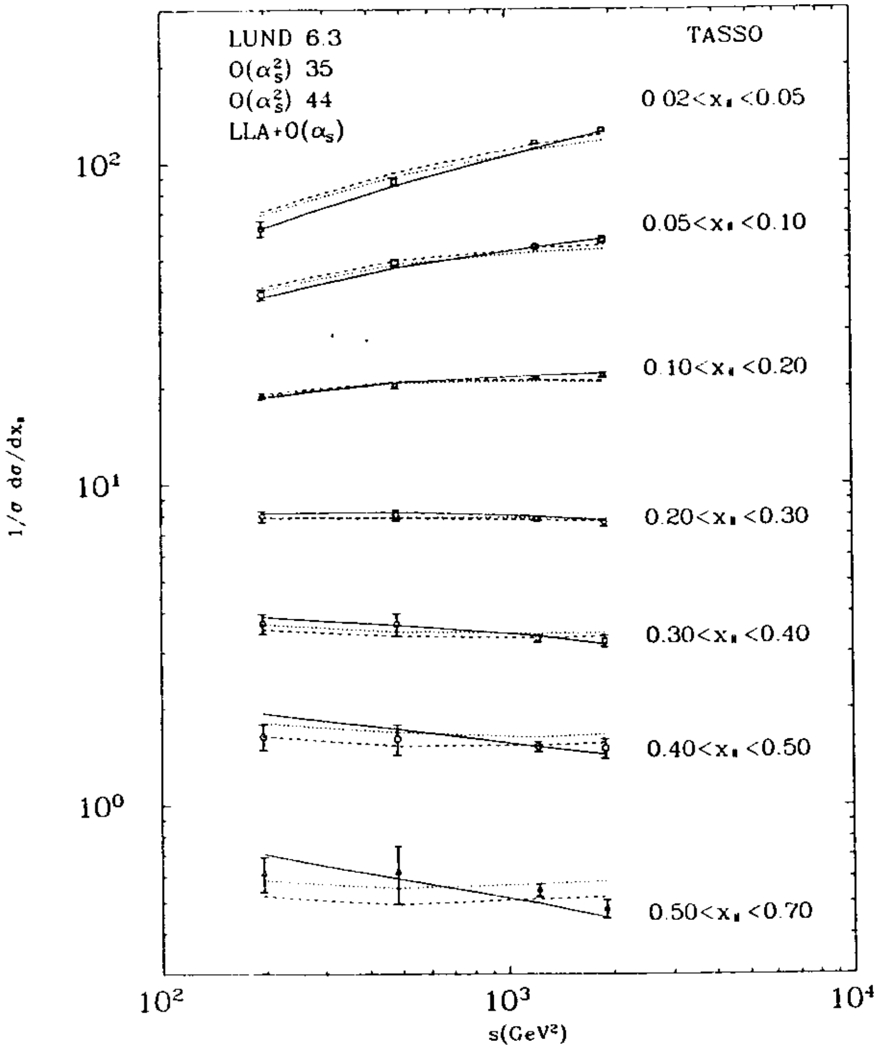

Fig. 7.25. Normalized distributions of the scaled longitudinal momentum $1/\sigma_{tot}\, d\sigma/dx_\parallel$, where $x_\parallel = 2p_\parallel/W$ at $\overline{W}$=14, 22, 35 and 44 GeV.

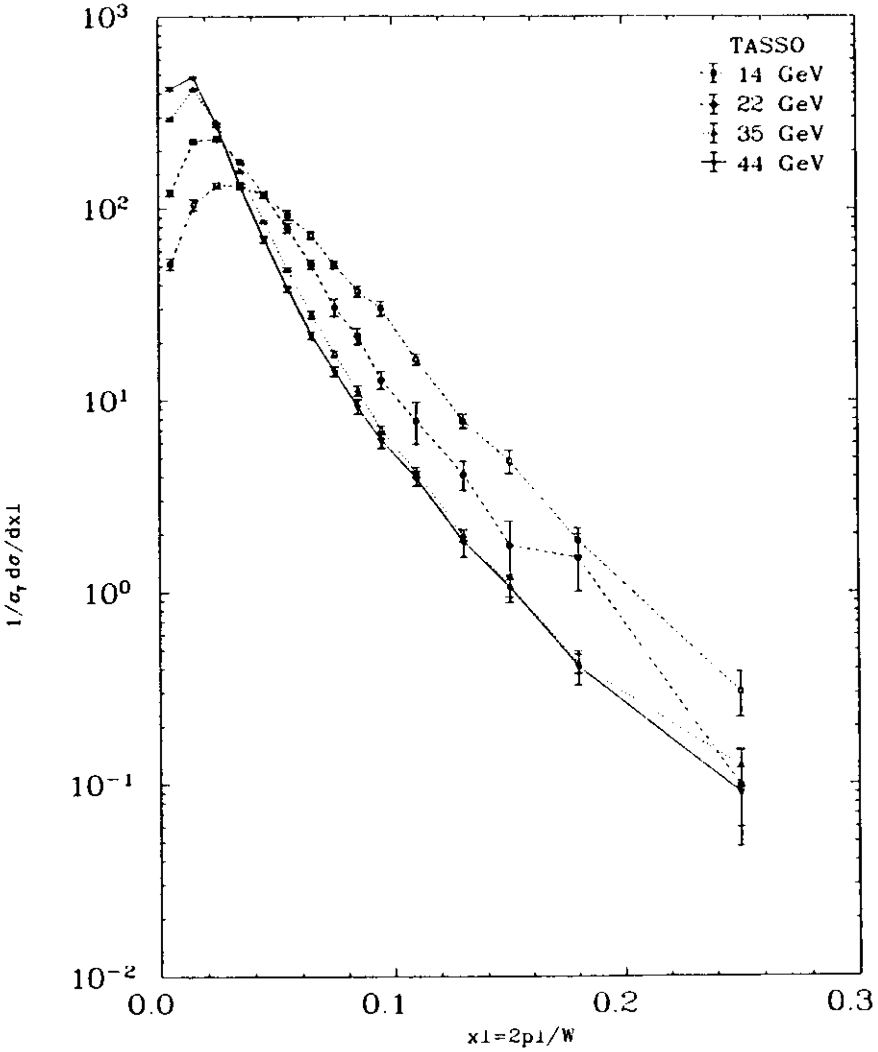

Fig. 7.26. Normalized distributions of the scaled transverse momentum $1/\sigma_{tot}\, d\sigma/dx_\perp$, where $x_\perp = 2p_\perp/W$ at $\overline{W}$=14, 22, 35 and 44 GeV.

Table 7.26

Normalized distributions of the scaled transverse momentum $1/\sigma_{tot}\, d\sigma/dx_\perp$, where $x_\perp = 2p_\perp/W$.

$x_\perp$	14 GeV	22 GeV	35 GeV	44 GeV
0.00 – 0.01	51.5 ± 3.7	120.7 ± 4.7	293.0 ± 6.4	421.9 ± 9.8
0.01 – 0.02	104.9 ± 6.7	224.4 ± 6.6	418.5 ± 5.2	485.8 ± 5.9
0.02 – 0.03	132.3 ± 4.9	230.8 ± 7.6	281.4 ± 3.3	270.5 ± 4.4
0.03 – 0.04	131.9 ± 5.6	175.8 ± 4.7	156.2 ± 2.2	131.6 ± 3.6
0.04 – 0.05	118.5 ± 4.9	118.6 ± 5.2	85.7 ± 1.6	69.3 ± 2.8
0.05 – 0.06	92.0 ± 5.5	79.4 ± 4.4	48.3 ± 1.1	38.4 ± 1.4
0.06 – 0.07	72.9 ± 3.4	51.4 ± 2.9	28.1 ± 1.3	21.86 ± 0.96
0.07 – 0.08	51.4 ± 2.5	30.7 ± 3.2	17.59 ± 0.68	14.21 ± 0.81
0.08 – 0.09	37.2 ± 2.4	21.8 ± 2.1	11.32 ± 0.69	9.28 ± 0.77
0.09 – 0.10	30.4 ± 2.6	12.8 ± 1.4	7.03 ± 0.34	6.21 ± 0.57
0.10 – 0.12	16.4 ± 1.1	7.8 ± 1.9	4.22 ± 0.26	3.91 ± 0.36
0.12 – 0.14	7.82 ± 0.66	4.12 ± 0.72	1.97 ± 0.13	1.83 ± 0.31
0.14 – 0.16	4.84 ± 0.67	1.76 ± 0.59	1.07 ± 0.13	1.06 ± 0.17
0.16 – 0.18	2.63 ± 0.53	1.46 ± 0.51	0.519 ± 0.061	0.53 ± 0.14
0.18 – 0.20	1.05 ± 0.33	1.8 ± 1.3	0.331 ± 0.061	0.296 ± 0.094
0.20 – 0.25	0.41 ± 0.15	0.15 ± 0.12	0.183 ± 0.043	0.153 ± 0.056
0.25 – 0.30	0.22 ± 0.11		0.061 ± 0.021	0.026 ± 0.017

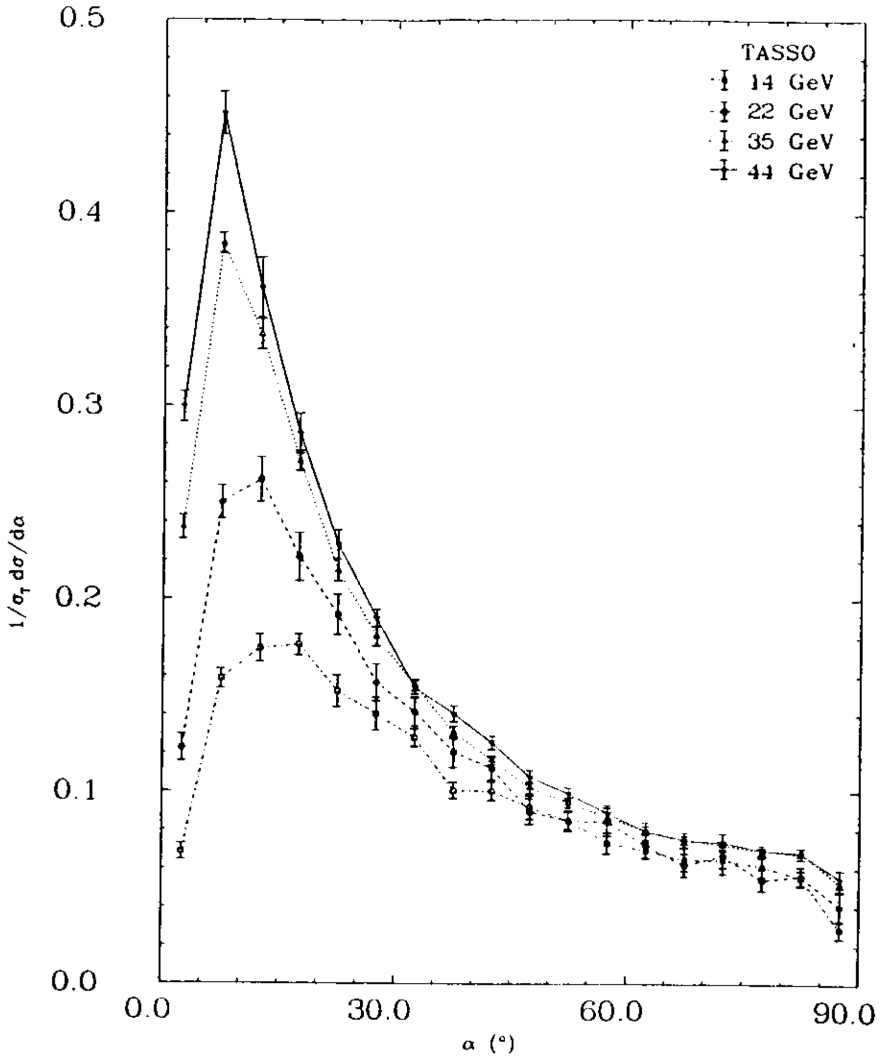

Fig. 7.27. Normalized distributions of the angle α between the charged particle direction and the thrust axis $1/\sigma_{tot}\, d\sigma/d\alpha$ at $\overline{W}$=14, 22, 35 and 44 GeV.

Table 7.27

Normalized distributions of the angle α between the charged particle direction and the thrust axis $1/\sigma_{tot}\, d\sigma/d\alpha$.

α (°)	14 GeV	22 GeV	35 GeV	44 GeV
0. - 5.	0.0686 ± 0.0043	0.1227 ± 0.0069	0.2371 ± 0.0062	0.2995 ± 0.0080
5. - 10.	0.1586 ± 0.0051	0.2500 ± 0.0086	0.3841 ± 0.0052	0.452 ± 0.011
10. - 15.	0.1743 ± 0.0070	0.262 ± 0.012	0.3370 ± 0.0079	0.361 ± 0.016
15. - 20.	0.1762 ± 0.0054	0.222 ± 0.013	0.2715 ± 0.0052	0.286 ± 0.010
20. - 25.	0.1521 ± 0.0083	0.192 ± 0.010	0.2148 ± 0.0057	0.2281 ± 0.0076
25. - 30.	0.1404 ± 0.0085	0.1567 ± 0.0096	0.1807 ± 0.0051	0.1900 ± 0.0045
30. - 35.	0.1282 ± 0.0047	0.1416 ± 0.0075	0.1554 ± 0.0030	0.1541 ± 0.0036
35. - 40.	0.1007 ± 0.0043	0.1208 ± 0.0081	0.1310 ± 0.0033	0.1406 ± 0.0042
40. - 45.	0.1004 ± 0.0048	0.1122 ± 0.0058	0.1167 ± 0.0023	0.1256 ± 0.0034
45. - 50.	0.0920 ± 0.0060	0.0898 ± 0.0066	0.1024 ± 0.0031	0.1077 ± 0.0034
50. - 55.	0.0851 ± 0.0044	0.0849 ± 0.0053	0.0944 ± 0.0026	0.0990 ± 0.0033
55. - 60.	0.0735 ± 0.0055	0.0846 ± 0.0073	0.0868 ± 0.0029	0.0890 ± 0.0042
60. - 65.	0.0696 ± 0.0042	0.0721 ± 0.0062	0.0801 ± 0.0020	0.0796 ± 0.0046
65. - 70.	0.0650 ± 0.0061	0.0622 ± 0.0059	0.0752 ± 0.0020	0.0751 ± 0.0039
70. - 75.	0.0647 ± 0.0072	0.0670 ± 0.0061	0.0726 ± 0.0022	0.0741 ± 0.0046
75. - 80.	0.0614 ± 0.0048	0.0545 ± 0.0057	0.0694 ± 0.0019	0.0698 ± 0.0029
80. - 85.	0.0556 ± 0.0037	0.0563 ± 0.0050	0.0690 ± 0.0022	0.0679 ± 0.0028
85. - 90.	0.0287 ± 0.0049	0.0406 ± 0.0079	0.0521 ± 0.0039	0.0550 ± 0.0044

close to the event axis but they also show, that the particles emitted close to that axis carry more and more momentum as compared to the particles emitted at larger angles.

7.4.4 Rapidity Distribution

The particle production is often studied in terms of the rapidity (see Chapter 2) $y = \frac{1}{2}\ln\left(\frac{E+p_\parallel}{E-p_\parallel}\right)$ with the longitudinal momenta defined with respect to the thrust axis. To produce Fig. 7.29 (and Table 7.29) it was assumed, that all the particles were pions (both in the Monte Carlo and in the data). As the thrust axis was not oriented, the distributions were folded around $y = 0$. The normalized cross section increases with energy and the distributions become broader. There is a dip near $y = 0$ and the distributions have a maximum for $1 \lesssim y \lesssim 2$. Of course one can plot rapidity with respect to an other axis e.g. the Parisi tensor axis. Such a distribution is presented in Fig. 7.30 (Table 7.30). As one can see the dip at $y = 0$ is much less pronounced and there are even small maxima at $y = 0$ at 35 and 44 GeV. To investigate the rapidity spectrum in more details some Monte Carlo studies were done, the results of which are presented in the next section.

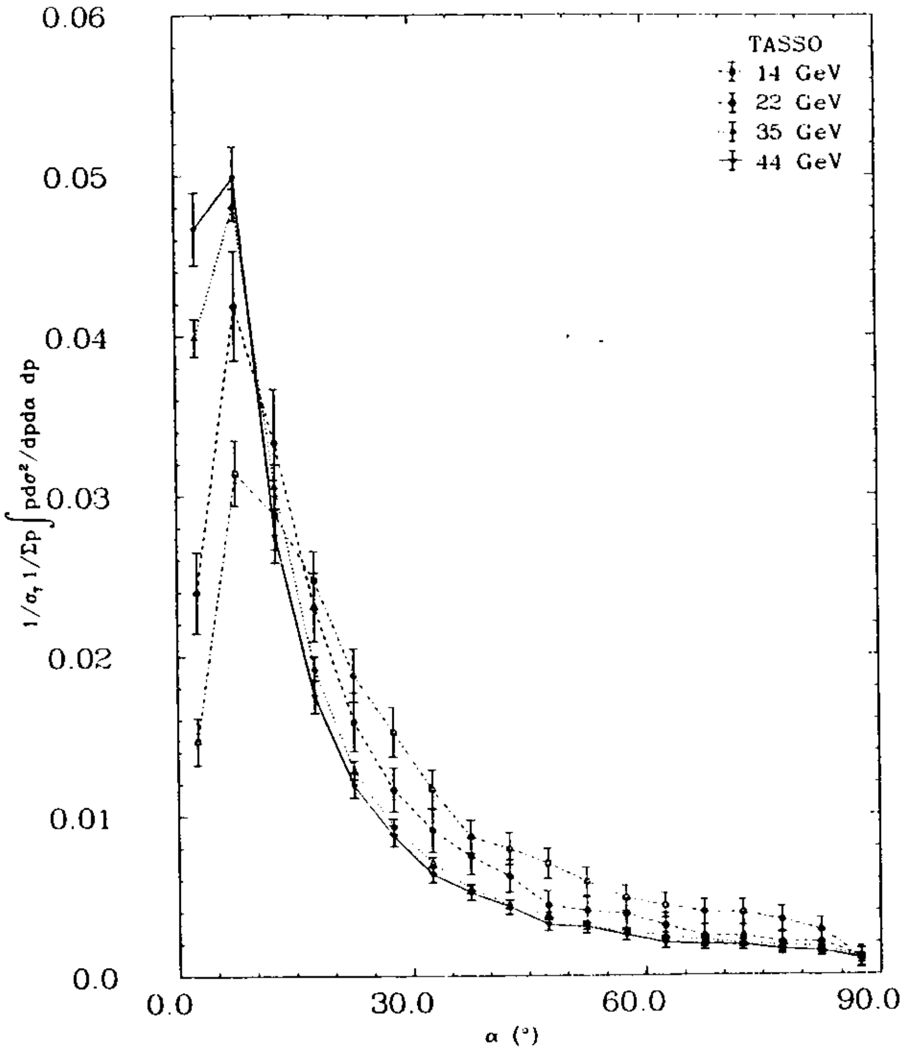

Fig. 7.28. Charged momentum flow $\frac{d\Phi_p}{d\alpha} = \frac{1}{\sigma_{tot}}\frac{1}{\sum_p}\int p \frac{d^2\sigma}{dp\, d\alpha} dp$ around the thrust axis at $\overline{W}$=14, 22, 35 and 44 GeV.

Table 7.28

Charged momentum flow $\frac{d\Sigma_p}{d\alpha} = \frac{1}{\sigma_{tot}} \frac{1}{\sum_p} \int p \frac{d^2\sigma}{dp\, d\alpha} dp$ around the thrust axis.

α (°)	14 GeV	22 GeV	35 GeV	44 GeV
0. - 5.	0.0147 ± 0.0015	0.0240 ± 0.0025	0.0399 ± 0.0012	0.0467 ± 0.0023
5. - 10.	0.0314 ± 0.0020	0.0419 ± 0.0034	0.04820 ± 0.00100	0.0499 ± 0.0019
10. - 15.	0.0288 ± 0.0022	0.0333 ± 0.0033	0.0306 ± 0.0014	0.0275 ± 0.0017
15. - 20.	0.0247 ± 0.0018	0.0230 ± 0.0022	0.01918 ± 0.00075	0.0175 ± 0.0010
20. - 25.	0.0188 ± 0.0017	0.0159 ± 0.0018	0.01283 ± 0.00058	0.01187 ± 0.00077
25. - 30.	0.0152 ± 0.0016	0.0116 ± 0.0014	0.00933 ± 0.00047	0.00873 ± 0.00066
30. - 35.	0.0116 ± 0.0012	0.0091 ± 0.0014	0.00707 ± 0.00031	0.00633 ± 0.00052
35. - 40.	0.0087 ± 0.0010	0.0075 ± 0.0011	0.00543 ± 0.00028	0.00520 ± 0.00049
40. - 45.	0.00794 ± 0.00099	0.0062 ± 0.0010	0.00446 ± 0.00025	0.00430 ± 0.00047
45. - 50.	0.00701 ± 0.00094	0.00441 ± 0.00089	0.00371 ± 0.00024	0.00320 ± 0.00040
50. - 55.	0.00586 ± 0.00088	0.00405 ± 0.00083	0.00309 ± 0.00022	0.00303 ± 0.00039
55. - 60.	0.00482 ± 0.00080	0.00383 ± 0.00095	0.00275 ± 0.00022	0.00252 ± 0.00035
60. - 65.	0.00435 ± 0.00077	0.00312 ± 0.00073	0.00245 ± 0.00020	0.00202 ± 0.00035
65. - 70.	0.00394 ± 0.00079	0.00246 ± 0.00068	0.00217 ± 0.00019	0.00192 ± 0.00034
70. - 75.	0.00390 ± 0.00079	0.00243 ± 0.00067	0.00200 ± 0.00019	0.00190 ± 0.00033
75. - 80.	0.00344 ± 0.00079	0.00207 ± 0.00065	0.00184 ± 0.00018	0.00157 ± 0.00030
80. - 85.	0.00281 ± 0.00075	0.00204 ± 0.00071	0.00174 ± 0.00019	0.00148 ± 0.00031
85. - 90.	0.00102 ± 0.00059	0.00112 ± 0.00065	0.00110 ± 0.00019	0.00100 ± 0.00029

7.5 Single Particle Distributions with Respect to the oriented Event Axis

7.5.1 Orientation of the Event Axis

Based on the QCD picture one expects a relatively large percentage of gluons, which are soft or parallel to the emitting quark. In such a case an event will look two-jet like, with one jet broader than the other one. If for such an event one determines an event axis (using e.g. thrust axis), cuts the event in two parts by a plane perpendicular to this axis and calculates $\sum p_\perp$ for each side of the plane separately, one will deal mostly with quark jets for the side with smaller $\sum p_\perp$ (thereafter called "narrow jets") and with a mixture of quark and gluon jets on the opposite side (thereafter called "wide jets"). Since the direction of the event axis may differ from the direction of the most energetic quark and since it is difficult or sometimes undesirable [see e.g. DOK88] to assign a particle to a specific jet, in order to orient the event axis the following procedure was applied.

First an event axis was determined, (thrust, sphericity or Parisi tensor axis) then all soft ($x_p < .05$) particles from the middle region ($70° \leq \theta \leq 110°$, where θ is the angle between the event axis and the particle direction) <u>and</u> all perpendicular ($85° \leq \theta \leq 95°$) particles were rejected. Then the $\sum p_\perp$ was calculated for each of the event side and the

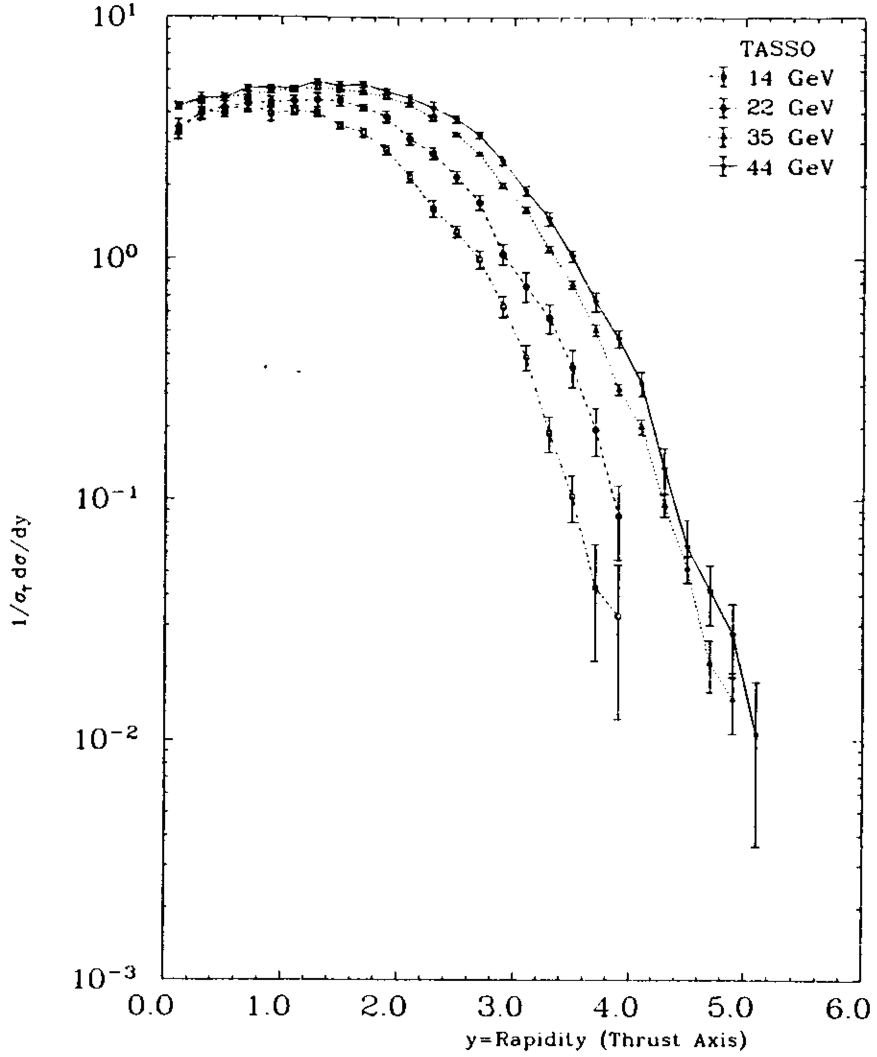

Fig. 7.20. Normalized rapidity distributions with respect to the thrust axis $1/\sigma_{tot}\, d\sigma/dy$ (folded around $y = 0$) at $\overline{W}$=14, 22, 35 and 44 GeV.

Table 7.29

Normalized rapidity distributions with respect to the thrust axis $1/\sigma_{tot}\, d\sigma/dy$ (folded around $y = 0$).

y	14 GeV	22 GeV	35 GeV	44 GeV
0.0 – 0.2	3.30 ± 0.20	3.50 ± 0.26	4.26 ± 0.13	4.26 ± 0.17
0.2 – 0.4	4.08 ± 0.38	3.98 ± 0.21	4.52 ± 0.12	4.58 ± 0.24
0.4 – 0.6	3.99 ± 0.18	4.19 ± 0.23	4.66 ± 0.12	4.61 ± 0.18
0.6 – 0.8	4.33 ± 0.23	4.35 ± 0.36	4.66 ± 0.19	5.04 ± 0.15
0.8 – 1.0	3.95 ± 0.25	4.41 ± 0.24	4.90 ± 0.12	5.10 ± 0.11
1.0 – 1.2	4.07 ± 0.14	4.45 ± 0.22	4.97 ± 0.12	5.04 ± 0.15
1.2 – 1.4	3.98 ± 0.13	4.51 ± 0.30	5.10 ± 0.12	5.38 ± 0.12
1.4 – 1.6	3.55 ± 0.12	4.48 ± 0.22	5.01 ± 0.14	5.19 ± 0.20
1.6 – 1.8	3.31 ± 0.15	4.21 ± 0.14	4.857 ± 0.089	5.26 ± 0.15
1.8 – 2.0	2.82 ± 0.14	3.87 ± 0.22	4.679 ± 0.096	4.93 ± 0.14
2.0 – 2.2	2.18 ± 0.11	3.12 ± 0.17	4.321 ± 0.080	4.62 ± 0.18
2.2 – 2.4	1.61 ± 0.13	2.73 ± 0.15	3.792 ± 0.067	4.21 ± 0.26
2.4 – 2.6	1.292 ± 0.072	2.18 ± 0.13	3.270 ± 0.059	3.79 ± 0.13
2.6 – 2.8	0.991 ± 0.085	1.71 ± 0.12	2.716 ± 0.047	3.25 ± 0.10
2.8 – 3.0	0.634 ± 0.064	1.04 ± 0.10	2.009 ± 0.057	2.54 ± 0.11
3.0 – 3.2	0.390 ± 0.047	0.77 ± 0.11	1.593 ± 0.050	1.908 ± 0.085
3.2 – 3.4	0.189 ± 0.032	0.568 ± 0.078	1.092 ± 0.033	1.460 ± 0.096
3.4 – 3.6	0.103 ± 0.023	0.354 ± 0.063	0.780 ± 0.033	1.022 ± 0.056
3.6 – 3.8	0.043 ± 0.022	0.195 ± 0.044	0.504 ± 0.028	0.663 ± 0.060
3.8 – 4.0	0.033 ± 0.021	0.085 ± 0.029	0.287 ± 0.015	0.465 ± 0.039
4.0 – 4.2	0.017 ± 0.011		0.200 ± 0.015	0.304 ± 0.036
4.2 – 4.4			0.095 ± 0.010	0.135 ± 0.029
4.4 – 4.6			0.0516 ± 0.0064	0.064 ± 0.019
4.6 – 4.8			0.0209 ± 0.0051	0.042 ± 0.012
4.8 – 5.0			0.0148 ± 0.0042	0.0275 ± 0.0093
5.0 – 5.2			0.0045 ± 0.0037	0.0105 ± 0.0069

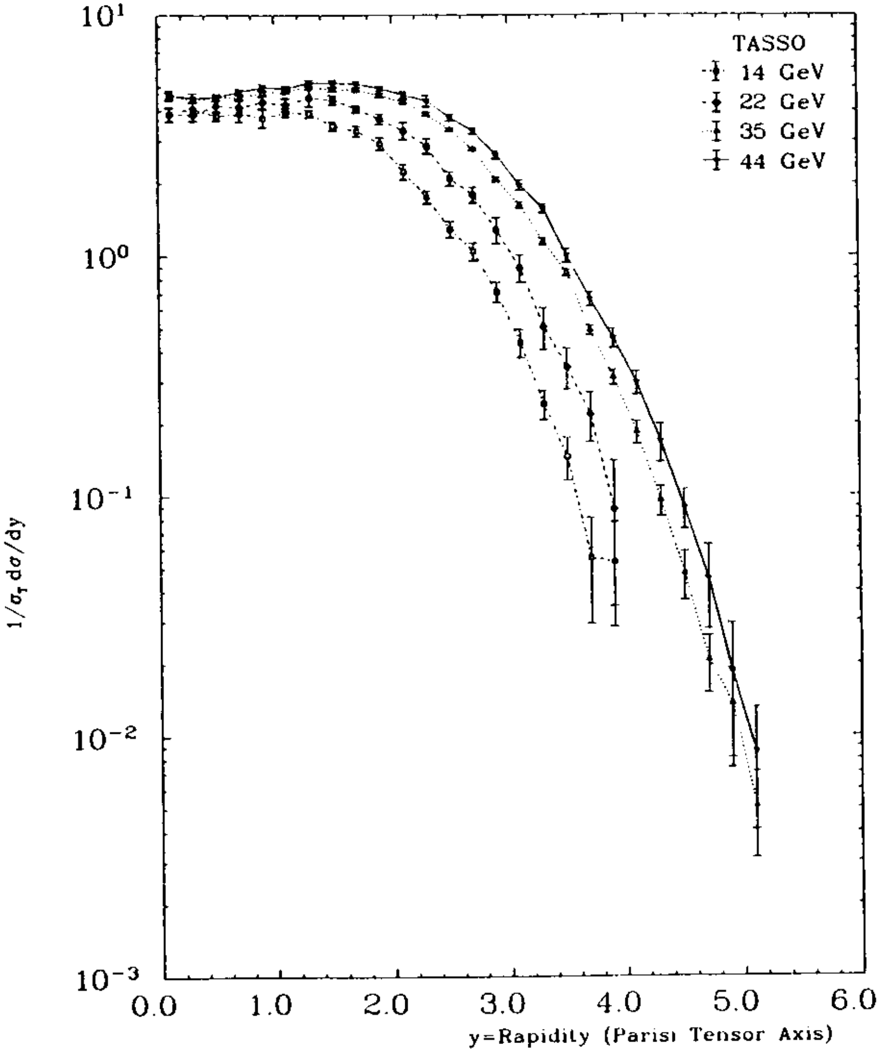

Fig. 7.30. Normalized rapidity distributions with respect to the Parisi tensor axis $1/\sigma_{tot}\, d\sigma/dy$ (folded around $y = 0$) at $\overline{W}$=14, 22, 35 and 44 GeV.

Table 7.30

Normalized rapidity distributions with respect to the Parisi tensor axis $1/\sigma_{tot}\, d\sigma/dy$ (folded around $y = 0$).

y	14 GeV	22 GeV	35 GeV	44 GeV
0.0 – 0.2	3.90 ± 0.27	3.86 ± 0.24	4.63 ± 0.13	4.65 ± 0.22
0.2 – 0.4	4.07 ± 0.25	3.86 ± 0.23	4.438 ± 0.094	4.53 ± 0.18
0.4 – 0.6	3.79 ± 0.15	4.20 ± 0.22	4.55 ± 0.15	4.56 ± 0.16
0.6 – 0.8	3.89 ± 0.30	4.13 ± 0.31	4.54 ± 0.16	4.80 ± 0.13
0.8 – 1.0	3.73 ± 0.32	4.34 ± 0.24	4.73 ± 0.14	4.00 ± 0.17
1.0 – 1.2	3.94 ± 0.16	4.25 ± 0.25	4.83 ± 0.10	4.96 ± 0.14
1.2 – 1.4	3.90 ± 0.14	4.53 ± 0.37	5.04 ± 0.14	5.22 ± 0.16
1.4 – 1.6	3.47 ± 0.15	4.45 ± 0.18	4.913 ± 0.092	5.23 ± 0.18
1.6 – 1.8	3.29 ± 0.16	4.08 ± 0.15	4.899 ± 0.097	5.17 ± 0.17
1.8 – 2.0	2.90 ± 0.17	3.68 ± 0.18	4.621 ± 0.071	4.94 ± 0.12
2.0 – 2.2	2.23 ± 0.16	3.30 ± 0.27	4.362 ± 0.082	4.67 ± 0.15
2.2 – 2.4	1.75 ± 0.11	2.85 ± 0.21	3.862 ± 0.060	4.39 ± 0.24
2.4 – 2.6	1.285 ± 0.096	2.09 ± 0.14	3.337 ± 0.048	3.74 ± 0.11
2.6 – 2.8	1.040 ± 0.089	1.78 ± 0.13	2.771 ± 0.041	3.30 ± 0.10
2.8 – 3.0	0.706 ± 0.068	1.27 ± 0.16	2.073 ± 0.049	2.62 ± 0.10
3.0 – 3.2	0.435 ± 0.059	0.89 ± 0.12	1.622 ± 0.050	1.958 ± 0.096
3.2 – 3.4	0.240 ± 0.034	0.505 ± 0.099	1.143 ± 0.039	1.565 ± 0.066
3.4 – 3.6	0.145 ± 0.029	0.343 ± 0.067	0.847 ± 0.027	0.999 ± 0.064
3.6 – 3.8	0.055 ± 0.026	0.218 ± 0.051	0.489 ± 0.021	0.658 ± 0.045
3.8 – 4.0	0.053 ± 0.024	0.087 ± 0.053	0.310 ± 0.022	0.453 ± 0.043
4.0 – 4.2	0.0110 ± 0.0077		0.184 ± 0.020	0.295 ± 0.033
4.2 – 4.4			0.095 ± 0.013	0.168 ± 0.030
4.4 – 4.6			0.047 ± 0.011	0.089 ± 0.017
4.6 – 4.8			0.0206 ± 0.0055	0.045 ± 0.017
4.8 – 5.0			0.0136 ± 0.0055	0.018 ± 0.011
5.0 – 5.2			0.0051 ± 0.0020	0.0086 ± 0.0045

direction of the narrow jet momentum was declared to be positive. The above mentioned cuts on particles emitted at specific angles were done to define the orientation of the axis only, so no particle was rejected due to those cuts in the further analysis and all of them enter into the shown distributions.

7.5.2 Rapidity Distribution

Fig. 7.31-7.33 show the rapidity distributions with respect to the oriented thrust, sphericity and Parisi tensor axis, compared to the rapidity distributions with respect to the most energetic quark direction obtained with the Lund $O(\alpha_s^2)$ Monte Carlo programme. A small dip near $y = 0$ in Fig. 7.31 showing rapidity plotted with respect to thrust axis is visible. In further analysis the Parisi tensor axis was used to determine the event axis, because the rapidity spectrum plotted with respect to this axis resembles more closely the Monte Carlo spectrum with respect to the most energetic quark momentum direction. (The distributions with respect to that tensor axis are shifted towards the left by about .2, as compared to the distribution with respect to the quark momentum vector.) Fig. 7.34 shows how the assumption, that all the emitted particles are pions, changes the rapidity spectrum. As one can see, this causes the distribution to be broader by about .1 unit.

Fig. 7.35 shows a comparison of the Lund plus MONSTER Monte Carlo calculations with the data. The rapidity distributions as measurement by the TASSO detector at 44 GeV are well described by the Monte Carlo.

Fig. 7.36 is based on the Monte Carlo studies performed with Lund $O(\alpha_s^2)$ Monte Carlo in order to understand the shape of the rapidity spectrum. The corrected (in the sense described at the beginning of this chapter) rapidity spectrum with respect to the oriented Parisi tensor axis is given in Fig. 7.37 (Table 7.31 and 7.32). The spectrum reveals the following features: It is asymmetric with respect to the $y = 0$. There are more particles on the wide jet (quark-gluon jet or wider quark jet) side. The wide jet spectrum is softer i.e. its maximum falls closer to the $y = 0$ as compared to the narrow jet maximum. If one compares Fig. 7.36 and 7.37, one sees, that this is the influence of gluons, which shifts the maximum of the wide jet towards $y = 0$ and increases the multiplicity of that jet. b and c quarks affect the spectrum by increasing the overall multiplicity, but they also increase the particle yield especially in the $y = 2$ region (compare dashed and full line in Fig. 7.36). Furthermore the gluon emission changes the shape of both jets especially in the region close to $y = 0$, which may be due to the contamination of the narrow jet by the quark-gluon jets, or by having a gluon in the central region. Going back to Fig. 7.30 one sees, that the plateau in the region $1 \lesssim y \lesssim 2$ is caused by the fact, that the maxima for the narrow and wide jet appear at different y values (due to the gluon emission).

7.5.3 Scaled Momentum Distribution

One of the variables to study multigluon phenomena (suggested e.g. in [DOK88]) is $\ln(1/x_p)$. A distribution of such a variable was already shown in Fig. 7.5, where all charged particles were taken into account.

Fig. 7.38 and 7.39 (Table 7.34 and 7.35) give similar distributions, but this time for charged particles in the narrow and wide jet separately. The Parisi tensor axis was used to define the jets; for the details see the previous section. This time, at least for the narrow

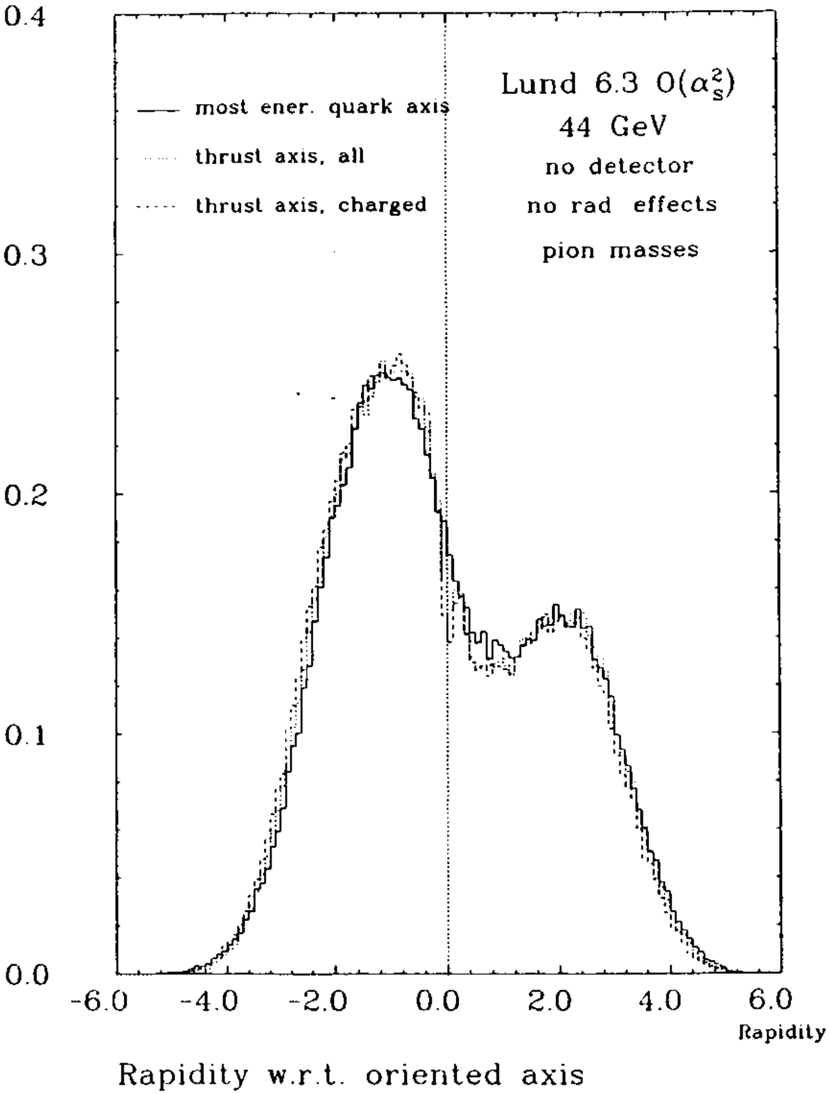

Fig. 7.31. Lund $O(\alpha_s^2)$ Monte Carlo programme rapidity distributions with respect to the oriented thrust axis $1/\sigma_{tot}\, d\sigma/dy$ at $W=44$ GeV, compared to the rapidity plot with respect to the most energetic quark direction. The rapidity with respect to the quark direction is plotted for all particles (full line) and with respect to thrust axis for all (dotted line) and only charged (dashed line) particles.

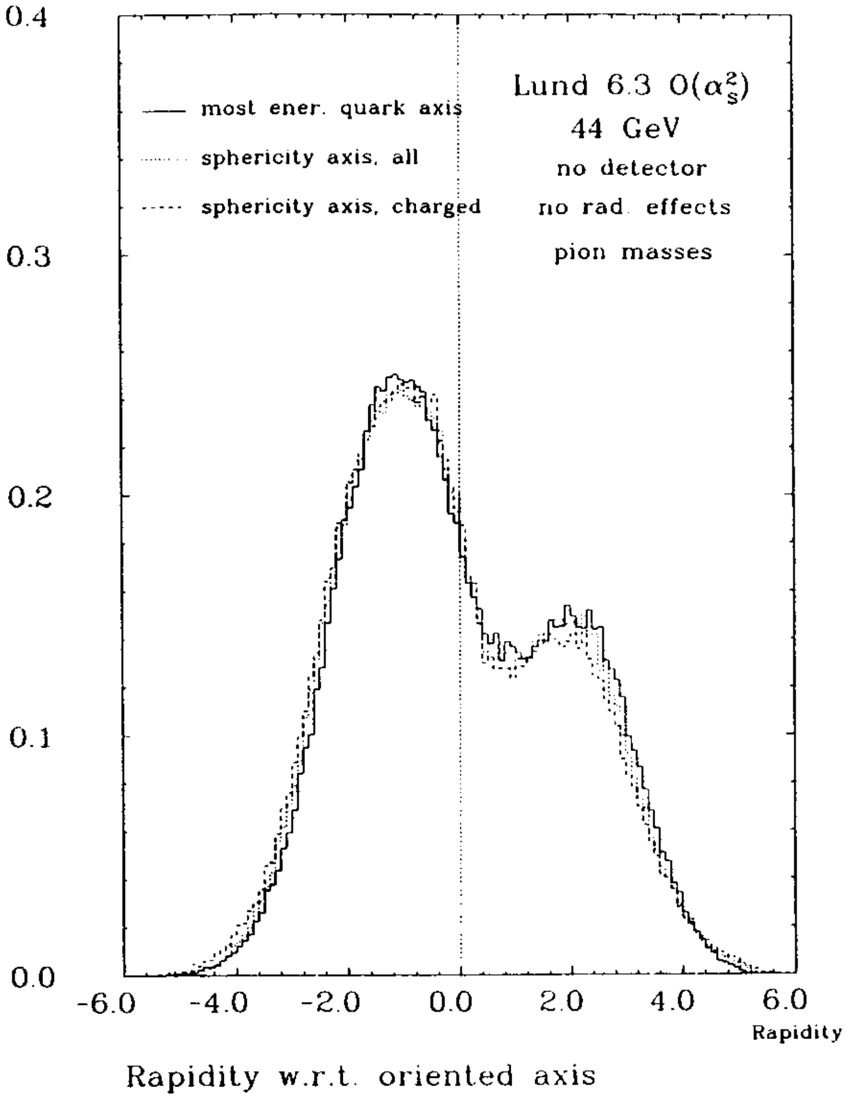

Fig. 7.32. Lund $O(\alpha_s^2)$ Monte Carlo programme rapidity distributions with respect to the oriented sphericity axis $1/\sigma_{tot}\, d\sigma/dy$ at $W=44$ GeV, compared to the rapidity plot with respect to the most energetic quark direction. The rapidity with respect to the quark direction is plotted for all particles (full line) and with respect to sphericity axis for all (dotted line) and only charged (dashed line) particles.

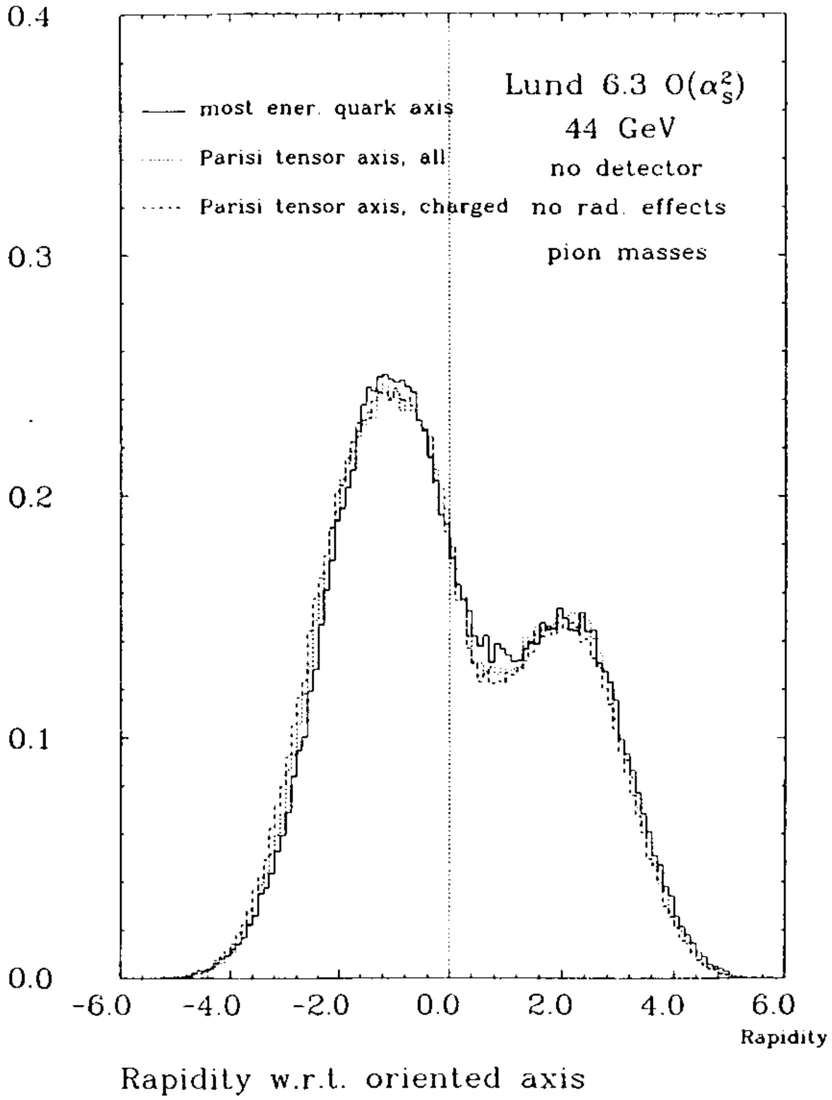

Fig. 7.33. Lund O(α_s^2) Monte Carlo programme rapidity distributions with respect to the oriented Parisi tensor axis $1/\sigma_{tot}\, d\sigma/dy$ at W=44 GeV, compared to the rapidity plot with respect to the most energetic quark direction. The rapidity with respect to the quark direction is plotted for all particles (full line) and with respect to Parisi tensor axis for all (dotted line) and only charged (dashed line) particles.

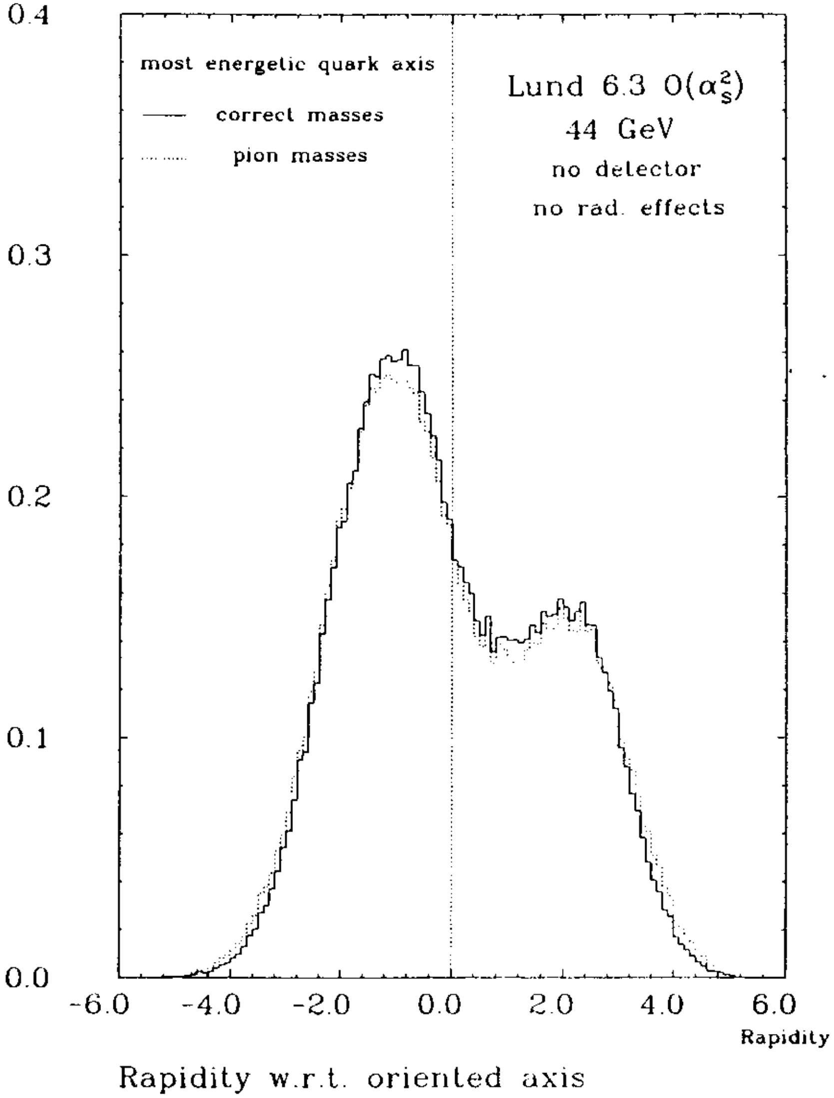

Fig. 7.34. Lund O(α_s^2) Monte Carlo programme rapidity distributions with respect to the most energetic quark direction at W=44 GeV with correct particle masses (full line) and with pion masses assumed for all the particles (dashed line).

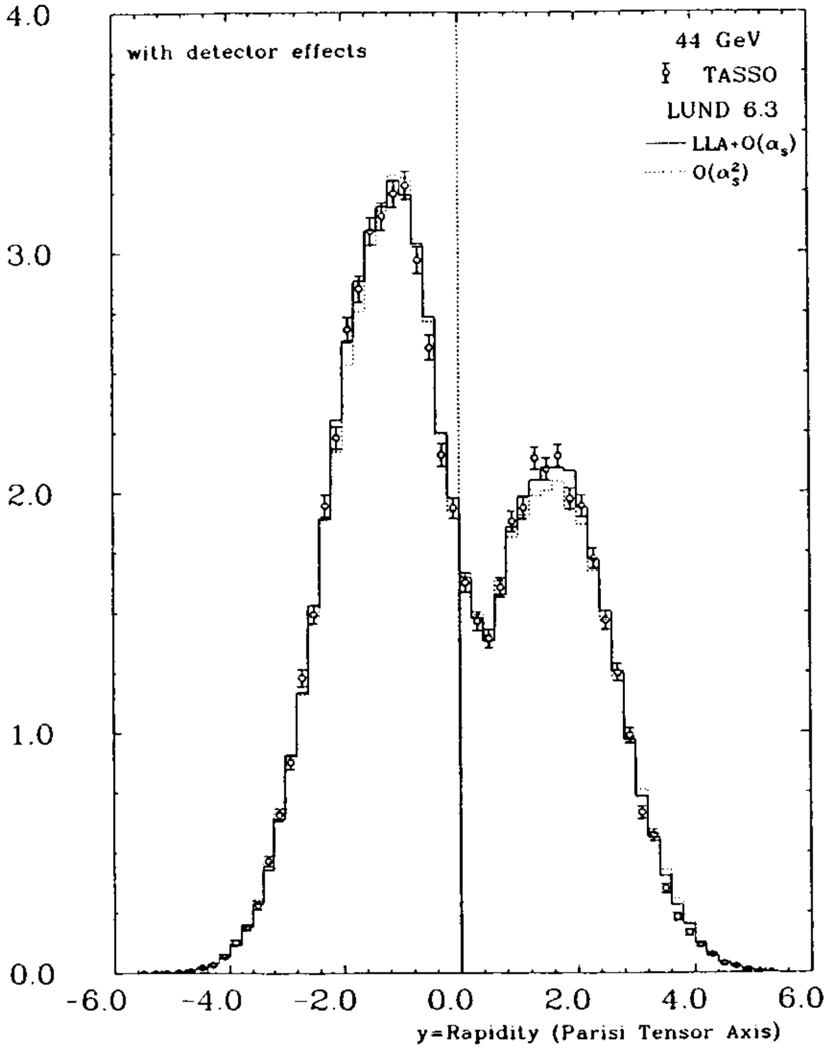

Fig. 7.35. Uncorrected rapidity distributions with respect to Parisi tensor axis at $\overline{W}$=44 GeV. TASSO data (points) and Lund LLA+O(α_s) Monte Carlo (full line) Lund O(α_s^2) Monte Carlo (dotted line).

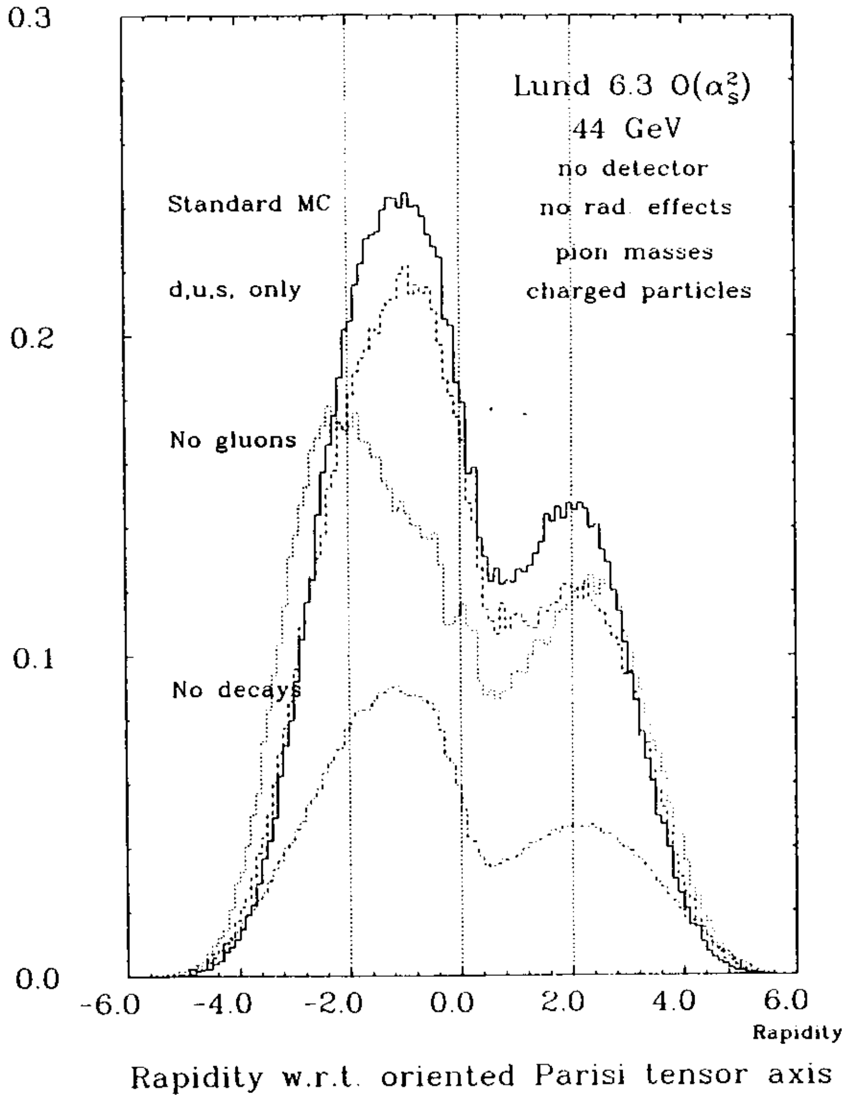

Fig. 7.36. Lund O(α_s^2) Monte Carlo programme rapidity distributions with respect to the oriented Parisi tensor axis $1/\sigma_{tot}\, d\sigma/dy$ at W=44 GeV (full line), with only d, u and s quarks produced in the e^+e^- annihilation (dashed line), with primary resonances not allowed to decay (dashed-dotted line), with the QCD gluon radiation switched off (dotted line).

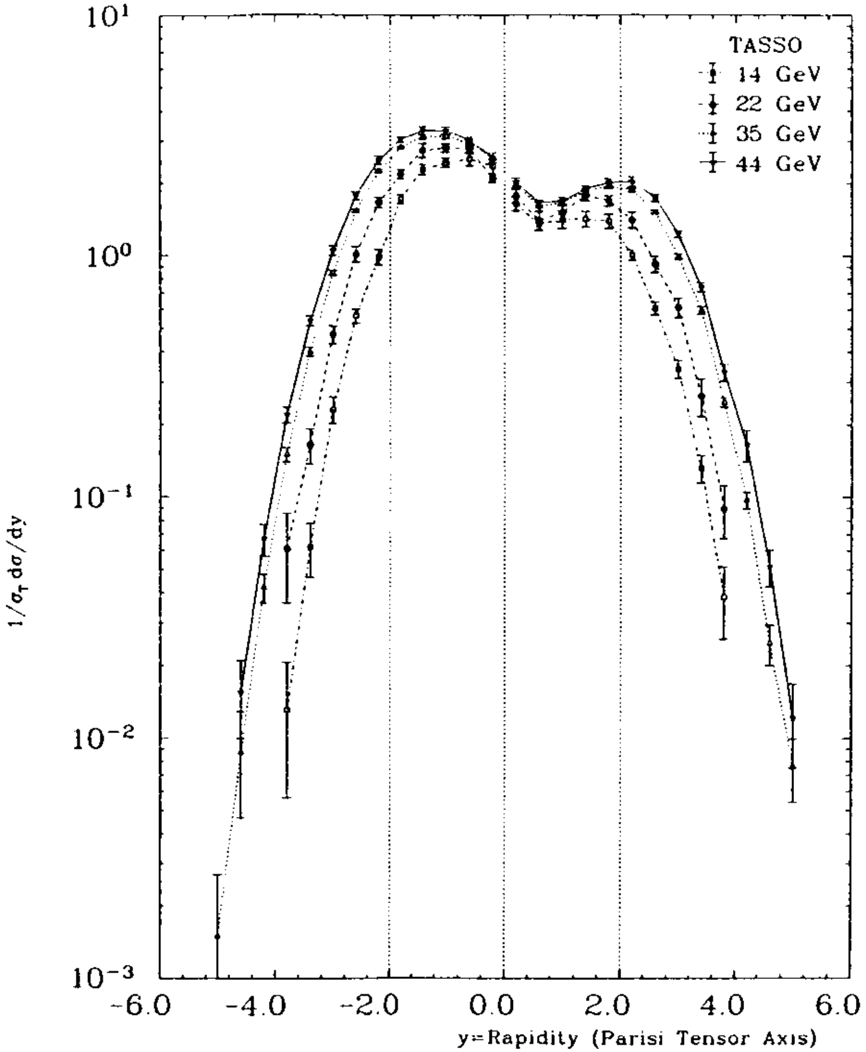

Fig. 7.37. Normalized rapidity distributions with respect to the oriented Parisi tensor axis $1/\sigma_{tot}\, d\sigma/dy$ at $\overline{W}=14$, 22, 35 and 44 GeV.

Table 7.31

Normalized rapidity distributions with respect to the oriented Parisi tensor axis $1/\sigma_{tot}\, d\sigma/dy$ (part 1).

y	14 GeV	22 GeV	35 GeV	44 GeV
-4.8 - -4.6			0.0048 ± 0.0022	0.0073 ± 0.0061
-4.6 - -4.4			0.0127 ± 0.0072	0.0247 ± 0.0078
-4.4 - -4.2			0.0269 ± 0.0050	0.043 ± 0.015
-4.2 - -4.0			0.057 ± 0.012	0.092 ± 0.015
-4.0 - -3.8			0.111 ± 0.020	0.175 ± 0.026
-3.8 - -3.6	0.016 ± 0.012	0.091 ± 0.034	0.189 ± 0.018	0.263 ± 0.031
-3.6 - -3.4	0.044 ± 0.034	0.143 ± 0.043	0.318 ± 0.017	0.412 ± 0.036
-3.4 - -3.2	0.080 ± 0.018	0.188 ± 0.047	0.479 ± 0.026	0.656 ± 0.043
-3.2 - -3.0	0.145 ± 0.028	0.358 ± 0.058	0.701 ± 0.036	0.917 ± 0.058
-3.0 - -2.8	0.315 ± 0.047	0.583 ± 0.077	0.991 ± 0.027	1.179 ± 0.070
-2.8 - -2.6	0.514 ± 0.056	0.935 ± 0.089	1.373 ± 0.032	1.639 ± 0.070
-2.6 - -2.4	0.614 ± 0.057	1.09 ± 0.13	1.694 ± 0.035	1.91 ± 0.11
-2.4 - -2.2	0.841 ± 0.078	1.54 ± 0.15	2.056 ± 0.040	2.40 ± 0.17
-2.2 - -2.0	1.13 ± 0.11	1.78 ± 0.11	2.429 ± 0.058	2.583 ± 0.072
-2.0 - -1.8	1.60 ± 0.14	2.05 ± 0.13	2.716 ± 0.062	2.98 ± 0.11
-1.8 - -1.6	1.84 ± 0.11	2.32 ± 0.17	2.911 ± 0.050	3.11 ± 0.12
-1.6 - -1.4	2.10 ± 0.12	2.74 ± 0.15	3.080 ± 0.075	3.32 ± 0.15
-1.4 - -1.2	2.47 ± 0.16	2.74 ± 0.35	3.164 ± 0.076	3.32 ± 0.13
-1.2 - -1.0	2.53 ± 0.11	2.74 ± 0.13	3.152 ± 0.083	3.29 ± 0.14
-1.0 - -0.8	2.34 ± 0.17	2.87 ± 0.18	3.109 ± 0.083	3.31 ± 0.16
-0.8 - -0.6	2.60 ± 0.24	2.71 ± 0.20	2.965 ± 0.094	3.134 ± 0.099
-0.6 - -0.4	2.43 ± 0.15	2.86 ± 0.20	2.937 ± 0.083	2.91 ± 0.13
-0.4 - -0.2	2.61 ± 0.15	2.27 ± 0.12	2.631 ± 0.054	2.65 ± 0.12
-0.2 - 0.0	2.10 ± 0.25	1.92 ± 0.15	2.480 ± 0.067	2.47 ± 0.16

Table 7.32

Normalized rapidity distributions with respect to the oriented Parisi tensor axis $1/\sigma_{tot}\, d\sigma/dy$ (part 2).

y	14 GeV	22 GeV	35 GeV	44 GeV
0.0 – 0.2	1.82 ± 0.16	1.94 ± 0.14	2.154 ± 0.075	2.180 ± 0.088
0.2 – 0.4	1.48 ± 0.16	1.60 ± 0.19	1.812 ± 0.074	1.87 ± 0.12
0.4 – 0.6	1.39 ± 0.12	1.36 ± 0.15	1.633 ± 0.092	1.661 ± 0.068
0.6 – 0.8	1.331 ± 0.096	1.44 ± 0.14	1.589 ± 0.088	1.675 ± 0.085
0.8 – 1.0	1.41 ± 0.18	1.51 ± 0.15	1.630 ± 0.068	1.692 ± 0.085
1.0 – 1.2	1.426 ± 0.090	1.52 ± 0.18	1.687 ± 0.047	1.683 ± 0.077
1.2 – 1.4	1.45 ± 0.11	1.81 ± 0.12	1.875 ± 0.079	1.903 ± 0.062
1.4 – 1.6	1.40 ± 0.13	1.76 ± 0.14	1.843 ± 0.033	1.919 ± 0.074
1.6 – 1.8	1.480 ± 0.096	1.76 ± 0.12	1.996 ± 0.096	2.07 ± 0.14
1.8 – 2.0	1.32 ± 0.16	1.638 ± 0.099	1.917 ± 0.032	1.97 ± 0.11
2.0 – 2.2	1.10 ± 0.11	1.52 ± 0.20	1.944 ± 0.039	2.09 ± 0.13
2.2 – 2.4	0.921 ± 0.073	1.31 ± 0.11	1.816 ± 0.049	1.993 ± 0.097
2.4 – 2.6	0.682 ± 0.084	1.02 ± 0.14	1.646 ± 0.048	1.837 ± 0.097
2.6 – 2.8	0.536 ± 0.054	0.847 ± 0.099	1.405 ± 0.034	1.663 ± 0.075
2.8 – 3.0	0.392 ± 0.060	0.69 ± 0.11	1.082 ± 0.039	1.442 ± 0.077
3.0 – 3.2	0.290 ± 0.045	0.545 ± 0.099	0.919 ± 0.049	1.034 ± 0.063
3.2 – 3.4	0.162 ± 0.027	0.32 ± 0.10	0.664 ± 0.031	0.905 ± 0.049
3.4 – 3.6	0.102 ± 0.023	0.202 ± 0.044	0.532 ± 0.027	0.581 ± 0.050
3.6 – 3.8	0.039 ± 0.018	0.125 ± 0.042	0.300 ± 0.020	0.391 ± 0.038
3.8 – 4.0	0.041 ± 0.019	0.055 ± 0.031	0.197 ± 0.013	0.272 ± 0.035
4.0 – 4.2	0.0103 ± 0.0090		0.126 ± 0.013	0.202 ± 0.037
4.2 – 4.4			0.069 ± 0.011	0.129 ± 0.029
4.4 – 4.6			0.0341 ± 0.0071	0.062 ± 0.015
4.6 – 4.8			0.0155 ± 0.0042	0.041 ± 0.017
4.8 – 5.0			0.0114 ± 0.0044	0.016 ± 0.011
5.0 – 5.2			0.0040 ± 0.0016	0.0088 ± 0.0062

jet one deals mostly with a quark jet. Fig. 7.40 and 7.41 (Table 7.36 and 7.37) present the same distributions as in the previous figures, but for particles emitted at angles smaller than 20° to the event axis. Dokshitzer and Troyan in [DOK84] predicted the asymptotic shape of the soft hadron spectrum $1/\sigma_{tot}\, d\sigma/d\ln(1/x_p)$ in the e^+e^- annihilation in the framework of the Modified Leading Logarithm Approximation and with the assumption of the Local Parton–Hadron Duality. They also predicted, that the shape of the distribution for the gluon and quark jets should be the same and that these spectra should only be different by a multiplicative constant when the jet energies are the same [DOK86]. In [DOK88] they give an expression for the position of the maximum x_{p_0} of the hadrons

spectrum. The formula reads:

$$\ln\left(\frac{1}{x_{p_0}}\right) = \frac{1}{2}Y + B\sqrt{\frac{b}{16N_c}Y},$$

where

$$Y = \ln\left(\frac{E_{jet}\sin\left(\frac{\Theta}{2}\right)}{\Lambda}\right), \quad B = \frac{1}{b}\left(\frac{11}{3}N_c + \frac{2}{3}\frac{n_f}{N_c^2}\right) \text{ and } b = \frac{11}{3}N_c - \frac{2}{3}n_f,$$

where N_c and n_f are the number of colours and the number of quark flavours, E_{jet} and Θ are the jet energy and the opening angle of the cone, which has the event axis as its axis and Λ is a QCD scale parameter.

One can invert the above formula and knowing the position of the maximum of the $1/\sigma_{tot}\, d\sigma/d\ln(1/x_p)$ spectrum, calculate the value of Λ. Then

$$\Lambda = E_{jet}\sin\left(\frac{\Theta}{2}\right)\exp\left(-2\left(\ln\left(\frac{1}{x_{p_0}}\right) + c^2 - \sqrt{c^2\left(2\ln\left(\frac{1}{x_{p_0}}\right) + c^2\right)}\right)\right),$$

where $c^2 = B^2\frac{b}{16N_c}$.

Table 7.33 shows the position of the maximum $\ln(1/x_{p_0})$ of spectra presented in Fig. 7.5, Fig. 7.38 and 7.39 and calculated corresponding values of Λ. It was assumed, that $E_{jet} = W/2, N_c = 3, n_f = 5$.

Table 7.33

Maxima of the $1/\sigma_{tot}\, d\sigma/d\ln(1/x_p)$ and the corresponding Λ values for all particles and for narrow and wide jet separately (for $\Theta = 180°$ and $\Theta = 40°$).

Energy (GeV)	$\Theta = 180°$ all		$\Theta = 180°$ narrow		$\Theta = 180°$ wide		$\Theta = 40°$ narrow		$\Theta = 40°$ wide	
	$\ln(x_{p_0}^{-1})$	Λ (GeV)	$\ln(x_{p_0}^{-1})$	Λ (GeV)	$\ln(x_{p_0}^{-1})$	Λ (GeV)	$\ln(x_{p_0}^{-1})$	Λ (GeV)	$\ln(x_{p_0}^{-1})$	Λ (GeV)
14	2.5 ± .2	$.36^{+.12}_{-.09}$	2.5 ± .2	$.36^{+.12}_{-.09}$	2.4 ± .2	$.42^{+.12}_{-.11}$	1.5 ± .2	$.52^{+.16}_{-.12}$	1.5 ± .2	$.52^{+.16}_{-.12}$
22	2.7 ± .2	$.42^{+.16}_{-.11}$	2.7 ± .2	$.42^{+.15}_{-.11}$	2.7 ± .2	$.42^{+.15}_{-.11}$	1.8 ± .2	$.54^{+.17}_{-.13}$	1.8 ± .2	$.54^{+.17}_{-.13}$
35	3.1 ± .2	$.37^{+.13}_{-.10}$	3.2 ± .2	$.31^{+.11}_{-.08}$	3.0 ± .2	$.43^{+.16}_{-.11}$	2.1 ± .2	$.56^{+.18}_{-.14}$	2.2 ± .2	$.48^{+.16}_{-.12}$
44	3.3 ± .2	$.34^{+.12}_{-.09}$	3.4 ± .2	$.29^{+.10}_{-.08}$	3.2 ± .2	$.39^{+.14}_{-.10}$	2.4 ± .2	$.45^{+.16}_{-.12}$	2.2 ± .2	$.60^{+.20}_{-.15}$
$< \Lambda >$		$.38^{+.13}_{-.10}$		$.35^{+.13}_{-.09}$		$.42^{+.15}_{-.11}$		$.52^{+.17}_{-.13}$		$.54^{+.18}_{-.14}$

The values of the position of the maximum for one single energy and for one Θ value are consistent with each other. It is also the case for the derived values of Λ. When Θ=40° the Λ values are systematically by about .15 higher than the corresponding values for Θ=180°.

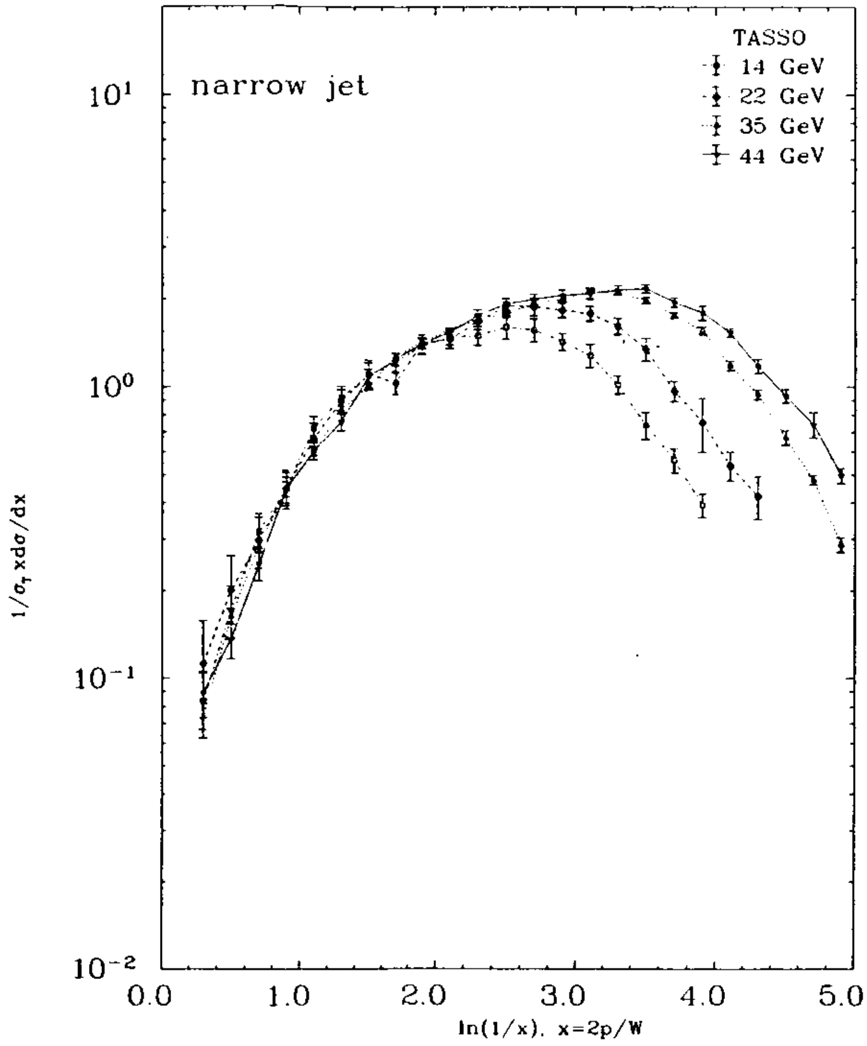

Fig. 7.38. Normalized $\ln(1/x_p)$ distributions $1/\sigma_{tot}\, d\sigma/d\ln(1/x_p)$, where $x_p = 2p/W$, for charged particles in the narrow jet at $\overline{W}$=14, 22, 35 and 44 GeV.

Table 7.34

Normalized $\ln(1/x_p)$ distributions $1/\sigma_{tot}\, d\sigma/d\ln(1/x_p)$, where $x_p = 2p/W$, for charged particles in the narrow jet.

$\ln(1/x_p)$	14 GeV	22 GeV	35 GeV	44 GeV
0.0 - 0.2	0.038 ± 0.023	0.029 ± 0.018	0.0149 ± 0.0049	0.0114 ± 0.0039
0.2 - 0.4	0.083 ± 0.021	0.112 ± 0.046	0.074 ± 0.011	0.089 ± 0.016
0.4 - 0.6	0.171 ± 0.036	0.200 ± 0.062	0.163 ± 0.010	0.136 ± 0.020
0.6 - 0.8	0.319 ± 0.047	0.297 ± 0.059	0.283 ± 0.014	0.246 ± 0.031
0.8 - 1.0	0.449 ± 0.059	0.449 ± 0.070	0.445 ± 0.026	0.444 ± 0.045
1.0 - 1.2	0.720 ± 0.070	0.663 ± 0.085	0.600 ± 0.020	0.601 ± 0.040
1.2 - 1.4	0.916 ± 0.086	0.889 ± 0.087	0.831 ± 0.024	0.758 ± 0.053
1.4 - 1.6	1.10 ± 0.11	1.10 ± 0.13	1.005 ± 0.028	1.079 ± 0.063
1.6 - 1.8	1.209 ± 0.084	1.027 ± 0.085	1.269 ± 0.030	1.240 ± 0.065
1.8 - 2.0	1.377 ± 0.093	1.40 ± 0.10	1.427 ± 0.028	1.399 ± 0.053
2.0 - 2.2	1.482 ± 0.095	1.46 ± 0.11	1.570 ± 0.030	1.539 ± 0.058
2.2 - 2.4	1.49 ± 0.11	1.67 ± 0.11	1.706 ± 0.043	1.755 ± 0.080
2.4 - 2.6	1.60 ± 0.15	1.90 ± 0.11	1.772 ± 0.044	1.929 ± 0.091
2.6 - 2.8	1.56 ± 0.14	1.88 ± 0.13	1.937 ± 0.041	1.992 ± 0.083
2.8 - 3.0	1.428 ± 0.095	1.83 ± 0.11	1.997 ± 0.047	2.057 ± 0.090
3.0 - 3.2	1.28 ± 0.12	1.78 ± 0.10	2.141 ± 0.044	2.082 ± 0.083
3.2 - 3.4	1.020 ± 0.074	1.62 ± 0.11	2.115 ± 0.038	2.146 ± 0.078
3.4 - 3.6	0.741 ± 0.080	1.35 ± 0.12	1.975 ± 0.047	2.169 ± 0.075
3.6 - 3.8	0.562 ± 0.053	0.970 ± 0.078	1.763 ± 0.038	1.954 ± 0.072
3.8 - 4.0	0.393 ± 0.036	0.76 ± 0.16	1.560 ± 0.046	1.80 ± 0.10
4.0 - 4.2	0.229 ± 0.074	0.538 ± 0.061	1.183 ± 0.044	1.534 ± 0.055
4.2 - 4.4		0.422 ± 0.071	0.942 ± 0.036	1.179 ± 0.065
4.4 - 4.6		0.240 ± 0.055	0.672 ± 0.039	0.932 ± 0.049
4.6 - 4.8			0.479 ± 0.018	0.743 ± 0.074
4.8 - 5.0			0.287 ± 0.016	0.496 ± 0.031

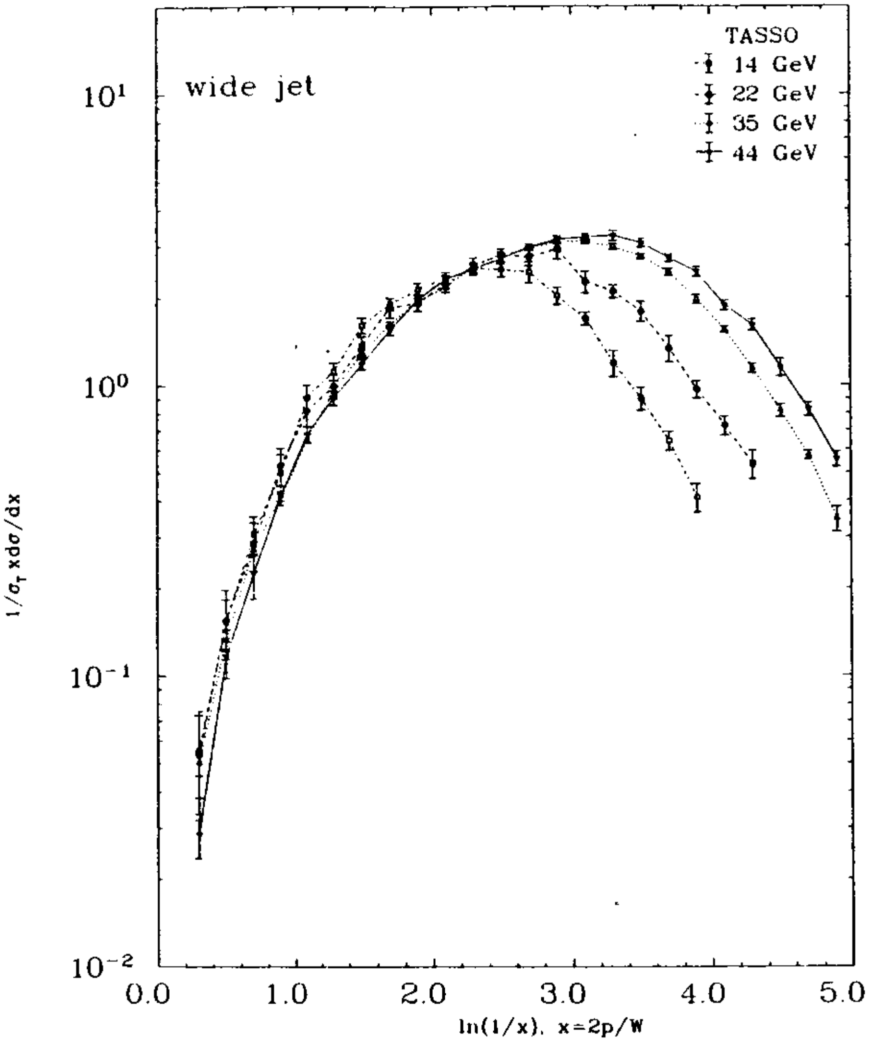

Fig. 7.39. Normalized $\ln(1/x_p)$ distributions $1/\sigma_{tot}\, d\sigma/d\ln(1/x_p)$, where $x_p = 2p/W$, for charged particles in the wide jet at W=14, 22, 35 and 44 GeV.

Table 7.35

Normalized $\ln(1/x_p)$ distributions $1/\sigma_{tot}\, d\sigma/d\ln(1/x_p)$, where $x_p = 2p/W$, for charged particles in the wide jet.

$\ln(1/x_p)$	14 GeV	22 GeV	35 GeV	44 GeV
0.0 - 0.2	0.0115 ± 0.0091	0.0046 ± 0.0037	0.0040 ± 0.0039	0.0056 ± 0.0018
0.2 - 0.4	0.056 ± 0.018	0.054 ± 0.022	0.0503 ± 0.0050	0.0286 ± 0.0050
0.4 - 0.6	0.154 ± 0.030	0.156 ± 0.042	0.133 ± 0.011	0.117 ± 0.018
0.6 - 0.8	0.310 ± 0.046	0.284 ± 0.053	0.276 ± 0.015	0.227 ± 0.042
0.8 - 1.0	0.504 ± 0.077	0.534 ± 0.077	0.418 ± 0.016	0.420 ± 0.032
1.0 - 1.2	0.913 ± 0.093	0.820 ± 0.095	0.659 ± 0.024	0.682 ± 0.041
1.2 - 1.4	1.118 ± 0.076	0.996 ± 0.094	0.950 ± 0.030	0.906 ± 0.052
1.4 - 1.6	1.606 ± 0.097	1.373 ± 0.096	1.295 ± 0.035	1.184 ± 0.051
1.6 - 1.8	1.904 ± 0.096	1.85 ± 0.14	1.622 ± 0.030	1.550 ± 0.063
1.8 - 2.0	2.14 ± 0.10	1.91 ± 0.12	1.947 ± 0.035	1.972 ± 0.085
2.0 - 2.2	2.34 ± 0.10	2.23 ± 0.14	2.174 ± 0.034	2.317 ± 0.072
2.2 - 2.4	2.52 ± 0.12	2.59 ± 0.15	2.571 ± 0.059	2.512 ± 0.087
2.4 - 2.6	2.50 ± 0.15	2.80 ± 0.14	2.821 ± 0.057	2.73 ± 0.12
2.6 - 2.8	2.45 ± 0.20	2.77 ± 0.20	2.948 ± 0.050	2.993 ± 0.079
2.8 - 3.0	2.03 ± 0.14	2.94 ± 0.22	3.115 ± 0.057	3.180 ± 0.081
3.0 - 3.2	1.698 ± 0.085	2.27 ± 0.19	3.120 ± 0.053	3.237 ± 0.090
3.2 - 3.4	1.19 ± 0.12	2.11 ± 0.11	2.993 ± 0.063	3.27 ± 0.13
3.4 - 3.6	0.901 ± 0.082	1.80 ± 0.14	2.777 ± 0.056	3.084 ± 0.098
3.6 - 3.8	0.644 ± 0.048	1.34 ± 0.14	2.451 ± 0.065	2.739 ± 0.081
3.8 - 4.0	0.412 ± 0.046	0.969 ± 0.067	1.977 ± 0.066	2.461 ± 0.095
4.0 - 4.2	0.256 ± 0.074	0.726 ± 0.056	1.554 ± 0.039	1.885 ± 0.074
4.2 - 4.4		0.536 ± 0.060	1.143 ± 0.042	1.613 ± 0.071
4.4 - 4.6		0.321 ± 0.084	0.818 ± 0.042	1.152 ± 0.080
4.6 - 4.8			0.574 ± 0.019	0.826 ± 0.045
4.8 - 5.0			0.346 ± 0.034	0.557 ± 0.033

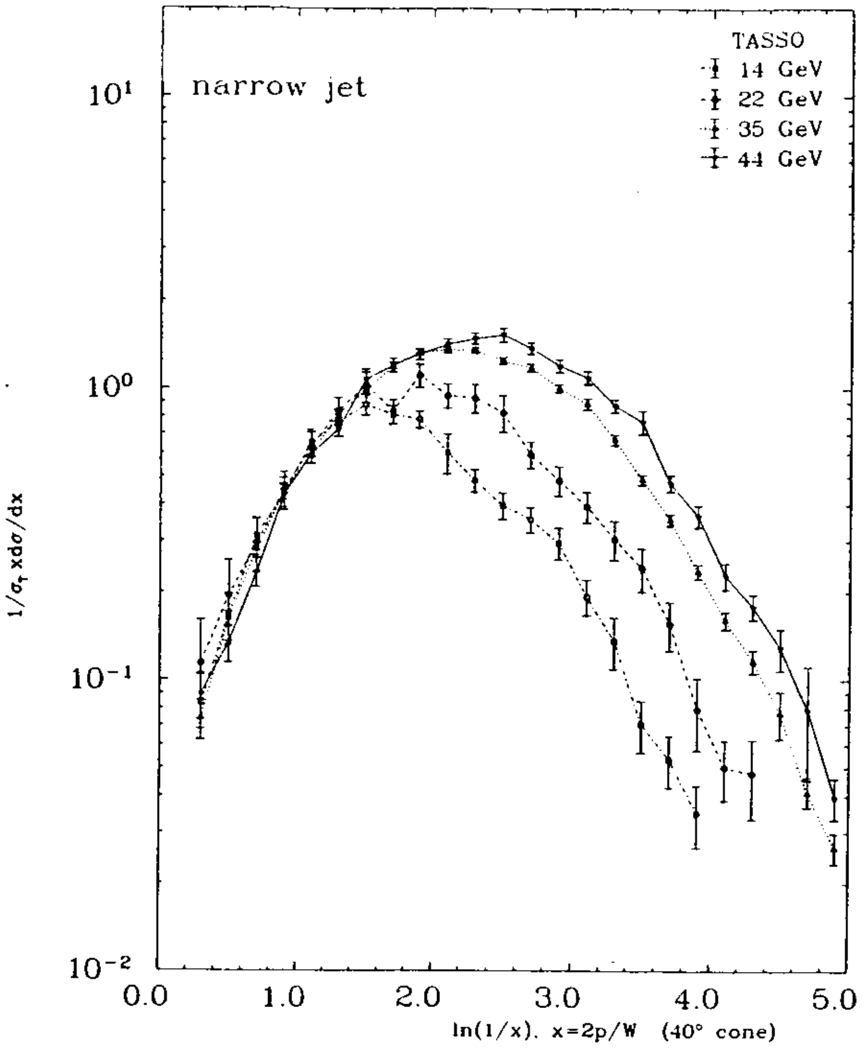

Fig. 7.40. Normalized $\ln(1/x_p)$ distributions $1/\sigma_{tot}\, d\sigma/d\ln(1/x_p)$, where $x_p = 2p/W$, for charged particles in the narrow jet emitted in a 40° cone around the event axis at $\overline{W}$=14, 22, 35 and 44 GeV.

Table 7.36

Normalized $\ln(1/x_p)$ distributions $1/\sigma_{tot}\, d\sigma/d\ln(1/x_p)$, where $x_p = 2p/W$, for charged particles in the narrow jet emitted in a 40° cone around the event axis.

$\ln(1/x_p)$	14 GeV	22 GeV	35 GeV	44 GeV
0.0 - 0.2	0.038 ± 0.023	0.029 ± 0.018	0.0149 ± 0.0050	0.0116 ± 0.0040
0.2 - 0.4	0.083 ± 0.021	0.114 ± 0.046	0.074 ± 0.012	0.089 ± 0.016
0.4 - 0.6	0.166 ± 0.031	0.194 ± 0.063	0.1618 ± 0.0099	0.134 ± 0.020
0.6 - 0.8	0.312 ± 0.046	0.295 ± 0.062	0.280 ± 0.015	0.234 ± 0.027
0.8 - 1.0	0.437 ± 0.056	0.448 ± 0.067	0.440 ± 0.025	0.431 ± 0.041
1.0 - 1.2	0.653 ± 0.068	0.627 ± 0.077	0.596 ± 0.020	0.591 ± 0.039
1.2 - 1.4	0.763 ± 0.080	0.835 ± 0.091	0.813 ± 0.025	0.723 ± 0.045
1.4 - 1.6	0.876 ± 0.069	1.02 ± 0.14	0.981 ± 0.027	1.067 ± 0.061
1.6 - 1.8	0.810 ± 0.058	0.833 ± 0.078	1.191 ± 0.031	1.198 ± 0.064
1.8 - 2.0	0.783 ± 0.052	1.11 ± 0.10	1.329 ± 0.029	1.310 ± 0.058
2.0 - 2.2	0.602 ± 0.094	0.945 ± 0.090	1.350 ± 0.032	1.414 ± 0.063
2.2 - 2.4	0.484 ± 0.043	0.93 ± 0.10	1.349 ± 0.033	1.482 ± 0.062
2.4 - 2.6	0.397 ± 0.042	0.83 ± 0.12	1.244 ± 0.032	1.524 ± 0.083
2.6 - 2.8	0.355 ± 0.035	0.593 ± 0.062	1.177 ± 0.036	1.372 ± 0.061
2.8 - 3.0	0.295 ± 0.037	0.484 ± 0.056	1.002 ± 0.032	1.194 ± 0.059
3.0 - 3.2	0.194 ± 0.027	0.394 ± 0.047	0.885 ± 0.039	1.088 ± 0.056
3.2 - 3.4	0.136 ± 0.027	0.304 ± 0.047	0.667 ± 0.028	0.874 ± 0.045
3.4 - 3.6	0.071 ± 0.014	0.242 ± 0.041	0.488 ± 0.019	0.770 ± 0.070
3.6 - 3.8	0.053 ± 0.011	0.156 ± 0.030	0.355 ± 0.015	0.474 ± 0.030
3.8 - 4.0	0.0350 ± 0.0084	0.080 ± 0.022	0.236 ± 0.014	0.366 ± 0.031
4.0 - 4.2	0.009 ± 0.011	0.050 ± 0.012	0.161 ± 0.011	0.228 ± 0.024
4.2 - 4.4		0.048 ± 0.015	0.116 ± 0.011	0.179 ± 0.018
4.4 - 4.6		0.0028 ± 0.0031	0.077 ± 0.014	0.129 ± 0.021
4.6 - 4.8			0.0410 ± 0.0044	0.079 ± 0.033
4.8 - 5.0			0.0266 ± 0.0032	0.0396 ± 0.0065

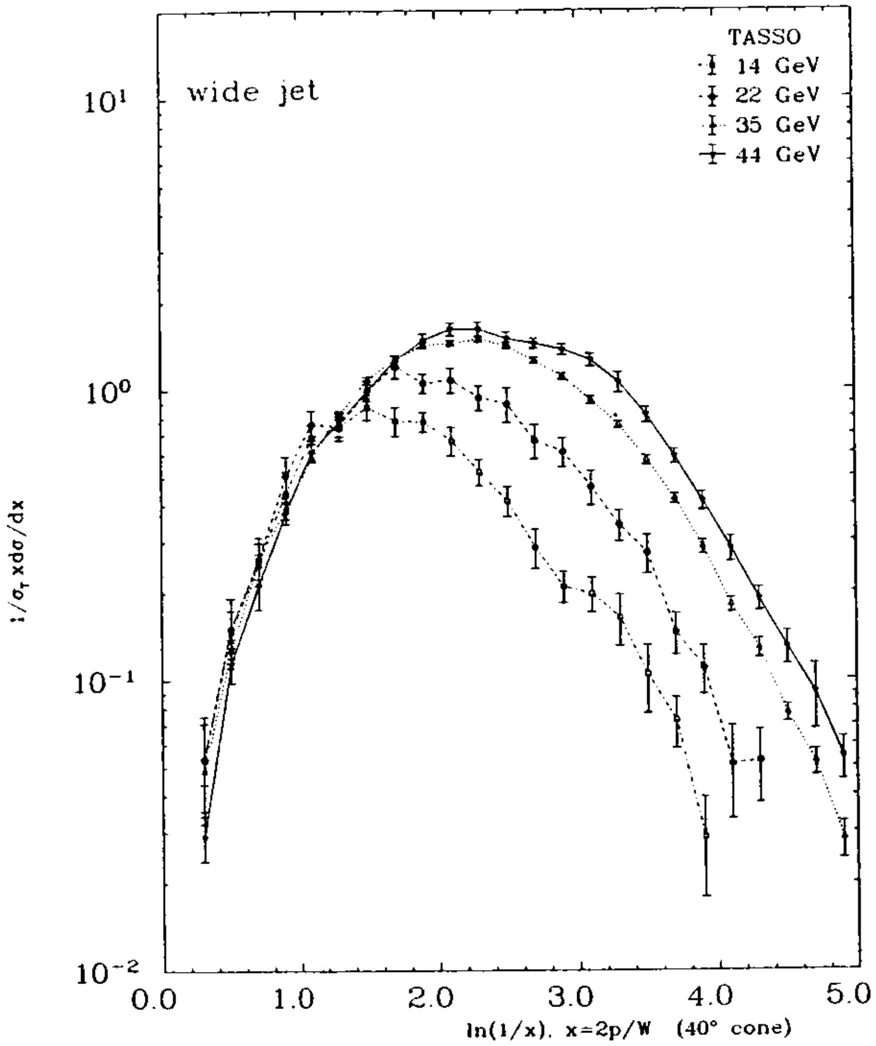

Fig. 7.41. Normalized $\ln(1/x_p)$ distributions $1/\sigma_{tot}\, d\sigma/d\ln(1/x_p)$, where $x_p = 2p/W$, for charged particles in the wide jet emitted in a 40° cone around the event axis at $\overline{W}$=14, 22, 35 and 44 GeV.

Table 7.37

Normalized $\ln(1/x_p)$ distributions $1/\sigma_{tot}\, d\sigma/d\ln(1/x_p)$, where $x_p = 2p/W$, for charged particles in the wide jet emitted in a 40° cone around the event axis.

$\ln(1/x_p)$	14 GeV	22 GeV	35 GeV	44 GeV
0.0 - 0.2	0.013 ± 0.011	0.0050 ± 0.0039	0.0038 ± 0.0036	0.0052 ± 0.0016
0.2 - 0.4	0.053 ± 0.018	0.054 ± 0.022	0.0486 ± 0.0048	0.0289 ± 0.0051
0.4 - 0.6	0.147 ± 0.027	0.151 ± 0.041	0.127 ± 0.012	0.114 ± 0.016
0.6 - 0.8	0.260 ± 0.037	0.261 ± 0.050	0.260 ± 0.013	0.214 ± 0.038
0.8 - 1.0	0.442 ± 0.083	0.509 ± 0.080	0.392 ± 0.015	0.379 ± 0.034
1.0 - 1.2	0.683 ± 0.077	0.758 ± 0.089	0.584 ± 0.022	0.611 ± 0.039
1.2 - 1.4	0.747 ± 0.058	0.750 ± 0.084	0.816 ± 0.028	0.776 ± 0.050
1.4 - 1.6	0.868 ± 0.086	0.992 ± 0.080	1.075 ± 0.033	0.987 ± 0.055
1.6 - 1.8	0.778 ± 0.089	1.20 ± 0.11	1.272 ± 0.034	1.254 ± 0.051
1.8 - 2.0	0.772 ± 0.060	1.048 ± 0.080	1.415 ± 0.033	1.469 ± 0.078
2.0 - 2.2	0.664 ± 0.075	1.07 ± 0.11	1.435 ± 0.031	1.607 ± 0.082
2.2 - 2.4	0.518 ± 0.055	0.934 ± 0.090	1.484 ± 0.034	1.605 ± 0.093
2.4 - 2.6	0.412 ± 0.048	0.89 ± 0.12	1.409 ± 0.034	1.491 ± 0.078
2.6 - 2.8	0.285 ± 0.044	0.664 ± 0.090	1.252 ± 0.028	1.434 ± 0.056
2.8 - 3.0	0.209 ± 0.026	0.609 ± 0.068	1.104 ± 0.030	1.368 ± 0.059
3.0 - 3.2	0.197 ± 0.027	0.460 ± 0.062	0.916 ± 0.029	1.261 ± 0.065
3.2 - 3.4	0.163 ± 0.033	0.341 ± 0.042	0.754 ± 0.020	1.056 ± 0.085
3.4 - 3.6	0.104 ± 0.027	0.273 ± 0.042	0.569 ± 0.019	0.814 ± 0.049
3.6 - 3.8	0.072 ± 0.014	0.145 ± 0.024	0.419 ± 0.016	0.587 ± 0.035
3.8 - 4.0	0.029 ± 0.011	0.110 ± 0.021	0.286 ± 0.015	0.412 ± 0.030
4.0 - 4.2	0.039 ± 0.023	0.051 ± 0.018	0.180 ± 0.010	0.282 ± 0.028
4.2 - 4.4		0.052 ± 0.015	0.1278 ± 0.0095	0.189 ± 0.017
4.4 - 4.6		0.027 ± 0.011	0.0765 ± 0.0052	0.130 ± 0.017
4.6 - 4.8			0.0519 ± 0.0053	0.090 ± 0.023
4.8 - 5.0			0.0283 ± 0.0041	0.0541 ± 0.0091

Table 7.38 gives the calculated positions of the maximum $\ln(1/x_{p_0})$, assuming Λ=.38 GeV. It shows that the formula for $\ln(1/x_{p_0})$ predicts the position of the maximum and its energy dependence quite well for $\Theta = 180°$. For $\Theta = 40°$ the formula gives slightly to soft particle spectrum, but still the positions of the maximum agree with the values from Table 7.33 within .2. It is probably the $\sin(\Theta/2)$ angular dependence, which may be too simple to describe the real angular distribution of the particles within a jet. Besides, the formula is derived for soft particles and for high ($\approx 50 \div 100$ GeV) jet energies. At the actual energies of this experiment, especially for $\Theta = 40°$, the maximum of the spectrum falls already in the region $x_p \approx .1$ and there particles have their total energy not too different from their rest mass, which sets kinematical constrains on their production (as pointed out in [DOK86]).

Table 7.38

Maxima of the $1/\sigma_{tot}\, d\sigma/d\ln(1/x_p)$ spectra for $\Lambda = .38$ and $\Theta = 180°$ and $\Theta = 40°$.

Energy (GeV)	$\Theta = 180°$ $\ln(1/x_{p_0})$	$\Theta = 40°$ $\ln(1/x_{p_0})$
14	2.5 ± .2	1.7 ± .2
22	2.8 ± .2	2.0 ± .2
35	3.1 ± .2	2.4 ± .2
44	3.2 ± .2	2.5 ± .2

If one compares Fig. 7.38 and Fig. 7.40 or Fig. 7.39 and Fig. 7.37 one sees, that the $\Theta = 40°$ cut removes mainly soft particles starting from $\ln(1/x_p) \gtrsim 1.6$ for the narrow jet and $\ln(1/x_p) \gtrsim 1.0$ for the wide jet. After this cut the particle spectra, which were quite different initially (much higher multiplicity and much softer spectrum in the wider jet) become very similar (the only big difference at $\ln(1/x_p) \approx .5$ is compensated by small difference of the cross section in the remaining range $.5 \lesssim \ln(1/x_p) \lesssim 5$). This suggests, that this cut removes the soft particles coming from the gloun jets in the $q\bar{q}g$ events and what remains are mostly the "kernels" of the quark jets from the $q\bar{q}$ and $q\bar{q}g$ events.

CHAPTER 8

Comparison of the Data with the Monte Carlo Calculations and with Data from other Experiments

8.1 Data at 44 GeV versus Lund LLA+O(α_s) and Lund O(α_s^2) Monte Carlo programs

8.1.1 Introduction

As already pointed out in the introduction, the main goal of this thesis was to obtain the corrected data at a center-of-mass energy of 44 GeV. The Monte Carlo programs used were treated only as tools in the correcting procedure. However, it is tempting to do a comparison between the corrected data and the Monte Carlo used for correcting.

At this very high center-of-mass energy the corrected data were compared with the Lund LLA+O(α_s) Monte Carlo calculations with the parameter values obtained during the tuning procedure described in section 4.1, namely:

$$\Lambda_{LLA} = .44 \text{ GeV}, \quad a = .87, \quad b = 1.05, \quad \sigma_q = .371 \text{ GeV/c}.$$

To be able to make fair comparisons between Lund LLA+O(α_s) and Lund O(α_s^2) programs, Lund O(α_s^2) Monte Carlo was tuned once again using the same corrected data sample as in Lund LLA+O(α_s) case (see section 4.1). The following parameter values were obtained:

$$\Lambda_{\overline{MS}} = .81 \text{ GeV}, \quad a = 1.00, \quad b = .74, \quad \sigma_q = .425 \text{ GeV/c}.$$

(ϵ_c and ϵ_b were kept at .07 and .01 correspondingly). One should note that the $\Lambda_{\overline{MS}}$ parameter had to be chosen quite large (.81 GeV as compared to the default value of .50 GeV).

8.1.2 Event Parameters and Inclusive Spectra

Since observables such as S, A, C, D, $p^2_{\perp in}$, $p^2_{\perp out}$, x_p were directly or indirectly used in the tuning procedure, they should — at least in principle — be well reproduced by the Monte Carlo calculations. It is indeed the case for both S and A (see Fig. 8.1 and 8.2), although the Lund O(α_s^2) Monte Carlo predicts fever aplanar events than Lund LLA+O(α_s).

The Monte Carlo $< p^2_{\perp in} >$ and $< p^2_{\perp out} >$ (Fig. 8.3 and 8.4) distributions also agree with the data, although again Lund O(α_s^2) Monte Carlo predicts fever aplanar events than Lund LLA+O(α_s), but the deviation is still within the errors of the data. The x_p and $\ln(1/x_p)$ distributions (Fig. 8.5 and 8.6) are well represented by the Monte Carlo too. Very closely related distributions, namely $\ln(1/x_p)$ for the narrow and wide jet for the opening angle of 180°and 40°, although were not tuned, are also well represented by the Monte Carlo programs (Fig. 8.8-8.11). Other Monte Carlo distribution, which was not used in the tunning process, e.g. the thrust distribution (Fig. 8.7) is well in agreement with the data.

Based on above results one can conclude, that both Lund LLA+O(α_s) and Lund O(α_s^2) Monte Carlo programs are able to reproduce most of the features of e^+e^- data at a center-of-mass energy of 44 GeV, although the agreement between the data and the Lund LLA+O(α_s) Monte Carlo seems to be better. It should be remembered, that the Peterson fragmentation function was used for c and b quarks, which played an important role and led to the significant decrease of χ^2 (see section 4.1), although it my be, that this is not due to the specific shape of the Peterson fragmentation function, but it is the uncoupling of c and b quarks from the light quarks, which enabled to get the better agreement between the Monte Carlo and the data.

8.1.3 Energy Dependence of the Observables

Another question is how the Monte Carlo programs tuned at one energy reproduces the data at other energies.

The energy dependence of $< S >$ and $< A >$ is shown on Fig. 7.8, compared with the Monte Carlo predictions. It is seen, that Lund O(α_s^2) Monte Carlo tuned at one energy, has some problems with the reproducing the data at other energies, while Lund LLA+O(α_s) Monte Carlo does well over the whole energy range.

The energy dependence of $< T >$ (Fig. 7.10) is in principle well reproduced by all the Monte Carlo programs. The average momenta (Fig. 7.2) are well described too. The same applies to the average momenta squared (Fig. 7.19 and 7.20), although there are some indications of problems with reproducing high $\ll p_{\perp out} \gg$ rate by Lund O(α_s^2) Monte Carlo at higher energies.

The energy dependence of the cross section for different x_p and $x_{\parallel}$ intervals is shown in Fig. 7.4 and 7.25 and it is seen, that the Monte Carlo reproduces the data quite satisfactorily.

One can conclude, that the energy dependence of most of the studied observables is well represented by both Lund O(α_s^2) and Lund LLA+O(α_s) Monte Carlo programs, although the Lund LLA+O(α_s) reproduces data better over a wider energy range.

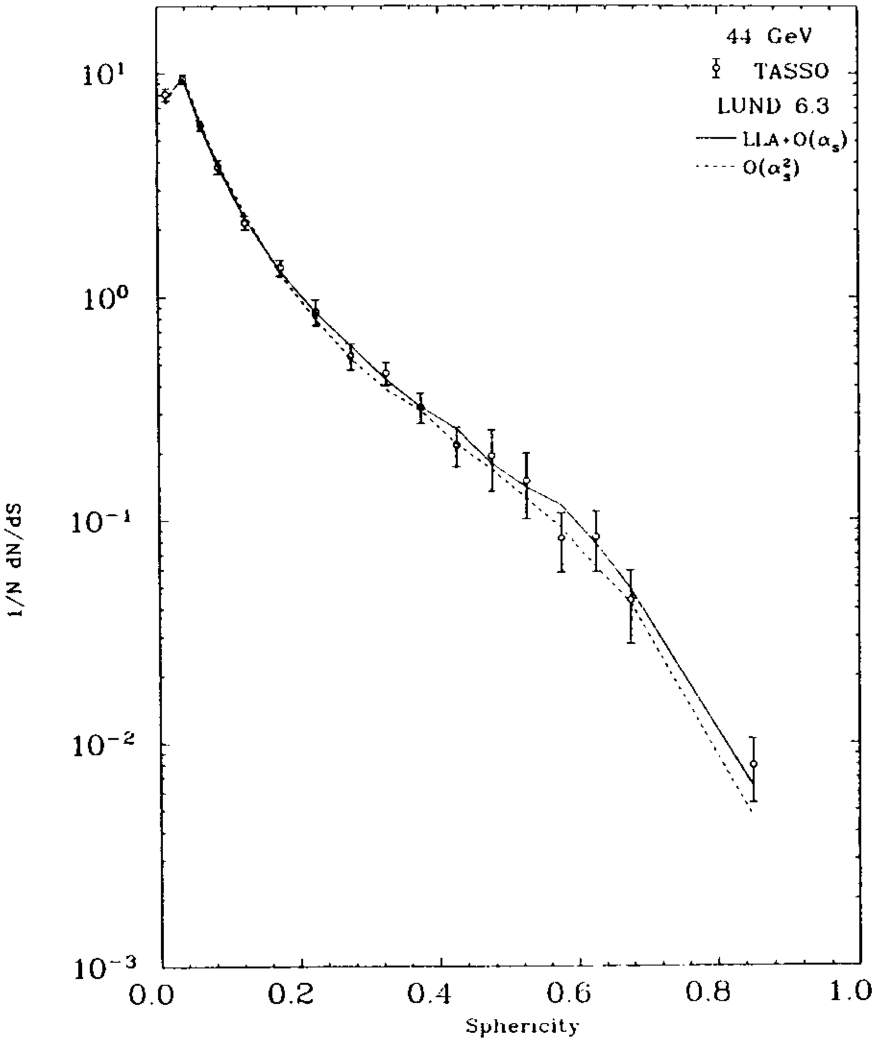

Fig. 8.1. Normalized sphericity distributions $1/N\, dN/dS$ at $\overline{W}$=44 GeV. TASSO data (points) and Lund LLA+O(α_s) Monte Carlo (full line), Lund O(α_s^2) Monte Carlo (dotted line).

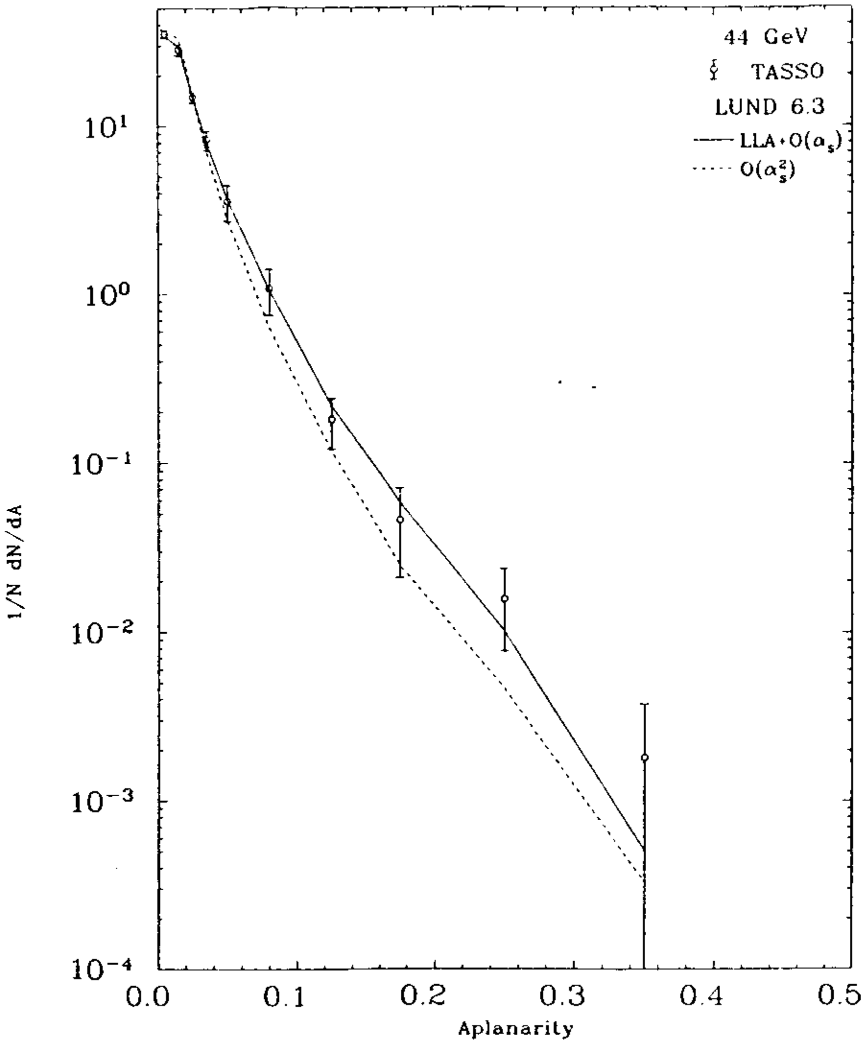

Fig. 8.2. Normalized aplanarity distributions $1/N\, dN/dA$ at $\overline{W}$=44 GeV. TASSO data (points) and Lund LLA+O(α_s) Monte Carlo (full line), Lund O(α_s^2) Monte Carlo (dotted line).

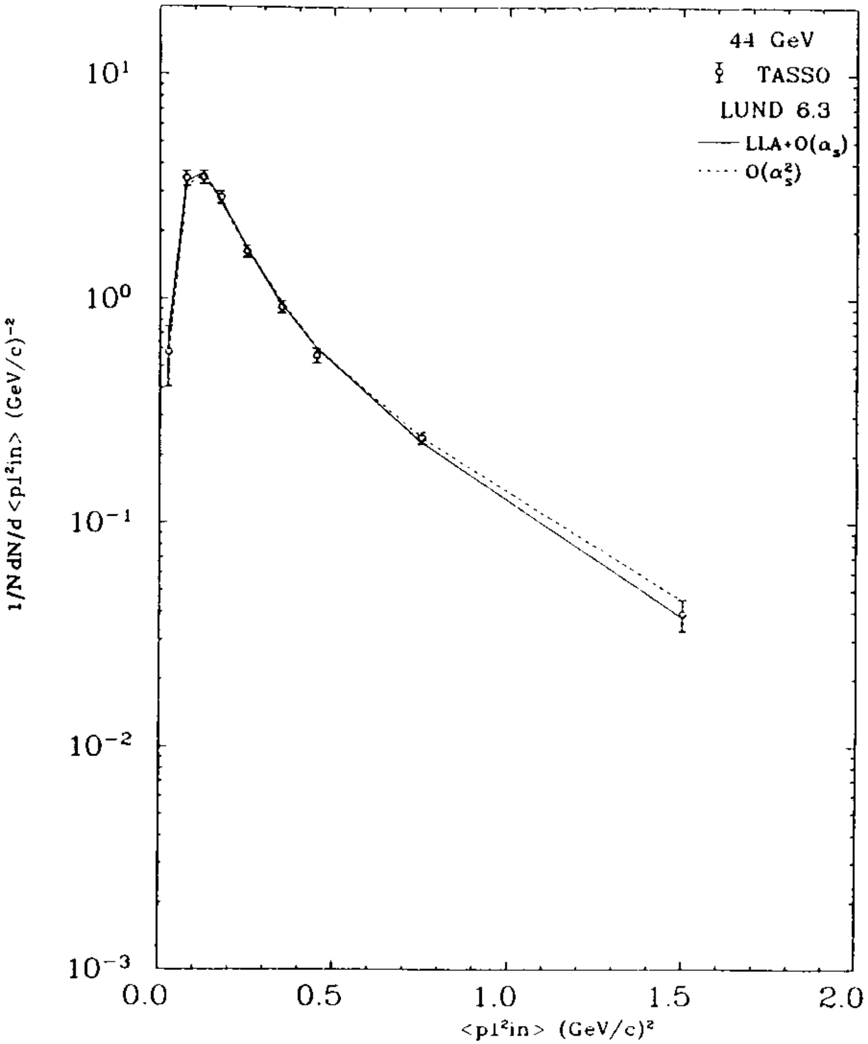

Fig. 8.3. Normalized distributions of the average transverse momentum squared in the event plane $1/N\, dN/d < p_{\perp in}^2 >$ $(\mathrm{GeV}/c)^{-2}$ at $\overline{W}$=44 GeV. TASSO data (points) and Lund LLA+O(α_s) Monte Carlo (full line), Lund O(α_s^2) Monte Carlo (dotted line).

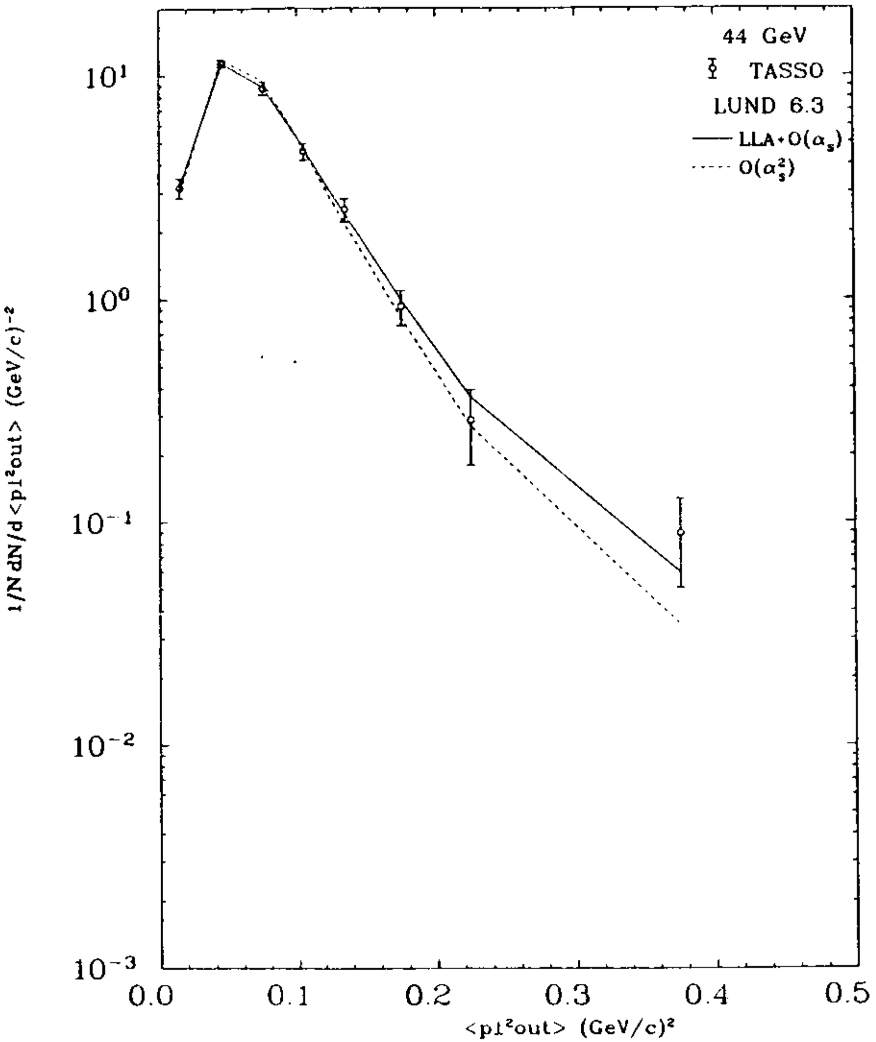

Fig. 8.4. Normalized distributions of the average transverse momentum squared *out* the event plane $1/N\, dN/d < p^2_{\perp out} >$ $(\mathrm{GeV}/c)^{-2}$ at $\overline{W}=44$ GeV. TASSO data (points) and Lund LLA+O(α_s) Monte Carlo (full line), Lund O(α_s^2) Monte Carlo (dotted line).

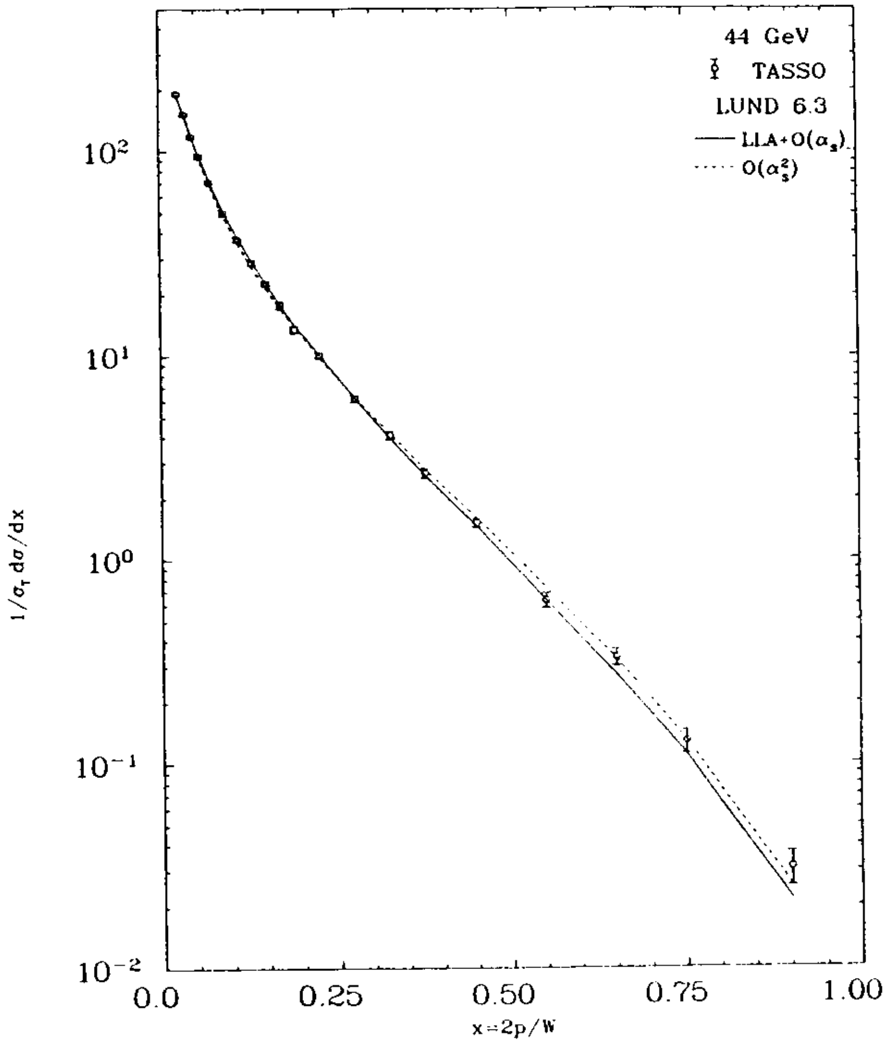

Fig. 8.5. Normalized scaled momentum distributions $1/\sigma_{tot}\, d\sigma/dx_p$, where $x_p = 2p/W$ at $\overline{W}=44$ GeV. TASSO data (points) and Lund LLA+O(α_s) Monte Carlo (full line), Lund O(α_s^2) Monte Carlo (dotted line).

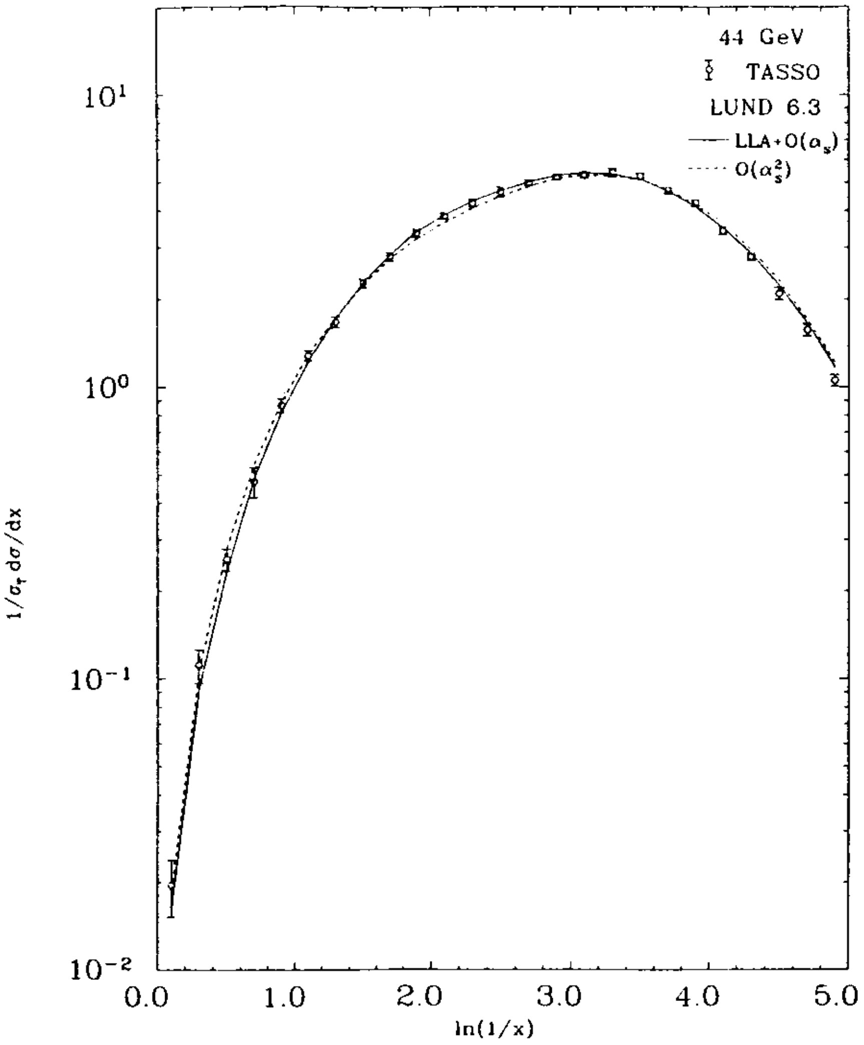

Fig. 8.6. Normalized $\ln(1/x_p)$ distributions $1/\sigma_{tot}\, d\sigma/d\ln(1/x_p)$, where $x_p = 2p/W$ at $\overline{W}$=44 GeV. TASSO data (points) and Lund LLA+O(α_s) Monte Carlo (full line), Lund O(α_s^2) Monte Carlo (dotted line).

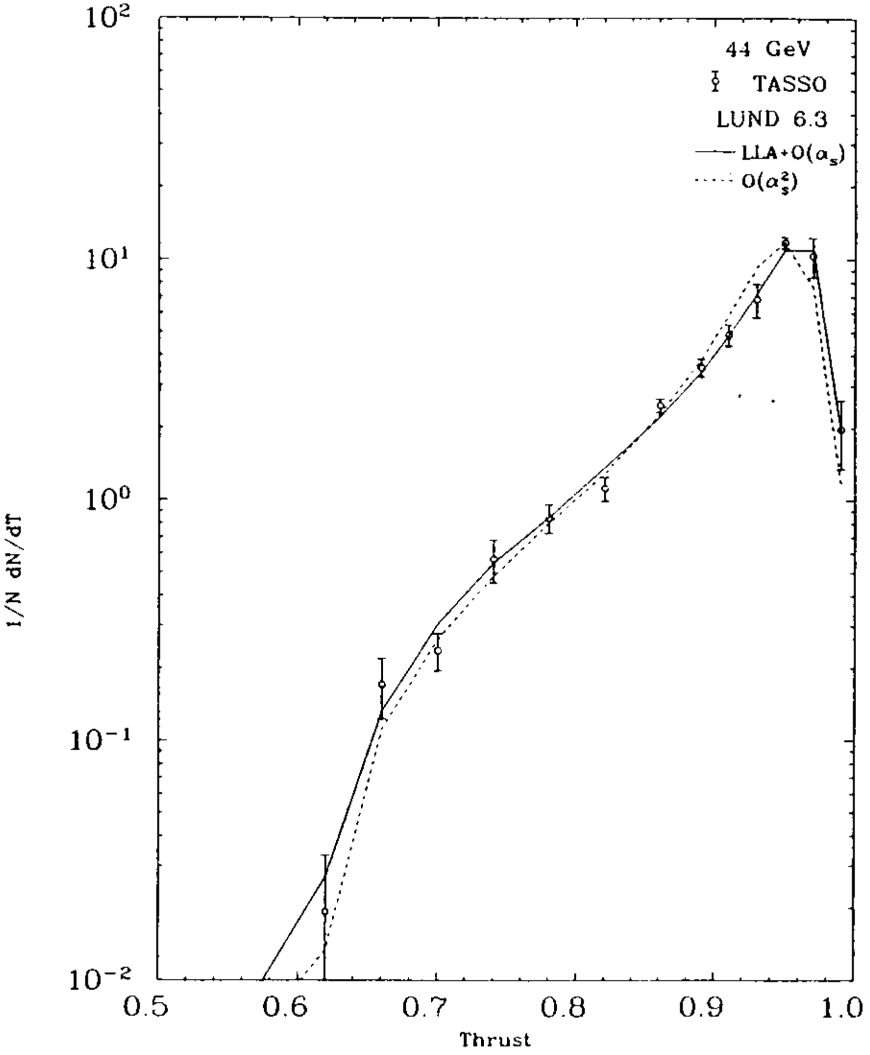

Fig. 8.7. Normalized thrust distributions $1/N\, dN/dT$ at $\overline{W}$=44 GeV. TASSO data (points) and Lund LLA+O(α_s) Monte Carlo (full line), Lund O(α_s^2) Monte Carlo (dotted line).

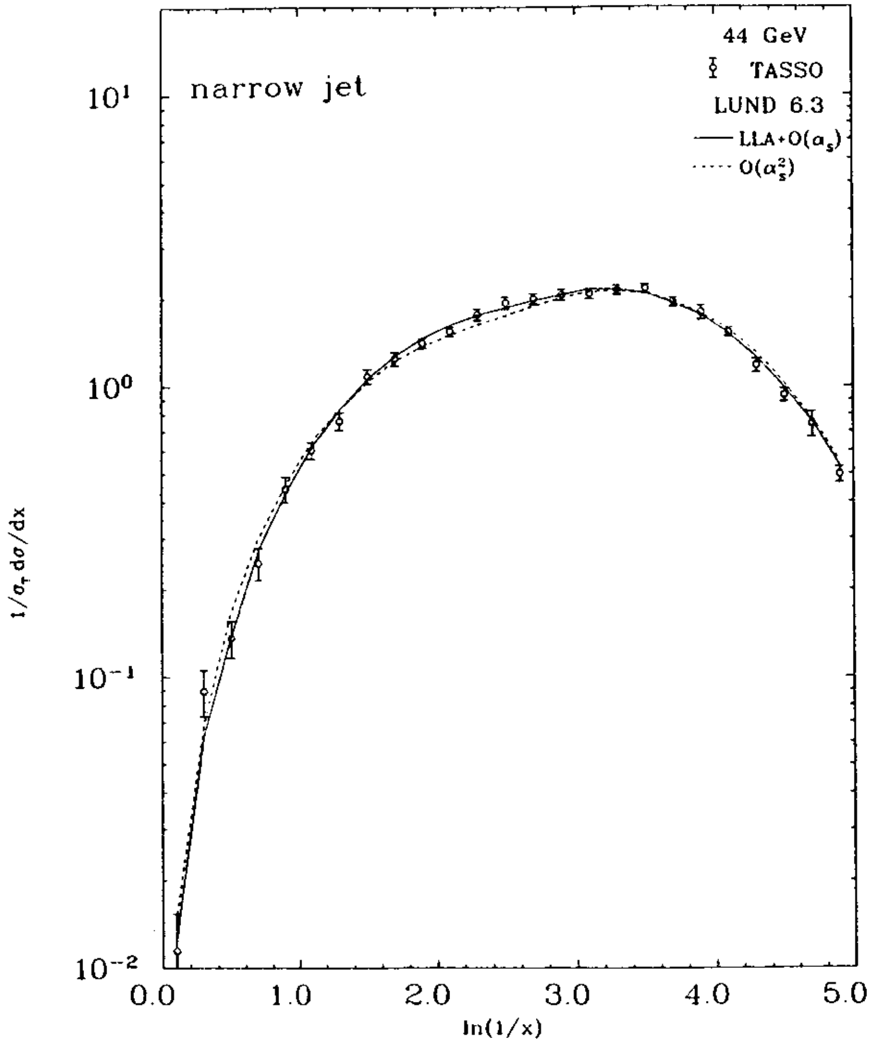

Fig. 8.8. Normalized $\ln(1/x_p)$ distributions $1/\sigma_{tot}\, d\sigma/d\ln(1/x_p)$, where $x_p = 2p/W$, for charged particles in the narrow jet at $\overline{W}$=44 GeV. TASSO data (points) and Lund LLA+O(α_s) Monte Carlo (full line), Lund O(α_s^2) Monte Carlo (dotted line).

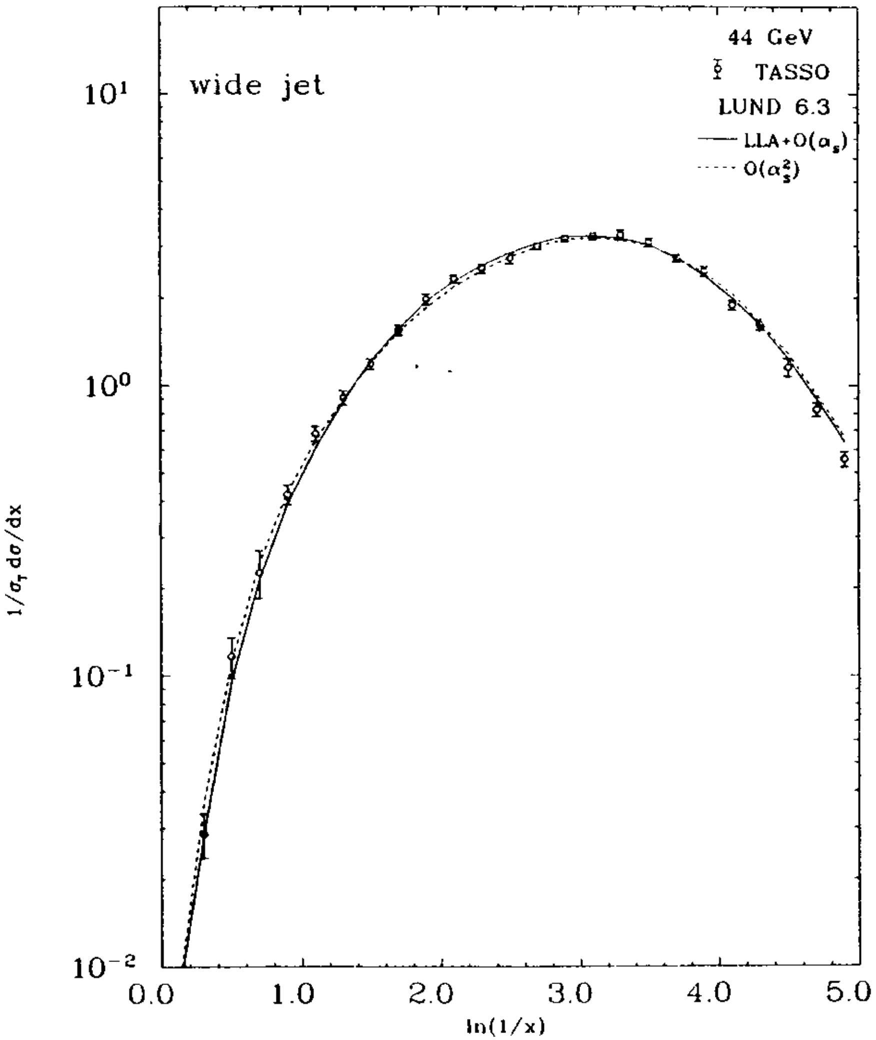

Fig. 8.9. Normalized $\ln(1/x_p)$ distributions $1/\sigma_{tot}\, d\sigma/d\ln(1/x_p)$, where $x_p = 2p/W$, for charged particles in the wide jet at $\overline{W}$=44 GeV. TASSO data (points) and Lund LLA+O(α_s) Monte Carlo (full line), Lund O(α_s^2) Monte Carlo (dotted line).

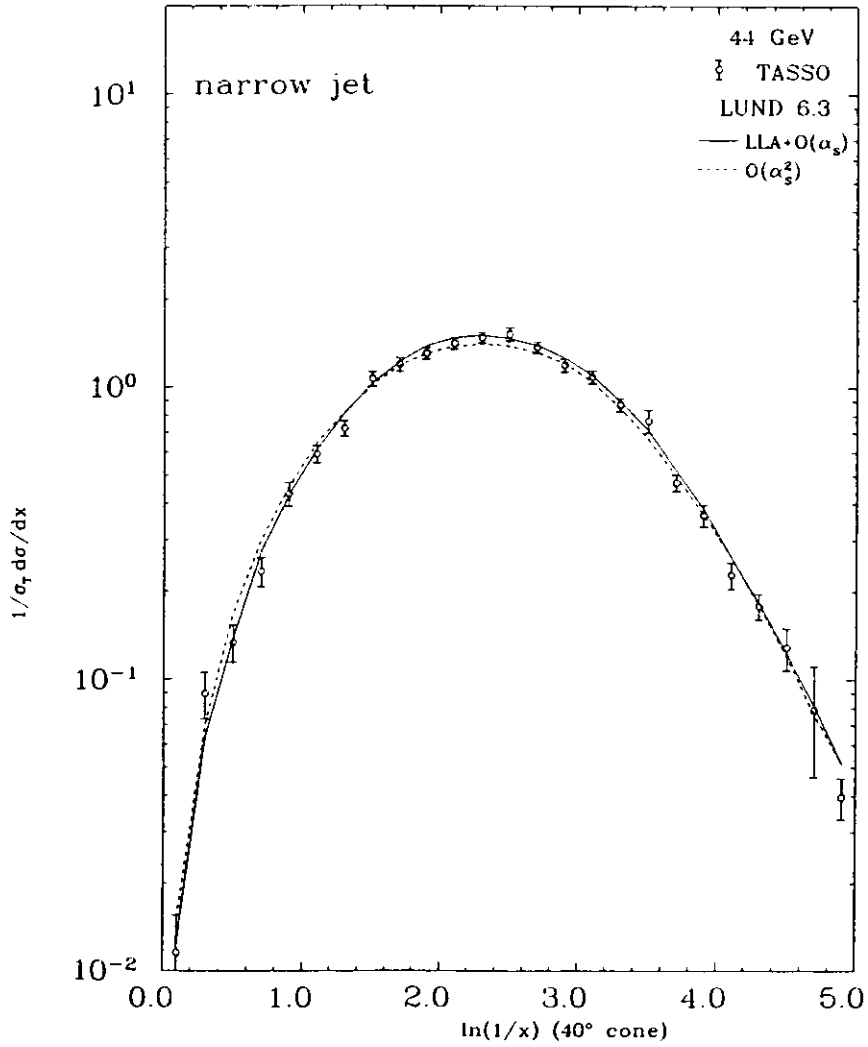

Fig. 8.10. Normalized $\ln(1/x_p)$ distributions $1/\sigma_{tot}\, d\sigma/d\ln(1/x_p)$, where $x_p = 2p/W$, for charged particles in the narrow jet emitted in a 40°cone around the event axis at $\overline{W}$=44 GeV. TASSO data (points) and Lund LLA+O(α_s) Monte Carlo (full line), Lund O(α_s^2) Monte Carlo (dotted line).

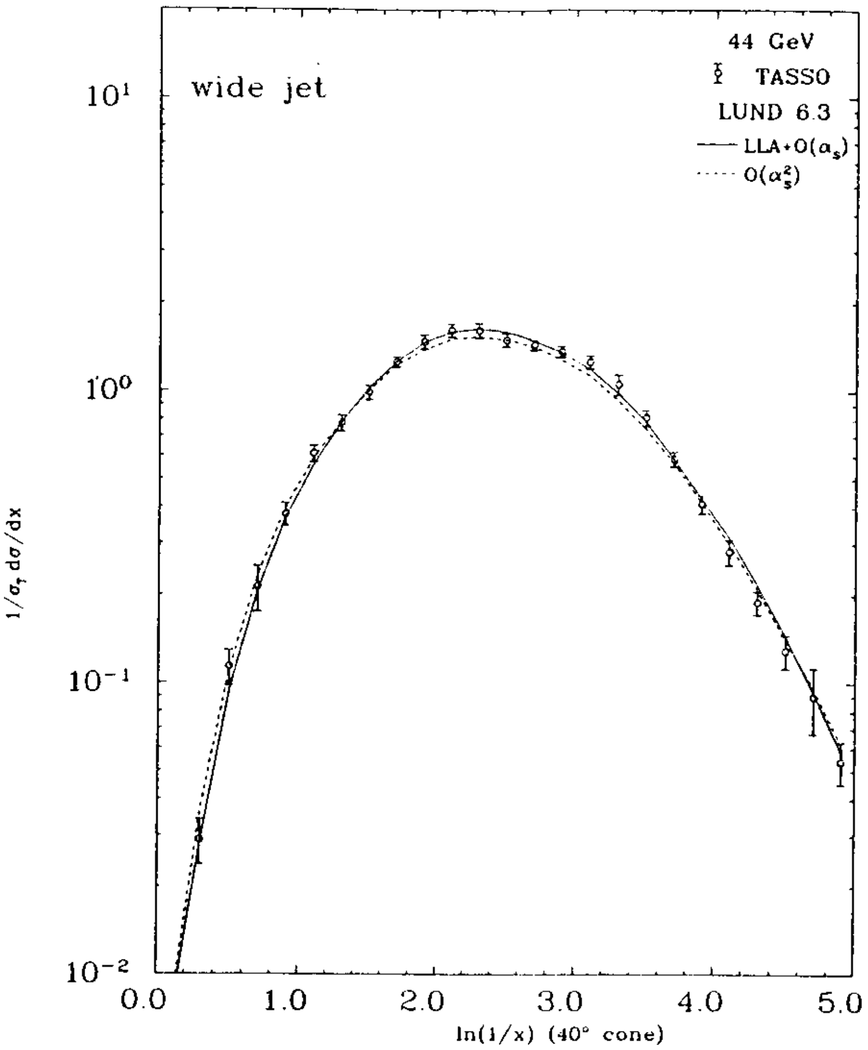

Fig. 8.11. Normalized $\ln(1/x_p)$ distributions $1/\sigma_{tot}\, d\sigma/d\ln(1/x_p)$, where $x_p = 2p/W$, for charged particles in the wide jet emitted in a 40°cone around the event axis at $\overline{W}$=44 GeV. TASSO data (points) and Lund LLA+O(α_s) Monte Carlo (full line), Lund O(α_s^2) Monte Carlo (dotted line).

8.2 Comparison of the TASSO and MARK II Results

A comparison of the TASSO data with the most recently published MARK II [MKII88] data is shown on Fig. 8.12-8.18, where x_p, S, A, T, $p_\perp$, $p_\perp^2$ and y distributions are presented. The MARK II data were chosen, because their work contains detailed numerical tables and the analysis was done using (among others) JETSET 6.3 Monte Carlo for correcting of their data.

MARK II and TASSO data agree well except for the $p_\perp$ distributions for $p_\perp \lesssim .4$ GeV/c, where MARK II reports higher yield. The average values of the S, A, $p_\perp$ and $p_\perp^2$, $\ll p^2_{\perp in} \gg$, $\ll p^2_{\perp out} \gg$ are shown in Fig. 7.8, Fig. 7.2, Fig. 7.19, Fig. 7.20, respectively. Again, consistently, MARK II reports lower transverse momentum values, that the corresponding TASSO values. The difference appears to be in the region, where the detector effects such as the angular resolution, the tracking efficiency and the electromagnetic and strong interactions with the detector material are important. The TASSO predictions [TAS88b] based on another (simplified) detector simulation programme [SIMPLE] give a higher yield at low momenta, than the yield presented in this thesis. It indicates, that until the situation is clarified the momentum distribution in this region ($p_\perp \lesssim .4$ GeV/c) should have attributed additional systematic errors of about $5 \div 10\%$.

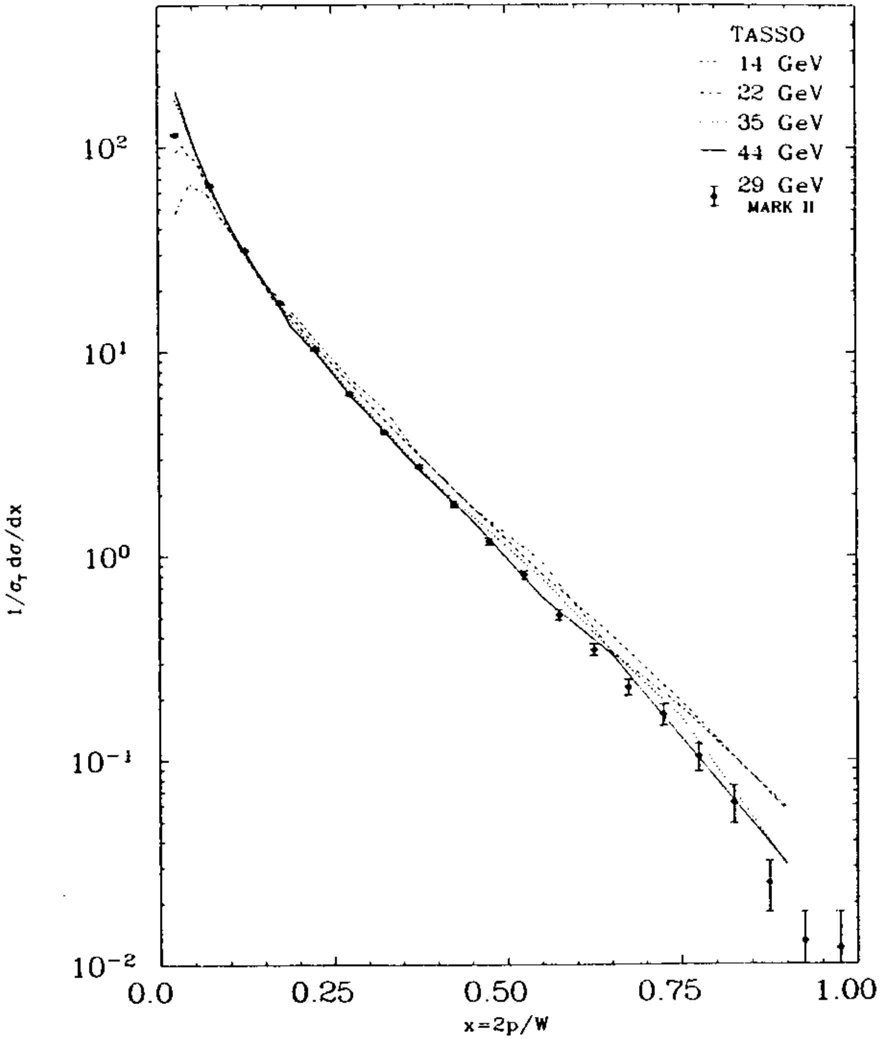

Fig. 8.12. Normalized scaled momentum distributions $1/\sigma_{tot}\, d\sigma/dx_p$, where $x_p = 2p/W$. TASSO (lines) and MARK II (points) data.

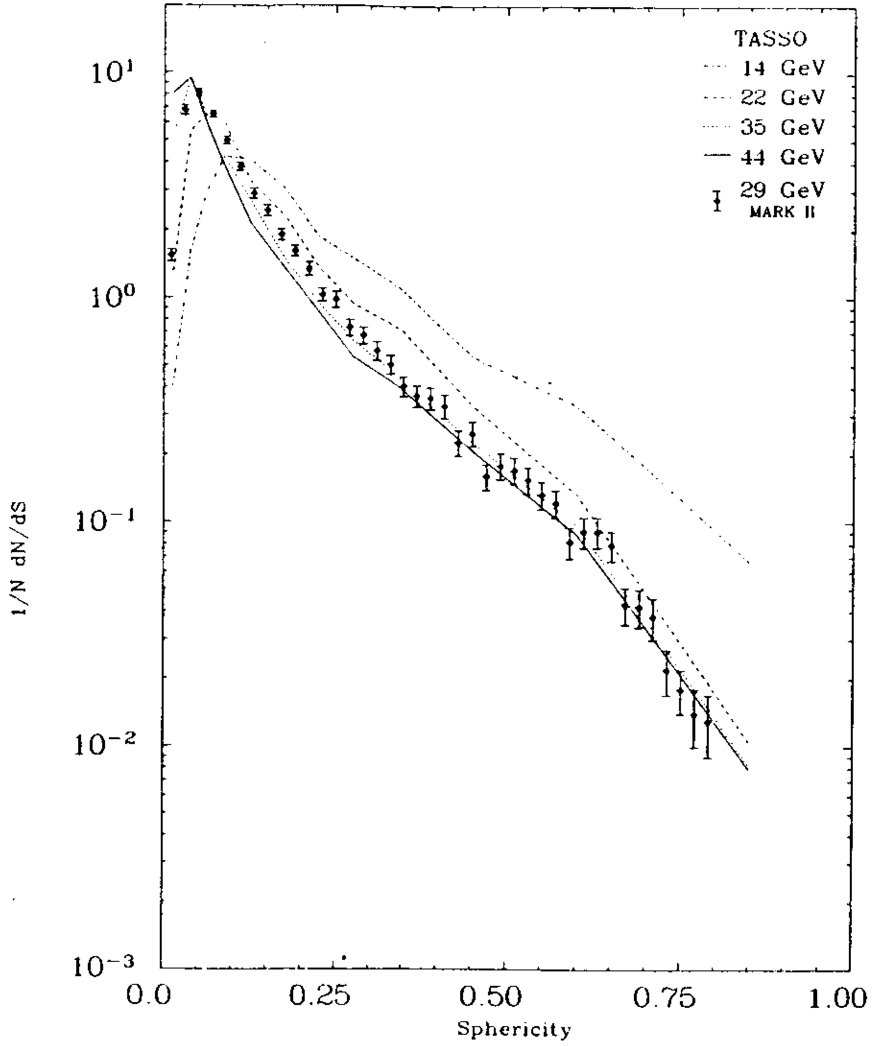

Fig. 8.13. Normalized sphericity distributions $1/N\, dN/dS$. TASSO (lines) and MARK II (points) data.

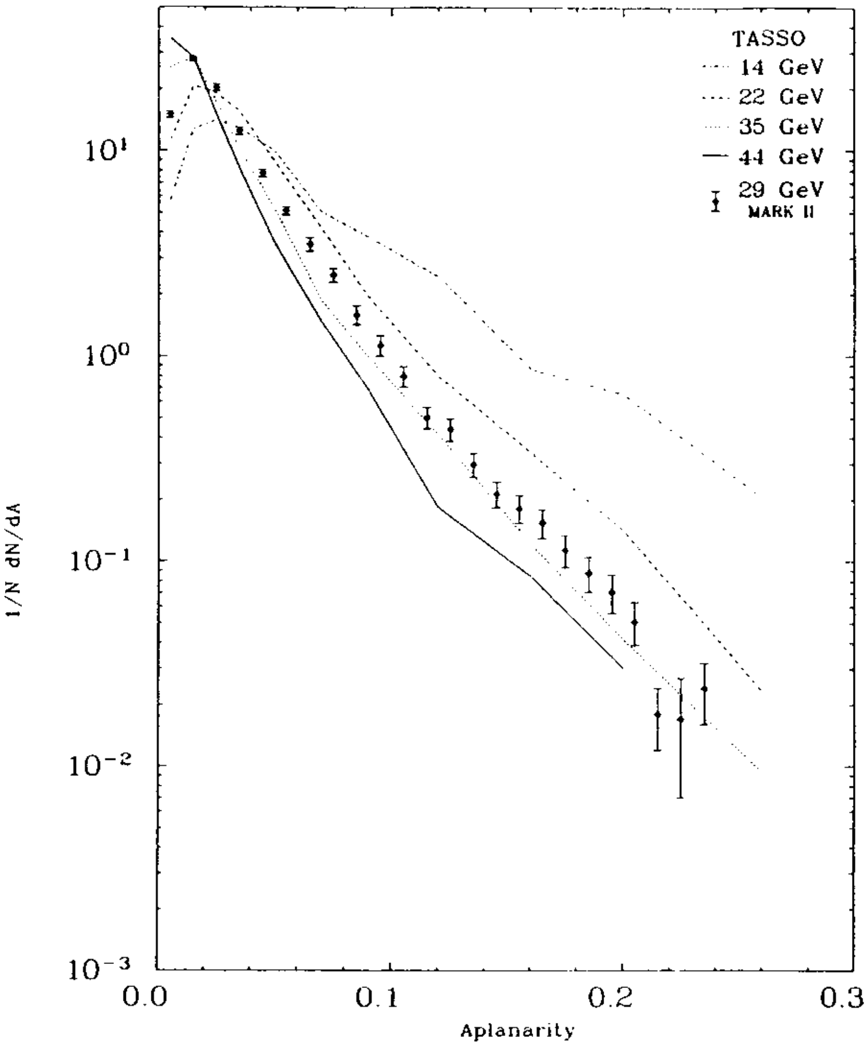

Fig. 8.14. Normalized aplanarity distributions $1/N\, dN/dA$. TASSO (lines) and MARK II (points) data.

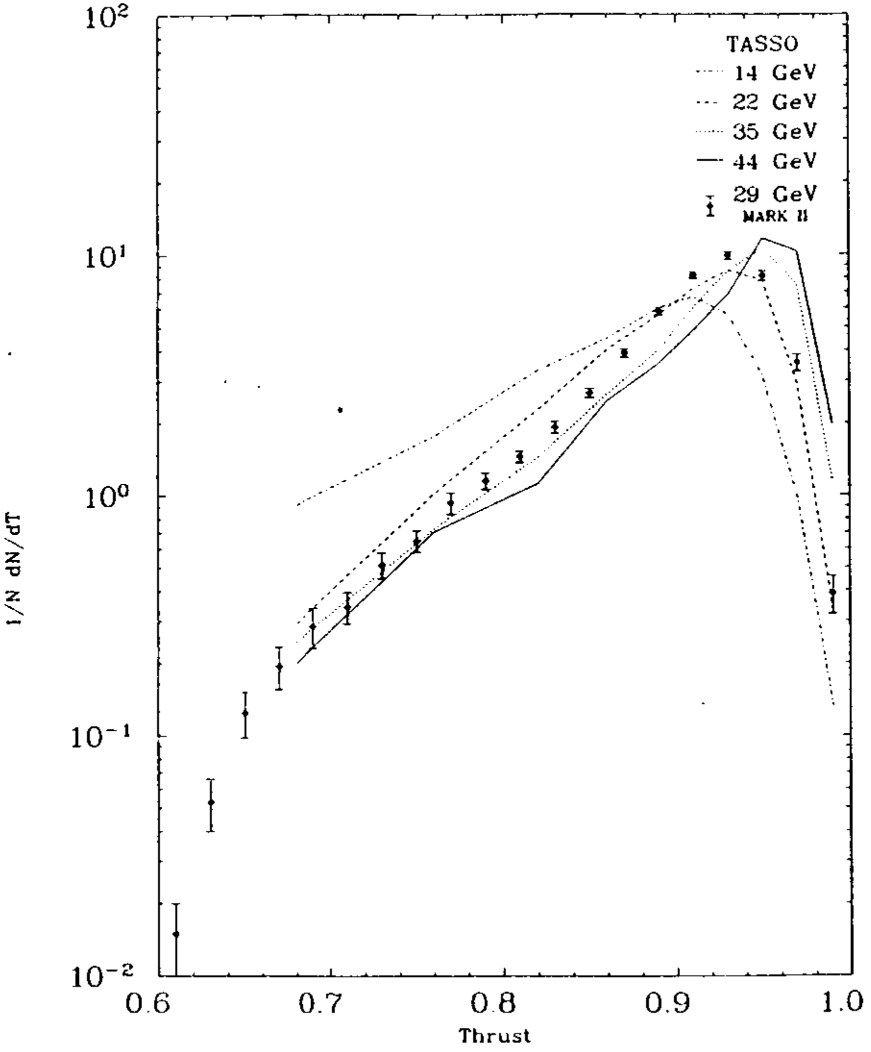

Fig. 8.15. Normalized thrust distributions $1/N\, dN/dT$. TASSO (lines) and MARK II (points) data.

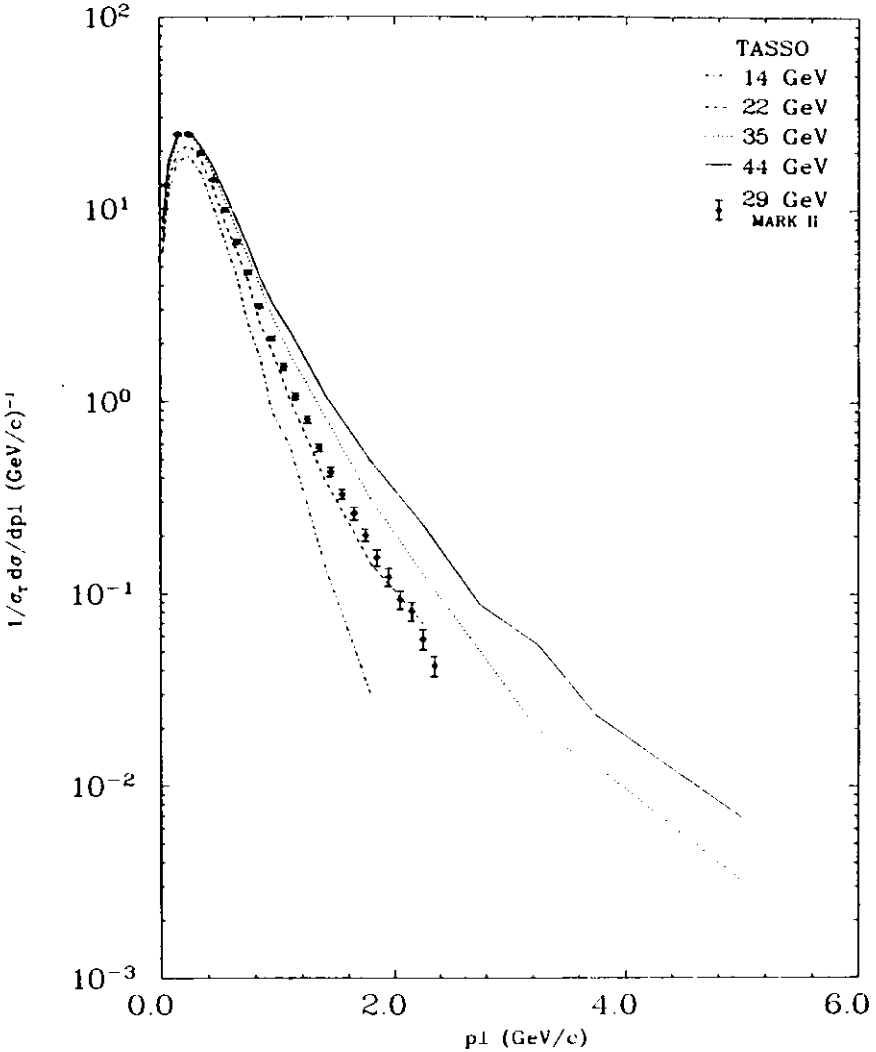

Fig. 8.16. Normalized transverse momentum distributions $1/\sigma_{tot}\, d\sigma/dp_\perp$ $(\mathrm{GeV}/c)^{-1}$. TASSO (lines) and MARK II (points) data.

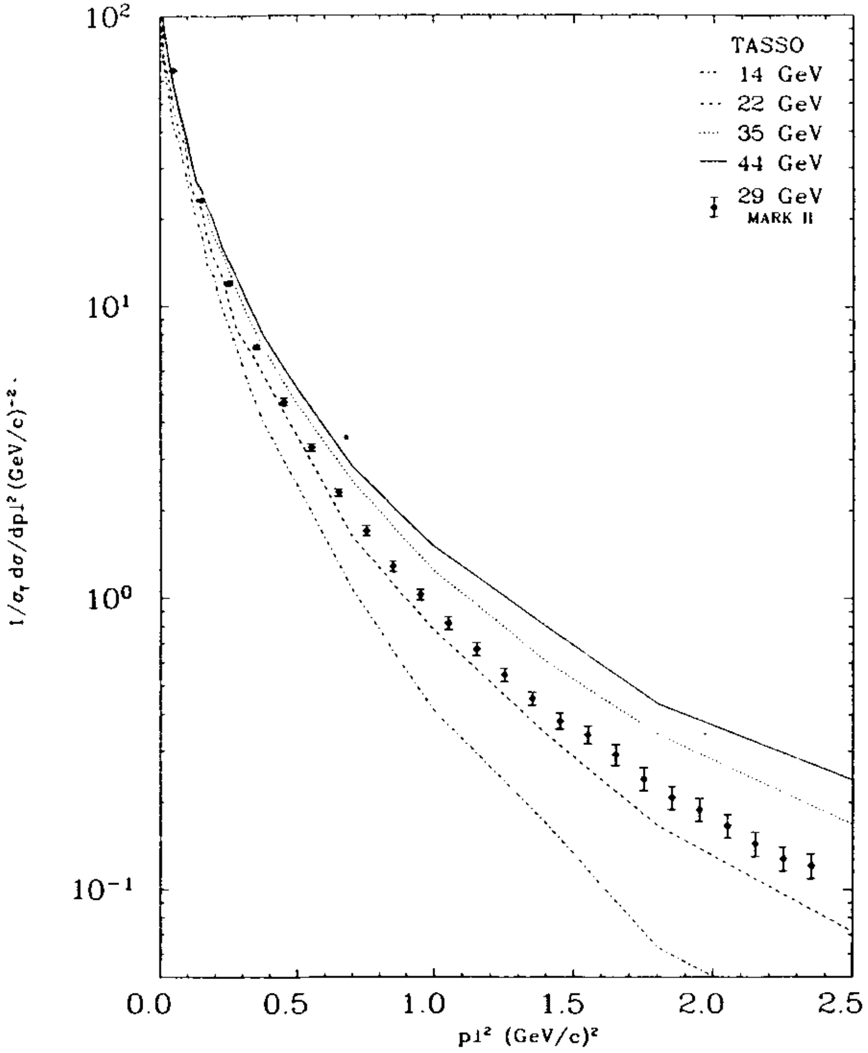

Fig. 8.17. Normalized distributions of the transverse momentum squared $1/\sigma_{tot}\, d\sigma/dp_\perp^2$ $(\mathrm{GeV}/c)^{-2}$. TASSO (lines) and MARK II (points) data.

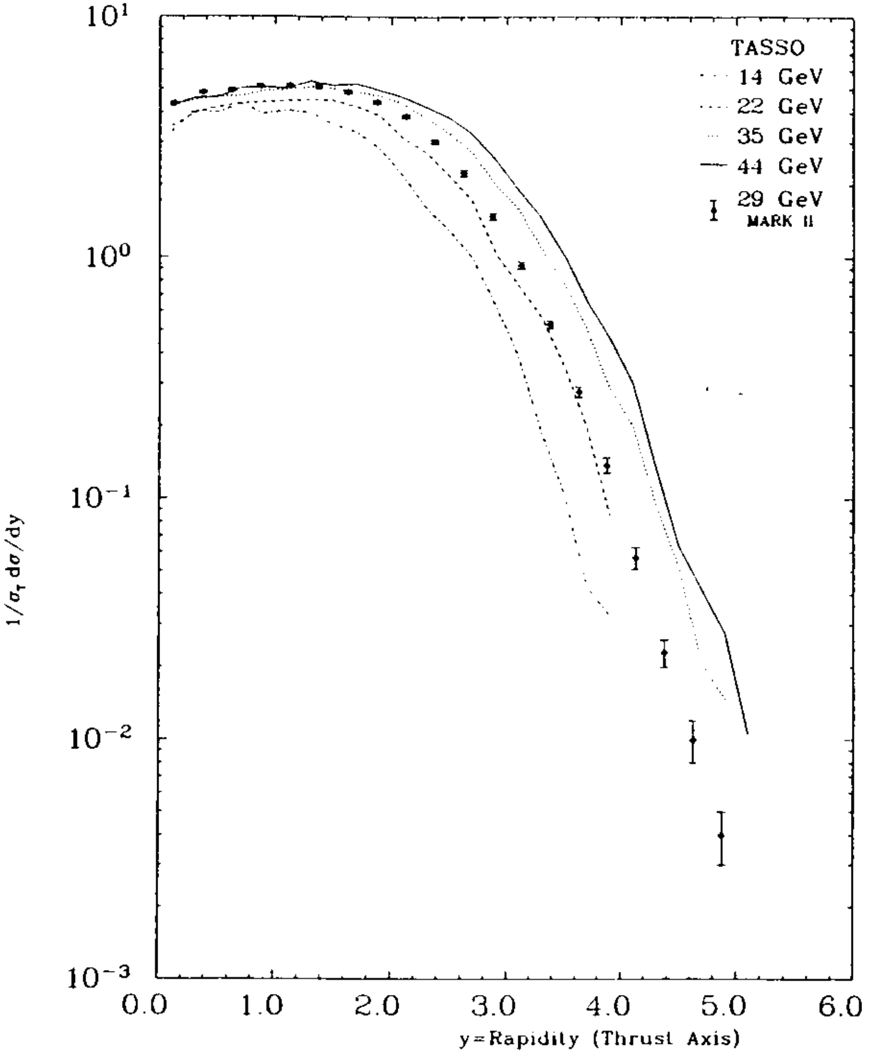

Fig. 8.18. Normalized rapidity distributions with respect to the thrust axis $1/\sigma_{tot}\, d\sigma/dy$ (folded around $y = 0$). TASSO (lines) and MARK II (points) data.

Summary

Jet properties in the center-of-mass energy energy range from 14 to 44 GeV were studied with the data collected in the TASSO detector. Corrected distributions of global shape variables such as sphericity, aplanarity, thrust and Parisi C and D variables, angular distributions of event axis, inclusive charged particle momenta, rapidities and other variables were obtained. For all distributions the statistical errors coming from the data and from the corrections and also the systematic errors originating from Monte Carlo generator used in the correcting procedure and from the selection criteria applied to the data were determined. It was made sure, that the detector response was simulated properly by the Monte Carloalso at a center-of-mass energy of 44 GeV. At all energies the same Monte Carlo event generator was used to calculate the corrections. At all energies the same correcting technique was applied to avoid systematic biases.

The total hadronic cross section for the energy interval 39 ÷ 47 GeV was found to be equal 4.11 ± .19. Energy dependence of average sphericity, aplanarity, thrust, and average momenta was studied and compared with the Lund LLA+O(α_s) and Lund O(α_s^2) Monte Carlo event generators. Results of those Monte Carlo programs were also compared with the data at a center-of-mass energy of 44 GeV.

The Lund LLA+O(α_s) Monte Carlo describes data better than Lund O(α_s^2) and has more predictive power over a larger center-of-mass energy range.

Data at a center-of-mass energy of 44 GeV in the aspects studied are in general agreement with the model predictions of Lund LLA+O(α_s) Monte Carlo calculations based on the data at lower energies.

Literature

ALI80a A. Ali *et al.*, Nucl. Phys. **B167** (1980) 454.
ALI80b A. Ali *et al.*, Nucl. Phys. **B168** (1980) 409, Phys. Lett. **93B** (1980) 155.
ALI84 A. Ali, F. Bareiro, Nucl Phys. **B236** (1984) 269.
ALI88 A. Ali, F. Bareiro, DESY report 88-075, 1988.
ALT77 G. Altarelli, G. Parisi, Nucl. Phys. **B126** (1977) 298.
ALT79 G. Altarelli *et al.*, Nucl. Phys. **B160** (1979) 301.
ALT82 G. Altarelli, Phys. Rep. **81** (1982) 1.
AND79 B. Anderson *et al.*, Z. Phys. **C1** (1979) 105.
AND83a B. Anderson *et al.*, Phys. Rep. **97** (1983) 31.
AND83b B. Anderson *et al.*, Z. Phys. **C20** (1983) 317.
AND85 B. Anderson *et al.*, Physica Scripta **32** (1985) 574.
ART74 X. Artru, G. Mennessier, Nucl. Phys. **B70** (1974) 93.
BAS83 A. Bassetto *et al.*, Phys. Rep. **100** (1983) 201.
BEI79 R. Baier and K. Fey *et al.*, Z. Phys. **C2** (1979) 339.
BEL81 K.W. Bell *et al.*, Nucl. Instr. and Meth. **179** (1981) 27.
BEN87a M. Bengtsson, T. Sjöstrand, Phys. Lett. **185B** (1987) 435.
BEN87b M. Bengtsson, T. Sjöstrand, Nucl. Phys. **B289** (1987) 810.
BER73 F.A. Berends *et al.*, Nucl. Phys. **B63** (1973) 81.
BER74 F.A. Berends *et al.*, Nucl. Phys. **B68** (1974) 541.
BER78 PLUTO Collab., Ch. Berger *et al.*, Phys. Lett. **76B** (1978) 243.
BER81 F.A. Berends and R.Kleiss, Nucl. Phys. **B177** (1981) 231, **B178** (1981) 141.
BER81p Ch. Berger *et al.*, Z. Phys. **8C** (1981) 101.
BER84 F.A. Berends *et al.*, Phys. Lett. **148B** (1984) 489.
BIE78 J.K. Bienlein *et al.*, Phys. Lett. **78B** (1978) 360.
BIN85 D.M. Binnie *et al.*, Nucl. Instr. and Meth. **228** (1985) 267.
BJO70 J. Bjorken, S. Brodsky, Phys. Rev. **D1** (1970) 1416.
BOE80 H. Boerner at al., Nucl. Instr. and Meth. **176** (1980) 151.
BOE81 H. Boerner, Ph.D. Thesis, University of Bonn, 1981.
BRA64 S. Brandt *et al.*, Phys. Lett. **12** (1964) 57.

BRO87 N. Brown *et al.*, J. Phys. **G14** (1988) 519.

CAM83 A.J. Campbell, Ph.D. Thesis, Imperial College, University of London, 1983.

CAS81 D.G. Cassel, H. Kowalski, Nucl. Instr. and Meth. **185** (1981) 235.

CEL87 CELLO Collab., H.-J. Behrend *et al.*, Phys. Lett. **183B** (1987) 400.

DAR79 C.W. Darden *et al.*, Phys. Lett. **76B** (1978) 246.

DAU86 P. Dauncey, Ph.D. Thesis, Imperial College, University of Oxford, 1986, RAL-T-034.

DOK80 Yu.L. Doksitzer *et al.*, Phys. Rep. **58** (1980) 269.

DOK84 Yu.L. Doksitzer, S. I. Troyan, Leningrad Nucl. Phys. Inst. preprint 922, 1984 (in Russian).

DOK86 Yu.L. Doksitzer *et al.*, Leningrad Nucl. Phys. Inst. preprint 1230, 1986 (in Russian).

DOK88 Yu.L. Doksitzer *et al.*, Rev. Mod. Phys. **60** (1988) 373.

DOR87 J. Dorfan, SLAC-PUB-4287, 1987.

DOW80 N. Downie, Ph.D. Thesis, Imperial College, University of London, 1980.

ELL76 J. Ellis *et al.*, Nucl. Phys. **B111** (1976) 253.

ELL79 J. Ellis, I. Karliner, Nucl. Phys. **B148** (1979) 141.

ELL81 R.K. Ellis *et al.*, Phys. Lett. **45B** (1980) 1226, Nucl. Phys. **B178** (1981) 321.

ERM81 B.I. Ermolaev, V.S. Fadin, JETP. Lett. **33** (1981) 269.

FAB82 K. Fabricius, Z. Phys. **C11** (1982) 315.

FAR77 E. Farhi, Phys. Rev. Lett. **39** (1977) 1587.

FEY69 R.P. Feynman, in *High Energy Collisions*, Gordon and Breach, New York 1969, p. 237.

FIE78 R. Field, R.P. Feynman, Nucl. Phys. **B136** (1978) 1.

FIE83 R. Field, S. Wolfram, Nucl. Phys. **B213** (1983) 65.

FIS80 H. Fischer and N. Wermes, DESY report F12-80/01, 1980.

FOX80 G.C. Fox, S. Wolfram, Nucl. Phys. **B168** (1980) 285.

GAE80 K.J.F. Gaemers, J.A.M. Vermasern, Z. Phys. **C7** (1990) 81.

GOT82 T.D. Gottschalk, Phys. Lett. **109B** (1982) 331.

GOT84 T.D. Gottschalk, Nucl. Phys. **B239** (1984) 325, 349.

GOT85 T.D. Gottschalk, M.P. Shatz, Phys. Lett. **150B** (1985) 451.

GOT87 T.D. Gottschalk, D.A. Moris, Nucl. Phys. **B288** (1987) 729.

GUT84 F. Gutbrod *et al.*, Z. Phys. **C21** (1984) 235.

GUT87 F. Gutbrod *et al.*, Z. Phys. **C35** (1987) 543.

HAN75 G.G. Hanson *et al.*, Phys. Rev. Lett. **35** (1975) 1609.

HIL80 E. Hilger *et al.*, TASSO Note N° 118, unpublished.

HOY79 D. Hoyer *et al.*, Nucl. Phys. **B161** (1979) 349.

JAD81 JADE Collab., W. Bartel *et al.*, Phys. Lett. **101B** (1981) 361.

JAD83 JADE Collab., W. Bartel *et al.*, Phys. Lett. **129B** (1983) 145.

JAD85 JADE Collab., W. Bartel *et al.*, Phys. Lett. **160B** (1985) 337.

JAM75 F.James, M. Ross, Comput. Phys. Commun. **10** (1975) 343.

JAR80 S. Jaroslawski, Nucl. Instr. and Meth. **176** (1980) 263.

JOC84 A. Jocksch *et al.*, TASSO Note N° 298, unpublished.

KOL79 K. Koller, H. Krasemann, Phys. Lett. **88B** (1979) 243.

KRA84 G. Kramer, Springer Tracts in Modern Physics, Vol 102 (1984).

KRA86 G. Kramer, B. Lampe, DESY report 86-119, 1986.

KUN81 Z. Kunszt, Phys. Lett. **99B** (1981) 429, **107B** (1981) 123.

LOE87 B. Löhr, TASSO Note N° 372, unpublished.

MAE85 P. Mättig, TASSO Note N° 336, unpublished.

MAE87p P. Mättig, private communication.

MAR82 H.-U. Martyn, TASSO Note N° 201, unpublished.

MJ81 MARK J Collab., D. P. Barber, *et al.*, Phys. Lett. **46**, (1981) 1663.

MJ86 B. Adeva, *et al.*, Phys. Rev. **D34**, (1986) 681.

MONST T. Gilead, E. Kogan, D. Revel, E. Ronat, E. Stern, U. Karshon, Y. Eisenberg, P. Dornan, E. Wicklund, TASSO Notes N° 60, 69, 80, 89, 155, 175, 184, 207, 234, 242, 268, 304, unpublished.

MII88 MARK II Collab., A. Petersen *et al.*, Phys. Lett. **D37**, (1988) 1.

MUE81 A. H. Mueller, Phys. Lett. **B104** (1981) 161.

MUT87 T. Muta, World Scientific Lecture Notes in Physics, Vol 5 (1987).

OGG81 M. Ogg, Ph.D. Thesis, Hertford College, University of Oxford, 1981.

PAR78 G. Parisi, Phys. Lett. **74B** (1978) 65.

PDG86 Particle Data Group, Phys. Lett. **170B** (1986) 12.

PET1 Deutsches Elektronen-Synchrotron, PETRA — Proposal for Extending the Storage-Ring facilities at DESY to higher Energies, DESY, Hamburg, November 1974.

PET2 Deutsches Elektronen-Synchrotron, PETRA — updated Version of the PETRA Proposal, DESY, Hamburg, February 1976.

PET3 G.A. Voss, IEEE Trans. Nucl. Sci. **NS-24** (1977) 1842.

PET4 A. Febel and G. Hemmie, IEEE Trans. Nucl. Sci. **NS-26** (1979) 3244.

PET5 D. Degele *et al.*, IEEE Trans. Nucl. Sci. **NS-28** (1981) 2025.

PET83 C. Peterson *et al.*, Phys. Rev. **D27** (1983) 105.

PLU79 PLUTO Collab., Ch. Berger *et al.*, Phys. Lett. **81B** (1979) 410.

REY81 E. Reya, Phys. Rep. **69** (1981) 195.

SCH75 R.F. Schwitters *et al.*, Phys. Rev. Let. **35** (1975) 1320.

SHI80 P. Shild *et al.*, Nucl. Instr. and Meth. **178** (1980) 571.

SIE83 H. Siebke, W. Braunschweig, TASSO Note 277, unpublished.

SIMPLE B. Foster, S. Lloyd, SIMPLE writeup, internal TASSO communication.

SOE81 P. Soeding, G. Wolf, Ann. Rev. Nucl. Sci. **31** (1981) 31.

SJO84 T. Sjöstrand, Phys. Lett. **142B** (1984) 420, Nucl. Phys. **B248** (1984) 469.

SJO86 T. Sjöstrand, M. Bengtsson, Comput. Phys. Commun. **39** (1986) 347.

SJO87 T. Sjöstrand, M. Bengtsson, Comput. Phys. Commun. **43** (1987) 367.

SJO88 T. Sjöstrand, Int. J. Mod. Phys. **A3** (1988) 751.

SU86 Su Dong, TASSO Note N° 359, unpublished.

SU87 Su Dong, Ph.D. Thesis, Imperial College, University of London, 1987.

TAS79 TASSO Collab., R. Brandelik *et al.*, Phys. Lett. **83B** (1979) 261.

TAS79b TASSO Collab., R. Brandelik *et al.*, Phys. Lett. **86B** (1979) 243.

TAS80 TASSO Collab., R. Brandelik *et al.*, Phys. Lett. **92B** (1980) 199.

TAS80b TASSO Collab., R. Brandelik *et al.*, Phys. Lett. **97B** (1980) 453.

TAS81 H. Burkhardt *et al.*, Nucl. Instr. and Meth. **184** (1981) 319.

TAS82a TASSO Collab., R. Brandelik *et al.*, Phys. Lett. **108B** (1982) 71.

TAS82b TASSO Collab., R. Brandelik *et al.*, Phys. Lett. **113B** (1982) 499.

TAS84a TASSO Collab., M. Althoff *et al.*, Phys. Lett. **146B** (1984) 443.

TAS84aa TASSO Collab., M. Althoff *et al.*, Z. Phys. **C26** (1984) 157.

TAS84b TASSO Collab., M. Althoff *et al.*, Z. Phys. **C22** (1984) 219.

TAS84c TASSO Collab., M. Althoff *et al.*, Phys. Lett. **138B** (1984) 441.

TAS84j TASSO Collab., M. Althoff *et al.*, Z. Phys. **C22** (1984) 307.

TAS88a TASSO Collab., W. Braunschweig *et al.*, Z. Phys. **C37** (1988) 171.

TAS88b TASSO Collab., W. Braunschweig *et al.*, DESY 88-109, 1988.

VER81 J.A.M. Vermasern *et al.*, Nucl. Phys. **B187** (1981) 301.

WEB84 B.R. Weber, Nucl. Phys. **B238** (1984) 492.

WIC84 E.J. Wicklund, Ph.D. Thesis, University of Wisconsin, 1984.

WU84 S.L. Wu, Phys. Rep. **107** (1984) 59.

YOU80a C. Youngman, Ph.D. Thesis, Imperial College, University of London, 1980.

YOU80 C. Youngman, TASSO Note N° 147, unpublished.

Acknowledgements

I would like to express my thanks to the following persons:

Dr. R. Walczak, Prof. J. Zakrzewski and the DESY Directorate, for enabling me to work with the TASSO Collaboration at DESY;

Prof. E. Lohrmann the thesis advisor for his inestimable supervision and care;

Dr. B. Löhr for his support and guidance through the components of the TASSO detector;

Drs. G. Rudolph and S. Ritz for introducing me into the problems of Monte Carlo tuning;

Dr. P. Mättig for explaining me the problems of data correcting;

T. Gilead and N. Wainer for help with the MONSTER Monte Carlo and for useful discussions;

all the TASSO members, former and present, for their efforts and for a fruitful collaboration;

DESY Directorate for the hospitality and financial support during my stay at DESY, and for financial support during the 25-th CERN Summer School in Physics, the Lepton-Photon Symposium in Hamburg and the German Physical Society Meeting in Freiburg,

my wife Dorota for her great help while typesetting of this manuscript.

This work was partially supported by the Polish Government Reserch Grant CPBP 01.06

Members of the TASSO Collaboration

W. Braunschweig, R. Gerhards, F.J. Kirschfink, H.-U. Martyn
I. Physikalisches Institut der RWTH Aachen, Federal Republic of Germany [a]

B. Bock[1], H.M. Fischer, H. Hartmann, J. Hartmann, E. Hilger, A. Jocksch, R. Wedemeyer
Physikalisches Institut der Universität Bonn, Federal Republic of Germany[a]

B. Foster, A.J. Martin, A.J. Sephton
H.H. Wills Physics Laboratory, University of Bristol, Bristol, UK[b]

E. Bernardi[2], J. Chwastowski[3], A. Eskreys[4], K.Gather, K. Genser[5], H. Hultschig, P. Joos,
H. Kowalski, A. Ladage, B. Löhr, D. Lüke, P. Mättig[6], D. Notz, J.M. Pawlak[5],
K.-U. Pösnecker E. Ros, D. Trines, R. Walczak[5], G. Wolf
Deutsches Elektronen-Synchrotron DESY, Hamburg, Federal Republic of Germany

H. Kolanoski
Institut für Physik, Universität Dortmund, Federal Republic of Germany[a]

W. Gerhardt, T. Kracht[7], H.L. Krasemann, J. Krüger, E. Lohrmann,G. Poelz, P. Rehders,
G. Tysarczyk, C. Winand, W. Zeuner
II. Institut für Experimentalphysik der Universität Hamburg, Federal Republic of Germany[a]

J. Hassard, J. Shulman, D. Su
Dept. of Physics, Imperial College, London, UK[b]

F. Barreiro, A. Leites, J. del Peso
Universidad Autonoma de Madrid, Madrid, Spain[c]

C. Balkwill, M.G. Bowler, P.N. Burrows, R. Cashmore G.P. Heath, P. Ratoff, I. Silvester,
I.R. Tomalin, M.E. Veitch
Dept. of Nuclear Physics, Oxford University, Oxford, UK[b]

G.E. Forden[8], J.C. Hart, D.H. Saxon
Rutherford Appleton Laboratory, Chilton, Didcot, UK[b]

S. Brandt, M. Holder, L. Labarga[9]
Fachbereich Physik der Universität-Gesamthochschule Siegen,
Federal Republic of Germany[a]

Y. Eisenberg, U. Karshon, G. Mikenberg, A. Montag, D. Revel, E. Ronat, A. Shapira,
N. Wainer, G. Yekutieli
Weizmann Institute, Rehovot, Israel[d]

D. Muller, S. Ritz, D. Strom[10], M. Takashima, Sau Lan Wu, G. Zobernig
Dept. of Physics, University of Wisconsin, Madison, WI, U.S.A.[e]

[1] Now at Krupp Atlas Elektr. GmbH, Bremen, F.R.G.
[2] Now at Robert Bosch GmbH, Schwieberdingen, F.R.G.
[3] On leave from Inst. of Nuclear Physics, Cracow, Poland
[4] Now at Inst. of Nuclear Physics, Cracow, Poland
[5] Now at Warsaw University [f], Poland
[6] Now at IPP Canada, Carleton University, Ottowa, Canada
[7] Now at Hasylab, DESY.
[8] Now at SUNY Stony Brook, Stony Brook, NY, USA
[9] Now at SLAC, Stanford, CA, U.S.A.
[10] Now at University of Chicago, Chicago, IL, U.S.A.
[a] Supported by Bundesministerium für Forschung und Technologie
[b] Supported by UK Science and Engineering Research Council
[c] Supported by CAICYT
[d] Supported by the Minerva Gesellschaft für Forschung GmbH
[e] Supported by US Dept. of Energy, contract DE-AC02-76ER000881 and by US Nat. Sci. Foundation Grant number INT-8313994 for travel
[f] Partially supported by grant CPBP 01.06